Physikalisches Institut
Fakultät für Mathematik und Physik

Albert-Ludwigs-Universität
Freiburg im Breisgau

Development of a Two-Photon Absorption - TCT system and Study of Radiation Damage in Silicon Detectors

Dissertation

Author: Moritz Wiehe

Supervisors: Dr. Ulrich Parzefall
Dr. Christian Weiser
Dr. Michael Moll

Submission: August, 2021

Abstract

This work is a contribution to the development of radiation hard silicon detectors for the application in high energy physics experiments.
First, a study was carried out to investigate radiation induced effects in Low Gain Avalanche Detectors (LGADs) and how these effects change with annealing of the devices. For this, two LGADs were irradiated with 24 GeV/c-protons to a fluence of 10^{14} n_{eq}/cm^2. The sensors were then characterized as a function of annealing time by measurements of the leakage current and the capacitance and by measurements using the Transient Current Technique (TCT). An initial decrease of gain, as well as a reduction of the gain layer depletion voltage was observed after irradiation. No further change of gain with annealing was observed. The decrease of gain with irradiation and the change of the gain layer depletion voltage was attributed to a deactivation of the gain layer, mainly due to the acceptor removal effect. A change of the charge collection onset voltage for top-TCT measurements with annealing time was explained by a build-up of charge at the backside, which changes the electric field configuration in the sensor. This effect vanished after reverse annealing.
In addition, a tabletop TCT-setup, using two-photon absorption (TPA-TCT), was constructed and commissioned. TPA-TCT is a novel technique for sensor characterization with improved spatial resolution in 3D. Strong focusing of laser light with sub-bandgap photon energy is used to create free charge carriers in silicon only at the focal point of the beam. Measurements performed so far were carried out at dedicated laser laboratories. The setup, developed in the course of this work, serves as a prototype for other research institutes. All components of the setup, including free-space laser optics, the electrical and mechanical devices, were acquired and installed. First tests revealed shortcomings of the laser source, which were addressed by the manufacturer in an upgrade of the source. The setup is now operational and initial measurements were successful. A description and characterization of the setup, as well as the results of first measurements are presented.

Contents

1. Introduction

Silicon sensors are the backbone of modern day particle tracking detectors due to their high radiation hardness, good spatial and timing resolution and the possibility to produce them at commercial vendors in large quantities. Silicon, as a material for the construction of all kinds of electronic devices, is very well understood. Design and manufacturing processes have been refined over decades. However, in high energy physics silicon sensors have to withstand an intense radiation environment, which poses unique challenges for the design and operation of these sensors. The most demanding environment for particle detectors today is the Large Hadron Collider (LHC). In all LHC-experiments silicon sensors are used closest to the interaction point for particle track reconstruction and vertex identification. The total radiation fluence, which current detectors have to withstand in the innermost layers, is as high as 10^{15} n_{eq}/cm^2. The continuous radiation degrades the charge collection properties of the sensors and leads to a higher leakage current. Up to a certain degree these effects can be mitigated by an increased bias voltage and sufficient cooling, but eventually the detectors reach their end of life. To increase the radiation hardness of silicon sensors in these environments, and to develop new detector technologies with improved resolution and speed, the RD50 collaboration[1] was established. The LHC will undergo an upgrade to the High-Luminosity LHC (HL-LHC) with an increased number of particle interactions per bunch crossing and, as a result, a much increased radiation fluence. The higher particle rates also pose higher demands on the resolution of the detector. To successfully disentangle up to 200 primary vertices during a single bunch crossing, timing detectors are becoming more important. The experiments ATLAS [1], CMS [2] and LHCb [3] are planning to use dedicated timing planes equipped with Low Gain Avalanche Detectors (LGADs). LGADs feature a highly doped gain layer to increase their signal charge by avalanche multiplication of the primary electrons. The high signal at a moderate device thickness leads to a low signal rise time, which makes this type of detector very suited for timing measurements. Radiation damage changes the gain layer and bulk properties of LGADs, leading to a reduction in gain and a change in the electric field distribution within the sensor. The first part of this work is devoted to investigating these effects and the interplay of gain reduction, a changing space charge region and annealing of the devices. LGADs were tested after irradiation with 24 GeV/c protons to a fluence of 1×10^{14} n_{eq}/cm^2 and successive annealing, using the Transient Current Technique (TCT) and IV- and CV-measurements.

The development of novel silicon sensors with higher spatial and timing resolution is not possible without precise sensor characterization setups. The Transient Current Technique is an important tool to investigate a multitude of sensor parameters. Laser light in the red or near-infrared is used to create charge carriers near the surface or throughout the full device thickness, depending on the laser wavelength. Spatial scans are carried out to investigate the charge collection homogeneity or probe the electric field as a function of depth inside the detector, by injecting light from the edge of a device. The drift of electrons and holes can be investigated independently by light injection from the front or backside. In recent years a new measurement method, Two-Photon Absorption-TCT (TPA-TCT), was developed. TPA-TCT uses light in the near infrared, but with a photon energy below the silicon bandgap. Generating charge carriers by light absorption is only possible by two-photon absorption,

[1] RD50, CERN, https://rd50.web.cern.ch

which requires a high light intensity. By using strong focusing optics, it can be achieved that charges are only created at the focal point of the beam in a volume of approximately $1 \times 1 \times 10\ \mu m^3$. The focal point of the beam can be moved inside the silicon sensor, allowing for 3D spatial resolution. The method of TPA-TCT for the characterization of silicon particle detectors was proposed in 2014 and successfully tested at the UPV/EHU laser facility[2] [4, 5, 6, 7]. The goal of this thesis work is to develop the first tabletop TPA-TCT setup to make it possible to use this technique easily on a daily basis for the characterization of silicon sensors.

This thesis is grouped into two parts. A brief introduction to silicon sensors and radiation damage is followed by a description of the existing measurement setups and a summary of the findings of the study of radiation damage in LGADs (chapters 2-4). The second part starts with an introduction to the principles of TPA-TCT (chapter 5). Some concepts of optics, which are important for the development and operation of the new setup, are briefly discussed. In the last chapter (chapter 6) the setup is described and first measurements are presented to show the strengths and weaknesses of TPA-TCT.

[2] UPV/EHU Singular Laser Facility Laboratory, Bilbao, Spain, http://www.ehu.eus/en/web/sgiker/laser-tresna-aurkezpena

2. Silicon Particle Detectors

For high precision particle tracking, solid state detectors are widely used in high energy physics experiments. Silicon became the prevalent choice as detector material due to its high availability, comparably small bandgap, leading to a high signal charge, and its high radiation hardness. Silicon is used widely in the electronics industry, enabling the possibility for synergies in the development and production of detectors. Silicon sensors can be segmented with high granularity, giving them a high spatial resolution. In recent years the timing capabilities of detectors became more important. The increase in luminosity after the upgrade of the LHC to the High-Luminosity LHC leads to an increase in event pile-up, making it necessary to distinguish different particle events by measuring their separation in time. New sensor designs, e.g. the Low Gain Avalanche Detector (LGAD), have been developed for this purpose.
In this chapter, silicon detectors and their functionality are introduced. It follows a brief discussion of LGADs and the effects of radiation damage on silicon sensors. A more detailed description of silicon sensors can e.g. be found in [8] or [9]. A comprehensive overview of semiconductor physics can be found in [10].

2.1. Working Principle

When a charged particle traverses a silicon detector, pairs of weakly bound electrons and holes are created in ionizing interactions of the particle with the silicon atoms. By applying an external electric field the electron-hole-pairs can be separated before recombination is possible. The resulting drift of the charge carriers in the direction of the electrodes can be measured as a signal current.
The two main considerations when choosing a material to build a detector is how much charge can be generated for a given amount of deposited energy and how this charge can be transformed into a measurable signal. In principle, a low energy deposition is desirable for tracking detectors to maintain a low material budget of the detector and reduce multiple scattering. Therefore materials with a low atomic number are favored (silicon: $Z = 14$). The signal yield, i.e. the amount of charge generated for a given amount of deposited energy, depends mostly on the ionization energy of the material. The ionization energy is the average amount of deposited energy needed to create a single electron-hole-pair (or electron-ion-pair for gases) and is 3.6 eV for silicon. In comparison, germanium has an ionization energy of 3 eV, diamond about 13 eV and gas detectors have a significantly higher ionization energy of about 30 eV. Electronic properties, the charge transport and generation of charges in solids are usually described in an energy band picture. The discrete energy levels of the respective atomic orbitals which electrons can occupy form energy bands when atoms are bound in a crystal lattice. Conduction in a material is possible if little energy is required to promote an electron to an unoccupied (anti-bonding) state. Metals have a high number of available energy states and no energy gap between filled and unoccupied states. Electrons are therefore loosely bound to single atoms (delocalized) and can move relatively freely in the lattice. Silicon, a semiconductor, is a type IV material with four valence electrons which occupy the two 3s- and two of the six available 3p-orbitals. In a silicon crystal lattice all four valence electrons are contributing to the four covalent bonds to the respective neighboring

atoms. Therefore the valence band in a silicon crystal is completely filled with no electrons in higher energy states. The bandgap between the highest filled electronic state and the lowest unoccupied electronic state (the difference between valence and conduction band) is $E_g = 1.12$ eV. The value of the bandgap determines if a material is classified as a semiconductor, like silicon, or insulator. In insulators the bandgap is large enough to prohibit any thermal excitation of electrons to the conduction band. In semiconductors the conductivity depends strongly on temperature because electrons can be promoted to the conduction band by thermal excitation. In solid-state physics the Fermi-level E_F is used to quantize the electronic behavior of a material. It is defined as a hypothetical energy level which, at thermal equilibrium, has a 50% chance of being filled with an electron. The Fermi-level of an intrinsic semiconductor lies very close to the middle of the bandgap. The probability of a given energy state at energy E to be occupied with an electron is described by the Fermi-Dirac distribution [8]

$$f(E) = \frac{1}{e^{(E-E_F)/kT} + 1}. \tag{2.1}$$

In this and the following equations k and T denote the Boltzmann constant and temperature, respectively. The picture of homogeneous energy bands, which can be filled or not filled is simplified. In reality, also the density of states in an individual band depends on energy. The difference of the bandgap and the average ionization energy is due to the fact that silicon is a semiconductor with an indirect bandgap. Any transition of an electron across the bandgap has to satisfy conservation of crystal momentum (or wave vector k). This happens by absorbing or emitting phonons to the crystal lattice. It is for this reason that semiconductors with an indirect bandgap are usually not used for constructing LEDs or lasers. The probability of radiative transitions across the bandgap is much lower for indirect bandgap semiconductors than for direct bandgap semiconductors. In addition, light emission and absorption in indirect bandgap semiconductors shows a stronger temperature dependence.
In intrinsic silicon the number of electrons and holes is equal. The intrinsic charge carrier density at 300 K is $n_i = 9.65 \cdot 10^9$ cm^{-3} [11]. The number of free charge carriers due to thermal excitation and the larger number of impurities in the crystal is too high to measure the comparably small signal current resulting from ionization by a charged particle. The technique to deplete the detector material from free charge carriers is to form a pn-junction.

2.1.1. PN-junction

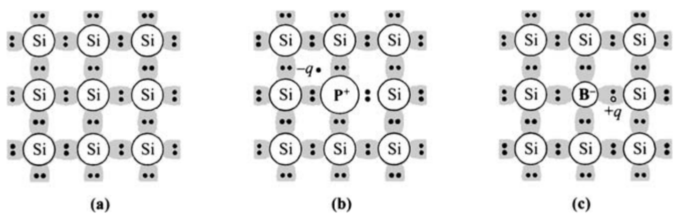

Figure 2.1. – (a) Intrinsic silicon with no additional impurities. (b) N-type silicon with donor (phosphorus) and free electron. (c) P-type silicon with acceptor (boron) and hole. Image from [10]

The conductivity of silicon can be increased by doping with foreign atoms. In this process a low number of atoms with a different number of valence electrons is introduced to the crystal lattice. If the artificially introduced atom has one valence electron more than silicon, this electron will not be used in bonding to neighboring silicon atoms and only a small amount of energy is needed to excite this

electron to the conduction band. The energy state that is introduced in this process lies in the bandgap but very close to the conduction band. Since the dopant introduces a quasi-free electron to the silicon crystal it is referred to as donor. The silicon, which was intrinsic before, is now of n-type. Commonly phosphorus is used as a donor atom. Due to the introduction of additional energy states close to the conduction band the Fermi level is shifted to higher energies in n-type silicon. In the opposite case, if an atom with one valence electron less than silicon is introduced into the crystal (commonly boron), one of the crystal bonds remains with a vacant position which can be filled by neighboring valence electrons or by recombination. Effectively this introduces a hole to the crystal, thus the dopant atom is referred to as acceptor. In this case the additional energy state is located just above the valence band and the Fermi level in so-called p-type material is shifted to lower energies. A schematic view of the bonding of phosphorus and boron dopants in the silicon lattice is shown in fig. 2.1. The density of introduced donors or acceptors very much depends on the desired behavior of the semiconductor and can be fine tuned in the production process. Typical dopant densities can range from 10^{12} cm^{-3} to 10^{16} cm^{-3} and 10^{18} cm^{-3} to 10^{19} cm^{-3} for strip/pixel and backplane implants. Compared to the overall density of silicon atoms of about 10^{22} cm^{-3} these numbers are comparably small but since the charge carrier density is low in intrinsic silicon the deliberate introduction of dopants has a very significant effect on the material's conductivity.
A pn-junction is formed by combining both p- and n-type doping in a single silicon wafer. Usually this means introducing a shallow, heavily doped n (or p) -type layer onto a wafer of the opposite type. The interface between p-type and n-type volumes is called junction. For understanding the basic principle of operation the junction can be assumed to be abrupt. In reality the doping profile changes gradually. Due to the difference in carrier concentration on either side of the junction, electrons will diffuse from the n-side to the p-side and holes will diffuse from the p-side to the n-side. The minority carriers (electrons in p-type material and holes in n-type material) will then recombine with one of the majority carriers. This process leads to a diffusion current across the junction. Since both n-type and p-type silicon is electrically neutral initially, the diffusion of charge carriers leads to the build up of a zone of negative space charge on the p-side due to the excess electrons and to one of positive space charge on the n-side of the junction. This causes the build up of an electric field leading to a drift current. Drift and diffusion currents have opposite directions and balance each other in amplitude when the pn-junction is in thermal equilibrium. In this condition the Fermi level has to be constant across the junction. Because the Fermi level is closer to the conduction band on the n-side and closer to the valence band on the p-side, this leads to a distortion of the band structure across the junction which manifests itself in a potential difference. This voltage is commonly referred to as build-in voltage [8]

$$V_{bi} = -\frac{kT}{q_e} \log \frac{N_a N_d}{n_i^2}. \tag{2.2}$$

The build-in voltage depends only on the acceptor and donor densities N_a and N_d. The electron charge is denoted by q_e. The space charge region is depleted of free charge carriers.

PN-junction under external bias

The pn-junction, or diode, is used widely in electronics due to its rectifying properties and is the fundamental building block of a transistor. In general, if a positive voltage is applied to the p-side (forward bias) a current can flow through the junction. If a negative voltage is applied to the p-side (reverse bias) on the other hand, no current will flow, except for a small leakage or dark current.
Fig. 2.2 shows the band structure of a pn-diode in thermal equilibrium and under forward and reverse

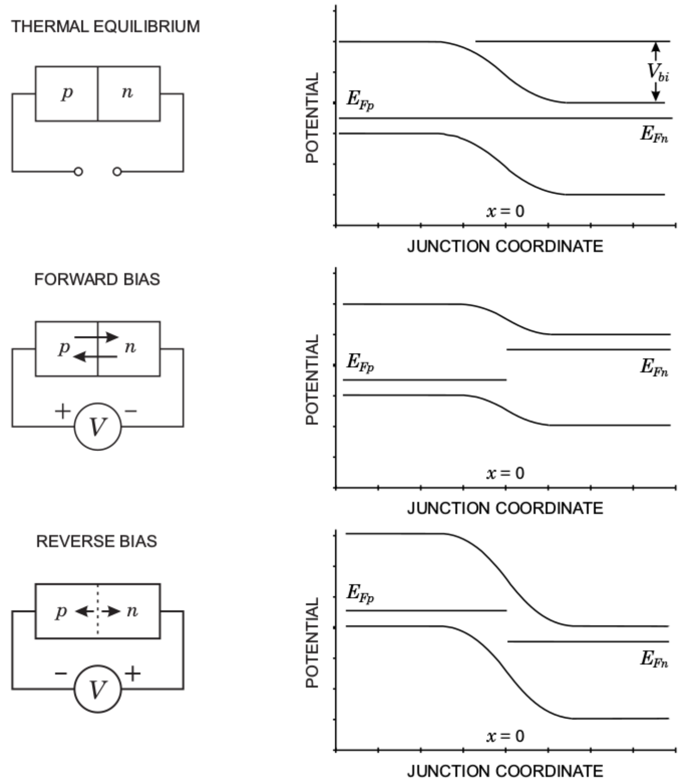

Figure 2.2. – In a pn-junction in thermal equilibrium, without bias voltage, (top image) the Fermi-level has to be constant across the whole device. The different position of the Fermi-level with respect to the conduction and valence band edges in n- and p-doped silicon, leads to the build-in potential V_{bi} at the junction. Application of a forward bias (middle image) lowers the potential difference between p- and n-doped silicon and facilitates the current flow across the junction. Under reverse bias (bottom image) the potential difference increases. Free charge carriers are drawn away from the junction, leading to an enlargement of the depletion zone. [8]

bias. In case of a forward bias, the external voltage counteracts the build-in potential and reduces the width of the depletion zone. Because of the reduced space charge the electric field opposing the diffusion of charge carriers across the junction is smaller, allowing a net current to flow across the junction. Under reverse bias (negative potential on the p-side) the majority carriers are further drawn away from the junction leading to an enlarged depletion region and a higher electric field across the junction. The applied external potential thus enlarges the potential barrier between p- and n-side, effectively prohibiting any current to flow. This process is schematically shown in fig. 2.3. A small current can be measured even under reverse bias, due to the diffusion of carriers into the depletion zone.

The diffusion currents across the junction for electrons and holes are [8]

$$J_{n/p} = q_e D_{n/p} \frac{n_i^2}{N_{a/d} L_{n/p}} \left(e^{q_e V/kT} - 1 \right). \tag{2.3}$$

The resulting total current is

$$J = J_n + J_p = J_0 \left(e^{q_e V/kT} - 1 \right) \tag{2.4}$$

with

$$J_0 = q_e n_i^2 \left(\frac{D_n}{N_a L_n} + \frac{D_p}{N_d L_p} \right). \tag{2.5}$$

This equation is called Shockley equation and describes the current-voltage characteristic of an ideal pn-diode under reverse and forward bias. The current under forward bias increases exponentially. Under reverse bias the exponential term vanishes and the current saturates at $-J_0$. The reverse current depends on the diffusion constants $D_{n/p}$ and diffusion lengths $L_{n/p}$. The behavior of a semiconductor diode according to equation 2.4 is shown in fig. 2.4. The ratio of the electron and hole components of the total current is given by the ratio of the numbers of donors and acceptors. In reality the reverse current is much higher than in the ideal case due to additional defects in the bandgap which act as generation and recombination centers. As the voltage is increased and the depletion zone reaches the location of the defects, they start to contribute significantly to the current, which therefore exhibits a strong bias dependence until the whole diode is fully depleted.
By applying a reverse bias to a silicon diode a volume free of charge carriers can be created. Any charges that are generated in this volume by a traversing particle will drift in the electric field to the respective electrode.

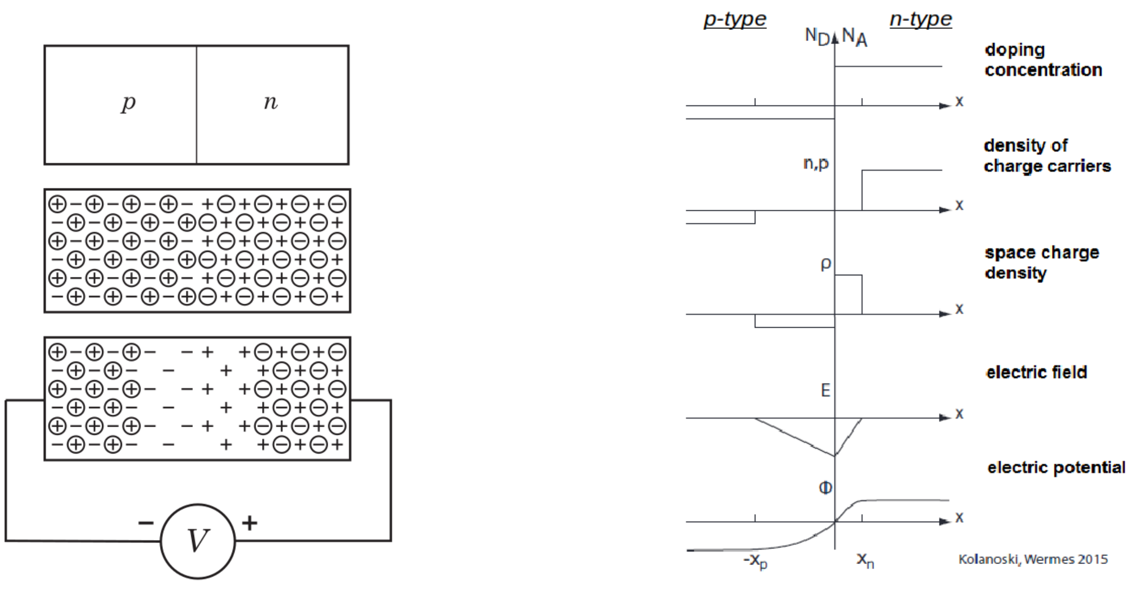

(a) (b)

Figure 2.3. – (a) Mobile charge carriers (circles) diffuse across the junction and recombine. Thus the initially neutral donor and acceptor atoms are being ionized and form a space charge region. The space charge region is further increased when a reverse bias voltage is applied. [8]
(b) The build up of a space charge region leads to an electric field which has its maximum value at the junction. The space charge region and therefore the field extends further into the lesser doped side (here p-side). [12]

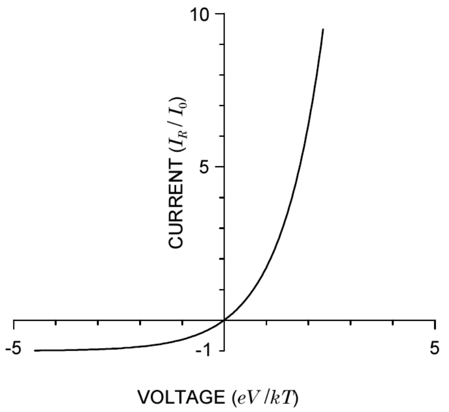

Figure 2.4. – Current vs. voltage for an ideal pn-diode. The current grows exponentially under forward bias and saturates to I_0 under reverse bias. [8]

2.1.2. Silicon detectors

By the use of a reverse biased pn-junction a silicon sensor can be depleted of free charge carriers, making it possible to measure the additional charges created from the energy deposit of a traversing particle. Material parameters and geometry have a multitude of effects, which have to be taken into account when designing a detector. Traditionally p-in-n or n-in-n sensors were used because of the availability of high resistivity n-type material. Studies of the effects of radiation damage led to the development of p-type detectors [13], which are now the baseline design for future tracking systems. To obtain spatial resolution the read-out electrodes are either structured into pixels or strips. Fig. 2.5 shows a schematic cross-section of a segmented n-type (a) and p-type (b) silicon detector. The n-type sensor consists of a high resistivity n-type bulk with p^+-implants on the sensor front. In this case, the electrodes are AC-coupled to aluminum contacts which are connected to the readout electronics. The front electrodes are connected to high-voltage via bias resistors (not shown). For isolation and passivation the sensor top is covered with a layer of SiO_2. Backside connection is established with a homogeneous n^+-implant and aluminum backside contact. The type of dopants is inverted for the p-type sensor. P-type sensors have to be equipped with an inter-pixel or -strip isolation in the form of a p-spray or p-stop implant. This is due to an accumulation of positive charges in the oxide layer, effectively shortening the region between strips. In the figure, the drift direction of charge carriers to the respective electrode is also indicated. Since electrons have a higher drift velocity in silicon than holes, it is favorable to collect electrons at the read-out electrodes. The active area of silicon pad detectors is usually surrounded by one or more guard rings (not shown in the figure) to avoid a current flow from the surface or edges of the device into the pad region.

Depletion width

The depletion width of a planar pn-junction with an abrupt doping profile as a function of the applied reverse bias voltage can be calculated by solving Poisson's equation. Usually the top electrode is much stronger doped than the sensor bulk. This leads to an asymmetric growth of the depleted zone, which mainly extends into the lower depleted sensor bulk, so that the depletion zone inside the collecting electrode can be neglected. The depletion width w_d of a silicon sensor depends on the applied bias

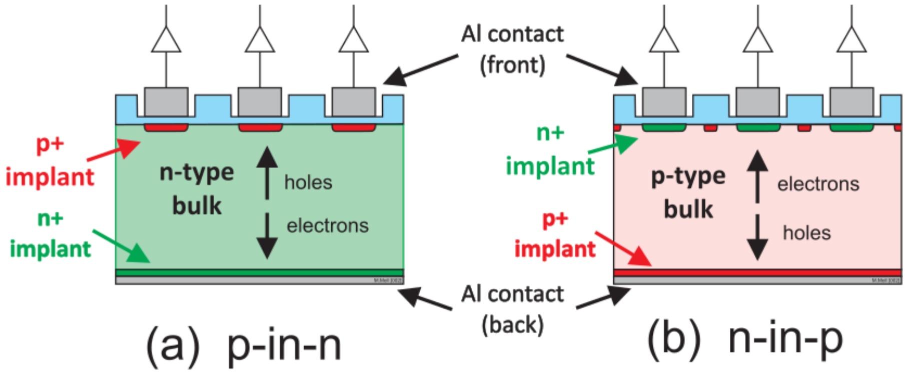

Figure 2.5. – Schematic cross-section of a segmented n-type (a) and p-type (b) silicon detector [14].

voltage V_{bias} and the effective doping concentration N_{eff} [8]:

$$w_d = \sqrt{\frac{2\epsilon(V_{bi} + V_{bias})}{q_e \| N_{eff} \|}}, \tag{2.6}$$

where ϵ and q_e are the electric permittivity and the electron charge, respectively. The built-in voltage V_{bi} for silicon sensors is usually 0.5 V and is therefore often neglected because of the much higher bias voltage. The effective doping concentration is the difference in the amount of acceptors and donors in the space charge region and subject to change by irradiation induced defects. The above equation can be used to calculate the effective doping concentration from a measurement of the full depletion voltage and the physical thickness of a device. This assumes a constant distribution of space charge throughout the sensor, which is not necessarily the case after irradiation. The depletion voltage itself is often deduced from measurements of the capacitance-voltage (CV) characteristic and is therefore subject to uncertainty resulting from the dependence on measurement frequency of the CV-measurement in the case of irradiated detectors [15]. Another commonly used method is to obtain the depletion width from TCT measurements.

Sensor capacitance

Because no mobile charges are present in the depleted volume, the pn-junction, with surface A, under reverse bias V_{bias}, has the characteristic of a capacitor with capacitance [8]

$$C = \epsilon \frac{A}{w_d} = A\sqrt{\frac{\epsilon q_e \| N_{eff} \|}{2(V_{bi} + V_{bias})}}. \tag{2.7}$$

The depletion width increases with the square root of the reverse bias voltage until the sensor is fully depleted. Therefore, a plot of the value of $1/C^2$ as a function of the applied bias voltage is frequently used to extract the value of the full depletion voltage. In addition, the slope of the voltage dependent part of the graph depends on the effective doping concentration. The depletion depth x of the silicon sensor can be calculated from the measured sensor capacitance C and the active area of the sensor A

$$x = \frac{\epsilon A}{C} \tag{2.8}$$

The local effective doping concentration is [16]

$$N_{eff}(x) = -\frac{C^3}{\epsilon q_e A^2}\left(\frac{dC}{dV}\right)^{-1}. \tag{2.9}$$

These equations can be used to obtain the doping profile of the sensor under test.

Leakage current

Under reverse bias, even in absence of particle radiation or any other external excitation of charge carriers, a current can be measured across the pn-junction. This current originates from different sources. Most importantly free charge carriers are thermally generated at generation-recombination centers in the depleted region and separated by the electric field. This contribution is called volume- or generation current and usually dominates the total leakage current. In addition, free charge carriers will diffuse from the undepleted into the depleted region of the detector and thus contribute to the leakage current. The volume current increases significantly after irradiation of the sensor due to the introduction of mostly acceptor-like defects in the middle of the bandgap, which act as generation-recombination centers.
For scaling the leakage current to temperature T the formula

$$I(T) = I(T_0)\left(\frac{T}{T_0}\right)^2 \exp\left[-\frac{E_{eff}}{2k_B}\cdot\left(\frac{1}{T}-\frac{1}{T_0}\right)\right] \tag{2.10}$$

can be used [17]. $I(T_0)$ is the measured leakage current at temperature T_0, k_B is the Boltzmann constant and $E_{eff} = 1.214$ eV.

Signal generation: Ramo theorem

The detector signal is a result of the current induced on the read-out electrodes by the movement of charge carriers inside the sensor. To be able to calculate the induced current for a given configuration of electrodes the so called weighting field $\vec{E}_w$ was introduced [18, 19]. The weighting field is calculated for an individual electrode by assuming this electrode to be on unit potential and all other electrodes on zero potential. Only if a charge carrier moves along this weighting field a signal will be induced. The weighting field is solely based on the detector geometry and has to be distinguished from the electric field, which is acting on the charge carriers. The induced current of a charge q, moving with velocity $\vec{v}$ in the vicinity of an electrode with corresponding weighting field $\vec{E}_w$ is

$$I = q\vec{v}\cdot\vec{E}_w. \tag{2.11}$$

While the original theorem was introduced for the design of vacuum tubes, it was later shown that it also holds in the case of semiconductors with charges moving in a space-charge region [20, 21]. Later extensions include the calculation of signals in detectors that contain non-linear materials and readout-electrodes connected by an arbitrary impedance network by time-dependent weighting fields [22].
It is important to note that, in the case of a silicon detector, electrons and holes have a different mobility, so that the drift velocity is different. The induced current at a given time after charge generation is the

sum of the contributions from the drifting electrons and holes

$$I = N_{eh} q_e (\vec{v}_e + \vec{v}_h) \cdot \vec{E}_w, \tag{2.12}$$

with the elementary charge q_e and the number of generated electron-hole pairs N_{eh}. For a pad detector with thickness d, the weighting field is parallel to the electric field and has the constant magnitude $1/d$. For segmented sensors the weighting field has a more complex shape. The weighting field peaks strongly at the segmented read-out electrodes, which leads to an unequal contribution of the different carriers to the overall signal, depending on their respective drift direction.

2.2. Low Gain Avalanche Detectors

For high luminosity environments, sensors for timing applications become more and more important: Due to the higher number of particle interactions, disentangling primary vertices purely by spatial track measurements becomes increasingly challenging. Resolving different particle interactions also in time will help to reconstruct tracks and assign them to the correct primary vertex. Plans to include silicon detectors designed for timing applications exist for example for the ATLAS High Granularity Timing Detector [1], the CMS MIP Timing Detector [2], the CMS/TOTEM Precision Proton Spectrometer [23] or the LHCb detector [3].

2.2.1. Charge multiplication in silicon detectors

Charge multiplication occurs when electrons and eventually holes are accelerated in a strong E-field so that they acquire enough energy to themselves create an electron-hole pair from an interaction with a valence electron. As soon as holes start to contribute significantly to the multiplication process, the device will undergo breakdown. Charge multiplication is widely used in gaseous detectors. In the field of silicon detectors the phenomenon is studied since the 1950s. More recently, charge multiplication was observed in highly irradiated detectors [24] and is today used to build silicon detectors with internal amplification (Avalanche Photo Diodes, Low Gain Avalanche Detectors) for increased radiation hardness and timing resolution.
The dependence of the multiplication process on the electric field strength and on temperature is up to date best described by empirical models. Most parametrizations use the so called *Chynoweth*-law [25, 26], which is used for gaseous detectors but was found to be well in agreement with experimental data from silicon devices. Multiplication is described in terms of the ionization rate, which is the number of electron-hole pairs generated by a carrier per unit distance traveled and, in this model, only depends on the local electric field and temperature

$$\alpha_{n,p}(E) = a_{n,p}^{\infty} \exp\left(-\frac{b_{n,p}(T)}{E}\right). \tag{2.13}$$

Coefficients a and b, which differ for electrons and holes, are determined experimentally. An abundance of different parameter sets, valid for different ranges of electric field strength, can be found in literature (e.g. [27, 28]). A parametrization of the temperature dependence of the multiplication process can, for example, be found in [29]. The multiplication process depends on the distance a charge carrier can travel to reach the required threshold energy for ionization. Therefore a lower temperature (longer mean free path) leads to a higher rate of ionization. The temperature dependence is more significant for lower field strengths because the carriers can travel several mean free paths before a collision, whereas in high field regions, the energy loss per unit distance is more significant compared to the mean free path. A description of the implementation of this formalism into device simulation tools can be found in [30, 31]. Avalanche multiplication is distinct from the so called *Zener*-effect or *Zener*-tunneling. The Zener-effect is a breakdown mechanism under reverse bias of a semiconductor, in which a high electric field enables tunneling of electrons from the valence to the conduction band, suddenly increasing the leakage current.

2.2.2. Timing measurements

The measurement of the arrival time of a particle is usually done by recording the time at which the sensor signal crosses a given threshold. The signal shape is affected by both physical effects in the detector and electronics, leading to fluctuations of the measured time of incidence. The time resolution that can be achieved by a detector system is limited by several distinct factors. These are most importantly the effect of Landau noise, time walk, jitter and signal distortions [32]. The energy deposition of a charged particle in silicon varies from event to event and, in addition, the amount of charge deposited along the track of the particle is not homogeneous. These are the so called Landau fluctuations. Landau fluctuations affect the time measurement in two ways: (1) Variations in the overall amount of deposited charge lead to variations of the signal amplitude. Two signals with different amplitudes but otherwise identical shape will cross a given threshold at different times with respect to the arrival of the particle. This effect is called *time walk*. To reduce time walk the signal rise time should be as low as possible. In addition time walk can be reduced by using constant fraction discrimination (CFD) instead of a fixed threshold. (2) Even for the same amount of overall deposited charge, the charge deposit varies along the track. Even for a constant weighting field and saturated drift velocities throughout the whole sensor, depending on where most of the charge is deposited, the relative hole and electron contribution to the signal changes. This variation changes the signal shape and therefore leads to fluctuations in the threshold crossing time. This effect is called *Landau noise*. Landau noise can not be avoided and ultimately limits the time resolution that can possibly be achieved. *Jitter* is a result of additional noise on the signal, which originates mainly from the electronic read-out. For a given noise level N, a fast rise time t_r of the signal will reduce the time variation due to noise fluctuations and thus lead to a decrease in timing jitter [32]:

$$\sigma_{jitter} = \frac{N}{\left.\frac{dV}{dt}\right|_{V_T}} \approx \frac{t_r}{S/N}. \tag{2.14}$$

Setting the trigger threshold V_T to the point of maximal signal slope ($\frac{dV}{dt}$) will therefore improve time resolution. For the development of fast silicon detectors, increasing the signal rise time while maintaining or improving the signal-to-noise ratio is the key goal [33]. Under the term *signal distortions* all additional effects that change the signal shape from one event to another are summarized. Since silicon sensors for timing are likely to be segmented for spatial resolution the weighting field will not be constant throughout the sensor. Depending on where charge is deposited with respect to the electrodes the signal shape will vary. A dependence of the signal shape on the position of charge deposition is also given if the drift velocity is not constant (saturated) throughout the device.

2.2.3. Working principle of LGADs

Following from the previous section it is clear that a sensor featuring a high signal to noise ratio with a short rise time (high slew rate) is desirable for timing measurements. The current signals of standard silicon sensors (without internal gain) have a fixed amplitude which is limited by the saturation of the drift velocity and the maximum value of the weighting field [32]. The number of charge carriers can indeed be increased by using a thicker sensor but since the weighting field is inversely proportional to the sensor thickness, this has no effect on the amplitude of the current signal. The choice of the sensor thickness best suited for timing measurements depends on many factors. E.g. if a charge sensitive amplifier is used, the lower noise and higher charge signal can improve the time resolution. A detailed comparison of different approaches can be found in [34]. Internal gain by multiplication of charge carriers can increase the signal amplitude so that the time resolution improves. Employing an external amplifier to increase the signal does not increase the time resolution, since it affects the noise in the same way. In fact, internal gain increases the sensor noise more than the signal because the leakage current is also multiplied and the stochastic nature of charge multiplication (excess noise factor) leads to additional noise. However, since the total noise is usually dominated by electronics, a better signal to noise ratio (SNR) can be achieved by implementing gain in the sensor design. If the gain is too high the additional noise becomes dominant and can lead to a reduction of the SNR. In addition, the sensor operation can be negatively affected if the gain is too high: Very high electric fields can lead to breakdown and the range of possible operation voltage is reduced, which can render the sensor useless after irradiation. Avalanche photodiodes (APDs) [35] or silicon photomultipliers (SiPM) with high gain values are mostly operated in an avalanche regime where the effects of a very high gain, described above, are not of great concern. To maintain a good signal-to-noise ratio and to decrease the signal rise time, thin sensors with comparably low gain have been developed [36, 37, 38, 39], which are designed for increased temperature and voltage stability, lower fluctuations in signal amplitude and to allow for finer segmented sensors [36]. The increase of signal charge is obtained by exploiting the effect of avalanche multiplication of drifting charge carriers in a high electric field. Low Gain Avalanche Detectors (LGADs, [40]) are based on the technology of avalanche photo diodes. LGADs have an n-doped read-out electrode and a thin (several µm) p-doped multiplication layer directly beneath it. The electric field at the junction is high enough for charge multiplication to occur. Read-out and multiplication layers are implanted in a p-type bulk. The gain of the device is defined by the doping profile and doping concentration of the multiplication layer. A schematic drawing is shown in fig. 2.6. The Junction Termination Extension (JTE) is used to obtain a more homogeneous electric field profile along the edge of the multiplication implant, to increase gain homogeneity and high voltage stability. The amplitude of the signal current is defined by the sensor gain. But, in contrast to sensors without gain, the signal rise time depends on the sensor thickness. This is because the current signal continues to increase until all charges have undergone multiplication. Therefore the signal rise time is given by the maximum drift time of an initial charge carrier. For this reason a thin sensor will have the same signal amplitude but a faster rise time compared to a thick sensor with the same amount of gain. Since the thermally generated charge carriers, comprising the leakage current, are amplified in the same manner as the signal charge, the increase of leakage current due to irradiation can lead to a significant increase in noise with respect to the signal, also since the latter is reduced by trapping [41]. The intrinsic gain is temperature dependent. Increased vibrations of the silicon lattice at higher temperatures lead to an increased loss of energy of moving electrons to the lattice. This reduces the energy available for impact ionization and the amount of charge multiplication is reduced [28].

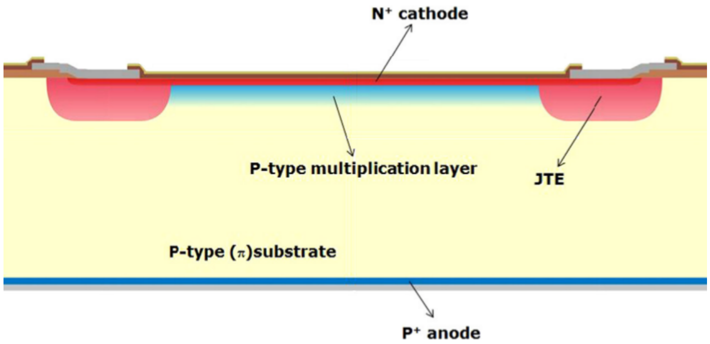

Figure 2.6. – Schematic cross-section of the LGAD pad design with a JTE structure protecting the junction edge termination. [40]

2.3. Radiation Damage

Particles with high energy are produced in interactions in hadron colliders in large quantities. All detector components, mechanics and electronics that are placed close to the interaction points have to withstand this flux of potentially damaging particles to ensure the functionality over the full operation time. The innermost detectors currently installed at the LHC have to withstand a fluence of approximately $2 \times 10^{15}\ n_{eq}/cm^2$ until they will be replaced. For the upgrade of the LHC to the High-Luminosity LHC (HL-LHC, [42]) the total integrated luminosity and with this also the total particle fluence will be larger by a factor of about ten. For the innermost pixel layers, radiation doses will be as high as $1.5 \times 10^{16}\ n_{eq}/cm^2$. Foreseen radiation levels at the FCC are as high as $8 \times 10^{17}\ n_{eq}/cm^2$ [43]. Current sensor technologies could not withstand such high radiation fluence, so that further research and development of novel techniques is needed.

2.3.1. Damage mechanisms

When a particle collides with a silicon atom a minimum amount of energy needs to be transferred to dislodge the silicon atom from its lattice position. To remove a silicon atom from its position in the crystal lattice with a probability of more than 50 %, an energy of at least 25 eV is necessary [44, 45]. A neutron with an energy of about 175 eV or an electron with an energy of at least 260 keV is necessary to form such point defects. Below this threshold, the transferred energy is dissipated in the form of phonons, which does not lead to any damage. In case the silicon atom was removed from its position, it can occupy an intermediate position in the lattice, called an Interstitial (I). The now unoccupied original lattice position is called Vacancy (V). The resulting V and I defects can interact with other V/I states or with other defects and foreign atoms. A combination of a vacancy and an atom on an interstitial position is called Frenkel pair. If the energy transfer was high enough, the primary knock on atom (PKA) has enough energy to remove further silicon atoms from their lattice position and produce a cascade of radiation defects [46]. This can lead to the development of defect clusters, which usually have a spatial spread of about 10 nm × 200 nm along the direction of impact and form at the end of the PKA track [12]. To form clusters, neutrons and electrons have to have an energy of about 35 keV and 8 MeV, respectively [47]. The amount and distribution of defects depend on the type and energy of the incident particle. Neutrons tend to produce isolated clusters of defects with few point defects. Protons with different energies produce clusters and in addition more or less point defects, as can be seen in fig. 2.7. The image shows a simulated distribution of vacancies in silicon after different types of irradiation. In this context it is important to note that, depending on

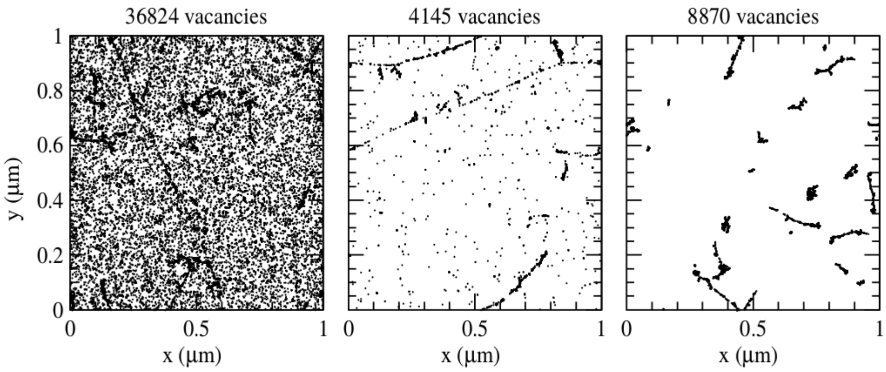

Figure 2.7. – Comparison of initial vacancy distribution in a 1 μm^3 volume after irradiation with 10 MeV protons (left), 24 GeV protons (middle) and 1 MeV neutrons (right) to a fluence of 10^{14} cm^{-2}. [46]

their position inside an experiment, detector components can be exposed to different types of particles. The component of charged hadrons (mostly charged pions) is larger for the pixel sensors, whereas the outer detector layers are mostly exposed to neutrons [14].

2.3.2. NIEL - Scaling of radiation damage

In a particle physics experiment a complex radiation field of a multitude of different particles at different energies is present. In addition, different irradiation facilities use different particles for irradiation of detectors. A scaling procedure based on the amount of Non-Ionizing-Energy-Loss (NIEL) was developed to scale a particle fluence to a corresponding reference fluence to be able to compare and predict radiation damage by different particles at different energies. The NIEL scaling hypothesis assumes that the radiation damage induced changes of electrical properties of silicon detectors scale linearly with NIEL. The success of NIEL scaling is primarily based on the good agreement with the experimentally observed increase of leakage current, but it is not obvious how well NIEL scaling works on a microscopic level [46]. For example, point-defects (mainly created by low energy electrons and gammas) and clusters (mainly neutrons) have a different impact on the effective-space-charge [14]. The total fluence is given by

$$\Phi = \int_{E_{min}}^{E_{max}} \mathrm{d}E\ \phi(E), \tag{2.15}$$

with the energy spectrum $\phi(E)$ in the range of E_{min} to E_{max}. For several particles and energies the displacement damage cross section $D(E)$ has been calculated for silicon. The hardness factor κ is

$$\kappa = \frac{\int_{E_{min}}^{E_{max}} \mathrm{d}E\ \phi(E)D(E)}{D_N(1\,\mathrm{MeV}) \cdot \Phi}, \tag{2.16}$$

where $D_N(1\,\mathrm{MeV}) = 95\,\mathrm{MeV\,mb}$ corresponds to the damage cross section for irradiation with 1 MeV neutrons.

The fluence, scaled to an irradiation with 1 MeV neutrons thus is $\Phi_{eq} = \kappa \cdot \Phi$, $\left[\Phi_{eq}\right] = \mathrm{n_{eq}/cm^2}$. It is useful to keep in mind that the uncertainty on the total fluence can be as high as 15%, depending on the irradiation facility.

2.3.3. Effects of radiation on the detector performance

Leakage current

The increase of the leakage current after irradiation is a limiting factor in many aspects. With an increasing current, more power will be dissipated inside the sensor in form of heat. Due to the strong temperature dependence of the leakage current, this can lead to a thermal runaway, if no sufficient cooling is possible. In addition, the leakage current is one main contributor to the overall sensor noise. The leakage current is mostly produced by defect levels close to the middle of the bandgap, so called generation centers and can be calculated from Shockley-Read-Hall (SRH) theory [14, 48]. It follows the NIEL scaling hypothesis very well and is well predictable, leading to the application of leakage current measurements for dosimetry. In contrast to the effective space charge, the change of leakage current is not much influenced by defect engineering approaches. The leakage current increase due to irradiation is proportional to the particle fluence. The current related damage rate α is the change in leakage current after irradiation ΔI, normalized by the neutron equivalent fluence and the active sensor volume V:

$$\alpha = \frac{\Delta I}{\Phi_{eq} \times V}. \tag{2.17}$$

The current related damage rate was found to be independent of the specific type of sensor material and type of irradiation over a large range of particle fluences, as can be seen in figure 2.8 (a). A continuous

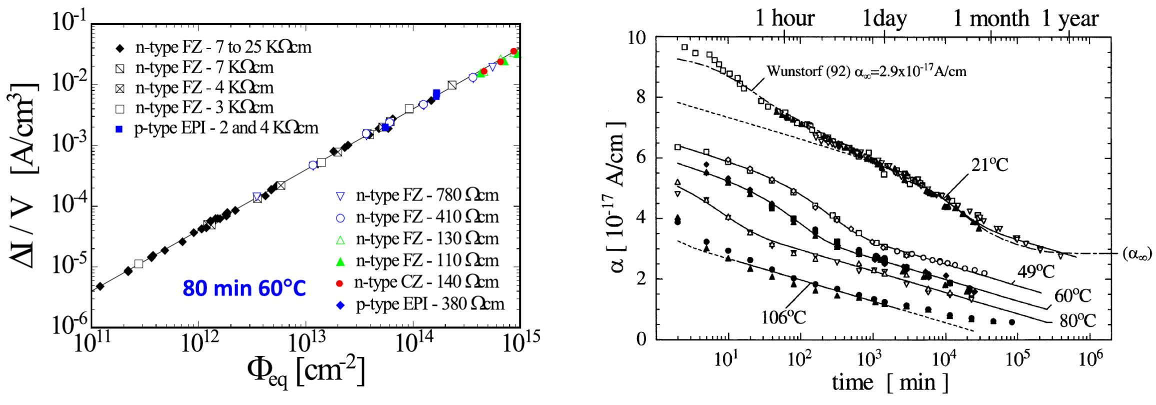

(a) (b)

Figure 2.8. – (a) Leakage current increase as a function of particle fluence for different detector types and process technologies. The currents were measured after 80 minutes of annealing at 60°C and normalized to 20°C. [14] (b) Current related damage rate as a function of annealing time at several different annealing temperatures. [49]

decrease of the leakage current is observed with annealing. The change of α with annealing time t can be parameterized by the equation [50]

$$\alpha(t) = \alpha_1 \cdot \exp\left(\frac{-t}{\tau_1}\right) + \alpha_0 - \alpha_2 \cdot \ln\left(\frac{t}{t_0}\right). \tag{2.18}$$

A detailed description of the parameters and interpretation of this equation can be found in [51, 49]. Fig. 2.8 (b) shows the evolution of the current related damage rate with annealing time. The annealing was performed at different temperatures as indicated in the figure.

Charge collection efficiency

Whereas the leakage current is predominantly produced by defect levels near the middle of the bandgap, levels which have an associated energy closer to the valence or conduction band, can act as charge traps. While free electrons and holes drift in the depleted region they can occupy these additional trap levels for a short amount of time until they are released. Each trap can be characterized by a trapping rate $1/\tau_{e/h}$. The trapping time $\tau_{e/h}$ depends on the capture cross-section for the respective charge carriers, the number of defects and their occupation with electrons. For highly irradiated detectors, trapping becomes the main limiting factor for detector operation. The signal can be delayed such that it does not fall anymore into the read-out time of the detector and is lost. Fig. 2.9 shows a comparison of the charge collection efficiency as a function of equivalent fluence for n- and p-type sensors. Segmented p-type sensors show a higher amount of collected charge after high particle fluence than n-type sensors. The effect of trapping can be reduced by using p-type detectors (collection of electrons with a higher mobility). Also, as can be seen from the figure, the decrease of charge collection efficiency can be mitigated partly by applying a higher reverse bias voltage. Ultimately the voltage supply is limited by the maximum allowable power dissipation, due to the limited cooling capacity. The probability for trapping of charge carriers depends on both the irradiation fluence and the temperature of the device. The trapping rate increases linearly with fluence and decreases with increasing temperature [52]. Annealing affects the effective trapping rate differently for electrons and holes. Less trapping is observed for electrons after annealing, while on the other hand, the trapping rate increases for holes [14]. In low- or unirradiated sensors the signal strength is proportional to the detector thickness: The

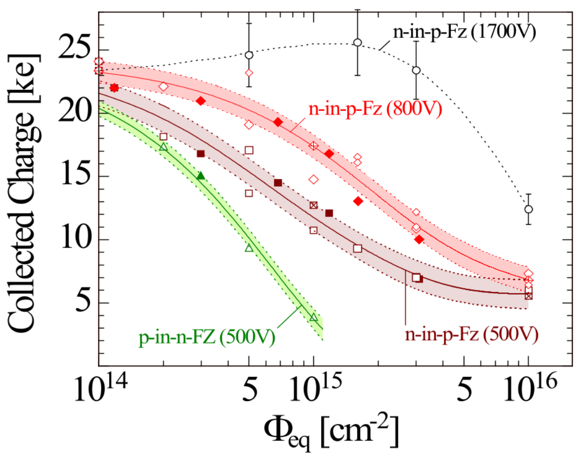

Figure 2.9. – Charge collection efficiency as a function of equivalent fluence for n-type and p-type sensors. The sensors are 300 μm-strip detectors, which were irradiated with 23-GeV protons, 26-MeV protons, and reactor neutrons. [14]

more material a charged particle traverses, the more charge is generated, which contributes to the drift current. In heavily irradiated detectors this is not true anymore. Rather the signal depends on the shape and strength of the electric field inside the device. A higher electric field reduces the collection time, but at fluences exceeding $1 \times 10^{15}\ n_{eq}/cm^2$ even at high bias voltages ($\approx$ 1000 V) the region, in which the electric field is high enough to guarantee reasonably short collection times, is often smaller than the typical sensor thickness of 300 μm. For this reason, thinner detectors, which have a higher electric field at the same bias voltage, perform better at high fluences of radiation. Also one observes that the onset of charge multiplication takes place at lower bias voltages for thinner devices.

After the observation of charge multiplication by impact ionization in regions with high electric fields near the pn-junction, the idea was developed to make use of this effect to compensate the effect of lower charge collection after irradiation [53, 54] and ultimately to develop sensors with intrinsic gain, already before irradiation, to enhance the timing capabilities of the devices [55].

Change of effective doping concentration

The space charge of an unirradiated detector is determined by the doping of the silicon substrate, which is high enough to neglect other defect states in the silicon. Therefore, the space charge is usually homogeneously distributed over the full thickness of the device, leading to a linear electric field, which has its highest value at the pn-junction. This picture changes after irradiation. Different defects contribute as acceptors or donors to the effective space charge and can lead to a distorted charge distribution and a change in the shape of the electric field. The charge carrier density plays an important role in this context, since, due to the drift direction, predominantly holes or electrons are captured near the p^+ and the n^+-electrode, respectively. These changes can lead to sensors being operated underdepleted or exhibiting the double junction effect (see sec. 2.3.3, p. 20). The doping concentration of irradiated sensors is usually described as an effective doping concentration, which is the difference of all donor-like and acceptor-like states. Since, depending on the type of material, it can be positive or negative, in equations usually the absolute value $|N_{eff}|$ is used. The effective doping concentration and the resulting space charge in the depleted region can be calculated from the respective number of defect states and their occupancy by electrons f_t [51, 14]:

$$N_{eff} = \sum_{donors} (1 - f_t) N_t - \sum_{acceptors} f_t N_t. \tag{2.19}$$

Values of f_t can be calculated from SRH theory. The effective doping concentration can be determined from the full depletion voltage, which in turn is often deduced from a measurement of the sensor capacitance (eq. 2.7). In contrast to the leakage current, the effects of irradiation on the effective space charge depend strongly on the specific material (e.g. oxygen content) and the type and energy of the incident particle, causing the damage.
A radiation induced change of the effective doping concentration has severe effects, especially for n-type sensors. In the general case, negative space charge is produced due to irradiation. For n-type sensors this has the effect, that the initial positive space charge is reduced up to a point where the effective space charge is close to the intrinsic value. Further increasing the irradiation adds more negative space charge and the detector becomes effectively p-type. This leads to a transition of the position of the junction to the n^+-side of the detector while the p^+-side loses sensitivity, when not fully depleted. This process is called 'type inversion' or 'space charge sign inversion' [56] and is shown in fig. 2.10. The space charge sign inversion has severe effects for segmented n-type detectors. The region around the segmented read out electrodes on the top of the device is left undepleted if no full depletion can be achieved anymore. Due to the shape of the weighting field, the spatial resolution of the sensor is reduced. This is one of the reasons, why for future upgrades of experiments p-type silicon detectors are preferred. The evolution of the effective doping concentration with fluence Φ and annealing time t is described by [14]

$$N_{eff}(t) = N_{eff,\Phi=0} - \Delta N_{eff} = N_{eff,\Phi=0} - N_A(t) - N_C - N_Y(t). \tag{2.20}$$

$N_{eff,\Phi=0}$ is the effective doping concentration before irradiation and ΔN_{eff} the radiation induced change of space charge. $N_A(t)$ and $N_Y(t)$ are the contributions from beneficial and reverse annealing,

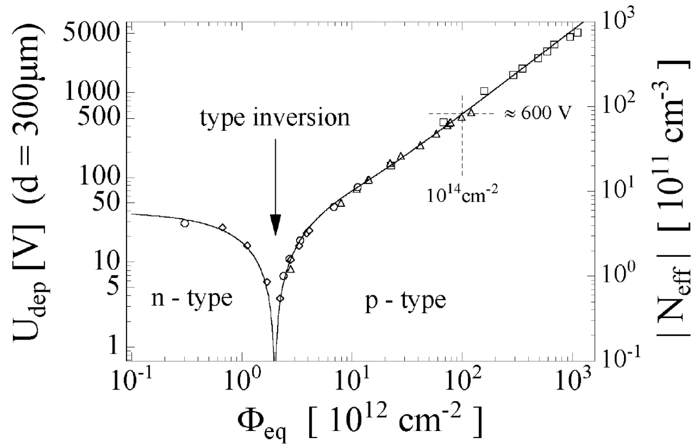

Figure 2.10. – Depletion voltage and effective doping concentration as a function of equivalent fluence. [51, 57]

respectively. N_C is the stable damage component, which is not affected by annealing. The three damage contributions are described by

$$N_A(t) = g_a \Phi_{eq} \exp(-t/\tau_a) \tag{2.21}$$

$$N_C = N_{C,0}[1 - \exp(-c\Phi_{eq})] + g_c \Phi_{eq} \tag{2.22}$$

$$N_Y(t) = g_y \Phi_{eq}[1 - \exp(-t/\tau_y)], \tag{2.23}$$

where c is the removal coefficient and g_a, g_c and g_y are called introduction rates. The dependence on annealing time is described by the time constants τ_a for beneficial annealing and τ_y for reverse annealing. Fig. 2.11 shows ΔN_{eff} as a function of annealing time. The three different contributions to the change in space charge are indicated in the figure. The rate by which the effective doping

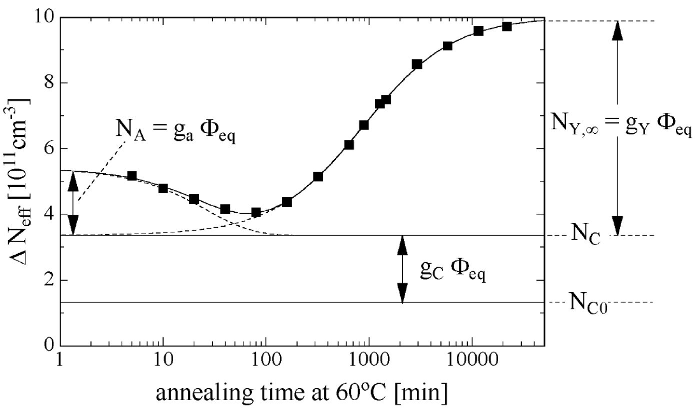

Figure 2.11. – Change of effective doping concentration as a function of annealing time at 60°C for a sample irradiated with a fluence of $1.4 \cdot 10^{13}$ cm^{-2}.[51]

concentration is altered by irradiation can be influenced by the addition of different types of co-dopants to the sensor material during production. For example, it was found that in n-type silicon a high oxygen concentration reduces the effect of donor removal, which leads to an increased radiation hardness of these devices in HEP experiments [58, 46, 13]. Current CMS and ATLAS pixel detectors have been produced from oxygen enriched material.

Donor and acceptor removal

Donor and Acceptor removal describe the effect of a deactivation of the shallow dopants by a formation of a complex defect state with other defects. The electrical properties of the dopant are altered and it does not contribute anymore to the overall space charge. Donor removal has been studied for n- and p-type silicon [59]. The effect of acceptor removal is becoming increasingly more important due to the shift to p-type detectors and the development of detectors with intrinsic gain.
The current understanding is that the main cause for acceptor removal in p-doped silicon is the formation of the B_iO_i (boron interstitial - oxygen interstitial) defect. A silicon interstitial, which was produced by the incident radiation, interacts with a boron substitutional, which is removed from its lattice site (*Watkins replacement mechanism*), and subsequently forms the B_iO_i defect with an oxygen atom [60, 61]. In this process the boron dopant is deactivated, in the sense that it does not act as a shallow p-dopant anymore. Instead, the B_iO_i defect contributes with positive space charge, thus changing the overall charge state by a factor of two. The change of effective doping concentration is parameterized by [61]

$$N_{eff}(\Phi_{eq}) = N_{A,0} \exp(-c_A \Phi_{eq}) + g\Phi_{eq}. \tag{2.24}$$

The first term describes the inactivation of boron atoms, with the acceptor removal coefficient c_A. The second term describes the formation of acceptor like defects with the introduction rate g. Fig. 2.12 (a) shows the change of effective doping concentration with particle fluence after proton irradiation for p-type sensors with different initial doping concentration. The initial decrease of N_{eff} is explained by acceptor removal and the subsequent increase at higher fluences by the formation of additional acceptor-like defects (eq. 2.24). Fig. 2.12 (b) shows a plot of the acceptor removal coefficient as a function of the initial doping concentration for various devices and types of irradiation. Following from eq. 2.24, the acceptor removal coefficient c_A is the inverse of a characteristic fluence $\Phi_0 = 1/c_A$ after which the boron content is reduced to $1/e$ of its initial value. A lower value of c_A is therefore an indication of a higher radiation hardness of the device. Acceptor removal is especially problematic for LGADs because the multiplication mechanism in the gain layer relies on a high boron concentration. It was shown recently that the co-doping of carbon into the gain layer can partly mitigate the effect of acceptor removal [62, 63]. In sensor and defect studies, using the TSC-technique (Thermally Stimulated Currents), it was found that acceptor removal is stronger after irradiation with charged hadrons than with neutrons and that thermal annealing of the irradiated devices does not change the B_iO_i concentration [65, 61].

Double junction

The formation of a double junction can be explained by increased positive space charge, i.e. increased occupancy of defects with holes, at the backside of the device, eventually leading to a positive space charge region in the bulk of an irradiated p-type sensor [66, 67]. The effect of a double junction is primarily observed with sensors, irradiated with protons. The cause of this effect is the different distribution of hole and electron components to the generation current. While the total current density is constant throughout the detector bulk, electron j_n and hole j_p contributions have a linear dependence on the depth inside the detector, with j_n being highest at the n^+-contact and j_p being highest at the p^+-contact. Assuming a constant distribution of defect levels (deep traps) throughout the bulk material,

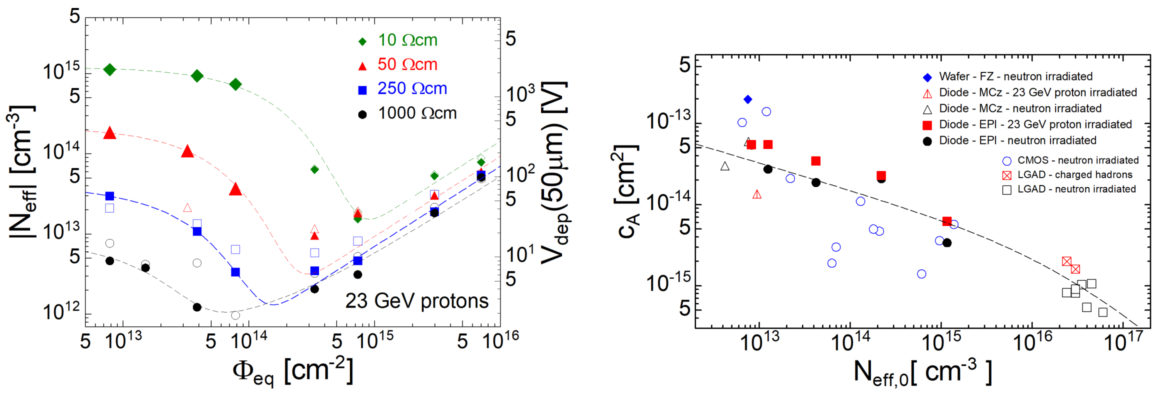

(a) (b)

Figure 2.12. – (a) Effective doping concentration as a function of 1-MeV neutron equivalent fluence (proton irradiation) for different initial doping concentrations. (b) Acceptor removal coefficient as a function of initial doping concentration for different devices and types of particles used for irradiation. [64, 61]

a varying distribution of free charge carriers leads to a non-uniform distribution of trapped charges. More positive charge will be accumulated at the p^+-contact and more negative charge at the n^+-contact. This change in effective doping concentration changes the shape of the electric field in a way that two peaks appear close to the two contacts. This effect is depicted in fig. 2.13. The double junction effect is one example, where a deduction of the effective space charge from the full depletion voltage by CV measurements fails. The effect can be measured with edge-TCT measurements, where the shape of the electric field can be inferred from a measurement of the drift velocity [68]. Due to the temperature dependence of trapping times, the double junction effect is reduced for higher temperatures.

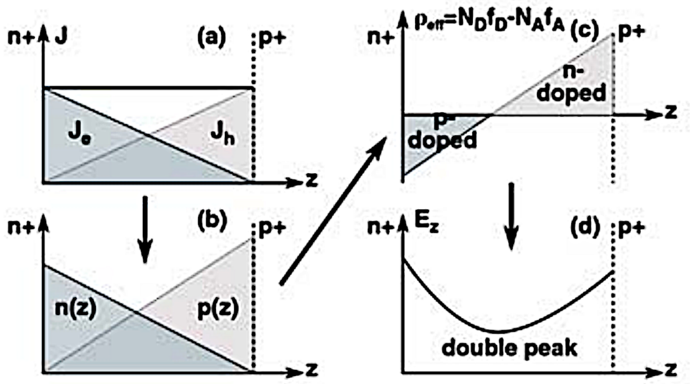

Figure 2.13. – Schematic to explain the origin of a double peak electric field. (a) Generation current densities in the silicon bulk; (b) Charge carrier densities; (c) Space charge resulting from predominantly trapping holes or electrons near the respective electrodes; (d) Double peak electric field due to the space charge formed by trapped charges. [66, 14]

Radiation effects on LGADs

Tests of LGADs revealed that the gain of the device is heavily degraded after irradiation beyond a fluence of about 10^{15} n_{eq}/cm^2, which is detrimental for operation in HEP experiments [69, 41]. It is known that the gain is more heavily reduced after irradiation with charged hadrons compared to neutrons [70]. A prominent way of explaining the reduction of gain after irradiation is the effect of acceptor removal [14, 61, 59] (see sec. 2.3.3, p. 20). By this process the effective doping concentration of the multiplication layer is reduced. This leads to a lower electric field at the junction and reduces the amount of multiplied charge. On the other hand, device simulations of radiation damage after proton irradiation on LGADs, even without implementation of the acceptor removal process, show a decrease in electric field strength, and therefore a reduction of gain, at the multiplication implant [71]. The radiation effects are explained by solely modelling two effective (donor/acceptor) trap levels and the predominant trapping of holes produced in the multiplication process. The reduction of the electric field at the multiplication implant is accompanied by the build up of an electric field region at the backside of the sensor (double junction) and a reduced electric field in the middle of the device and directly below the multiplication implant. The effective space charge is affected both in the multiplication implant and the sensor bulk, which becomes effectively n-type. In a similar approach, taking acceptor removal into account, the agreement with experimental data can be improved [72]. Likely both effects, acceptor removal and the compensation of space charge by trapping, are contributing to the overall reduction of gain after irradiation.

3. Experimental Methods

3.1. IV/CV Measurements

For measurements of the leakage current and capacitance, two different setups were used for the measurements presented in this work. Before sensors are glued onto a printed circuit board (PCB) for measurements in the TCT setups, IV and CV measurements can be carried out on the IV/CV probe station shown in fig. 3.1. The electrical setup is schematically shown in fig. 3.2. The sensors are placed on a temperature-controlled chuck, where they can be fixated with vacuum. Micro-meter needles and the chuck itself are used to establish the electrical connection. The chuck and needles are enclosed with a removable lid during the measuremets to prevent light from entering the sensor. If the sensor is cooled, the enclosure is flushed with dry air to avoid condensation. Bias voltage to the sensor is provided with a Keithley 2410 power supply. The pad current is measured with a Keithley 6487 picoammeter. For measurements of the capacitance, a Keysight E4980A LCR-meter is used. A CV/IV switch is used to change the setup configuration between IV and CV modes. When the capacitance is measured the bias voltage is modulated by a small amplitude (usually 0.5 V) with variable frequency (usually 10 kHz). The LCR meter measures the impedance. An equivalent RC-circuit in parallel (p) or series (s) has to be chosen to obtain the respective capacitance $C_{p/s}$. In general, the parallel mode is selected for CV measurements.
After sensors are mounted on a PCB, they can not be measured with the IV/CV-probe station because cooling and mechanical fixation with vacuum is not possible anymore. In this case IV and CV measurements are carried out inside a Binder MKT115 climate chamber, which is usually used for beta source measurements. The electrical setup is similar to the probe station described above.

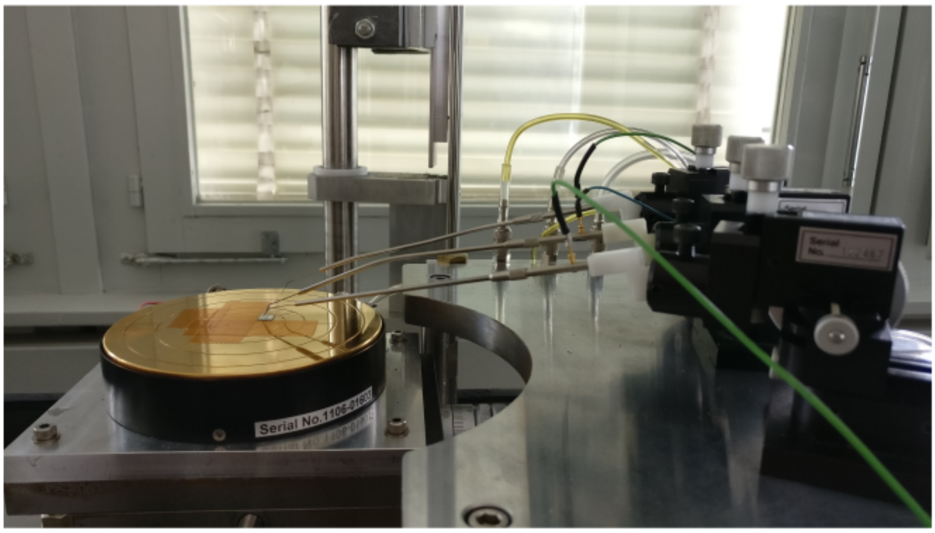

Figure 3.1. – IV/CV probestation. Photograph from [73].

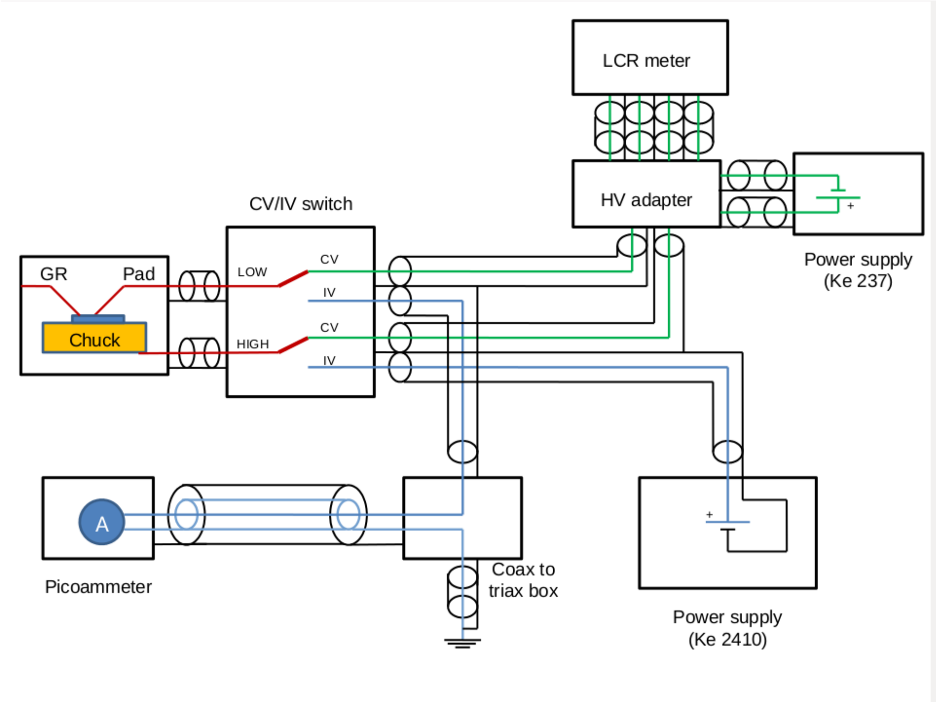

Figure 3.2. – Electrical setup of the IV/CV probestation.

3.2. Transient Current Technique

The Transient Current Technique (TCT) is a standard tool for the characterization of unirradiated and irradiated silicon particle detectors [74, 75]. It is based on the analysis of the transient current pulse, originating from the drift of charge carriers in the electric field inside a biased sensor. The signals are therefore directly recorded by an oscilloscope, which is connected to the sensor with a bias-T, or after amplification by a current sensitive amplifier. Charge injection is possible with the use of a radioactive source or pulsed laser sources. In this work, TCT refers to charge injection with laser light. Commonly used are laser wavelengths in the red (this work: 660 nm) or infrared (this work: 1064 nm) for SPA-TCT. Red light has a short penetration length in silicon and is absorbed in the first micrometers of the sensor. Red top and bottom light injection is therefore used to investigate the drift of electrons and holes separately in the bulk of the device. Infrared (IR) light at the stated wavelength is close to the bandgap energy of silicon and is therefore less absorbed and penetrates the whole sensor, creating charges all along the beam axis. This behavior is used to emulate the charge deposition by minimum ionizing particles (MIPs), although the charge deposition by a laser beam is broader and does not show Landau-fluctuations. IR light can also be injected from the edge of a sensor (edge-TCT, [76]) to probe the sensor as a function of the depth inside the bulk. For example, with edge-TCT it is possible to measure the width of the depleted region or the shape of the electric field. The measurement principles of red top TCT and edge-TCT are shown schematically in fig. 3.3 together with a corresponding current pulse. The signal was recorded with an unirradiated p-type PIN sensor. The red-top TCT waveform peaks directly after charge injection and decreases linearly, because the drifting holes are moving along a decreasing electric-field. Electrons are directly absorbed and are not visible in the signal. The edge-TCT measurement shows contributions from both electron and hole drift. The electron contribution has a larger amplitude and shorter duration because of the

electron's higher mobility. Notably, the electron and hole contributions have a positive and negative slope, respectively, again due to the linear decrease of the electric field strength towards the rear electrode of the sensor.
In general, for the analysis of TCT waveforms, the signals are baseline corrected. The baseline is calculated as the mean value of the first approximately 10 ns of the recorded waveform, before the laser pulse arrives. The baseline-corrected waveform is then divided by the the maximum amplitude of the baseline-corrected reference signal to correct for fluctuations in the laser power. The reference sensor is a commercial detector, which is sensitive to the respective laser wavelength, in the case of SPA-TCT. For TPA-TCT a silicon reference sensor is used, in which charge is created by TPA, similar to the DUT. Normalization of the waveform might be omitted, if the absolute value of the respective measurement is important. In the following, most often the charge, drift velocity and collection time (or time over threshold) are shown as a result of TCT measurements. The charge is calculated as the integral of the waveform, starting at the injection time of the pulse. The integration time is chosen such that the integration window contains the full waveform, depending on the thickness and bias voltage of the DUT. The time over threshold is simply the time, during which the transient signal stays over a predefined threshold. The selected threshold can depend on the noise level and the respective goal of the measurement. The calculation of the drift velocity is described in the next paragraph.

Prompt current method

In sec. 2.1.2 it was mentioned how the signal current depends on the drift velocity of the respective charge carriers. This relation is used in the prompt current method [76] to obtain information about the shape of the electric field inside a silicon sensor by e-TCT or TPA-TCT measurements. In the first hundreds of picoseconds the injected charge carriers have not moved significantly from their initial position. The transient current during this time is thus related to the initial drift velocity of the carriers at the point where they are generated by eq. 2.12. If a pad detector is used, such that the weighting field is constant, the initial current is proportional to the sum of the drift velocities of electrons and holes. Under the assumption of a constant mobility, the sum of the electron and hole drift velocities $\vec{v}_e + \vec{v}_h = \mu_e(\vec{E})\vec{E} + \mu_h(\vec{E})\vec{E}$ can be related to the electric field at this point, as long as the drift velocity has not yet saturated. In this work the drift velocity is usually calculated as the integral over the first 500 ps of the pulse.

3.2.1. TCT+ setup

TCT and edge-TCT measurements were carried out on the TCT+ setup of the SSD laboratory at CERN [77]. For TCT measurements the samples are glued to PCBs with conductive silver glue. An example is shown in fig. 3.4. Images of the setup are shown in figs. 3.5 and 3.6. The sensors used in this work are mostly small test diodes and not full size sensors. The PCBs are equipped with SMA connectors for the bias voltage supply, read-out and optional guard-ring connection. To facilitate measurements from the backside or the edge, the PCBs feature holes and cut-outs for the laser. Next to the sample a PT1000 temperature sensor is glued. The PCB is mounted on a copper plate which is cooled by a thermo electric element (Peltier element). The heat from the warm side of the Peltier is removed by a Huber CC505 chiller. The cooling is regulated using a Laird PR-59 proportional–integral–derivative (PID) controller. The sample can be moved using a Newport three-axis linear stage system. The stages have a stepping resolution of 300 nm in x and y and 100 nm in the z direction. Stage system and laser optics are contained in a Faraday-cage for electro-magnetic isolation. To avoid condensation, the whole cage is flushed with dry air. For light generation, two PicoQuant lasers with a pulse length

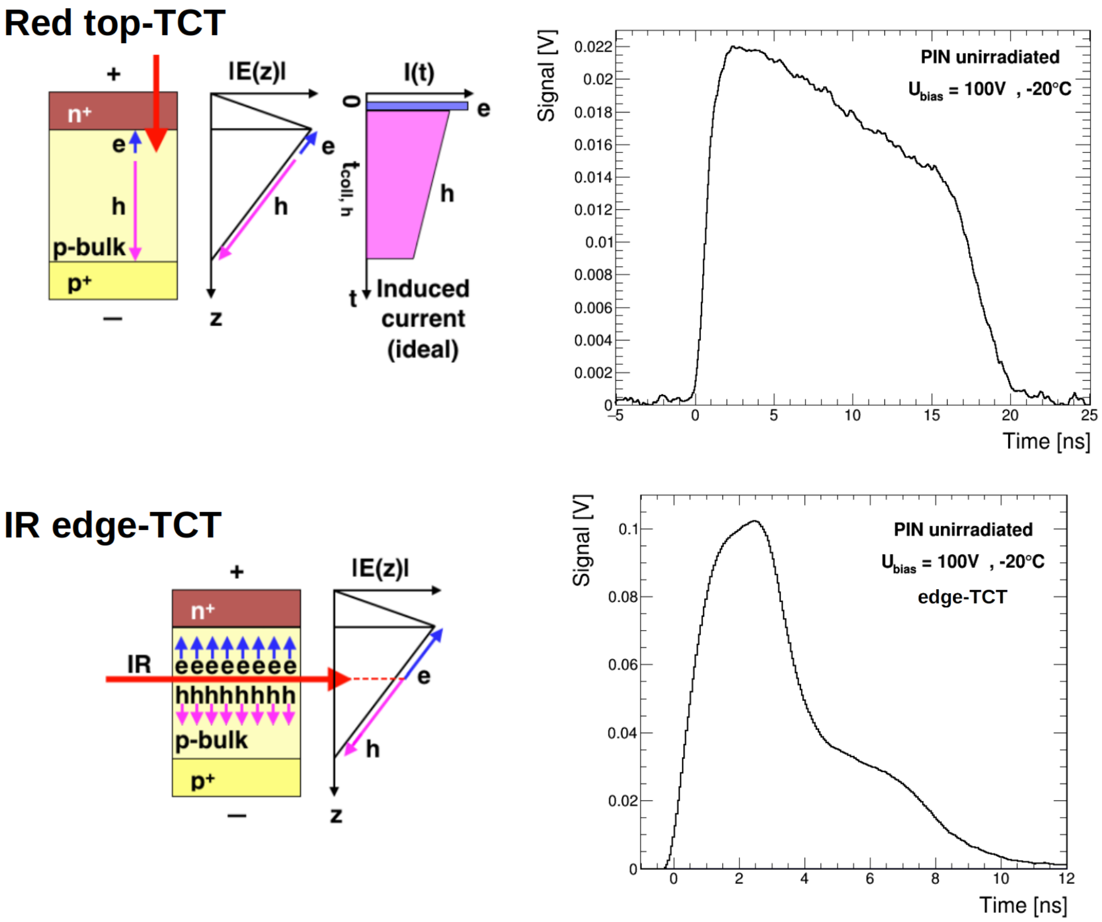

Figure 3.3. – Schematic drawing of red top-TCT (top part of image) and IR edge-TCT (bottom part) and corresponding measured signals. Schematic drawings from [73].

of 200 ps are used. The light is guided to the objectives using optical fibers. The signal from the device under test (DUT) is amplified by a Cividec 2 GHz/40 dB current amplifier and displayed on an Agilent Technologies DSO9254A digital oscilloscope. To monitor the power of the laser, part of the beam is directed onto a reference diode. Its signal is recorded with the DUT data and used in the analysis to normalize the signal to account for fluctuations in the laser output.

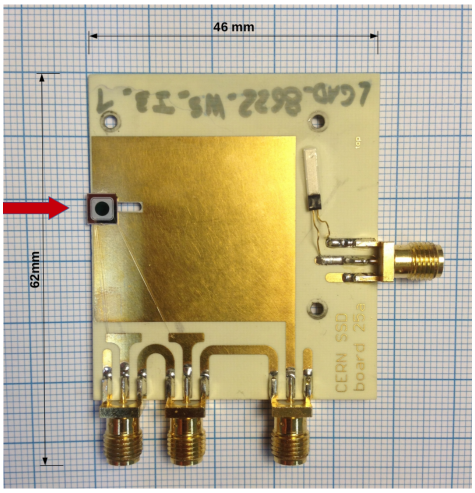

Figure 3.4. – Sensor mounted on a PCB for TCT and edge-TCT measurements. The direction of light injection from the edge is indicated by a red arrow. The PCB features connectors for the pad and guard ring, as well as for the backside of the sensor. A PT1000 sensor is used for temperature monitoring.

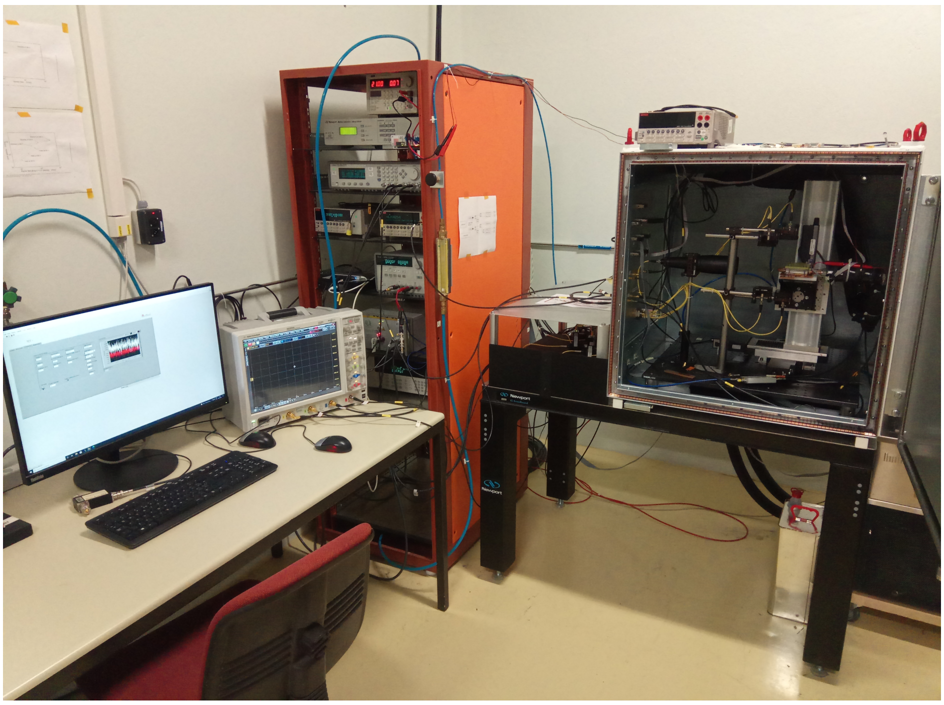

Figure 3.5. – The TCT+ setup with DAQ, electronics rack, optical table and Faraday cage.

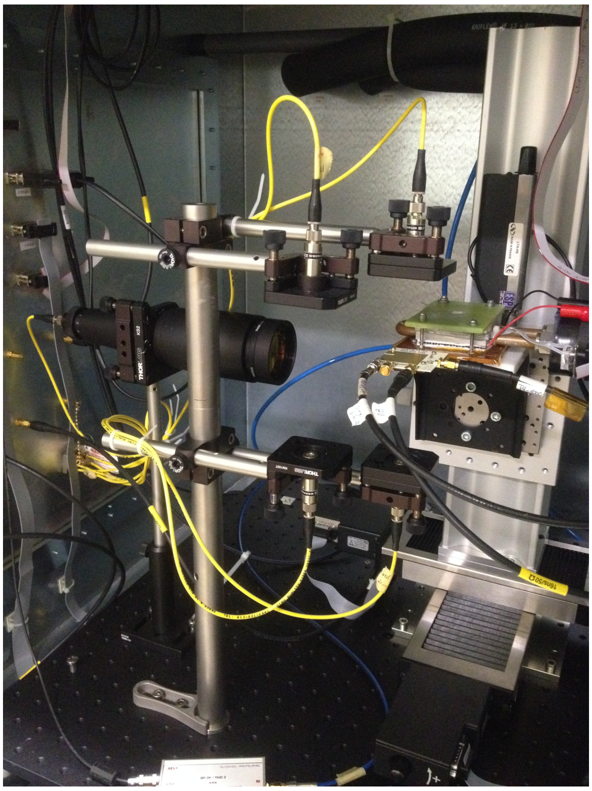

Figure 3.6. – View inside the TCT+ Faraday cage with the sample holder, translation stages and different focusing optics.

4. Irradiation and Annealing Study of Low Gain Avalanche Detectors

Low Gain Avalanche Detectors (LGADs) are a promising sensor concept for tracking and timing measurements in high energy physics experiments, as described in sec. 2.2, p. 11. One of the main limitations at the current state of development is the radiation hardness of the gain layer. It has been found that after irradiation the gain of the sensors is reduced. The main reason for this is the deactivation of the boron doping in the gain layer by radiation-induced defects [14, 61, 59]. In addition, the formation of charged defects in the space charge region of the device can lead to a change in the distribution of the electric field, reducing the electric field strength in the gain layer and therefore the gain [71]. The reduced effective doping concentration in the gain layer after irradiation leads to a reduced depletion voltage of the gain layer [41]. In contradiction to this, it had been observed that proton irradiated LGADs can show a higher depletion voltage of the gain layer [73]. The motivation for the study, presented in the following, was to resolve the question around the gain layer depletion voltage and to investigate the annealing behavior of the radiation damage. One important question in this regard was, whether or not the gain could be recovered by annealing. The measurements and results, presented here, were previously published in [78].

4.1. Description of Samples

The measurements presented in the following sections were performed on proton irradiated LGADs and PIN diodes, manufactured by CNM[1] in run 8622. The sensors from wafer 5 (W5) have a thickness of 277 μm, as stated by the manufacturer. The width of the n^+-implant is 3.2×3.2 mm^2 and the width of the gain layer implant of the LGADs is 3×3 mm^2. All sensors feature a Junction Termination Extension (JTE). A list of the sensors is given in table 4.1. The only difference between the PIN diodes and the LGADs is that the PIN diode does not feature a gain layer and thus can be used as a reference sensor, e.g. to calculate the gain from charge collection measurements. Proton irradiation of the samples was carried out at the CERN IRRAD[2] facility. The 1 MeV neutron equivalent fluence was calculated with a hardness factor of $\kappa = 0.62$.

The samples were subjected to an annealing study. IV, CV and TCT measurements were carried out after accumulated annealing times of 80, 240, 560, 1200, 2480 and 5040 minutes at 60 °C.

In addition to the results presented here, in the appendix (A.2, p. 121) the results of the electrical characterization of additional unirradiated LGADs from W2 and W5 from the same run are shown.

[1] Centre Nacional de Microelectrònica, IMB-CNM-CSIC, Barcelona, Spain
[2] PS IRRAD Proton Facility, CERN, https://ps-irrad.web.cern.ch/

Sensorname	Type	Gain layer doping [atm/cm^2]	Irradiation [n_{eq}/cm^2]	Particle
W5_E3_1	LGAD	$1.9 \cdot 10^{13}$	1×10^{14}	24 GeV/c proton
W5_I3_1	LGAD	$1.9 \cdot 10^{13}$	1×10^{14}	24 GeV/c proton
W5_E3_4	PIN	-	1×10^{14}	24 GeV/c proton

Table 4.1. – Sample properties

4.2. Leakage Current and Capacitance Measurements

Before irradiation the depletion voltage, obtained from CV measurements, was 70 V for the LGADs W5_E3_1 and W5_I3_1 and 40 V for the PIN sensor W5_E3_4. The current at full depletion ranged from 60 to 90 nA for the LGADs and was 30 nA for the PIN.
The sensors were used for an annealing study and thus had to be mounted on a PCB to be able to perform TCT measurements after each annealing step. Since the IV/CV probe station does not support PCB-mounted sensors, current and capacitance measurements for these samples were carried out in the climate chamber, as described in sec. 3.1. The guard ring was left floating during these measurements for technical reasons.
Measurements of the leakage current were carried out at −20°C which are shown in figure 4.1 for LGAD W5_I3_1. The measurements of the second LGAD give similar results and are shown in the appendix (fig. A.1, p. 117). The current was measured to up to 400 V. Since the region around the

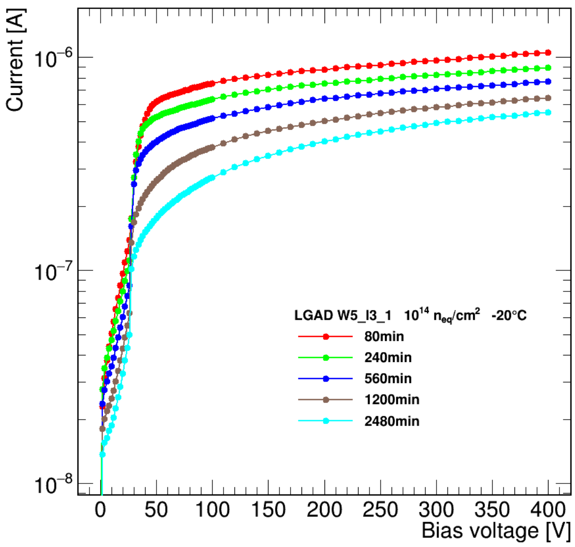

(a) Full plot range

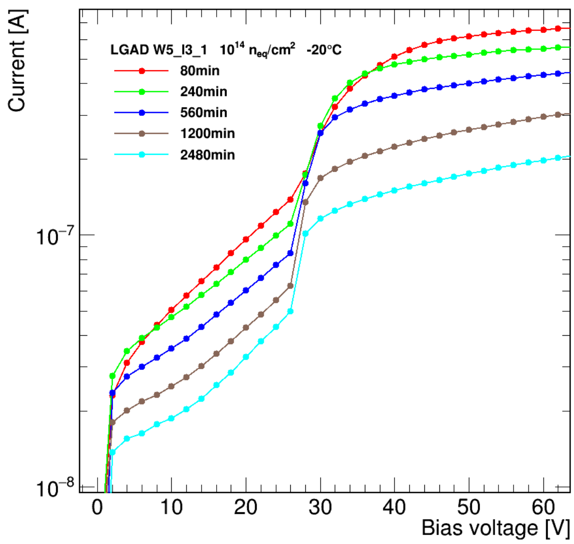

(b) Limited plot range

Figure 4.1. – Leakage current measurements of LGAD W5_I3_1 as a function of bias voltage after irradiation. Accumulated annealing times at 60 °C are indicated in the figure legend. The data is shown with a full and limited plot range. [78]

depletion voltage of the gain layer is of special interest, the data is shown separately with a limited voltage range. The measurements show an exponential trend below a reverse bias voltage of 26 V. At

this point a steep increase in current occurs, which reaches a plateau at higher voltages. This trend is observed for both LGADs and is independent of annealing time.
To compare the leakage current measurements after irradiation and annealing to expectation, the current related damage rate α was calculated, using the equation

$$\alpha = \frac{\Delta I}{\Phi_{eq} \times V}. \tag{4.1}$$

ΔI, in principle, is the difference in current, measured before and after irradiation. Since the current before irradiation is by orders of magnitude smaller, it can usually be neglected. Φ_{eq} is the 1 MeV-neutron equivalent fluence. The active sensor volume V was calculated from the geometrical specifications of the sensor: $V = 3.2 \times 3.2\ \text{mm}^2 \times 277\ \mu\text{m}$. The change of the current related damage rate with annealing time is parameterized by the equation (see also sec. 2.3.3, eq. 2.18)

$$\alpha(t) = \alpha_1 \cdot \exp\left(\frac{-t}{\tau_1}\right) + \alpha_0 - \alpha_2 \cdot \ln\left(\frac{t}{t_0}\right). \tag{4.2}$$

In leakage current measurements of irradiated detectors a dependence on the bias voltage above full depletion is observed, which is not described by this equation. On the other hand, the volume V is not known below full depletion. For those reasons, current measurements were selected for the calculation with a 10 – 20% margin above the full depletion voltage, ranging from 150 V for 80 min annealing to 400 V for 5040 min annealing. The bias voltages used are the same across the three devices. The choice of the voltages affects the calculated values, which leads to some uncertainty. During the measurements, the guard ring was not connected for technical reasons: The sensors were mounted on a PCB for TCT measurements so that current and capacitance measurements had to be carried out in the climate chamber, which is usually used for beta-source measurements. This setup did not have the possibility to measure the pad and guard ring currents separately. To estimate the pad current from measurements of the total current without connecting the guard ring, leakage current measurements after irradiation and 80 min of annealing, during which the pad and total current were measured separately before mounting the respective sensor on the PCB for TCT measurements, were used. The ratio of total current to pad current for both LGADs was measured to be 1.41 and independent of the applied bias voltage. For the PIN sensor a voltage dependence was measured, ranging from 2.06 (150 V) to 2.28 (400 V). To obtain the value of α resulting from the pad current generated in the volume V, the current measurements after annealing were scaled by these ratios. The calculated values for the proton irradiated PIN and LGADs are shown in fig. 4.2. Measurements are shown by markers, connecting lines are included to guide the eye. The measurement of the PIN after an annealing time of 560 min was excluded from the figure due an unexpectedly high leakage current, which is likely to be caused by an insufficient settling time of the sensor temperature before starting the measurement. Continuous lines indicate the predicted value, given by eq. 4.2, using the parameters $t_0 = 1$ min, $\tau_1 = 94$ min, $\alpha_0 = 1.26 \cdot 10^{-17}$ A/cm, $\alpha_1 = 4.87 \cdot 10^{-17}$ A/cm and $\alpha_2 = 3.16 \cdot 10^{-17}$ A/cm [49]. The theory prediction was scaled to the measurement temperature of −20°C, using eq. 2.10. A fit was performed to adjust the calculated values to the measurements. The only free parameter was a constant factor K, with which eq. 4.2 was multiplied. The resulting value is indicated in the legend of the figure for the three sets of measurements. The PIN is in rather good agreement with the expected values. The difference of 3% can be originating from the choice of the bias voltage and the the fact that the guard ring was not connected. The factor for the LGADs (≈ 3.3) is in good agreement with the measured gain of the devices (fig. 4.8), as expected. Measurements of the sensor capacitance of the

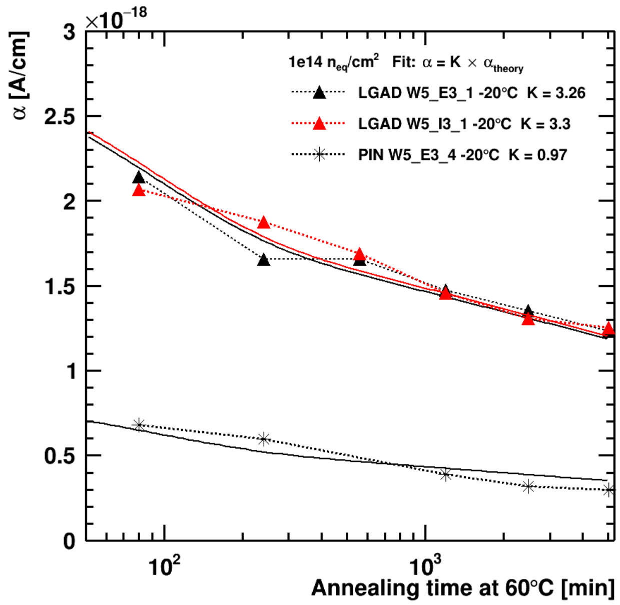

Figure 4.2. – Current related damage rate α as a function of annealing time. The samples were irradiated with protons to a fluence of $1 \times 10^{14}\,\mathrm{n_{eq}/cm^2}$. The leakage current measurements were scaled to 20°C. The data was fitted with eq. 2.18 [78]

irradiated LGAD W5_I3_1 at −20°C are shown in fig. 4.3. Measurements of the other LGAD show a similar behavior. As for the leakage current measurements, the capacitance measurements had to be carried out in the beta-setup without connecting the guard ring. Initially the measured capacitance decreases with increasing bias voltage until at 26 V a sudden increase of the capacitance is observed. This bias voltage coincides with the point, at which the leakage current rises abruptly (fig. 4.1). After this, the capacitance decreases to a stable value at high bias voltages. The increase at around 26 V is only observed in measurements of the LGADs and therefore has to be attributed to the multiplication layer. The bias voltage, at which the increase occurs is independent of annealing time but the effect changes in amplitude. The effect is visible already after 80 minutes of annealing but more pronounced for longer annealing times. The end capacitance at high bias voltages, after full depletion, agrees across different annealing times, as is expected. Before full depletion, the capacitance at a given bias voltage is higher for longer annealing times. The full depletion voltage was obtained for both proton irradiated LGADs from a fit to the rising slope of the values of $1/C^2$ as a function of bias voltage. Only values above a bias voltage of 30 V were included in the fit to avoid the aforementioned increase of capacitance at low voltages. The full depletion voltage is then the value at which the rising edge intersects a horizontal line through the highest measured capacitance. The obtained values for the full depletion voltage are shown in fig. 4.4. The determination of the full depletion voltage from capacitance measurements after irradiation has the limitation that the measurements usually do not show a clear transition from undepleted (decreasing capacitance) to full depletion (stable capacitance) which leads to some uncertainty in the values obtained. Especially for high irradiation the concept of a clear separation of depleted and undepleted volumes in the sensor for a given voltage is not applicable. The capacitance measurement of sensor W5_E3_1 after 80 minutes of annealing failed, which was

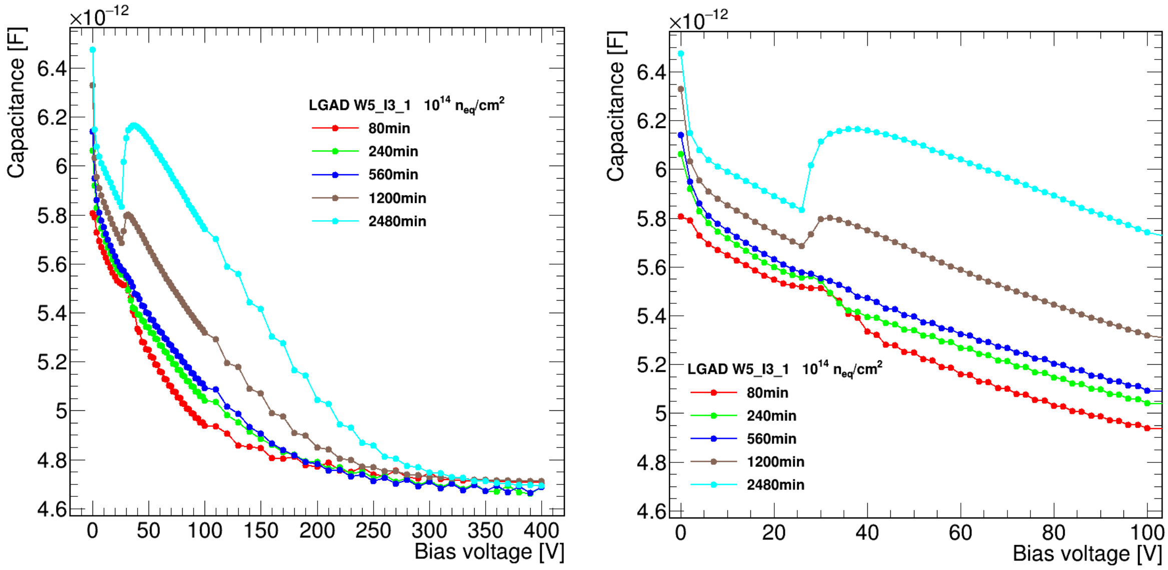

(a) Full plot range

(b) Limited plot range

Figure 4.3. – Capacitance measurements of LGAD W5_I3_1 as a function of bias voltage after irradiation. Accumulated annealing times at 60 °C are indicated in the figure legend. The data is shown with a full and limited plot range. [78]

only realized after performing the next annealing step. Therefore one point is missing in the graph.

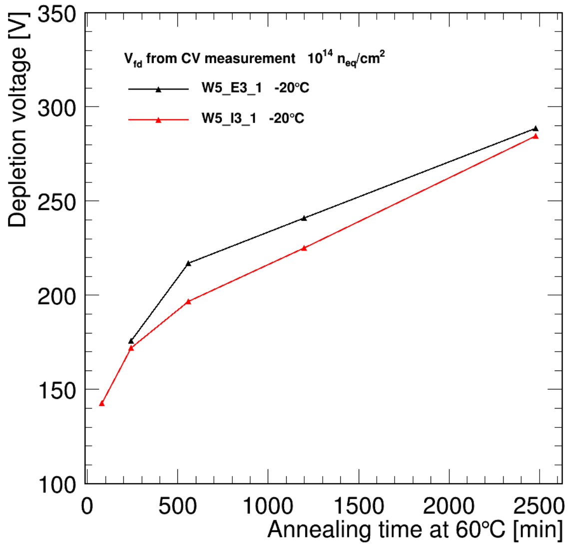

Figure 4.4. – Full depletion voltage of the proton irradiated LGADs as a function of annealing time. Values were obtained from capacitance measurements. [78]

4.3. TCT Measurements

Measurements with the transient current technique were carried out with the TCT+ setup (sec. 3.2.1). TCT measurements with light injection from the front of the sensor with red light (RF-TCT) and from the edge of the sensor with infrared light (e-TCT) were performed. The measurements were repeated for temperatures of −20°C and +20°C. The bias voltage was varied from 0 to 400 V, in steps of 2 V, for RF-TCT measurements. For e-TCT measurements the maximum voltage was 300 V with an incremental increase of 5 V. In addition, during e-TCT measurements the z-position of the laser beam was varied in steps of 2 to 3 μm. A single waveform consists of an average of 256 individual measurements. The sensor was biased from the backside with the front electrode on ground potential, while the guard ring was connected to ground via a 50 Ω resistor. The laser power was kept constant across all measurements and all recorded signals were normalized, using a reference diode.
Fig. 4.5 shows the integrated signal current (collected charge) within 25 ns from the start of the signal as a function of bias voltage for LGADs W5_I3_1 (red) and W5_E3_1 (black) at a measurement temperature of −20°C. The measurements were repeated after each successive annealing step. The measurements before irradiation reach a plateau at a value of 6000 in arbitrary units and then increase to a value of around 7000 at 400 V. For clarity these values are not included in the range of the figure. The different measurements after irradiation reach a similar amount of collected charge above 300 V. Below 300 V the collected charge is lower for longer annealing times at a given bias voltage. TCT measurements with red light injection from the front of an LGAD show a distinct behavior: Nearly zero charge is collected up to a certain bias voltage, at which the charge suddenly increases. This behavior is sometimes related to the depletion of the gain layer. The figure with a plot range limited to small bias voltages shows that the voltage at which the charge increases (TCT onset voltage) changes with irradiation and with annealing. But, as can be seen in the following, the measured onset voltage does not always directly correspond to the gain layer depletion voltage. From the measurements the

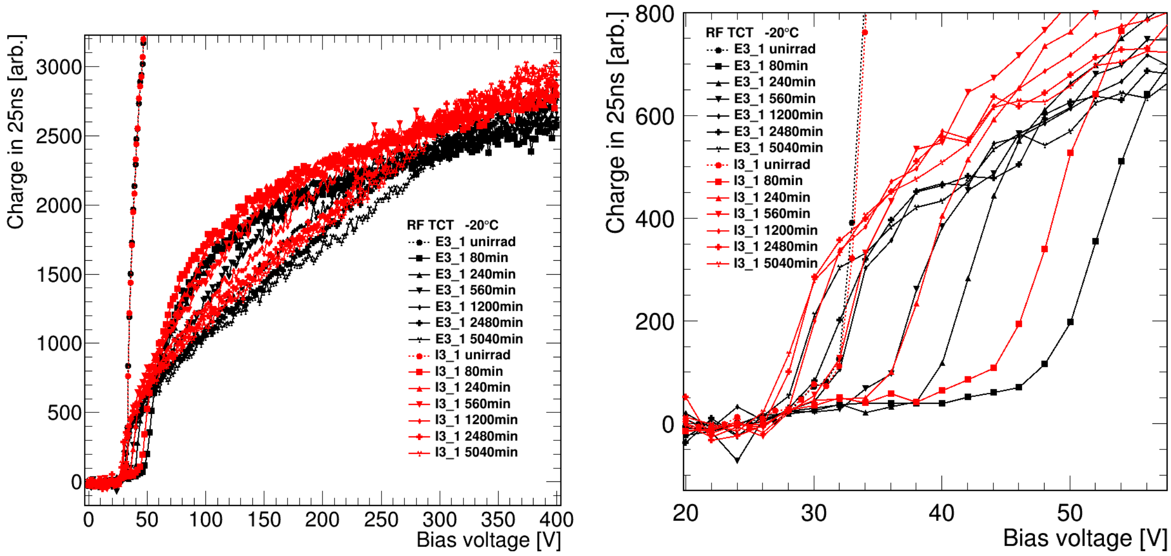

(a) Full plot range

(b) Limited plot range

Figure 4.5. – Collected charge as a function of bias voltage of LGADs W5_I3_1 and W5_E3_1 after charge injection by a red laser from the front side. Accumulated annealing times at 60 °C are indicated in the figure legend. The data is shown with a full and limited plot range. [78]

value of the onset voltage is determined with a fit to the collected charge with

$$Q_{25ns} \propto \begin{cases} \sqrt{V_{bias} - V_{onset}} & \text{for} \quad V_{bias} \geq V_{onset} \\ 0 & \text{for} \quad V_{bias} < V_{onset} \end{cases} . \tag{4.3}$$

Fit results for −20 °C can be found in the appendix (fig. A.2, p. 118). The values obtained for the onset voltage are shown in fig. 4.6 for the two irradiated LGADs for measurement temperatures of −20°C and +20°C. The onset voltage before irradiation is about 32 V. With irradiation this value increases to around 45 to 50 V. With increasing annealing time the onset voltage successively decreases to a value of approximately 26 V, which is the same value that was observed already in IV and CV measurements. No systematic dependence on temperature can be observed. Notably, the collected charge before reaching the onset voltage during measurements at higher annealing times is not exactly zero, as can be seen in fig. 4.7. Two distinct steps can be observed at different voltages: A slight increase which occurs always at around 26 V and the onset voltage described above at a slightly higher bias voltage. This plateau between 26 and 40 to 45 V is not described by eq. 4.3.

From measurements of the collected charge the gain of the LGADs can be calculated by comparison to a PIN diode. The PIN sensor W5_E3_4 has the same design as the LGADs W5_E3_4 and W5_I3_1, except for the fact that it does not feature a gain layer. All sensors were irradiated with protons to the same fluence of 10^{14} n_{eq}/cm^2 and annealed for the same time at the same temperature. After each annealing step the gain as a function of bias voltage is calculated as the ratio of collected charge measured with the LGADs and the charge measured with the PIN diode

$$Gain(V) = \frac{Q_{25ns}^{LGAD}(V)}{Q_{25ns}^{PIN}(V)}. \tag{4.4}$$

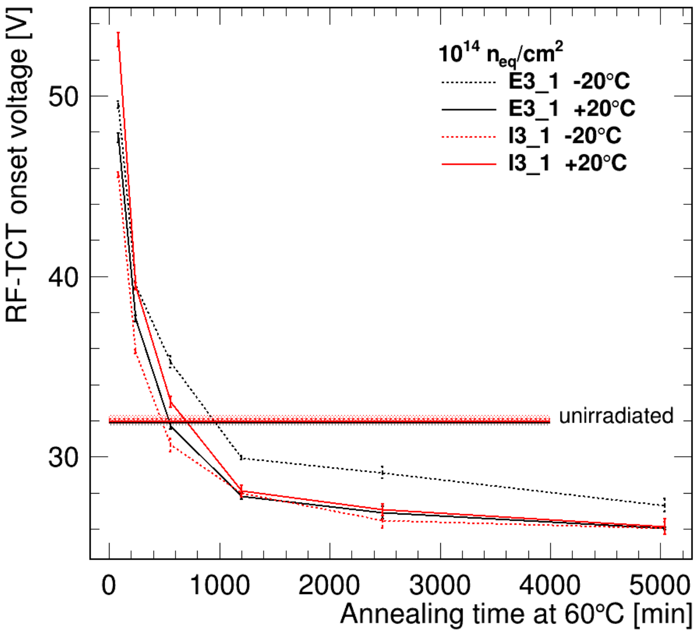

Figure 4.6. – TCT onset voltage as a function of annealing time for proton irradiated LGADs. The onset voltage before irradiation is indicated by a horizontal line. [78]

The current signal was integrated over 25 ns. Fig. 4.8 shows the measured gain at a bias voltage of 400 V for both LGADs at measurement temperatures of −20°C and +20°C as a function of annealing time. Corresponding measurements before irradiation are indicated as horizontal lines. Before irradiation the gain is around 4.75 and 6 for measurements at +20°C and −20°C, respectively. The different values at different temperatures are expected because of the temperature dependence of the impact ionization coefficient. The relative decrease in gain of about 20-25% with an increase in temperature of 40°C is comparable to observed and simulated values in literature [79, 80]. The sensor W5_E3_1 is in principal identical to W5_I3_1 but shows a slightly lower gain in all measurements. After irradiation, the gain is reduced to values ranging from 2.5 to 3.5. The relative decrease in gain is therefore about 40 to 45 %. This reduction of gain can be compared to other studies, where the gain almost completely vanished after charged hadron irradiation of LGADs to a fluence of 5×10^{14} n_{eq}/cm^2 [41]. No change of gain can be observed with annealing.

Edge-TCT measurements have been carried out to better understand the effects of irradiation and annealing at different bias voltages. From the relation between the signal current, drift velocity and electric field and under the assumption of a constant charge carrier mobility μ, it is possible to estimate the shape of the electric field [81]

$$I(t \approx 0) \propto v_{drift} \propto \mu(E)E(z). \tag{4.5}$$

Results of the measurements of sensor W5_I3_1 are shown in fig. 4.9. Again, the other LGAD W5_E3_1 showed a similar behavior (appendix, fig. A.7, p. 120). Fig. A.4 (appendix, p. 119) shows the full voltage range for 80 and 2480 minutes of annealing. During e-TCT measurements the sensor is illuminated from the side, with the laser beam passing through the sensor bulk, parallel to the front and rear electrodes. The z-axis, along which the beam position is varied, is oriented perpendicular to the front and rear surfaces of the sensor. The drift velocity, which is a measure of the electric field

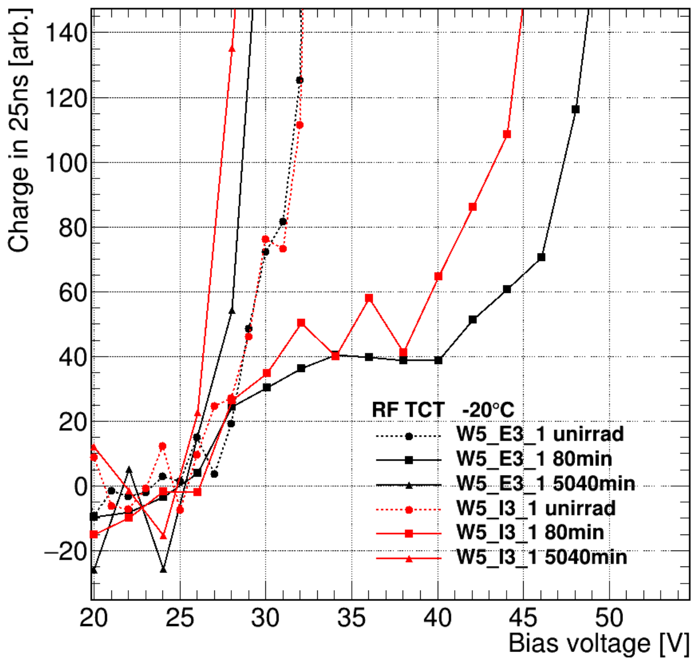

Figure 4.7. – Collected charge as a function of bias voltage of LGADs W5_I3_1 and W5_E3_1 after charge injection by a red laser from the front side. Same measurements as fig. 4.5 with different plot range. [78]

strength, can therefore be measured as a function of depth from the sensor top towards the backside of the sensor. Low values of z, on the left hand side of the respective figure, correspond to the front side of the sensor, which is the location of the gain layer. In the left figure (a) the drift velocity is shown after irradiation and 80 minutes of annealing for bias voltages ranging from 5 to 55 V. The figure on the right (b) shows the drift velocity at a bias voltage of 55 V for different annealing times. Because the graphs at different annealing times correspond to measurements on different days, the alignment of the z-axis changes slightly from one measurement to another. Therefore, the graphs have been aligned on the rising edge on the left hand side. Two important features can be identified in the electric field distribution as a function of bias voltage in fig. 4.9 (a). First, the electric field does not decrease linearly towards the backside of the detector, as would be expected in the case of homogeneous space charge, like in an unirradiated detector. Instead the field rises towards the backside, which is referred to as a double junction (sec. 2.3.3). The effect is explained by the trapping of mostly holes due to the higher concentration of holes towards the backside. The sign of the space charge in the p-bulk is therefore changed from negative to positive, leading to an electric field near the back contact of the sensor after irradiation. Second, one can see that after increasing the bias voltage from 25 to 30 V the electric field is prevalent across the whole device, instead of following the field distribution which is observed at lower voltages. The latter effect, the change of the field distribution moving from 25 to 30 V, is observed to be independent of annealing time and always occurs at the same voltages. Measurements before irradiation show a significant increase in signal only at higher voltages of about 35 V to 40 V. The electric field at the backside of the sensor, which can be clearly seen after irradiation and 80 minutes of annealing, appears to be reduced after longer annealing times. This can be seen in the right hand side (fig. 4.9 (b)). With increased annealing of the sensor, the overall field at the given bias voltage is reduced and the field at the backside vanishes. The sharp peak at about $z = 0.27$ mm

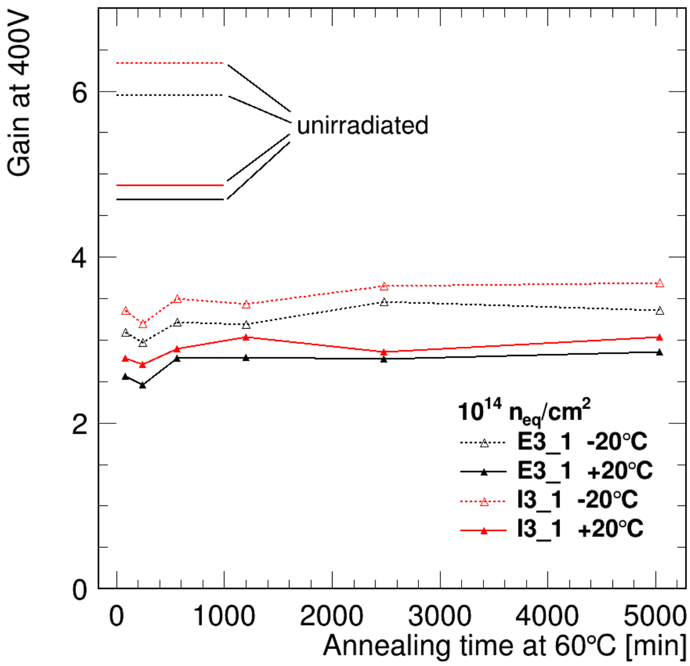

Figure 4.8. – Charge gain at 400 V as a function of annealing time at 60°C. The gain is calculated using RF-TCT measurements, comparing the PIN diode and the LGADs in the same annealing state. Measurements before irradiation are shown as horizontal lines. [78]

is an effect of the rear ohmic contact, which can often be observed in edge-TCT measurements and is not related to the rear electric field, discussed here. For reference, a measurement of the unirradiated device is shown as a black dotted line. In contrast to the measurements after irradiation, the field decreases linearly until reaching the backside of the sensor. This measurement shows some non-zero signal outside of the physical volume of the sensor ($z > 0.3$ mm) which is an artifact resulting from light being reflected into the sensor from the PCB or backside contact at a beam position at which no light should enter the sensor anymore. In addition, in both figures, the sharp peak of electric field which is expected at the position of gain layer, is not visible. This is attributed to the limited spatial resolution of the experimental method used.

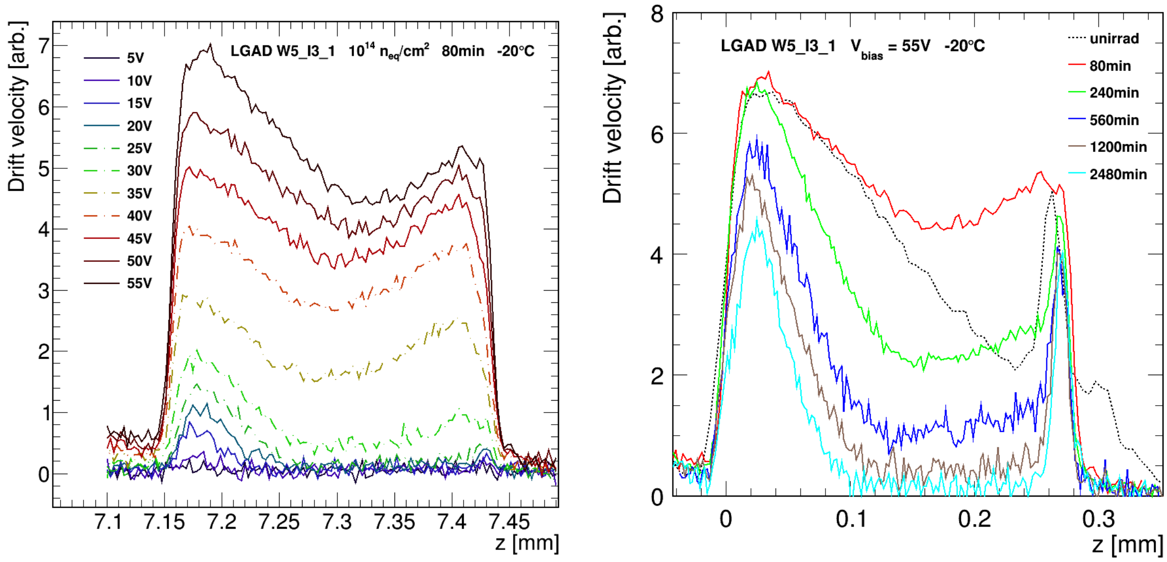

(a) (b)

Figure 4.9. – Drift velocity as a function of position of the laser beam inside the silicon bulk. (a) LGAD W5_I3_1 after irradiation and 80 minutes of annealing for different bias voltages. (b) LGAD W5_I3_1 at a bias voltage of 55 V for different annealing times. The left hand side of the figures, at low values of z, corresponds to the front side of the detector, where the gain layer is located. [78]

4.4. Discussion

The shape of the measurements of the leakage current, showing a sharp increase at a bias voltage of 26 V, can be explained by the sequential depletion of the gain layer and the sensor bulk, due to the difference in doping concentration. Due to the distinct shape of the doping profile of LGADs, before the gain layer is depleted the field strength increases exclusively in the gain layer when the bias voltage is increased. This leads to multiplication of the leakage current, which is expected to follow an exponential trend due to the dependence of impact ionization on the electric field strength. The prevalence of multiplication before the depletion of the gain layer can also be seen in current measurements with injection of continuous LED light. A dependence of the current, which is fully dominated by the charge carrier injection, on the gain layer doping concentration can be observed before the gain layer is depleted (fig. A.11, p. 124). As soon as the gain layer is depleted, the additionally applied voltage leads to the depletion of the bulk, leading to a sudden increase in current. As the voltage is further increased the field increases across the whole device, leading to a slower increase in leakage current than before depletion of the gain layer. The measurements of the leakage current indicate that the gain layer depletes always at 26 V after irradiation, independent of annealing time. Edge-TCT measurements after irradiation and low annealing show a double junction, the prevalence of an electric field at the backside of the detector, with a lower electric field strength in the middle of the detector. This effect is linked to the shift of the onset voltage measured with red light injection from the front of the device to higher voltages. On the other hand, edge-TCT measurements show as well that a non-zero drift velocity can be observed after irradiation for all annealing steps always between 25 to 30 V, which supports the observation in IV and CV measurements that the gain layer depletes always at 26 V. This bulk-field is observed at a bias voltage of 35 V to 40 V before irradiation, in agreement with the onset voltage measured with red front TCT. Concluding, the gain layer seems to always deplete at 26 V after irradiation. Before irradiation the gain layer depletion is around 32 to 33 V. TCT measurements with red light injection from the front of the sensor show a higher onset voltage which is linked to the effect of a double junction. The double junction effect decreases with annealing time and leads to a convergence of the TCT onset voltage towards the value of 26 V, which is expected from the gain layer depletion. The calculation of the current related damage rate shows that the PIN sensor follows the common parametrization in literature. One can further see that the current related damage rate of the LGADs differs by a factor (≈ 3.3), which is in agreement with the gain of the LGADs measured with TCT after irradiation. Besides this, the reduction of leakage current with increasing annealing time follows the same trend as the PIN. This shows that the reduction of gain after irradiation is equally observed in charge injection and current measurements and that no recovery nor degradation of gain can be observed with annealing of the sensors both in IV and TCT measurements. As explained in sec. 2.3.3 the reduction of gain is mostly explained by the effect of acceptor removal and by a redistribution of the electric field due to charged defects. One of the main reasons for acceptor removal is the formation of B_iO_i defect complexes, effectively deactivating the implanted boron. These defect levels were shown to be unaffected by annealing by using thermally stimulated currents (TSC) measurements [65].

The capacitance measurements of the sensors behave as expected, except for the abrupt increase of capacitance, which is observed in measurements of the LGADs at a bias voltage of 26 V. This effect is related to the multiplication layer and the voltage at which it occurs notably coincides with the depletion of the gain layer as observed in measurements of the leakage current. The origin of this behavior is not fully understood. A sudden increase in multiplied charge carriers as soon as the gain layer is depleted can lead to a reduced depleted region around the junction, effectively increasing the measured capacitance. A similar effect had been observed before [82] and was explained by the behavior of a Shockley diode (pnpn): If the sensor bulk behaves like an n-type bulk due to acceptor removal and trapping of charge carriers, the junction between the multiplication layer and the sensor bulk has the opposite polarity compared to the junction between n^+-implant and multiplication layer and the junction between sensor bulk and backside contact. In this configuration it is forward biased and can dominate the overall capacitance of the device.

The increase in depletion voltage indicates that the sensors are undergoing reverse annealing, which leads to an increase of negative space charge. This effect causes the suppression of the double junction effect at higher annealing times. In turn, the onset voltage, measured with TCT and red light injection from the top, is reduced to lower values than before irradiation, caused by the reduced depletion voltage of the gain layer.

5. Introduction to the Two-Photon Absorption - Transient Current Technique

Lasers are a very convenient way to inject charge in semiconductor devices for testing purposes. The beam properties can be adjusted to match the desired use-case and, given the high confinement of a laser pulse in space and time, very precise measurements can be performed. Charge injection with lasers is therefore widely used in the IC-industry and development of light and particle detectors. In the specific case of two-photon absorption, very high light intensities are required to create a detectable amount of charge. For this, lasers with a short pulse duration are used, which have a moderate average output power but a very high energy per pulse. Mainly short pulse lasers in the femtosecond-regime, that are used in industry, support pulse energies of about 1 nJ at high frequencies in the order of 100 MHz. For TPA-TCT the pulse energy should be between one and ten nanojoule, to ensure that enough charge is created. At too high energies a plasma can be created inside the silicon, which would alter the signal shape and distort the measurement result [83, 84]. Furthermore, to avoid an impact on the material properties, a lower repetition frequency of about 200 Hz is desired for TPA-TCT measurements. A compact laser system with these properties was not available on the market at the start of the project. Therefore, a laser fulfilling these requirements was developed specifically for TPA-TCT by the company Fyla[1]. The general introduction to optics in this chapter is based on [85] and [86]. A detailed description of non-linear optical effects and the generation and manipulation of ultra-short laser pulses can be found in [87] and [88]. Some examples in this chapter are calculated for a laser pulse duration of $\tau = 300$ fs, which was the nominal pulse duration of the upgraded Fyla laser (see sec. 6.1). The actual pulse duration is closer to $\tau = 430$ fs.

5.1. Spatial and Temporal Description of Laser Pulses

From the Maxwell equations, the wave equation

$$\nabla^2 \vec{E} - \mu\epsilon \frac{\partial^2 \vec{E}}{\partial t^2} = 0 \tag{5.1}$$

can be deduced (analogous for $\vec{B}$). An instructive, but physically unrealistic, solution is a plane wave in the form of

$$\vec{E}(\vec{r}, t) = \vec{E}_0(\vec{r}, t)\mathrm{e}^{i\phi(\vec{r},t)}, \tag{5.2}$$

with phase

$$\phi(\vec{r}, t) = \vec{k} \cdot \vec{r} - \omega t \tag{5.3}$$

and amplitude $\vec{E}_0(\vec{r}, t)$. The phase describes the evolution of the wave in space and time with the wave vector $\vec{k}$ and circular frequency ω. In TPA-TCT, short laser pulses are used together with strong focusing optics to generate charge in silicon. Therefore, some important aspects of beam propagation

[1]Fyla, Valencia, Spain, https://www.fyla.com

and light pulses are described in the following.

5.1.1. Gaussian beam propagation

In contrast to a plane wave, laser light has a high degree of directionality. The field amplitude drops quickly in the plane transverse to the propagation direction but remains constant over long distances otherwise (*slowly varying envelope approximation*, SVEA). Around the direction of propagation, the beam exhibits cylindrical symmetry. In addition, laser light is the closest approximation to a monochromatic wave that can be produced experimentally.
With these requirements a solution to the wave equation, describing a beam of light propagating in z-direction, in the form of

$$E(\vec{r},t) = A\frac{w_0}{w(z)}\exp\left[\frac{-r^2}{w^2(z)}\right]\exp\left[\frac{\mathrm{i}kr^2}{2R(z)}\right]\exp\left[\mathrm{i}(kz-\omega t-\phi(z))\right], \tag{5.4}$$

$$\text{with} \qquad R(z) = z + \frac{z_0^2}{z} \qquad \text{and} \qquad w(z) = w_0\sqrt{1+\left(\frac{z}{z_0}\right)^2} \tag{5.5}$$

can be found. The third exponential term describes the spatial and temporal oscillation of the electric field with frequency ω and constant phase ϕ. The second exponential term describes the curvature of the wavefront: At $z = 0$ the beam resembles a plane wave. At some distance away from the focal point, the surfaces of equal phase are curved, with curvature $1/R$ and are nearly spherical for very large z.
The amplitude of the beam-like solution is

$$E_0(\vec{r}) = A\frac{w_0}{w(z)}\exp\left[\frac{-r^2}{w^2(z)}\right], \tag{5.6}$$

which is a function of x, y and z, with $r^2 = x^2 + y^2$. At $z = 0$ the wave resembles a plane wave but at larger z the amplitude is reduced and the planes of constant phase approach a spherical form. For not too large z, the amplitude diverges much slower than the one for a spherical wave. For a constant value of z, the amplitude profile takes a Gaussian shape. At a distance from the center of the beam of $r = w(z)$ the field amplitude has dropped to 1/e of its maximum value. Note that, since the pulse irradiance $I \propto E^2$, the beam radius $w(z)$ corresponds to $1/e^2$ (or 2σ) of the irradiance at this point. The parameter w_0 is the beam waist at its narrowest point ($z = 0$). At the Rayleigh length z_0 the beam waist has increased, such that $w(z_0) = \sqrt{2}w_0$. Beam waist and Rayleigh length are related through

$$w_0^2 = \frac{2z_0}{k} = \frac{z_0\lambda}{\pi n}, \tag{5.7}$$

with the laser wavelength in vacuum λ and refractive index n of the material. The asymptotically defined beam divergence is

$$\tan\theta = \lim_{z\to\infty}\frac{dw(z)}{dz} = \frac{w_0}{z_0}. \tag{5.8}$$

The different parameters, describing the spatial profile of a laser beam are visualized in figure 5.1. A microscope objective is used in TPA-TCT to focus the laser beam onto the sample. The numerical

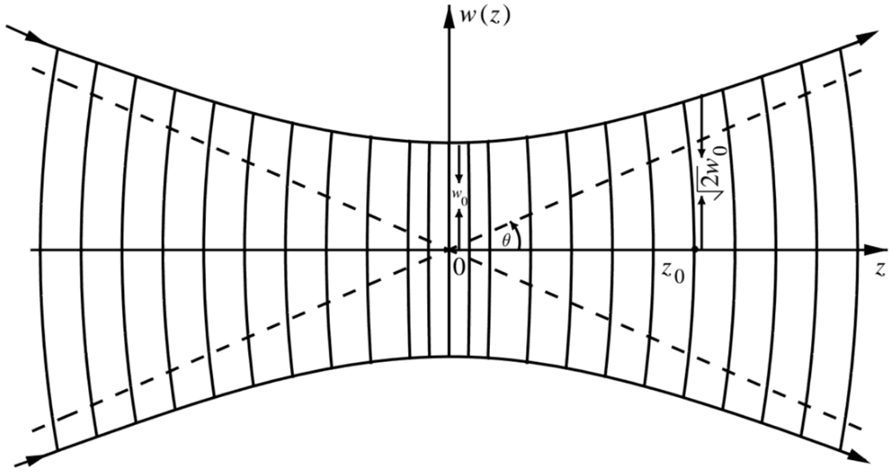

Figure 5.1. – Variation of the transverse profile of a beam propagating in z-direction. Divergence θ, beam waist w_0 and Rayleigh length z_0 are indicated. [85]

aperture (NA) of a microscope objective is defined by the half opening angle θ of the beam:

$$NA = n \sin\theta \approx \lambda/\pi w_0. \tag{5.9}$$

The angle θ, as well as the Rayleigh length change with the refraction index. The numerical aperture and the beam radius at the waist w_0 remain constant on the other hand. Using equations 5.5, 5.7 and 5.9, the beam radius can be written as a function of NA, n and λ:

$$w(z) = \sqrt{\left(\frac{\lambda}{\pi\, NA}\right)^2 + \left(\frac{z\, NA}{n}\right)^2}. \tag{5.10}$$

Equation 5.10 is plotted in fig. 5.2 for different focusing optics ($NA = 0.7$, $NA = 0.5$ and $NA = 0.14$) in silicon ($n = 3.4757$, black) and air (red). The focal point is located at the origin of the plot. The minimum beam radius is 0.7 μm for $NA = 0.7$, 1 μm for $NA = 0.5$ and about 3.5 μm for $NA = 0.14$. The beam diverges less in silicon, resulting in a longer Rayleigh length. The large opening angle of the beam has important experimental consequences. Usually spatial scans in depth (along the beam axis) are carried out, either from the top or the edge of a device. In this case, it needs to be considered that all of the beam should enter the sample at a given depth of the focal point. For example, as can be seen in the figure, at a depth of the focal point of 300 μm, the point where the beam enters the sample on the surface should have a distance to any obstacle (surface metallization, sensor edge) of at least 40 μm, for an objective with $NA = 0.5$. This fact is the main limitation for performing edge-TPA-TCT measurements. The opening angle θ, the beam radius at the waist w_0 and the Rayleigh length z_0 of an ideal Gaussian beam are also shown in table 5.1 for three different values of the numerical aperture.

5.1.2. Pulse duration and bandwidth

A plane wave, with its spectrum containing only a single wavelength, has an infinite duration. A laser pulse, which has a limited duration, always consists of a multitude of frequencies, defined by the spectral bandwidth. Starting from a plane wave a light pulse can be obtained mathematically by a

		$NA = 0.7$	$NA = 0.5$	$NA = 0.14$
Silicon	θ	11.6°	8.3°	2.3°
	$w_0[\mu m]$	0.705	0.987	3.524
	$z_0[\mu m]$	3.501	6.863	87.5
Air	θ	44.4°	30°	8°
	$w_0[\mu m]$	0.705	0.987	3.524
	$z_0[\mu m]$	1.007	1.974	25.170

Table 5.1. – Beam opening angle, radius at the beam waist and Rayleigh length for different focusing optics in silicon and air. A wavelength of $\lambda = 1.55$ μm and a refractive index of silicon of $n = 3.4757$ was used for the calculation.

multiplication with a Gaussian function and then has the form [88]

$$E(t) = \text{Re}\left[\exp\left[-\text{i}\omega_0 t - \Gamma t^2\right]\right]. \tag{5.11}$$

Γ is the shape form of the Gaussian field envelope and is related to the full width at half maximum (FWHM) of the intensity profile by $\Gamma = 2\ln 2/\tau^2$. Fig. 5.3 shows the time evolution (eq. 5.11) of the electric field of a laser pulse at a wavelength of $\lambda = 1.55$ μm. The central wavelength of $\lambda = 1.55$ μm corresponds to a frequency of $f = \omega/2\pi = 194$ THz. One optical cycle is $T = 2\pi/\omega = \lambda/c = 5$ fs. The intensity is proportional to the square of the electric field and is shown in fig. 5.4. The FWHM of the intensity profile in these examples is $\tau = 300$ fs. The spectral content of a light pulse is obtained by calculating the Fourier transform of the time evolution function:

$$E(\omega) = \int_{-\infty}^{\infty} \exp\left[-\text{i}\omega_0 t - \Gamma t^2\right] \exp\left[\text{i}\omega t\right] dt = \sqrt{\frac{\pi}{\Gamma}} \cdot \exp\left[-\frac{(\omega - \omega_0)^2}{4\Gamma}\right]. \tag{5.12}$$

The spectral content of a Gaussian pulse with a width of $\tau = 300$ fs and a central wavelength of $\lambda_0 = 1.55$ μm, calculated from eq. 5.12 with $\omega = 2\pi c/\lambda$, is shown in fig. 5.5. The FWHM bandwidth, resulting from the pulse duration given, is 11.7 nm, corresponding to $\Delta f = 1.471$ THz. The variance of the squared electric field in the time and frequency domain can be calculated from eq. 5.11 and 5.12, resulting in

$$\sigma_\omega^2 = \frac{\int_{-\infty}^{\infty} (\omega - \omega_0)^2 |E(\omega)|^2 d\omega}{\int_{-\infty}^{\infty} |E(\omega)|^2 d\omega} = \Gamma \tag{5.13}$$

$$\sigma_t^2 = \frac{\int_{-\infty}^{\infty} t^2 |E(t)|^2 dt}{\int_{-\infty}^{\infty} |E(t)|^2 dt} = \frac{1}{4\Gamma}, \tag{5.14}$$

which leads to

$$\sigma_t \sigma_\omega \geq \frac{1}{2}. \tag{5.15}$$

Often the FWHM is more accessible experimentally, thus the latter inequality can be expressed as

$$\tau\, \Delta f \geq 0.441, \tag{5.16}$$

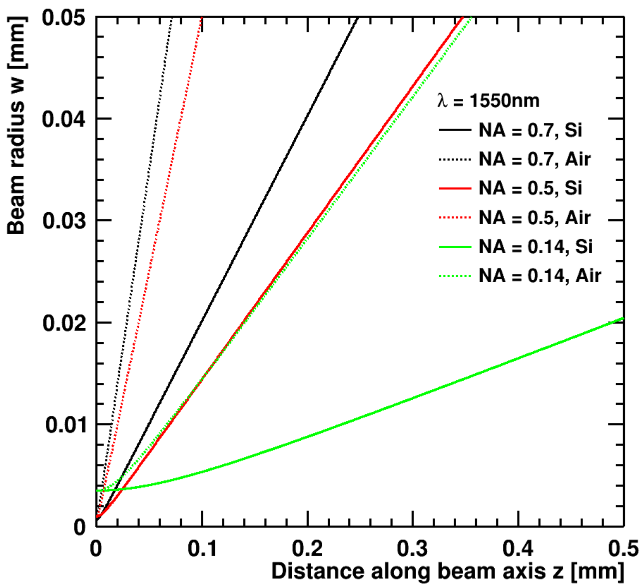

Figure 5.2. – Beam radius w as function of position along the beam axis for different NA, in air and silicon.

with $\tau = 2\sqrt{2\ln 2}\,\sigma_t$ and $\Delta f = 2\sqrt{2\ln 2}\,\sigma_\omega/2\pi$. With the example given above, equality is reached in eq. 5.15 (and eq. 5.16). Expressing the product of bandwidth and pulse duration as an inequality, accounts for the fact that the pulse duration can be larger for a given bandwidth, if a non-linear term is present in the temporal phase of the pulse. Conversely, a pulse with a larger bandwidth could potentially be further compressed to a shorter duration. When equality in eq. 5.16 is reached, the pulse is said to be Fourier-transform-limited, which means that it can not be shorter for the given bandwidth. To produce shorter light pulses, the spectral bandwidth would have to be increased. This example was calculated for a Gaussian shaped pulse. For a non-Gaussian shaped pulse a similar inequality applies, but with a constant larger than 0.441, depending on the shape of the envelope function.

5.1.3. Beam irradiance

The beam irradiance is the energy received by a surface per unit area and time and can be calculated as the magnitude of the time averaged Poynting vector

$$I = \langle S \rangle \propto |E|^2. \tag{5.17}$$

With the expression for the amplitude of the electric field of a Gaussian beam (eq. 5.6) and with the exponential term to describe a laser pulse in time (eq. 5.11) the beam irradiance (compare e.g. [86]) can be formulated as

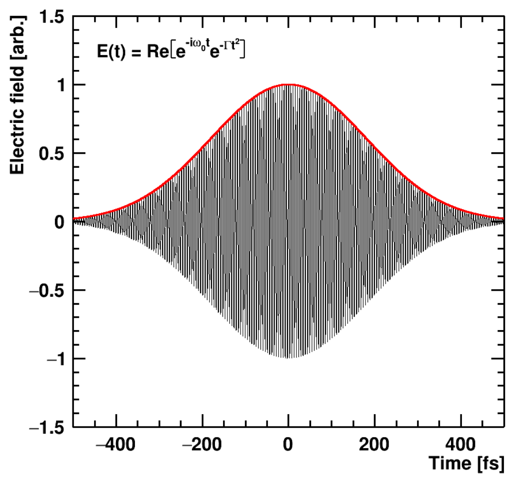

Figure 5.3. – Time evolution of the electric field of a Gaussian-shaped pulse. The pulse is constructed by multiplicatian of the plane wave equation and a Gaussian function.

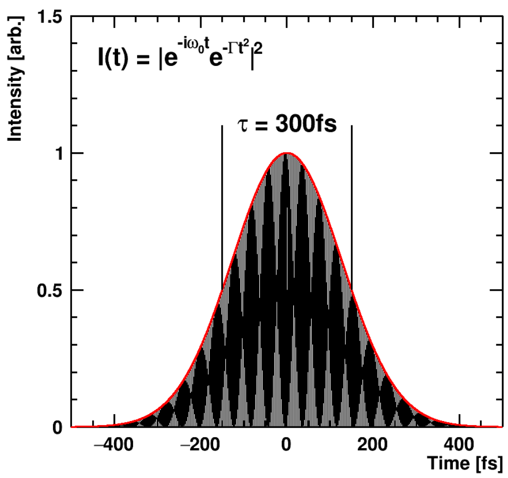

Figure 5.4. – Intensity profile of a Gaussian pulse with FWHM $\tau = 300$ fs.

$$I(r, z, t) = \frac{E_p}{\tau} \frac{4\sqrt{\ln 2}}{\pi^{\frac{3}{2}} w^2(z)} \exp\left[-\frac{2r^2}{w^2(z)}\right] \exp\left[-4\ln 2\frac{t^2}{\tau^2}\right]. \tag{5.18}$$

The FWHM of the beam temporal profile is denoted as τ. The beam radius $w(z)$ is the two-sigma radius of the beam intensity profile and is related to the FWHM of the beam by $w(z) = 2\sigma(z) = FWHM(z)/\sqrt{2\ln 2}$. The beam radius at the waist ($z = 0$) is $w_0 \approx \lambda/\pi NA$, with the numerical aperture $NA = n \sin\theta$. n is the refractive index of the material in which the beam propagates and θ is the opening angle of the beam with respect to the beam axis. A light wave propagating in a material has a reduced wavelength but the frequency, and thus the photon's energy $\hbar\omega = 2\pi\hbar c/\lambda$, remain unchanged. The Rayleigh length of a Gaussian beam is $z_0 = \pi w_0^2 n/\lambda$. At one Rayleigh length away from the focal point, the beam radius has increased to $w(z_0) = \sqrt{2}w_0$. Due to the square dependence of the two-photon absorption process on the beam irradiance, strong focusing and the shape of the focal point are of high importance for TPA-TCT experiments. Theoretically, in silicon with a laser wavelength of $\lambda = 1550$ nm and focusing optics with $NA = 0.5$, values of $w_0 = 1$ μm and $z_0 = 6.9$ μm can be achieved (see tab. 5.1). The measured values are usually slightly larger than the calculated ones (sec. 6.2.7). The beam irradiance is normalized such that an integral over time and spatial coordinates returns the pulse energy

$$E_p = \int_{-\infty}^{\infty} \int_0^{2\pi} \int_0^{\infty} I(r, z, t)\, r dr\, d\phi\, dt, \tag{5.19}$$

which can be readily measured experimentally as an average over many individual pulses, using a power-meter.

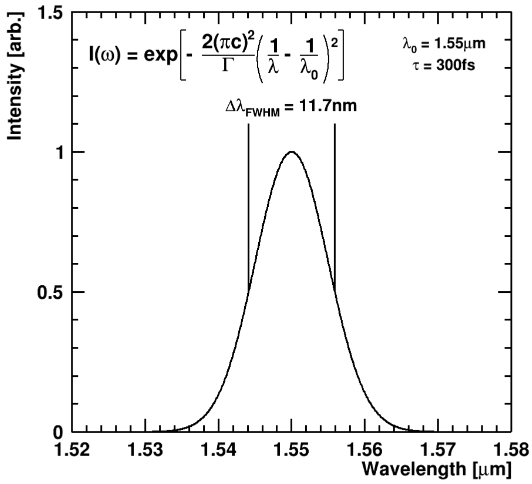

Figure 5.5. – Squared Fourier-transform of the time evolution of the electric field.

5.2. Light Interaction with Material

In this section some concepts from linear and non-linear optics, that are of relevance for TPA-TCT, are introduced.

In the regime of linear optics the superposition-principle can be applied to electromagnetic waves and the properties of matter do not depend on the light intensity [88]. This regime is relevant for low intensity light sources. Contrary, nonlinear optics is defined by the intensity dependence of the material response to light.

A displacement of bound charges in a material by an incident external electric field leads to a net dipole moment. The material is then said to be polarized. The macroscopic polarization can be expanded into a power series:

$$P_i = \epsilon_0 \left[\chi_{ij}^{(1)} E_j + \chi_{ijk}^{(2)} E_j E_k + \chi_{ijkl}^{(3)} E_j E_k E_l + ... \right], \tag{5.20}$$

with the electric field constant ϵ_0. $\vec{P}$ and $\vec{E}$ are related through the electric displacement field $\vec{D} = \epsilon_0 \vec{E} + \vec{P}$. E_j, E_k and E_l are the components of the electric field contributing to the ith component of the polarization $\vec{P}$. The coefficients $\chi^{(n)}$ are called electric susceptibility tensors and depend on the intrinsic material properties. In the regime of linear optics it is enough to consider the first order susceptibility of a material, so that

$$\vec{P}(\vec{r}, t) = \epsilon_0 \chi^{(1)} \vec{E}(r, t). \tag{5.21}$$

The forced oscillation of the bound electrons, in the field of the light wave, leads to the emission of secondary waves with the same frequency, or different frequencies in the case of non-linear optics. The emitted wave is delayed (is shifted in phase) with respect to the excitation wave. The speed of propagation (v_{ph}, phase velocity) of a light wave in a transparent medium is therefore different from its value in vacuum:

$$v_{ph}(\lambda) = \frac{c}{n(\lambda)}. \tag{5.22}$$

The refractive index n, as well as the phase velocity, are wavelength dependent, leading to the effect of dispersion. From Maxwell's macroscopic electromagnetic theory follows that $n = \sqrt{\epsilon\mu}$, with $\mu \approx 1$ in the optical spectral range, which can not explain the effect of dispersion. To explain the experimentally observed frequency dependence of the refractive index of a material, the electron theory of light dispersion (Lorentz) was developed [89]. From the definition of the dielectric constant, it follows that

$$n^2 = 1 + \chi = 1 + \frac{P}{\epsilon_0 E}, \tag{5.23}$$

with the (first order) dielectric susceptibility χ and the momentary value of the polarization P. The displaced electrons can be treated as harmonic oscillators with eigenfrequency ω_0, driven by the electric field of the light wave. The solution of the corresponding equation of motion (a solution for the polarization P) leads to a frequency dependent refractive index. Usually the refractive index increases with frequency (normal dispersion). Only around a resonance frequency the refractive index decreases with frequency (anomalous dispersion).
Interactions of light waves with matter are grouped into parametric and non-parametric interactions. Parametric interactions leave the quantum state of the medium unchanged and thus do not lead to any energy exchange between the light and the medium. All processes in which energy or momentum are exchanged with the medium are called non-parametric. As such, especially all absorption processes fall in this category. Parametric processes are described by the real part of the refractive index. Non-parametric interactions interact also with the imaginary part of n. The complex refractive index is expressed as

$$\underline{n} = n + i\kappa, \tag{5.24}$$

where n is the commonly used (real) refractive index and κ is the extinction coefficient. The extinction coefficient and absorption coefficient are related with $\alpha = 4\pi\kappa/\lambda$. A positive imaginary part of the refractive index implies that the wave is absorbed as it propagates through the medium. The imaginary part of the refractive index is only non-zero in a region around the resonant frequency ω_0 where anomalous dispersion takes place. The decrease in intensity of a light wave due to absorption in a medium is expressed by Lambert-Beer's law [89]

$$I(x) = I_0 \exp[-\alpha x], \tag{5.25}$$

in which I_0 is the initial intensity of the light wave and $I(x)$ is the intensity after traversing a length of x in the material. The absorption coefficient α does not depend on the intensity of the light, therefore this expression is only valid for linear absorption. The real (n) and imaginary (κ) part of the complex refractive index of silicon at room temperature are shown in fig. 5.6 (a) as a function of wavelength. The refractive index rises quickly in the UV range up to a peak of 6.87 at λ = 373 nm (= 3.3 eV) and decreases with higher wavelength. Fig. 5.6 (b) shows the extinction coefficient as a function of photon energy on a logarithmic scale. At a photon energy of about 1.1 eV (1100 nm wavelength), corresponding to the bandgap of silicon, the curve rises to a low value of about 10^{-2} due to phonon assisted absorption of light across the bandgap. After a steep increase at around 3 eV a first plateau is reached at 3.4 eV (365 nm), corresponding to the direct transition from the silicon valence to the conduction band [90, 91]. The dependence of the refractive index of silicon on temperature is shown in fig. 5.7. At a wavelength of 1550 nm the temperature variation of the refractive index ranges from 3.4681 at 250 K over 3.4757 at 293 K to 3.4865 at 350 K [92]. The refractive index of silicon depends on the amount of doping and changes also with irradiation [94]. This can have a strong effect on heavily doped devices like multiplication implants of LGADs. In these cases also the free carrier

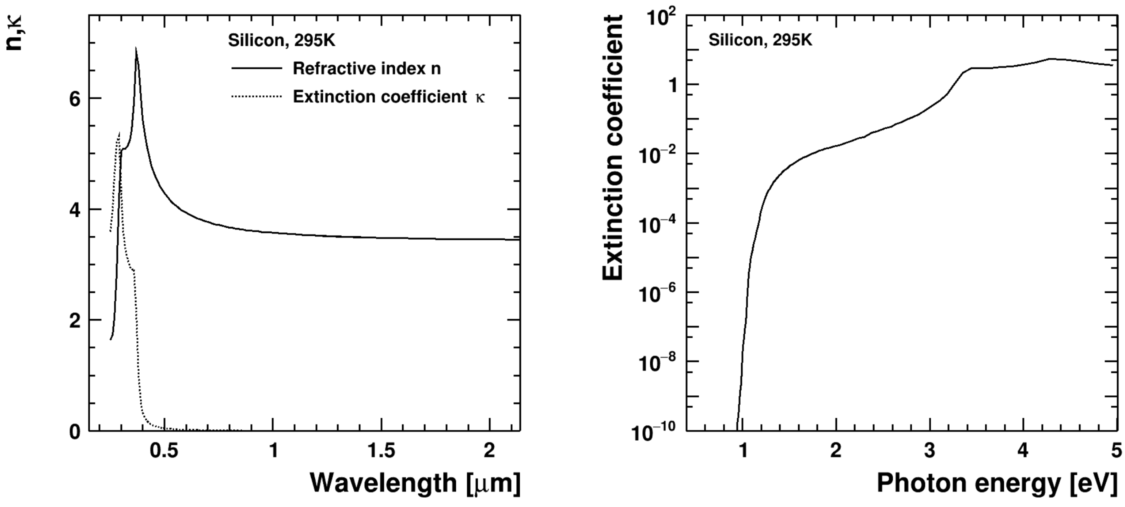

(a)

(b)

Figure 5.6. – (a) Refractive index and extinction coefficient of silicon at room temperature as a function of the wavelength. (b) Extinction coefficient as a function of photon energy. Data from [92, 93]

absorption might not be negligible.

5.2.1. Non-linear optical effects

Dealing with non-linear optical phenomena, the higher order terms in eq. 5.20 are important. For example, second-harmonic generation (SHG) is a process, originating from the second-order term in the above equation. Only non-centrosymmetric crystals can exhibit second-order non-linear effects. Two-photon absorption, on the other hand, is a non-parametric process which depends on the third-order susceptibility tensor. Since silicon has a centrosymmetric crystal structure, third order optical interactions are the lowest possible order of nonlinear response.

Second order non-linear interactions

Incident radiation with high enough intensity can lead to a non-linear polarization of the material. The resulting atomic dipole moments can oscillate at frequencies which are the sum (or difference) of the frequencies of the original waves. Under the right conditions, if the emitted radiation can interfere constructively, a beam of light can be obtained. As an example, in fig. 5.8 two processes are shown schematically: Sum frequency generation (SFG) is possible with two beams at different frequencies, which results in a third beam with frequency $\omega_3 = \omega_1 + \omega_2$ and the requirement of $k_3 = k_1 + k_2$. As a special case of sum-frequency generation, in SHG a beam with twice the frequency of the incident beam is created. To ensure efficient SFG (or SHG), phase matching has to be achieved. Chromatic dispersion leads to a phase mismatch between the incident radiation field and the second-harmonic. Different methods exist to overcome this limitation. A common example is the use of a beta barium borate (BBO) crystal for SHG and a single, focused laser beam. BBO is a birefringent material, which means that the crystal has one specific axis along which the refractive index is different (extraordinary

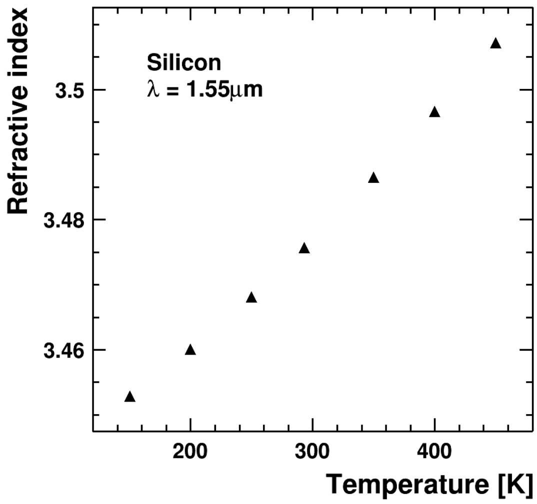

Figure 5.7. – Refractive index of silicon as a function of temperature for a wavelength of 1.55 μm. Data from [92]

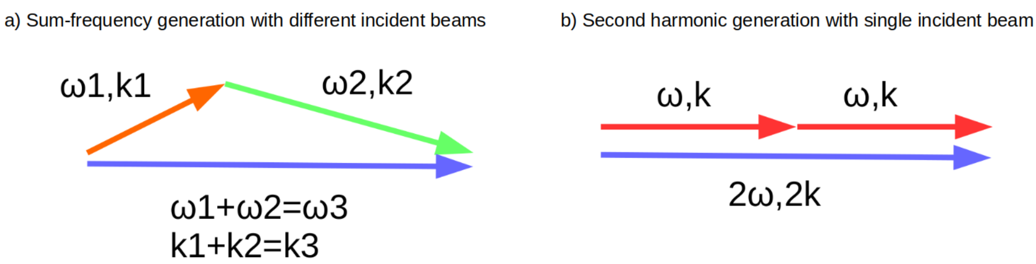

Figure 5.8. – a) Sum frequency generation as a consequence of incident fields with frequencies ω_1 and ω_2 in a $\chi^{(2)}$-material. b) Second-harmonic generation with a single incident beam.

refractive index n_e) than along the other directions (n_o, ordinary). BBO is a crystal with negative birefringence ($n_e < n_o$). The crystal is oriented in such a way that the incident beam is polarized perpendicular to the extraordinary crystal axis and thus always experiences the ordinary refractive index. By changing the angular orientation ('critical phase matching') of the crystal, the refractive index of the second-harmonic can be adjusted such that the phase mismatch vanishes. This procedure is schematically shown in fig. 5.9. The efficency of SHG generation is maximized when the focusing is such that the Rayleigh length of the focal point is comparable to the crystal length. Parametric second order processes are commonly used in laser physics for the up or down conversion of laser beams or e.g. in optical parametric oscillators. They can be of interest for an application in TPA-TCT, in which SHG can be used to create a reference signal for the correction of laser power fluctuations, since both TPA and SHG depend on the square of the beam intensity (see sec. 6.1.2).

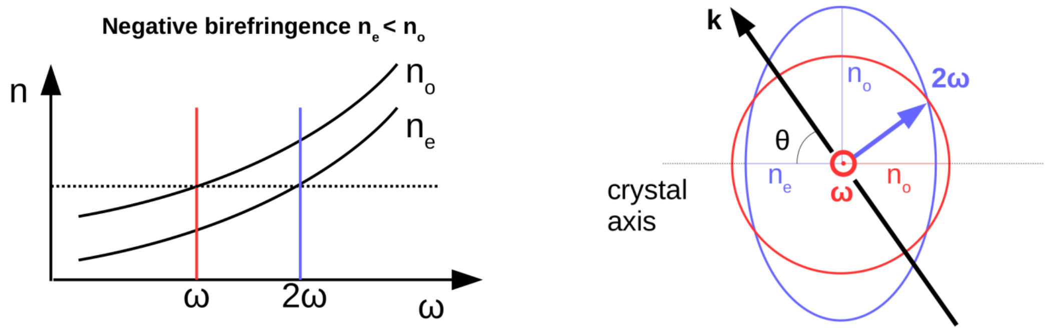

Figure 5.9. – Phase matching in a birefringent material. The first harmonic wave is polarized such that it experiences the ordinary refractive index (n_o, red circle in the figure on the right). Depending on the orientation of the crystal (angle θ), the refractive index of the second harmonic (blue ellipse) can be matched to that of the first harmonic.

Third order non-linear interactions

Third order non-linear interactions are possible in both centrosymmetric and non-centrosymmetric materials. For many centrosymmetric materials like liquids, gases, amorphous solids and also silicon, these interactions are the lowest possible order effects. As an example, fig. 5.10 schematically shows a four wave mixing process. In general, the four interacting waves need not have the same frequency. As for second order effects, phase matching is necessary to ensure that the wavenumbers add up to zero. Third-harmonic generation is a special case of sum frequency generation (analogous to SHG). In

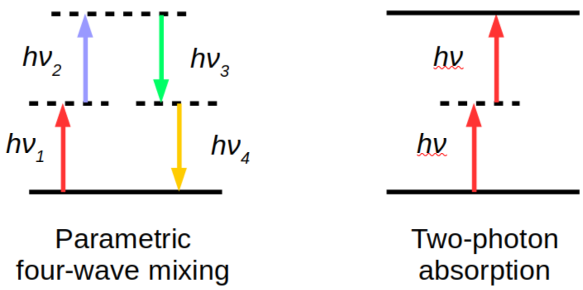

Figure 5.10. – Parametric four-wave mixing and two-photon absorption as a result of a $\chi^{(3)}$-interaction.

the degenerate case ($\omega_1 = \omega_2 = \omega_3 = \omega_4$) this class of interactions is the cause of the so called optical Kerr effect, which describes a change of the material's refractive index by the incident radiation itself. As a parametric process, the Kerr effect is described by the real part of the third order susceptibility tensor. Typical examples are self focusing of an intense laser beam or self-phase modulation (SPM). These effects can be described by an intensity dependent refractive index

$$n = n_0 + n_2 I. \tag{5.26}$$

Since the intensity of a laser beam $I(\vec{r},t)$ is a function of position and time, also the non-linear refractive index exhibits this dependency $n = n(\vec{r},t)$. The spatial dependence is a cause of Kerr lensing, while the temporal dependence can lead to SPM, which modifies the spectral characteristics of the pulse. Two-photon absorption (TPA) is a third order non-linear interaction which depends on the imaginary part of the third order susceptibility tensor. In analogy to single photon absorption, it can also be expressed by the imaginary part of the non-linear refractive index. In the case of negligible linear absorption, the relation between the non-linear refractive index, the non-linear absorption coefficient β and the real and imaginary part of the third order susceptibility is [95]

$$\chi_R^{(3)} = (4/3)n_0^2\epsilon_0 c n_2 \tag{5.27}$$

$$\chi_I^{(3)} = (n_0^2\epsilon_0 c\lambda/3\pi)\beta. \tag{5.28}$$

Corresponding expressions can be derived for the case of absorbing materials [95]. Two-photon absorption is a process, in which two photons are absorbed simultaneously from a laser beam, which results in the transition of an atom or molecule from the ground state to a real, excited state. For TPA in silicon this means that an electron is moved to the conduction band, consequently this results in the generation of one electron-hole pair per two absorbed photons. One finds that the cross section σ of this process increases linearly with the intensity $\sigma = \sigma^{(2)}I$, so that the transition rate becomes [87]

$$R = \frac{\sigma I}{\hbar\omega} = \frac{\sigma^{(2)}I^2}{\hbar\omega}. \tag{5.29}$$

The first theoretical description of TPA can be found in [96]. The first experimental confirmation of the process [97, 98] was only possible, after the invention of the laser. Two-photon absorption has a large variety of applications in many research fields and has already been used to simulate single event upsets in electronic devices (see e.g. [99, 100]).

5.2.2. Chromatic dispersion

Chromatic dispersion is caused by the frequency dependence of the refractive index. Each frequency component of a light pulse experiences a slightly different refractive index and thus propagates with a different phase velocity than the other components. As a first consequence, the group velocity, the velocity with which the pulse travels in a medium, is generally lower than the phase velocity. A second consequence is the broadening of the pulse. In a broadened (chirped) pulse the low frequency components are more shifted towards the leading part of the pulse and the high frequency components are moved towards the trailing part of the pulse (positive chirp). As a consequence of this, the pulse appears to be longer, without any change to the pulse spectrum. This means that the product of the pulse duration and the bandwidth is larger than that of a transform-limited pulse (eq. 5.16). After propagation through a medium the spectral phase of a pulse is modified by a propagation factor [88, 101]

$$E(\omega,x) = E_0(\omega)\exp[-\mathrm{i}k(\omega)x] \tag{5.30}$$

The wavenumber k describes the phase shift per unit length during propagation:

$$k(\omega) = n(\omega)\frac{\omega}{c} \tag{5.31}$$

To study the different effects of dispersion, it can be expanded into a power series

$$k(\omega) = k(\omega_0) + \frac{\partial k}{\partial \omega}(\omega - \omega_0) + \frac{1}{2}\frac{\partial^2 k}{\partial \omega^2}(\omega - \omega_0)^2 + \frac{1}{6}\frac{\partial^3 k}{\partial \omega^3}(\omega - \omega_0)^3 + \ ... \tag{5.32}$$

The first term of this expansion contains the phase velocity, with which phase fronts at a given optical frequency ω_0 propagate in a medium

$$v_{ph}(\omega_0) = \frac{\omega_0}{k(\omega_0)}. \tag{5.33}$$

This term causes a constant shift in phase for all spectral components after propagation through the medium and does therefore not have any observable effects, which are important in the context of this work. The second term contains the group velocity

$$v_g(\omega_0) = \left(\frac{dk}{d\omega}\right)^{-1}_{\omega_0}, \tag{5.34}$$

and results in a linear term in the spectral phase, causing the pulse envelope to propagate at a lower velocity (the group velocity) than the individual spectral components. The third term, with

$$\left(\frac{d^2k}{d\omega^2}\right)_{\omega 0} = \frac{d}{d\omega}\left(\frac{1}{v_g(\omega)}\right)_{\omega 0}, \tag{5.35}$$

is called group velocity dispersion. It leads to a quadratic time dependence of the phase and causes a shift of the instantaneous frequency to the red side of the spectrum for the leading part of the pulse and to the blue side of the spectrum for the trailing part of the pulse. This causes a longer duration of the pulse, the pulse is then said to be 'chirped'.

5.2.3. Pulse broadening as a result of chromatic dispersion

Due to their larger bandwidth, chromatic dispersion affects short pulses more than longer ones. For the design of the TPA-TCT laser system, it was important to avoid any pulse broadening when the pulses travel through the device under test. Silicon sensors are usually not thicker than 300 μm and thus the optimal pulse width was identified to be the shortest pulse at which no significant pulse broadening is expected after passing through 300 μm of silicon. Shorter pulses would lead to a pulse broadening and, since the TPA process depends on the pulse width, the amount of generated charge would depend on the position of the focal point in the sensor. The effect of dispersion on the pulse width can be calculated with [102]

$$\tau_{out} = \tau_{in}\sqrt{1 + \frac{16(\ln 2)^2 GDD^2}{\tau_{in}^4}}. \tag{5.36}$$

GDD is the group delay dispersion, which is calculated for a material with thickness L according to $GDD = GVD \cdot L$. The group velocity dispersion GVD (eq. 5.35 expressed in terms of λ and n) can be calculated with

$$GVD = \frac{\lambda^3}{2\pi c^2}\left(\frac{\partial^2 n}{\partial \lambda^2}\right), \tag{5.37}$$

where the value for $\partial^2 n/\partial\lambda^2$ can be obtained using the Sellmeier equation

$$n(\lambda) = \sqrt{1 + \sum_{i=1}^{3} \frac{A_i \lambda^2}{\lambda^2 - B_i^2}}. \tag{5.38}$$

The parameters A_i and B_i for silicon at room temperature, taken from [103], result in a value of $GVD = 1119.4$ fs^2/mm for a wavelength of 1.55 μm. The pulse width τ_{out} after traveling through 300 μm of silicon is shown as a function of the initial pulse width (solid line) in fig. 5.11. The values are calculated according to eqs. 5.36 - 5.38. Pulses that are shorter than $\approx$ 60 fs undergo a significant amount of dispersion, while traveling through the silicon sample.

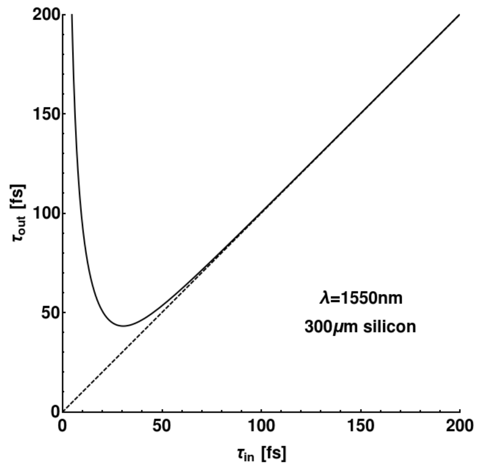

Figure 5.11. – Pulse length τ_{out} (1550 nm) after passing through 300 μm of silicon as a function of the initial pulse length τ_{in}. [104]

5.2.4. Impact of refraction on a focused laser beam

The refraction of light on the interface of two materials with different refractive indices is described by Snell's law

$$n_1 \sin\theta_1 = n_2 \sin\theta_2, \tag{5.39}$$

where $n_{1/2}$ are the refractive indices and $\theta_{1/2}$ are the angles of a ray of light to the normal of the material's interface. The change of direction of propagation of light changes the shape of a Gaussian laser beam and needs to be considered when moving the interface of the materials with respect to the laser beam's focal point. Of interest here is the case in which a Gaussian beam crosses the boundary between air and a silicon sensor. The opening angle of the beam θ, always measured with respect to the beam axis, becomes smaller. Therefore, while the beam radius remains unchanged, the Rayleigh length of the beam becomes larger. This is depicted in fig. 5.12: A focused beam, depicted by two converging rays, enters the silicon (refractive index n) under the angle θ. With $n = 1$ the focal point would be at position z from the sensor surface. Since $n > 1$ the opening angle changes to θ' and the focal point lies at position z'. The relation of the beam opening angle and the Rayleigh length in silicon is

$$\tan\theta' = w_0/z_0 \tag{5.40}$$

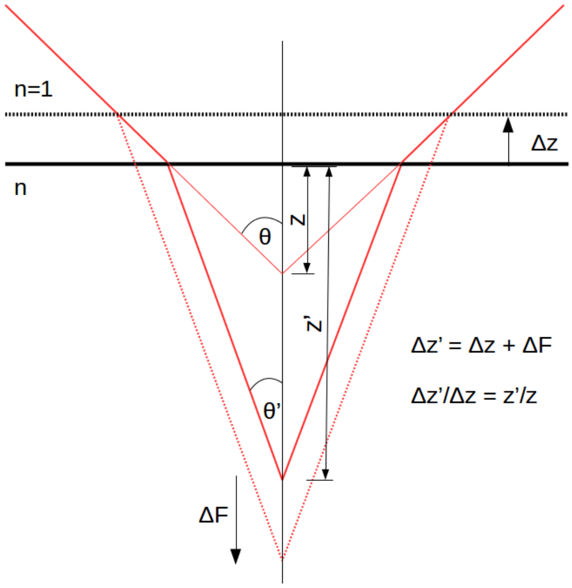

Figure 5.12. – Elongation of a laser beam, when entering from air into a material with refractive index n. A movement of the sensor surface by Δz results in a shift of the focal point in the opposite direction leading to a total displacement of $\Delta z'$. [104]

with

$$z_0 = \pi n w_0^2/\lambda. \tag{5.41}$$

From these equations and using Snell's law one obtains an expression for the new position of the focal point

$$z' = z\sqrt{\frac{z_0\,\pi n^3}{z_0\pi n - \lambda n^2 + \lambda}}. \tag{5.42}$$

Equivalently this expression can be expressed in terms of the numerical aperture NA,

$$z' = z\sqrt{\frac{n^2 - NA^2}{1 - NA^2}}. \tag{5.43}$$

Again, λ is the vacuum wavelength. With TPA-TCT also spatial scans along the beam axis are carried out. Usualy this is done by moving the silicon sensor with respect to the focal point of the beam, using a translation stage. In this context it is important to keep in mind that a translation of the silicon sensor by an amount Δz results in a change of the position of the focal point with respect to the sensor surface by ΔF in the opposite direction. The total change is thus $\Delta z' = \Delta z + \Delta F$. The factor derived above, relating length measurements z and z' is equally valid: $\Delta z'/\Delta z = z'/z$. The ratio z'/z as a function of the Rayleigh length in silicon is shown in fig. 5.13. For low focusing (long Rayleigh length) the elongation factor converges to the material's refractive index. For strong focusing, with a Rayleigh length in the range of 10-20µm, the deviation becomes significant and has to be considered. For example, for silicon at room temperature (n = 3.4757 for T = 293 K [92]), λ = 1.55 μm and a microscope objective with NA = 0.5 the elongation factor is z'/z = 3.97 (NA = 0.7: z'/z = 4.77). The Rayleigh length is used here as a parameter which can be easily obtained from z-scan measurements. The horizontal axis of fig. 5.13 could as well be given in terms

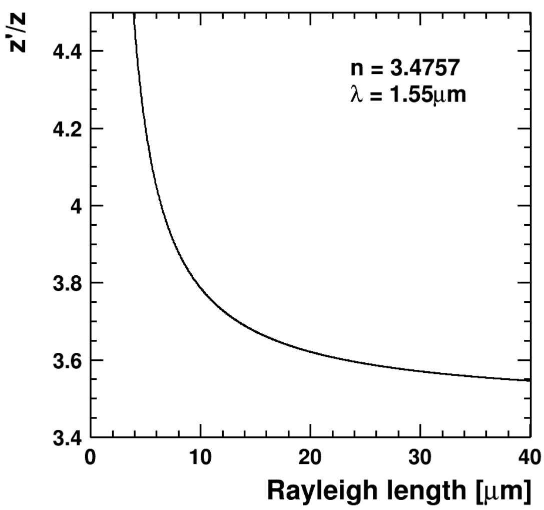

Figure 5.13. – Elongation factor z'/z as a function of the Rayleigh length of a focused laser beam in silicon.

of the numerical aperture NA for the given beam parameters using equations 5.9 and 5.41.
In addition to the effect of refraction, discussed above, spherical aberrations, e.g. discussed in [105, 106], can be caused by refraction on the air-si interface. Spherical aberrations result in an elongated and distorted focal point, depending on the depth of the focal point inside the DUT. The effect was not usually considered to be relevant, but measurements with a high numerical aperture objective on thick detectors suggest that it might be important (sec. 6.3.6).
In addition, chromatic aberrations are certainly present, but are neglected, due to the comparably small bandwidth of the laser.

5.2.5. Interferometric autocorrelation

A standard technique to analyze the temporal shape of short laser pulses is the Interferometric Autocorrelation (IAC or FRAC, fringe resolved autocorrelation) [107]. The basic principle of a FRAC measurement is, to split a laser pulse and introduce a variable delay to one of the two replicas. The separate pulses are combined again to allow them to interfere. The combined pulse is then directed onto a crystal, in which SHG is possible (schematically shown in fig. 5.14). The resulting second-harmonic signal is picked up by a detector. The recorded signal amplitude S depends on the optical delay Δt, that was introduced to one of the two pulse replicas

$$S(\Delta t) = \int_{-\infty}^{+\infty} |(E(t) + E(t - \Delta t))^2|^2 \, dt. \tag{5.44}$$

Scanning through a range of optical delay and recording the second-harmonic signal yields an interference pattern, whose shape allows to deduce properties of the original pulse, like the pulse duration and chirp. For optical delays that are much larger than the pulse duration $\Delta t \gg \tau$, the pulses enter the non-linear crystal without interfering, so that the recorded signal is the sum of the individual squared intensities. This signal level is referred to as the baseline of the autocorrelation (AC) trace. From eq. 5.44 one can see that the maximum signal amplitude over baseline is $S(\Delta t = 0)/S(\Delta t \gg \tau) = 8$. For a small delay, equivalent to a phase shift of π of one of the pulses, perfect destructive interference occurs and the signal amplitude drops to zero. For a full pulse analysis the spectral intensity of the first and second-harmonic has to be recorded as well, to be able to reconstruct the spectral phase, which is for example possible with the FROG [108] and SPIDER [109] techniques. Interferometric autocorrelation allows to obtain limited phase information. The pulse duration of a pulse near the Fourier transform limit can be estimated from the measured width of the FRAC trace by $FWHM_{pulse} = FWHM_{FRAC}/\sqrt{2}$. The factor of $1/\sqrt{2}$ is specific for a Gaussian pulse, for a sech^2 pulse this factor is $1/1.543$. In case of a chirped pulse, the pulse duration, estimated from the FWHM of the FRAC trace, will be underestimated, because the interference fringes of a chirped pulse disappear earlier than those of a bandwidth limited pulse of the same duration. The reason for this is that the instantaneous frequency of a chirped pulse is time dependent. Due to the wavelength mismatch between the leading and trailing edges of the pulse, a chirped pulse will show a narrower interference pattern. In this case, if a fit to the full trace is not a solution, the fringes can be removed by binning or calculation of the running average of the FRAC trace. The obtained curve resembles a conventional intensity autocorrelation scan (fringe averaged autocorrelation) with a corresponding signal level of 3:1 over baseline and no interference pattern. The pulse duration can then be calculated from the FWHM of this intensity AC trace, in the same way as described above for an interferometric measurement. As mentioned in sec. 5.2.2 a non-linear time dependence in the phase means that the

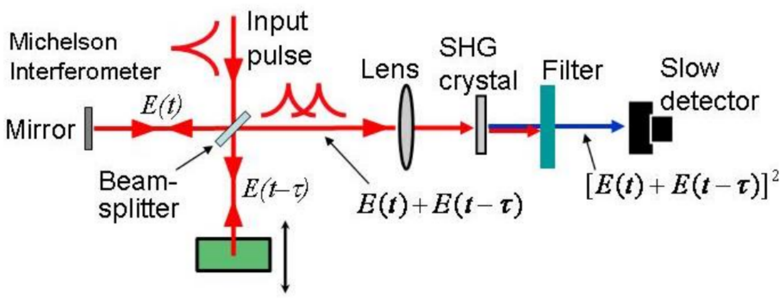

Figure 5.14. – Experimental layout for the fringe-resolved autocorrelation (FRAC). [110]

pulse is chirped. Therefore eq. 5.11 was modified, by introducing a quadratic time dependence with chirp parameter C:

$$E(t) = \exp\left[-i\omega_0 t - \Gamma t^2 - iCt^2\right]. \tag{5.45}$$

Eq. 5.44 can then be used to calculate the shape of an FRAC trace for different pulse duration and chirp parameters. Fig. 5.15 shows two calculated FRAC traces. Both pulses, used in the calculation, have a width of τ = 300fs, but the chirp parameter was varied. The FRAC trace, shown on the left (a), is a result of a transform limited pulse (C = 0 fs^{-2}), while on the right (b) the pulse is chirped ($C = 5\times10^{-5}$ fs^{-2}). From the obtained FRAC trace (black) the fringe averaged intensity autocorrelation trace (red) was calculated as the running average of the FRAC trace. The FWHM of the intensity autocorrelation is stated in the figure. The pulse duration is then calculated as $\tau = FWHM/\sqrt{2}$. For the reason described above, the FRAC trace of the chirped pulse shows a narrower fringe pattern, although the chirped and transform limited pulse have the same duration. Furthermore, it is evident that the intensity autocorrelation traces in both figures look exactly the same. A measurement of the intensity autocorrelation trace alone would not have revealed the non-linear temporal phase of one of the two pulses. The pulse duration can be obtained from the intensity autocorrelation trace

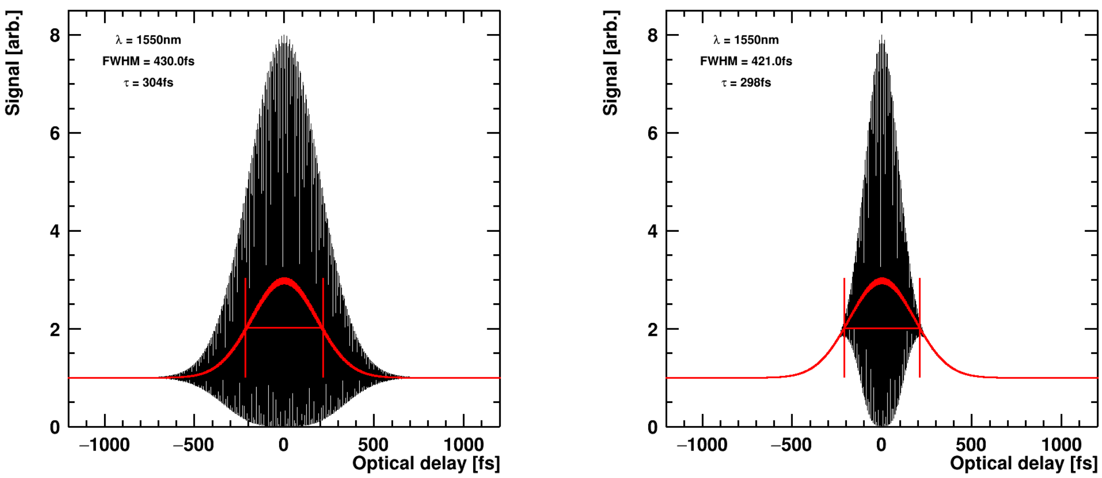

(a) Transform limited

(b) Chirped

Figure 5.15. – Calculated interferometric autocorrelation traces of a Fourier limited pulse (a) and a chirped pulse (b). The IAC trace was calculated from a pulse width of $\tau = 300$ fs

in both cases, which gives the expected result of $\tau \approx 300$ fs. The small deviation is the result of limited computational accuracy. Note that for the Fourier limited pulse (a) the FWHM of the FRAC trace is equal to the FWHM of the intensity AC trace. Usually an interferometric autocorrelation measurement consists of an average of many individual pulses per step in delay. This leads to an ambiguity in the interpretation of the obtained trace, since a given measurement can be understood as being the autocorrelation trace of equally chirped pulses of the same frequency or of bandwidth-limited pulses with a pulse-to-pulse variation in frequency. Therefore it is important to verify that the pulses are constant in energy, frequency and duration [111]. Also, since an autocorrelation trace is always symmetric, the measurement is insensitive to asymmetric pulse shapes. In the regime of ultrashort pulses special care has to be taken to build a symmetric, well aligned autocorrelator for FRAC measurements. At zero delay the FRAC trace should exhibit a maximum with a peak-to-background ratio of 8:1. If e.g. an asymmetric beamsplitter is used the measurement can result in a phase shifted trace with a lower peak-to-background ratio. It was shown that the envelope can still be used to obtain the pulse width, as long as the pulses are longer than several optical cycles. The asymmetry of a dielectric or metallic beamsplitter can be compensated by using a setup described in [112] or by using a cube beamsplitter. The latter, although facilitating the experimental setup, leads to an increase in material that the pulses pass through and therefore might lead to additional dispersion. In the case of TPA-TCT it is possible to perform interferometric autocorrelation measurements by placing an interferometer into the optical path. In this case both the SHG crystal and detector, described above, are replaced by a silicon detector. In silicon a signal is generated by two-photon absorption, which is a second order process and therefore can be used to obtain an autocorrelation trace.

5.3. Charge Carrier Generation in Silicon by Two-Photon Absorption

Two-photon absorption is a nonlinear optical effect due to the third order susceptibility term in the expansion of the polarization of a material. In this section the charge carrier generation due to TPA and the resulting profile of the charge carrier density in a silicon sensor are discussed. Light traveling through silicon can be absorbed by valence electrons leading to free carriers in the conduction band. Of relevance in the present work are the absorption of one (SPA) and two photons (TPA). The respective absorption coefficients are wavelength dependent and reflect the band structure of silicon. As can be seen in fig. 5.16 (see also fig. 5.6) the linear absorption coefficient of silicon tends towards zero as the photon energy becomes smaller than the bandgap ($E_\gamma(1.1\ \mu\text{m}) = hc/\lambda \approx 1.12$ eV) but, for high enough intensities, two-photon absorption is possible. As photons are absorbed by silicon, the

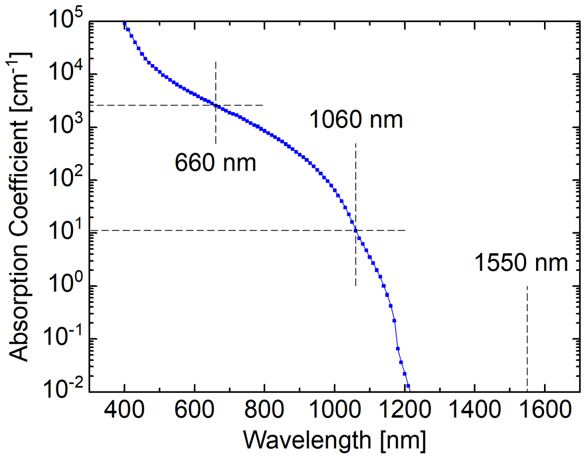

Figure 5.16. – Room temperature absorption spectrum of silicon in the visible and near-infrared region. Data from [113].

irradiance of an incident laser pulse changes as a function of the penetration depth. The change of pulse irradiance I and phase Φ along the propagation direction z are described by

$$\frac{dI(r,z,t)}{dz} = -\alpha I(r,z,t) - \beta_2 I^2(r,z,t) - \sigma_{ex} N I(r,z,t) \tag{5.46}$$

$$\frac{d\Phi(r,z,t)}{dz} = \beta_1 I(r,z,t) - \gamma_1 N(r,z,t), \tag{5.47}$$

with r being the distance to the beam axis [100]. α and β_2 are the linear (SPA) and non-linear (TPA) absorption coefficients. β_1 and β_2 are proportional to the real and imaginary part of the absorbing material's third order susceptibility $\chi^{(3)}$. σ_{ex} and N are the cross section for free-carrier-absorption and the number of free charge carriers. The second term in eq. 5.47 describes the refraction due to free carriers.

For light with sufficiently long wavelength the first term on the right hand side in eq. 5.46, describing SPA, is zero. Also the absorption by free carriers can be neglected for sufficiently short pulses [114] and silicon samples with high resistivity. The remaining second term in eq. 5.46 describes the depletion of the laser beam due to the two-photon absorption process we are interested in. The solution to this differential equation, only considering the z- dependence, is

$$I(z) = \frac{I_0}{1 + \beta_2 I_0 z}, \tag{5.48}$$

which describes the depletion of the beam due to two-photon absorption after traversing the distance z in the material with respect to the incidence irradiance I_0. For a correct treatment, the depletion of the beam had to be solved taking into account the radial dependence of the beam irradiance. It turns out that, under the given experimental conditions, the number of absorbed photons is small enough, so that beam depletion due to two-photon absorption along the beam axis can be neglected to first approximation. The spatial dependence of the beam irradiance and thus the density of created carriers is mostly dominated by the beam shape at the focal point of the focusing optics. The one- and two-photon absorption by valence electrons, described by the first two terms in eq. 5.46, leads to the creation of free charge carriers in the conduction band according to [100]

$$\frac{dn(r,z,t)}{dt} = \frac{\alpha I(r,z,t)}{\hbar\omega} + \frac{\beta_2 I^2(r,z,t)}{2\hbar\omega}. \tag{5.49}$$

The factor of 2 in the second term is a result from the fact that two photons need to be absorbed for TPA. The absorption of light by free carriers does not lead to additional carriers and is therefore an undesired effect. An integration over time of the above terms, together with eq. 5.18, yields the charge carrier density resulting from one and two-photon absorption respectively

$$n_{spa}(r,z) = \frac{2E_p\,\alpha}{\hbar\omega\,\pi w^2(z)} \exp\left[-\frac{2r^2}{w^2(z)}\right] \tag{5.50}$$

$$n_{tpa}(r,z) = \frac{E_p^2\,\beta_2\,4\ln 2}{\tau\,\hbar\omega\,\pi^{\frac{5}{2}} w^4(z)\,\sqrt{\ln 4}} \exp\left[-\frac{4r^2}{w^2(z)}\right]. \tag{5.51}$$

The calculated charge carrier density from two-photon absorption n_{tpa} is shown in fig. 5.17 as a function of the radial distance to the beam axis r and the longitudinal distance from the focal point z for two different values of the numerical aperture. The parameters, which were used for the calculation, are shown in the figure. Different values of the two-photon absorption coefficient β_2 can be found in literature [115]. Here a value of $\beta_2 = 1.5$ cm/GW [116] was used. It is evident from the figure that charge carriers are only created in close vicinity to the focal point. A higher numerical aperture results in a more confined charge carrier distribution, due to the smaller Rayleigh length and beam waist, which is beneficial for the measurement resolution. The higher charge carrier density at the focal point, on the other hand, leads to an earlier onset of plasma generation. Note that the beam radius w is the two-sigma radius of the beam irradiance, therefore 95% of the pulse energy are transmitted through a circle with radius w, but 99.5% of the charge are created in the same area since $w = \sqrt{8}\sigma_{ntpa}$. As already suggested from the calculation of w_0 and z_0, the resolution of the TPA-TCT method is best perpendicular to the beam axis. It is possible to use TPA-TCT in a configuration in which the light is injected from the edge of the detector, similar to edge-TCT [76], to study the device under test as a function of the depth inside the sensor. In this case it has to be taken into account, that the strong focusing limits the penetration depth of the light. For too large depths, the beam can be clipped on the top or bottom edge of the detector. For example, as follows from eq. 5.5 with the given beam parameters, the beam width is as large as $2w = 87$ μm for a penetration depth of $z = 300\mu$m. Since both red and infrared light are equally reflected from metallic surfaces, the sensor needs to be free of metallization, where the light is entering the device. A feature sometimes observed in conventional

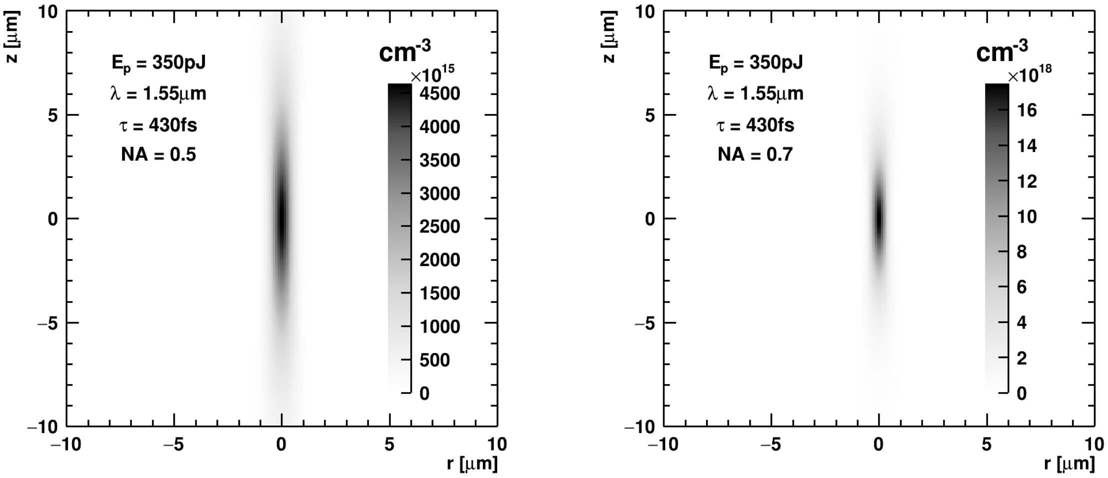

(a) $NA = 0.5$ (b) $NA = 0.7$

Figure 5.17. – Density of charge carriers created by TPA in silicon, calculated with eq. 5.51, for numerical apertures of $NA = 0.5$ (a) and $NA = 0.7$ (b). The vertical axis is parallel to the beam propagation direction with ($z = 0$) at the position of the focal point. A value of $\beta_2 = 1.5$ cm/GW [116] was used for the calculation.

TCT measurements are artifacts resulting from scattering or reflection of the beam back into the active area of the detector, e.g. on metallic surfaces on the backplane. While this is still possible in TPA-TCT it is less problematic because only focused light will lead to additional charge carriers. If the focal point is positioned inside the active area and the beam is reflected back into the device on a metallic backplane, this stray light will not be absorbed and not lead to a transient signal. If, on the other hand, the focal point lies behind the detector, a metallic surface or the silicon-air interface will reflect the focal point back into the active volume, which will lead to a signal. In this way, mirror images of the active volume can be observed in some measurements.
The total number of created charge carriers is obtained from integrating the charge carrier density over the full volume:

$$N_{tpa} = \int_V n_{tpa}(r, z)\, dV = \frac{E_p^2 n \beta_2 \sqrt{\ln 4}}{4\hbar c \tau \sqrt{\pi}}. \tag{5.52}$$

Inserting values of $E_p = 350$ pJ, $\tau = 430$ fs and $\beta_2 = 1.5$ cm/GW [116] yields a value of $N_{tpa} = 78 \cdot 10^6$. In a volume of approximately $V = \frac{4}{3}\pi w_0^2 z_0 \approx 30\ \mu\text{m}^3$, this corresponds to an average charge carrier density of about $n_{eh} = 2.6 \cdot 10^{18}$ cm^{-3}.
For irradiated detectors, the contribution to the signal from single photon absorption due to defects in the bandgap, can not be neglected anymore. The ratio of the TPA ($\propto I^2$) to the SPA ($\propto I$) signal can be improved by increasing the beam irradiance. Experimentally this can be achieved by increasing the pulse energy or reducing the pulse duration. The pulse energy is eventually limited by the creation of an electron hole plasma [83, 84]. To achieve the best possible resolution ultra-short laser pulses should be used. The lower limit of the pulse duration is given by dispersion, as explained in sec. 5.2.3.

Beam and ground state depletion

To achieve stable conditions for TPA measurements two additional conditions have to be met: Depletion of the beam should be negligible and depletion of the ground state has to be avoided [117].
The number of available photons can be calculated from the pulse energy as

$$N_\gamma = \frac{E_p}{\hbar\omega}, \tag{5.53}$$

which yields a value of $N_\gamma = 2.7 \cdot 10^9$, for a pulse energy of $E_p = 350$ pJ. The ratio of absorbed photons (TPA) to available photons is

$$\frac{2 \cdot N_{tpa}}{N_\gamma} = \frac{E_p n \beta_2 \omega \sqrt{\ln 4}}{2c\tau\sqrt{\pi}}. \tag{5.54}$$

For $E_p = 350$ pJ at a wavelength of 1.55 μm, $\beta_2 = 1.5$ cm/GW and a pulse duration of 430 fs, this ratio is about 5.7‰. This value is small enough to not have an immediate impact on the measurements but might be taken into account for a thorough analysis.
As can be seen from fig. 5.17, the peak charge carrier density due to two-photon absorption, for the strongest focusing, is in the order of $n_{tpa} = 1.8 \cdot 10^{19}$ cm^{-3}, which can be compared to the density of silicon atoms of $n_{si} = 5 \cdot 10^{22}$ cm^{-3}, to see that ground state depletion does not play any role for TPA-TCT.

Free carrier absorption

Electrons that have been exited by TPA can absorb an additional photon. The further excited electron will still contribute to the TCT signal but the additional photon is lost from the beam. This effect is called Free Carrier Absorption (FCA) (or more general Excited State Absorption, ESA) and is discussed in more detail, for several experimental configurations, in [117]. FCA is important for direct measurements of TPA by measuring the light intensity transmitted through a sample as a function of the focal point position (z-scan technique). It is not expected that FCA is directly observable in TCT measurements. The FCA process is efficient if the relaxation time from the exited state to the ground state is comparable to or larger than the pulse duration, or if the photon flux is very large. Different values for the free carrier absorption cross section of silicon can be found in literature. E.g. a measurement of $\sigma_{ex} = 1.69 \cdot 10^{-17}$ cm^2 in high purity silicon wafers at a probe wavelength of 1510 nm is reported in [118]. The FCA cross section in silicon nanocrystals embedded in a thin SiO2 film at 1540 nm, measured with a collinear pump–probe method was reported to be $\sigma_{ex} = 3.6 \cdot 10^{-17}$ cm^2 [119]. The process of free carrier absorption is described by the third term in eq. 5.46. Since TPA is the dominant absorption mechanism, the number of free carriers N depends on the square of the irradiance. Therefore the term $\sigma_{ex} N I$ effectively depends on the third power of the irradiance, which makes this effect a fifth order contribution to the optical response of the material. Even if the number of excited states is always small compared to the number of levels in the ground state and the number of absorbed photons is small against the number of available photons, FCA can still be of similar magnitude, or larger, than the TPA process. The relative contribution from FCA to TPA can be approximated by [117]

$$\frac{(\mathrm{d}\phi/\phi)_{FCA}}{(\mathrm{d}\phi/\phi)_{TPA}} \approx \frac{1}{2}\sigma_{ex}\phi\tau. \tag{5.55}$$

Inserting values of $\sigma_{ex} = 1.69 \cdot 10^{-17}$ cm^2, $\phi = I_0/\hbar\omega = 1.9 \cdot 10^{29}$ 1/cm^{2}s and $\tau = 430$ fs yields a value of FCA/TPA = 0.7. The peak irradiance I_0 was calculated from eq. 5.18 with $r = z = t = 0$, $E_p = 350$ pJ, $\tau = 430$ fs and $w_0 = 1.4$ μm. This shows that the magnitude of FCA can be comparable to the magnitude of TPA. The light absorption depends on the amount of free carriers, due to the doping concentration [120, 121], but the amount of free carriers resulting from the doping of silicon is not considered here. Therefore, this calculation should be understood as an estimate of FCA by TPA induced free carriers.

Other optical effects

Some other optical effects are described qualitatively in the following. These effects were not studied in depth and are usually considered to be negligible, but at very high powers or strong focusing they might become important. The description is primarily based on [121], in which non-linear light propagation and absorption phenomena are investigated in silicon at a laser wavelength of 1300 nm and a laser power of 30 nJ, using an objective with $NA = 0.5$. The laser power used in the quoted paper is much higher, than the available power of the laser used in this work.

- **Kerr lensing and plasma defocusing**
  As mentioned in sec. 5.2.1, Kerr lensing, like TPA, is an effect of the non-linear refractive index. It was reported that Kerr lensing, or a combination of Kerr lensing with plasma defocusing, can have an impact on the position and shape of the charge generation volume. It was observed that after long distances of propagation ($\approx$ 1 mm), non- linear propagation effects can accumulate, such that the position of the charge generation volume appears shifted with respect to the expected position of the focal point. In addition the generation volume appeared to be stretched in the direction of the beam axis, leading to a lower charge carrier density and a longer Rayleigh length. The first effect, if it would be present in TPA-TCT, would affect the accuracy, with which the position of the focal point, and therefore the thickness of the DUT or the width of the depletion zone, could be measured. This effect would have to be taken into account in addition to the common effect of refraction on the sensor surface. The second effect, the distortion of the focal point, affects the volume in which carriers are generated and thus affects the resolution of the scanning technique.

- **Avalanche ionization**
  Avalanche ionization (see also [122]) is a process, in which a free charge is accelerated in the light electric field and creates an additional carrier through impact ionization. In contrast to FCA, this process would be directly observable in TPA-TCT, because an additional charge carrier is excited to the conduction band, without TPA. Therefore a deviation from a purely quadratic dependence of the signal charge on the pulse energy would be expected.

- **Free carrier heating**
  Heating of free carriers describes the presence of additional kinetic energy of conduction band electrons, due to light absorption. FCA can lead to this process, but also the fact that the energy of two photons is higher than the silicon bandgap contributes. Free carrier heating could change the optical properties of the material and affect light propagation and absorption. Usually this process is relevant for much higher pulse energies, in a regime in which ablation becomes important [123, 124].

6. Development of a Compact TPA-TCT Setup

6.1. Description of the Setup

The TPA-TCT setup which was constructed at the Solid-State-Detectors laboratories at CERN is the first tabletop TCT-setup that uses two-photon absorption to characterize silicon detectors. As such, the experimental setup was continuously revised and improved during the development phase and, at the time of writing, is still undergoing changes. A first description of the setup together with a presentation of first measurement results was published in [104]. The laser source was developed specifically for this setup. After an initial development time of 1.5 years by the supplier, the laser was delivered to CERN. Initial testing revealed several points that needed improvement, especially the stability of the laser source. The laser was returned to the supplier to address the necessary changes. The final version of the laser was delivered to CERN in January 2021.
In the following the TPA-TCT setup will be discussed. A schematic drawing with the most important components is shown in fig. 6.1. The main difference to a conventional TCT setup is the use of a free-space infrared laser with a pulse duration of about 430 fs. The free-space output of the source made it necessary to develop an optical setup, routing the beam with mirrors to the DUT instead of using optical fibers. The short pulses require care in the choice of optical components to reduce the amount of dispersion. Fluctuations in the laser power and temporal shape made it necessary to generate a reference signal using two-photon absorption to ensure good correlation with the signal of the DUT. Because of the anticipated increase in spatial resolution, the positioning system of the DUT was required to match the precision of the beam focusing. For high-precision alignment a six-axis hexapod is used, which not only allows to position the DUT with nanometer precision in the three spatial coordinates but also allows for the correction of a tilt of the DUT. For precise sample positioning an IR-camera system was implemented, which allows to create an image of the DUT, to see structures on the DUT as well as the position of the laser beam spot. Fast read-out electronics are used to record the TCT-signal, in analogy to existing TCT setups. Finally, to test irradiated detectors at sub-zero temperatures a cooling system was set up, using a thermo-electric module and a liquid chiller.

6.1.1. Fyla laser

The laser source LFC1500X was custom developed by the company Fyla[1] for the application in a TPA-TCT setup. The laser has a central wavelength of 1.55 μm and a pulse duration of approximately 430 fs. The laser comes in two different modules: the laser source and the pulse management module (LPM module). The laser module contains the oscillator and amplifier, based on chirped pulse amplification (CPA). The output of the laser module is in free space with an average output power of about 200 mW and a pulse rate of 8.1 MHz. The output of the laser module is directed into the LPM, which is shown schematically in fig. 6.2. The LPM features an acousto-optic modulator (AOM) for selecting the pulse frequency from the fundamental 8.1 MHz down to single shot. Usually TCT measurements

[1] Fyla, Valencia, Spain, https://www.fyla.com

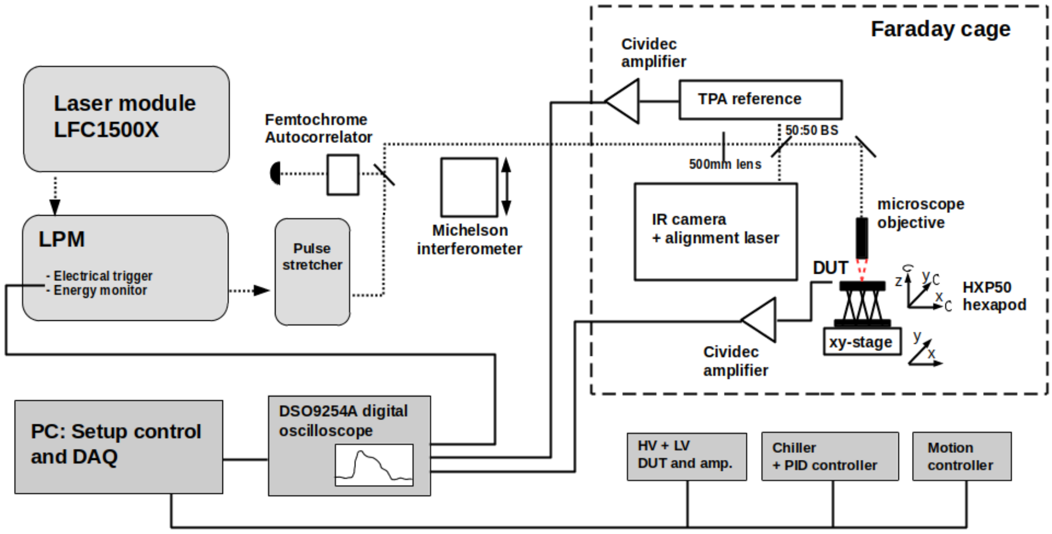

Figure 6.1. – TPA-TCT free-space laser setup.

are performed at a pulse rate of 200 Hz (corresponding to a time between pulses of 5 ms) to ensure full recovery of the DUT. The selected pulses are passing the first of two 99:1 beamsplitter. The 1% fraction of the pulse is directed onto an InGaAs detector, whose output is used as a trigger signal for the DAQ. The remainder of the pulse passes through a motorized, variable neutral density filter (NDF). The NDF angle defines the pulse energy. In the range from 0° to 70° the NDF is fully transmissive. For larger angles the pulse energy is reduced. A second beamsplitter directs a small part of the beam onto another InGaAs reference sensor, which is used to monitor the average pulse energy. It is referred to as 'energy monitor' or 'SPA reference'. A manual NDF is mounted in front of the energy monitor to adjust the dynamic range of the sensor. Special care has to be taken to leave this NDF unchanged, when a calibration of the energy monitor/SPA reference against the pulse energy is carried out. The remaining beam is passing a remotely controlled optical shutter when exiting the module. In addition to the laser source and the LPM, the laser comes with a pulse stretcher module. This pulse stretcher can be placed after the LPM. It adds dispersion to the beam by moving glass wedges into the beam to allow for a variation of the pulse duration from the optimum of 430 fs up to about 1.6 ps. This feature can be interesting to study two-photon absorption as a function of the laser pulse length but the optimum TPA/SPA ratio in case of an irradiated detector is obtained with the shortest possible pulse. Therefore, the stretcher module was not installed for the measurements presented in this work. Fig. 6.3 shows a measurement of the stability of the output power of the laser, carried out with a thermopile detector by Fyla. Due to the nature of this measurement, the resulting signal is an average of many pulses, so pulse to pulse fluctuations will be averaged, but the laser shows no drift in the power over several hours. Fig. 6.4 shows the spectrum of the laser source and fig. 6.5 shows an autocorrelation trace, both measured by Fyla. The spectrum is centered at 1550 nm and has a width of 33.7 nm. The autocorrelation measurement results in a measured pulse duration of 434 fs. The width of the AC trace was converted to the pulse duration according to pulsewidth = $FWHM_{AC} \cdot 0.648 \cdot 31$. The factor of 31 is specific for the used autocorrelator. The factor of 0.648 is for the conversion of the width of the

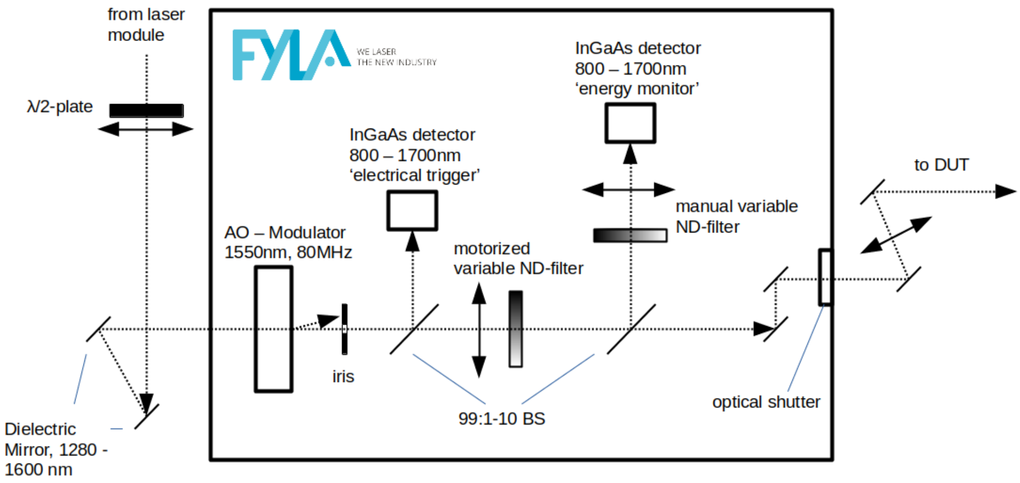

Figure 6.2. – Pulse management module (LPM) of FYLA LFC1500X laser source. Only optical components are shown.

autocorrelation trace to the pulse width, assuming a sech^2 pulse.

6.1.2. Mechanics and optical setup

For mechanical isolation the whole optical setup is mounted on a 2.5 m × 1 m Nexus passive isolation optical table. From the output of the laser source to the focusing optics the beam is routed with Low Group Delay Dispersion (GDD) mirrors (Thorlabs UM10-45C). These mirrors are used to limit the effect of dispersion. The manufacturer states a group delay dispersion (GDD) of $GDD < 30\ \text{fs}^2$ at the used laser wavelength and a reflectance of $R > 99\%$ under an angle of incidence of 45°. The mirrors are only reflective in a wavelength range of about 1400 to 1700 nm and can thus not be used to route light in the visible range. On the other hand, this makes it possible to use these mirrors as a dichroic beamsplitter although the transmitted intensity in the visible range is low. Wherever maintaining the pulse temporal shape is not crucial, protected aluminum mirrors (Thorlabs PF10-03-G01) are used. From the output of the laser source the beam is routed into a Faraday cage (ETS-Lindgren) in which the DUT is positioned for electro-magnetic isolation. Fig. 6.6 shows the inside of the Faraday cage and a schematic drawing of the optical setup. The laser beam is focused onto the DUT with a 100x NIR Mitutoyo microscope objective (M Plan Apo NIR 100x, NA = 0.5). The setup is such that the beam enters the DUT in the vertical direction. This configuration was chosen to avoid fluctuations in the beam due to convection of air resulting from the temperature difference between a cooled silicon sensor and the surrounding air. This effect could be amplified in a horizontal orientation, but it was not systematically studied how large the effect is. The requirement of a vertical focusing of the beam and small distance between the objective and camera setup together with the limited load capacity of

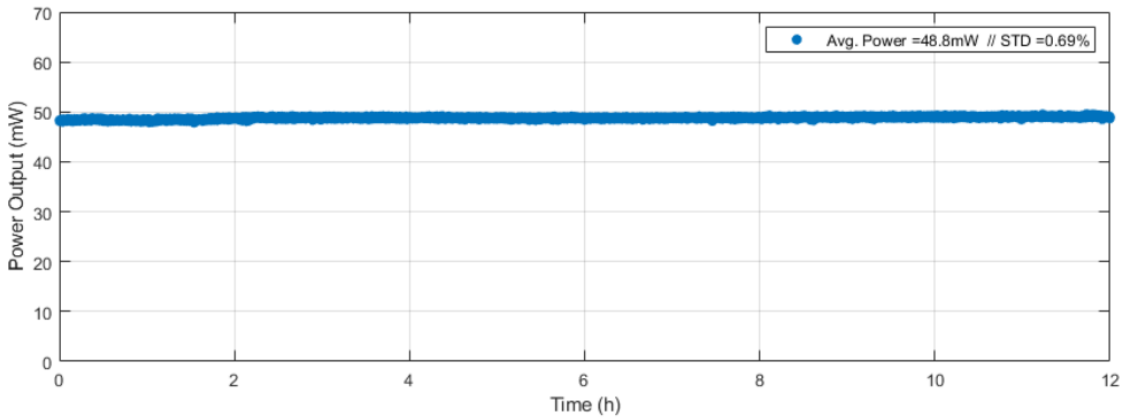

Figure 6.3. – Laser average power at final output. 48.8 mW that corresponds with 12.0 nJ pulse energy. From: LFC1500X Factory Acceptance Test.

the hexapod implied that the optical components had to be mounted in a vertical orientation. For this an aluminum breadboard is mounted vertically using L-brackets.
To improve the collimation of the beam as it enters the objective, a single lens with a focal length of 500 mm is mounted at a distance of approximately 30 mm from the objective. This increases the amount of light entering the objective but is not beneficial for the quality of the focusing (see sec. 6.2.7). As an alternative to a single lens an additional telescope setup could be implemented at this position, consisting of a combination of a convex and a concave lens (e.g. $f = 100$ mm and $f = -50$ mm) to improve the beam collimation. The only other option to change the beam width is to adjust a single lens which is mounted after the LPM (as a part of the laser system).
Half of the beam intensity is used to generate a TPA-reference signal. A 50:50 IR beamsplitter (Thorlabs BSW23) is used to direct part of the beam to the reference sensor and also to guide the reflected light from the DUT onto an IR camera. The beamsplitter is mounted on a flip-mount, which makes it possible to easily remove it from the optical setup without losing the alignment. Removing the beamsplitter doubles the light intensity on the DUT, which leads to a fourfold increase in TPA generated charge, but it is not anymore possible to use the reference sensor for corrections of power fluctuations nor the IR-camera. For an easy positioning of the DUT under the microscope objective an alignment laser is used, which emits visible red light. An iris and a neutral density filter are used to reduce the intensity and beam size. The red laser beam is made parallel with the main IR-beam by placing a mirror behind the last Low-GDD mirror above the objective.

IR-camera system

A camera system was installed to facilitate positioning of the DUT and to know, where the TPA-laser spot is located on the DUT. For imaging the DUT, the same optics as for focusing the beam are used. At an early stage of the development a camera setup in the visible range, with a CMOS camera and a conventional LED was used. The visible light for sample illumination as well as the reflected light are combined with/separated from the laser beam by means of placing an aluminum mirror behind the first Low-GDD mirror, which is located above the microscope objective. The laser beam would be reflected of the Low-GDD mirror, which would transmit the visible light. Later on, this setup was replaced by an IR-camera setup to be able to image through silicon to make the backside of the

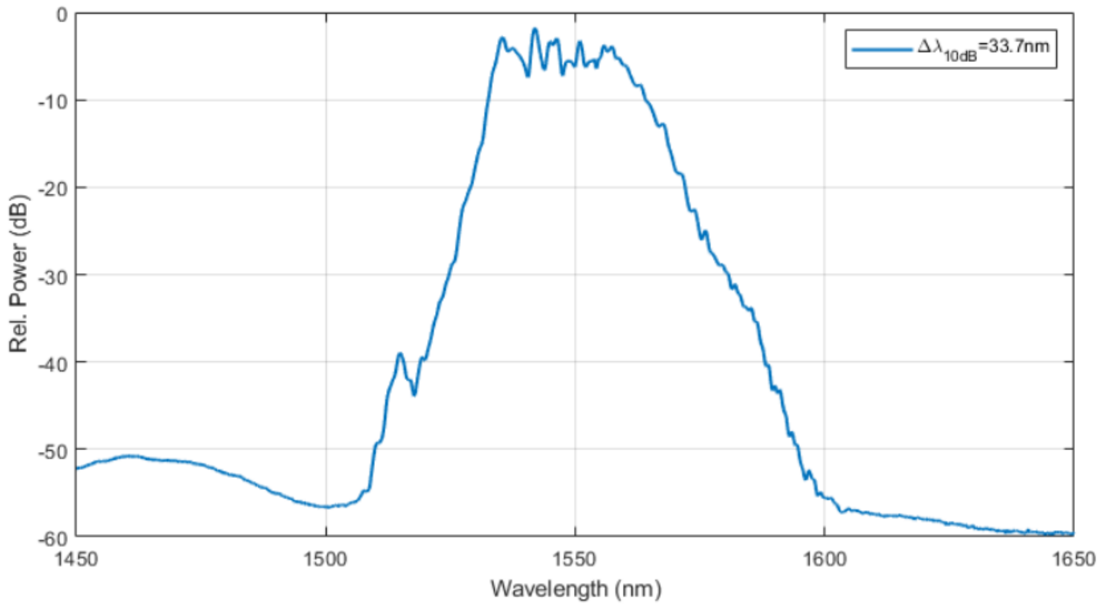

Figure 6.4. – Optical spectrum measured with OSA YOKOGAWA AQ-6375 (1200-2400 nm), at LFC1500X collimated output, 1 nm resolution. From: LFC1500X Factory Acceptance Test.

detector visible. The model name of the IR-camera is WiDy SenS 640G-STE from the company NIT[2]. The camera sensor consists of a 640x512 InGaAs pixel array with a pitch of 15 μm. The camera is mounted on a manual linear micro-meter stage for adjustments of the focal distance. A 200 mm lens is used for focusing the light onto the camera. For illumination of the DUT an IR-LED (Thorlabs M1550L3 + LEDD1B) is used. The LED is equipped with a $f = 16$ mm aspheric condenser lens (Thorlabs ACL25416U), which is used together with an additional 400 mm lens to focus the light on the input aperture of the microscope objective. The optical paths to the camera and the IR-LED are combined using an additional 50:50 IR beamsplitter (Thorlabs BSW23). This setup, although with reduced complexity, follows the principle of Köhler-illumination in reflected light microscopy (see e.g. [125]).

TPA/SHG - Reference signal

The power monitoring sensor that is included in the Fyla power management module is based on single photon absorption and thus scales linearly with the laser power. To correct fluctuations in the DUT-signal, which is generated by two-photon absorption, it is necessary to use a reference signal, which is generated by a non-linear process as well. Two methods were tested: 1) Using a silicon reference sensor and generating charge by two-photon absorption, 2) generating the second harmonic (SHG) in a beta barium borate (BBO) crystal and measuring the obtained light intensity by single photon absorption in a silicon sensor. Both methods resulted in similar amplitudes of the reference signal. Finally the method of a TPA-reference was chosen because it uses the same physical process as the primary signal. SHG is sensitive to temperature changes which could again lead to a sub-optimal correlation with the DUT-signal. In addition the TPA-reference is easier to set up, because it is less

[2] New Imaging Technologies, https://new-imaging-technologies.com/

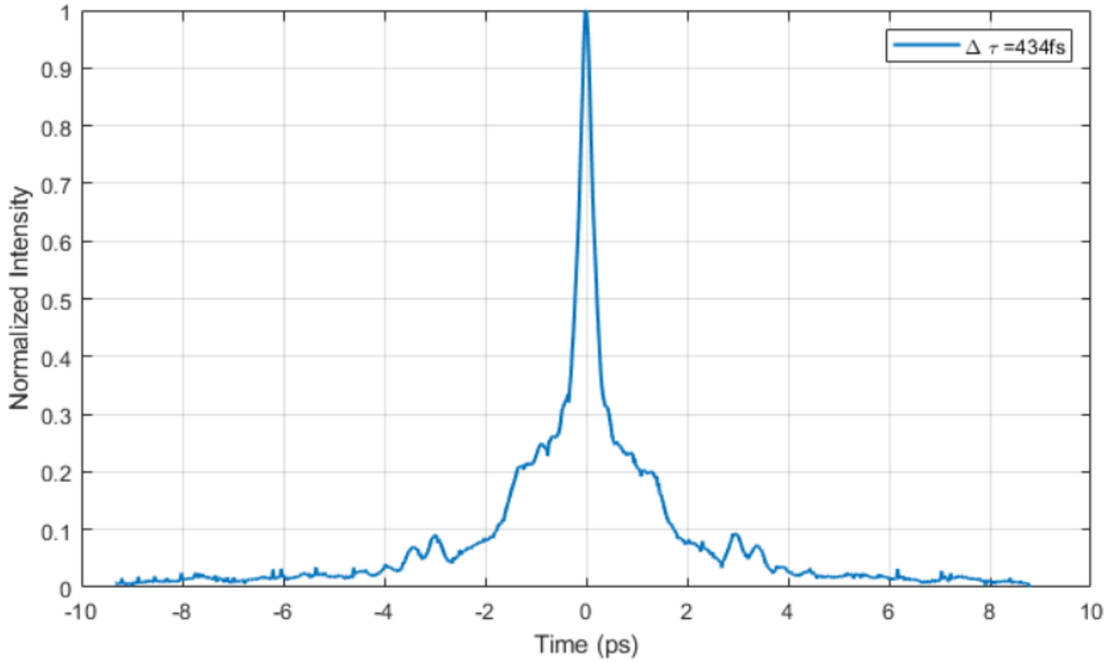

Figure 6.5. – Autocorrelator trace at laser output. Pulse Width 434fs, 10fs resolution. From: LFC1500X Factory Acceptance Test.

sensitive to changes in the focal point position and no phase matching is required. The sensor used for the TPA-reference is a silicon diode (Thorlabs DET36A2). The laser beam is focused with a 60 mm lens, which is mounted on a manual linear micro-meter stage. The sensor is connected to a Cividec amplifier and the resulting signal is displayed together with the DUT-signal on the oscilloscope. Since the reference sensor is as well in focus of the IR camera and equally illuminated through the 50:50 beamsplitter, it is mounted with a slight tilt to avoid back reflections of the IR-light and the laser beam onto the camera. In the setup described here, 50% of the beam is used to generate the reference signal. This loss in beam intensity could in principle be avoided with an SHG reference: Two lenses with equal focal length (e.g. 50 mm) separated by a distance of twice the focal length can be placed in the main laser beam to focus and recollimate the beam to the original size. The BBO crystal can be placed in the center between the two lenses to generate the second harmonic. The fundamental and second harmonic can then be separated by a dichroic beamsplitter. This method could as well be used with TPA charge generation, if the reference sensor can transmit the remainder of the beam, meaning it can not have any housing and has to feature an opening in the front- and backside metallization.

6.1.3. DUT positioning

To position the DUT under the objective and to perform spatial scans, two Newport large travel linear stages and a Newport hexapod (HXP50HA-MECA with HXP50-ELEC controller) are used. The linear stages are mounted on top of each other with a 90° angle to provide coarse movement in the x-y-plane. The hexapod is mounted on top of the linear stages. The sample holder is mounted on the carriage of the hexapod. The linear stages are usually only used for coarse alignment and to facilitate changing the DUT. All spatial scans during running measurements are carried out with the hexapod, while the linear stages are not moved. The most important specifications are listed in table

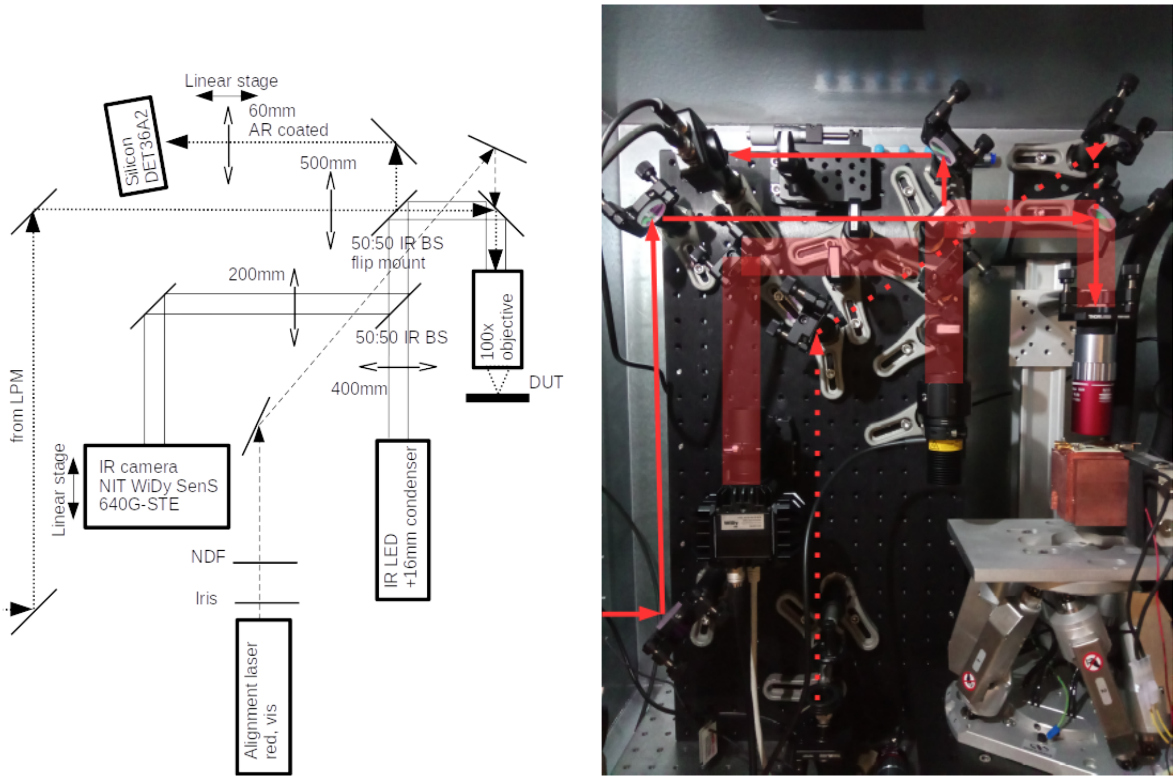

(a) (b)

Figure 6.6. – Optical setup inside the Faraday cage. (a) Schematic drawing. (b) Photograph, showing the TPA laser in solid red, the red alignment laser in dotted red and the IR-microscope light path in shaded red.

6.1 for reference. The hexapod satisfies two main requirements: The resolution of the TPA-TCT setup perpendicular to the beam direction is in the order of 1 μm. Therefore, to take several measurements on the rising edge of the signal, a positioning system with a sub-micrometer precision is necessary. In addition, it had to be possible to rotate the DUT to correct for an eventual misalignment caused by the mechanical fixation of the DUT. Since the Faraday cage can not be opened when the cooling system is active, it was required that the positioning system could be controlled remotely. The hexapod proved to be more compact, easier to install and more cost effective, than a combination of six individual motorized stages.

The DUTs are glued to printed circuit boards (PCBs), which are equipped with SMA-connectors. Electrical connection is established with wire-bonds from the PCB to the sensor front side and conductive silver glue to the backside. The PCBs can be equipped with a PT1000 temperature sensor. The PCBs can be mounted to the cooling block horizontally for top-TPA-TCT measurements or vertically for edge-TPA-TCT measurements. Photographs of the two different configurations are shown in fig. 6.7.

	HXP50HA-MECA
Travel range x,y,z [mm]	17, 15, 7
Travel range u,v,w [deg]	9, 8.5, 18
Minimum incremental motion x,y,z [nm]	100, 100, 50
Minimum incremental motion u,v,w [mdeg]	0.05, 0.05, 0.10
Uni-directional repeatability x,y,z [nm]	100, 100, 50
Uni-directional repeatability u,v,w [mdeg]	0.05, 0.05, 0.10
Accuracy x,y,z [µm]	5.0, 5.0, 2.5
Centered load capacity [N]	50

Table 6.1. – Specifications of Newport HXP50HA-MECA

6.1.4. Autocorrelation

For a characterization of the pulse temporal structure two auto-correlators, a commercial auto-correlator (Femtochrome[3] FR-103TPM) and a custom Michelson interferometer, are used.
Initially pulse compression and analysis should have been carried out with the so-called d-scan technique, which was included in the laser design. The setup consisted of a fixed prism compressor at the output of the laser with an additional variable, motorized stretcher (similar to the stretcher module described above). By measuring the spectral intensity of the first and second harmonic of the beam as a function of dispersion it should have been possible to fully characterize the beam. During this initial stage, to test the functionality of the d-scan technique, a Michelson interferometer was set up to obtain information about the temporal shape of the pulse independently. It was confirmed that the d-scan technique did not work with our setup, as the pulse shape was not sufficiently changed by the added dispersion. The plan to use the d-scan pulse characterization tool was discarded and in the latest version of the laser the autocorrelator FR-103TPM is used instead. The FR-103TPM consists of an ultra-thin ($< 1\ \mu$m) pellicle beamsplitter and a rotating mirror assembly, which introduces the delay to one of the pulse replicas [126]. The two collinear beams are then focused onto a photosensor, where the signal is produced by two-photon absorption. The integration time of the photosensor and the rotation speed of the mirror assembly can be adjusted. The FR-103TPM allows for interferometric measurements with a resolution of ≈ 1 fs and a scan range of > 50 ps. The signal of the autocorrelator is displayed on the oscilloscope screen and has to be converted to the correct time units with a factor that depends on the rotation frequency of the mirror assembly. In the current setup, the FR-103TPM is mounted close to the output of the laser source. The laser beam can be directed either to the autocorrelator or the rest of the setup by using a flip-mounted mirror.
The self-build interferometer (fig. 6.8) is mounted on an aluminum breadboard, which can be moved in and out of the beam. After the interferometer is moved into the beam, little fine adjustment is necessary to realign the beam with respect to the original optical path. The pulses are split with a 50:50 beamsplitter cube (Thorlabs BS012), which is made from NBK-7 glass and has a side length of 10mm. A variable delay is introduced to one of the pulse replicas with a linear stage (Newport M-423) with a motorized actuator (Newport TRA25PPD). The actuator has a minimum incremental motion of 100 nm, corresponding to an optical delay of 0.67 fs (6.67128 fs/μm). The combined beam follows the same optical path that the beam follows in the normal measurement configuration (without the interferometer). The non-linear signal, used for the autocorrelation measurement, is the TPA signal in the DUT or the TPA-reference sensor. In this way no additional sensors or electronic

[3] Femtochrome Research, http://www.femtochrome.com

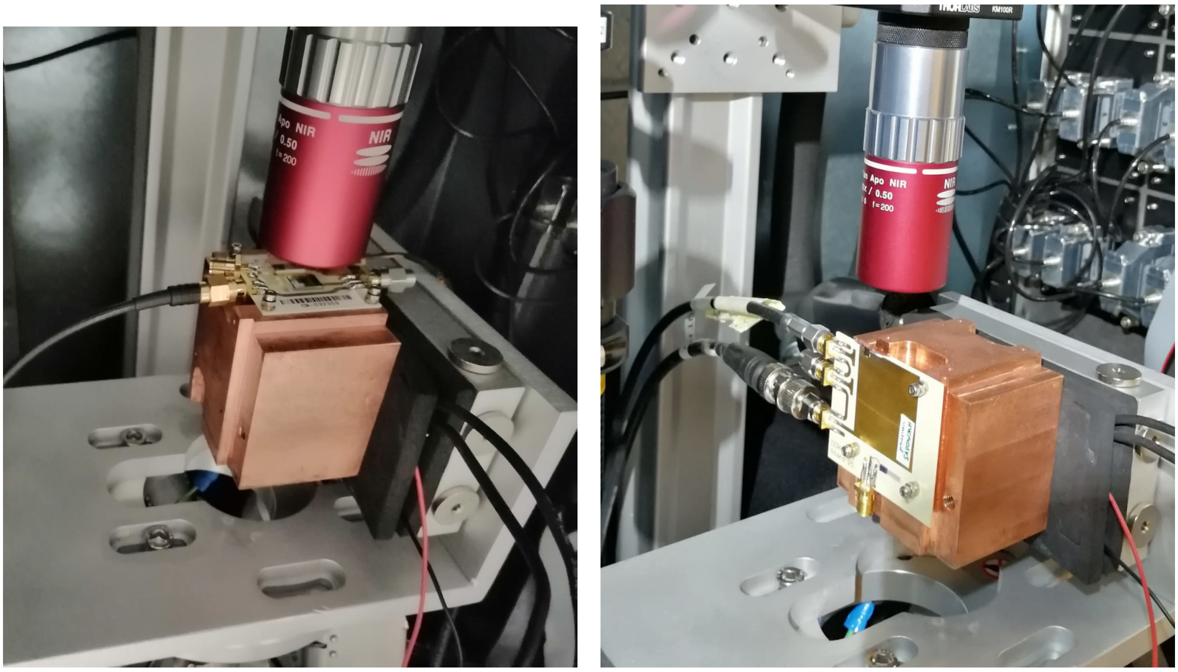

(a) Top-TCT configuration (b) Edge-TCT configuration

Figure 6.7. – Mounting options of the DUT on the sample holder. The copper block can be cooled by a Peltier element.

components are needed. In addition, this setup has the advantage that the pulse duration is measured at the DUT position. Some uncertainty stems from the fact that coated aluminum-mirrors (Thorlabs PF10-03-G01) are used at the end of the interferometer arms. The GDD of these mirrors is not specified, but it is not expected to have a significant effect on a 300 to 400 fs pulse. The reason for using these mirrors is that they have good reflectivity under 90° angle of incidence, in contrast to the low-GDD mirrors. It was not tested whether or not enough signal can be achieved by replacing the metallic mirrors with low-GDD mirrors. Another source of uncertainty is the beamsplitter: Each pulse passes through 20 mm of NBK-7 glass. The amount of dispersion can be calculated using the Sellmeier equation (as discussed for silicon in sec. 5.2.3) and the Sellmeier coefficients stated on the suppliers webpage [127]. The result is close to zero and it is assumed that the beamsplitter has a negligible impact on any pulse longer than $\approx$ 10 fs.

6.1.5. Electronics and readout

The DUT signal is amplified by a Cividec 2 GHz/40 dB amplifier and displayed on an Agilent Technologies DSO9254A digital oscilloscope. The bias voltage for the DUT is supplied by a Keithley 2410 1100V source-meter. The high voltage is either connected via the bias-T, which is included in the amplifier, or directly to the sensor, in which case the signal is read-out, with the oscilloscope providing connection to ground.
A Cividec Cx-L charge amplifier was used, when measuring the collected charge in absolute terms.

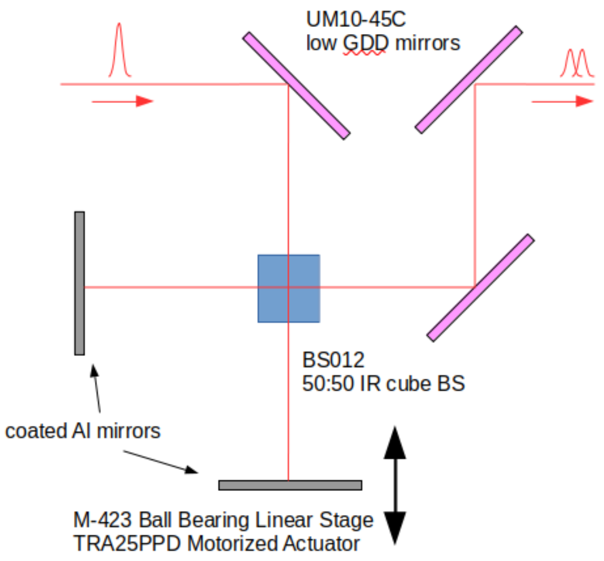

Figure 6.8. – Michelson interferometer for autocorrelation measurements.

6.1.6. Cooling

Cooling is provided by a two-stage system: The sensor itself is cooled using a thermoelectric module (Laird Thermal Systems DL-060-12-00-00-00). The current supply for the Peltier element is controlled with a Laird PR-59 temperature controller (PID). The PT1000, which is mounted on the sensor PCB, is connected to the PID regulator to provide a temperature measurement. The warm side of the Peltier element is cooled with a liquid chiller (Huber CC505 + CC3). To avoid condensation on the cold parts, the Faraday cage is continuously flushed with dry air, when the cooling system is active.

6.2. Commissioning

6.2.1. Pulse energy

Measurement of the pulse energy at the laser output

For measurements of the laser power a S401C thermal power sensor head from Thorlabs is used together with the PM100D console. The S401C is sensitive to wavelengths from 190 nm to 20 μm and powers from 10 μW to 1 W. Resolution and measurement uncertainty, as stated by the manufacturer, are 1 μW and $\pm$5%. The power of the laser was measured at the output of the LPM by placing the thermal sensor head into the beam and varying the motorized ND-filter from 150° (low power) to 0° (high power). At the same time the signal of the energy monitor (SPA reference) was recorded with an oscilloscope. The laser was pulsed at 4.051 MHz. In fig. 6.9 (a) the recorded power divided by the pulse frequency is shown as a function of the filter angle inside the power management module, which is used to adjust the laser power. The highest pulse energy is 11 nJ in a range from 0 to about 70°. In this range the neutral density filter has a fully transmissive window. For this reason, in the following, angles are only shown up to an angle of 70°. Fig. 6.9 (b) shows the signal amplitude of the energy monitor as a function of the power, measured with the thermal power sensor. Uncertainties on both measurements are estimated from the fluctuation of the respective displayed values. The SPA reference shows a good linearity over a wide power range. The amplitude of the SPA reference depends on the setting of a neutral density filter, which can be adjusted by hand inside the power management module of the laser.

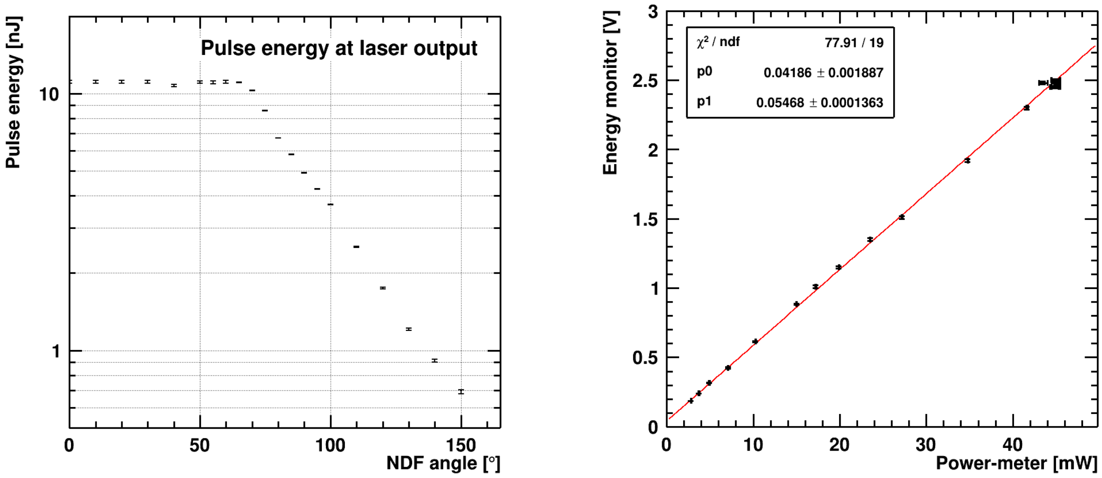

(a) Power-meter S401C normalized by pulse frequency

(b) Energy monitor against power-meter

Figure 6.9. – Measurements of the laser power with a thermal power sensor S401C (power meter) and the internal energy-monitor in the LPM. Measurements with the power meter are taken at the output of the LPM.

Measurement of the pulse energy at the DUT position

The laser power was measured at the position of the DUT, below the microscope objective. The measurements were again performed with the S401C+PM100D powermeter at room temperature. As outlined above, a 50:50 beamsplitter is mounted in the optical path on a flip mount. The beamsplitter can be easily removed to double the power that reaches the DUT, in which case the TPA reference sensor can not be used for power monitoring and the IR-camera setup can not be used. The measurement of the laser power was repeated with both settings at a laser frequency of 4.051 MHz. For each recorded power measurement, the signal of the SPA reference sensor was recorded as well. The SPA reference sensor is mounted upstream with respect to the beamsplitter. Fig. 6.10 shows the result of the measurement: (a) The pulse energy is shown as a function of the angle of the filter with (black) and without (red) the beamsplitter. Uncertainties are again estimated from the fluctuations observed on the digital display of the power meter. It is not known how exact the NDF setting is. Repeated measurements, also after several days with different measurements in between, showed good agreement. Nonetheless, for an exact calibration of the setup the SPA or TPA reference sensors should be used. (b) The pulse energy is shown as a function of the SPA reference sensor. Linear fits to the data are used to calibrate the SPA reference signal. The maximum pulse energy, which is about 10 nJ at the laser output, is reduced to about 0.8 nJ with the 50:50 beamsplitter in the optical path and to about 1.6 nJ without beamsplitter.

The amount of charge, that is generated inside a silicon sensor, was measured as a function of the

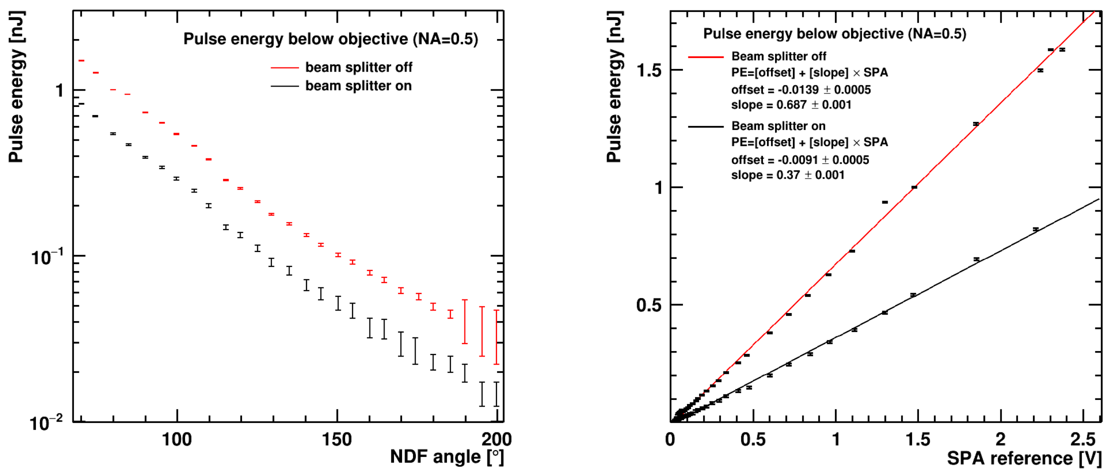

(a) Pulse energy as a function of the NDF angle

(b) Pulse energy as a function of the SPA reference

Figure 6.10. – Pulse energy as a function of the NDF setting and the SPA reference signal. The laser power was recorded below the objective (DUT position) with a thermal sesor head. The laser was pulsed at 4.051 MHz.

laser power with a p-type PIN sensor (7859-WL-A63-PIN4) with a thickness of 285 μm. The sensor is biased to 100 V, which is well above full depletion and was connected to a charge sensitive amplifier (Cividec CxL0058, Diamond Spectroscopic Amplifier, Gain = 12.5 mV/fC), with which it is possible to directly calculate the amount of charge in fC from the voltage output. The averaging option of the oscilloscope was set to 256 averages. For each setting of the laser power the focal point was moved across the full sensor (z-scan). The shown values of the charge correspond to the focal point position at the center of the DUT. The SPA reference signal was recorded with the data and was used to calculate the pulse energy in nJ from the calibration above. The beamsplitter was in the optical path and the measurement was only performed up to energies slightly below the maximum power to avoid saturation of the amplifier. The laser was pulsed at 200 Hz. The result of the measurement in shown in fig. 6.11. The data points were fitted with a quadratic function $Q(P) = K \cdot P^2$, resulting in a fit parameter of $K = 331.2 \pm 1.1$ fC/nJ^2. Fit and data show very good agreement except for the point at highest laser power. It is to date not clear what causes the discrepancy. Repeated measurements preferably at higher energies are needed to resolve this question. The observed quadratic behavior is in agreement with the expectation of a signal, purely generated by two-photon absorption (second term in eq. 5.49). Uncertainties on the pulse energy are calculated from the uncertainties on the calibration parameters (as shown in fig. 6.10) and the fluctuation of the SPA reference amplitude during a full z-scan. The SPA reference fluctuations are comparably low, in the order of 0.5%, due to the averaging of the oscilloscope. The uncertainty on the measurement of the charge is estimated from the fluctuations of signals in a region of ± 10 μm around the center of the detector, which range from 5% to 0.5%, for lowest and highest power, respectively.

A comparison with the theoretically expected amount of charge, reported in sec. 5.3 reveals a large discrepancy. From eq. 5.52 a total number of charge carriers of $N_{tpa} = 78 \cdot 10^6$ was calculated for a pulse energy of $E_p = 350$ pJ. For a comparison with fig. 6.11 reflection has to be taken into account. An injected energy of 350 pJ corresponds to a measured pulse energy below the objective of 500 pJ, assuming an energy loss, due to reflection at the silicon surface of 30%. At this pulse energy 80 fC were measured, which corresponds to a number of $0.5 \cdot 10^6$ electrons. The origin of this large difference to the calculated number of carriers remains unclear. Further measurements are needed for clarification. One possible explanation is the pulse temporal and spatial structure. For eq. 5.52 a perfectly Gaussian shaped beam, both in space and time, is assumed. If a large part of the pulse energy is transmitted in the observed picosecond pedestal (see sec. 6.2.3), this energy would be measured by the power meter, but would not contribute to TPA accordingly. It is also clear that the spatial shape of the beam is not entirely Gaussian (see sec. 6.2.2).

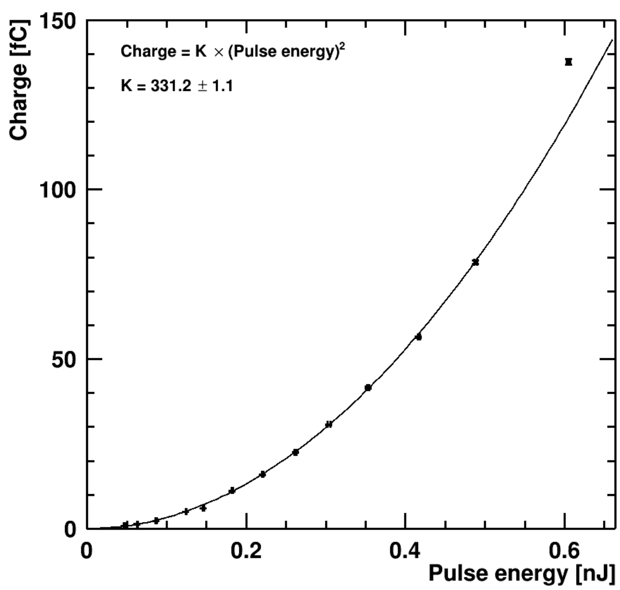

Figure 6.11. – Charge as a function of pulse energy. The measurement was performed with a p-type silicon sensor, connected to a charge sensitive amplifier. The pulse energy is inferred from a calibrated SPA reference measurement. The pulse energy is the energy below the objective, reflection on the silicon surface is not taken into account. A quadratic function was fitted to the data points.

Generation of e/h-plasma

If the charge carrier density, due to a high amount of absorption, becomes too high, an e/h-plasma can be created. In this case the cloud of charge carriers shields itself, for a certain amount of time, against the external electric field [83, 84]. The main observable to determine, whether or not a plasma is created, is the duration of the transient current pulses. In the case of plasma, the cloud of charge carriers is not immediately responding to the external electric field, which leads to an increased charge collection time. A measurement was carried out with different laser powers, using the same DUT as above (7859-WL-A63-PIN4 at 100V, 20°C). The DUT was connected to a current sensitive amplifier (Cividec C2-131) and the beamsplitter was in the optical path. The pulse energy was varied from 0.07

to 0.8 nJ, corresponding to NDF angles between 140° and 0°. In fig. 6.12 (a) the recorded signals are shown normalized by amplitude. The signals at higher laser power are significantly broader than the pulses at lower laser power. The pulses start to broaden at an energy of 0.32 nJ. The time during which the signal is higher than 10% of the maximum amplitude (time over threshold, TOT) is shown in fig. 6.12 (b) as a function of the pulse energy. For energies below about 0.3nJ the measured values of TOT(10%) form a plateau at around 10 ns. This time is expected for charge collection in a 300 μm thick detector. At higher energies the measured time rises to above 14 ns. At energies smaller than 0.2 nJ the measured time fluctuates because of a low signal to noise ratio. The same measurement was also carried out in the high energy range of up to 1.5 nJ pulse energy without the use of a signal amplifier for the DUT, to avoid saturation. Collection times of up to 30 ns were observed at the highest pulse energies. Fig. 6.13 shows the same set of measurements. This time, the charge is plotted as a

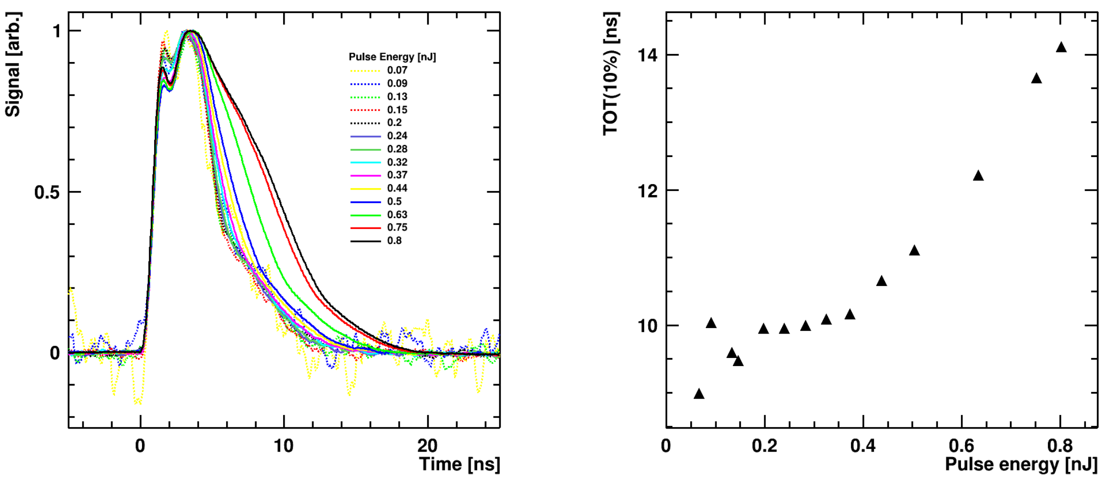

(a) Recorded signals at different pulse energies (b) Time over threshold as a function of pulse energy

Figure 6.12. – Waveforms for different laser pulse energies (a) and the corresponding time over threshold at 10% of the signal amplitude as a function of pulse energy (b). High powers show longer pulses, due to the creation of e/h-plasma.

function of the pulse energy. A fit to the data points is performed with a purely quadratic function, with the fit range limited to energies below 0.3 nJ. Below this value no plasma is expected, as can be seen from the pulse width (fig. 6.12), and the data points follow the expected behavior, as indicated by the fit. For higher pulse energies, in a regime in which plasma is present, the charge increases faster, than what would be expected from the increase of laser power. In the measurement, which was carried out with the charge sensitive amplifier (see fig. 6.11), only the point at the highest pulse energy of 0.6 nJ does not follow the expected square dependence on the pulse energy. The measurements with the current and charge sensitive amplifier were carried out on two consecutive days under the same experimental conditions (same focusing, same DUT and bias voltage). Therefore, it can be expected that the onset of plasma happens around the same pulse energy in both measurements. It is not obvious, why the charge should increase, if plasma is present. Under the assumption that the amount of carriers, which are initially created, behaves as expected, a delayed drift of the charges would not lead to a larger charge signal. If some charge carriers can recombine before being separated by the electric field, one would even expect a decrease in charge. A possible explanation of a stronger increase in charge at higher energies than expected, could be the onset of avalanche ionization. The onset of plasma, and the effects it has on the charge collection, need further investigations.

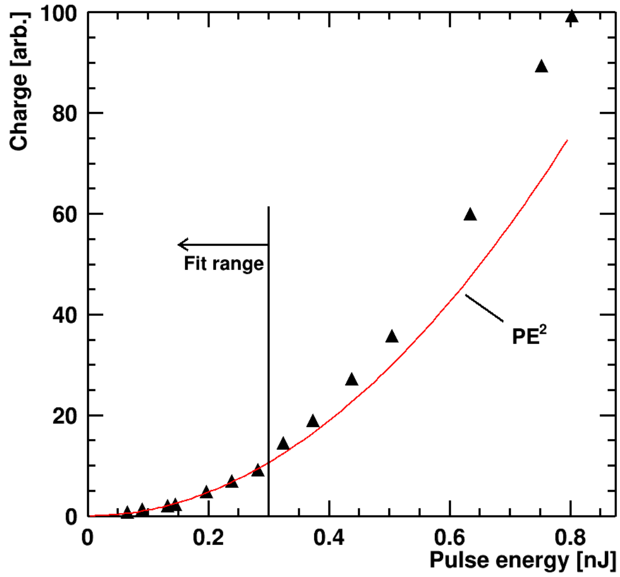

Figure 6.13. – Charge as a function of pulse energy. A quadratic function was fitted to the data points with the fit range limited to a pulse energy below 0.3 nJ.

6.2.2. Stability and reference signal

The reason to use a TPA reference sensor, in addition to the SPA reference, which is included in the pulse management module, was described in sec. 6.1.2. An examplary comparison of the reference signals, obtained by SPA and TPA, is shown in fig. 6.14. In both measurements the focal point of the beam was located at a constant position inside the DUT (FZ200P_05_DiodeL_9), which is a 200 μm thick, FZ p-type diode, while a given number of measurements is recorded with unchanged conditions. The DAQ software only allowed for two recorded signals at a time, therefore independent measurements were carried out with the SPA and TPA reference. Shown is the respective signal amplitude, normalized by the corresponding mean value, as a function of the event number. Between the events a waiting time of 1 s was programmed, so that each measurement corresponds to roughly one hour of data taking. The SPA reference signal (a) is very stable and shows a good signal to noise ratio. But it is clear, that the DUT signal shows a drift in the signal amplitude, which is not reflected in the SPA reference signal. The measurement with the TPA reference (b), on the other hand, shows an excellent correlation between the DUT and reference signal. This also confirms that the drift in signal amplitude, which is observed for the DUT, is not related to any thermal effect in the sensor or the focusing of the beam, but is an intrinsic fluctuation of the laser source. It is not exactly known what causes these variations. Since only the TPA (and SHG) signals are affected, while the SPA signal stays constant, it is assumed that instabilities in the laser spectrum lead to fluctuations in the pulse duration. The TPA reference signal shown here (b) has a very low signal to noise ratio, which is problematic especially for low laser powers. Connecting the sensor to an amplifier helped to increase the signal. At the time of writing, tests are ongoing to replace the commercial, mounted silicon sensor against a silicon detector comparable to the DUTs.

Many effects contribute to the overall stability of the setup. Variations in the laser output can lead to

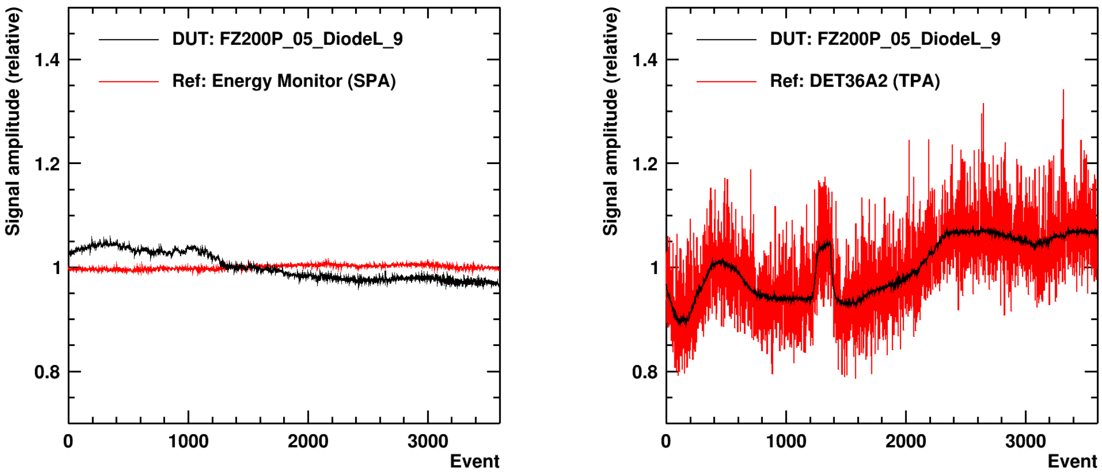

(a) SPA reference (b) TPA reference

Figure 6.14. – Relative signal amplitude as a function of event number for two measurements with the SPA and TPA reference sensors. Each measurement corresponds to about one hour of data taking.

pulse-to-pulse fluctuations of the signal, and to the observed drift over longer time scales. In addition, a small random movement of the laser beam at the laser output was observed, which can lead to pointing instabilities. Thermal instabilities have an effect on the laser and also change the absorption coefficient of the sensor material, therefore measurements should be carried out with active temperature control. The main contribution to random signal fluctuations is electronic noise. On short time scales (1000 events with 100 ms wait time) the signal in the DUT fluctuates with a standard deviation of about 7% of the mean value without any averaging in the oscilloscope. This value depends on the laser power, which was set to 110°/0.2 nJ. The standard measurement configuration is to record the signals with averaging by the oscilloscope enabled. This increases the measurement time but effectively suppresses statistical fluctuations in the signal. Typical settings range from 64 to 1024 averages per waveform. E.g. at 128 averages the signal fluctuation is already reduced to 0.7%. The SPA reference signal shows a fluctuation of about 2% without averaging and 0.2% with 128 averages. The TPA reference signal fluctuates significantly more due to the low signal amplitude but, as mentioned, this will be improved by replacing the reference sensor.

Beam shape and pointing stability

The beam shape and pointing stability was evaluated with an IR-camera of type Chameleon CMLN-13S2M. The image sensor is a Sony ICX445 CCD sensor with a 1,296 x 964 pixel array with a pixel pitch of 3.75 μm. This sensor is in principle not sensitive to IR-light. This camera model uses a phosphor sensor coating, which absorbs in the IR-range and emits in the visible range, to achieve some

IR sensitivity. This setup makes it possible to use this camera for simple beam monitoring. Images were taken directly at the laser output without any focusing. One image of the beam is shown in fig. 6.15. The image axis give the corresponding pixel number of the image sensor. The red dot marks the

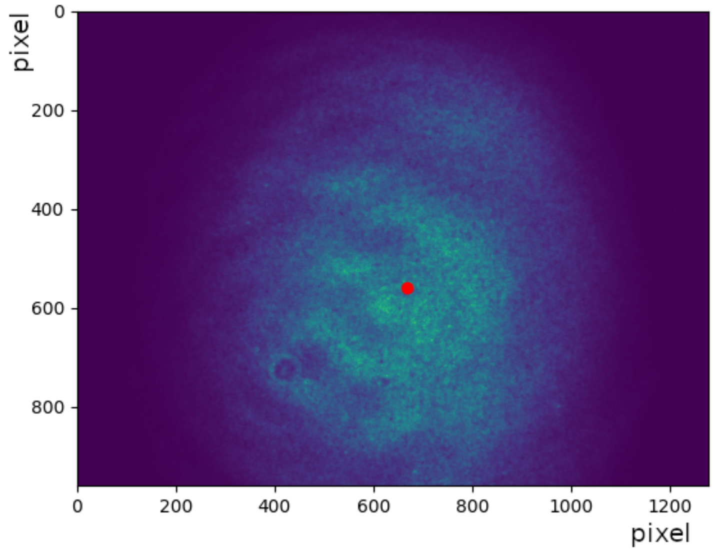

Figure 6.15. – Beam shape at the laser output, measured with an IR-camera. The red dot shows the position of the mean value of the intensity. Axis units are in number of pixel of the image sensor. The pixel pitch is 3.75 μm.

center of the beam, which is obtained as the mean of the intensity distribution in x and y. The beam is slightly asymmetric in x- and y-directions and shows some variation of the intensity. It was confirmed that this intensity pattern is in fact a feature of the laser beam and not the image sensor by moving the position of the beam on the sensor. In addition a rapid wiggling of the beam was observed. To quantify this effect, the position of the beam center was recorded for consecutive images. Histograms of the recorded coordinates for the x- and y-direction are shown in fig. 6.16. The standard deviation of the histogram in x-direction is 6 pixel, corresponding to 22.5 μm. In y-direction the beam position changes by 2 pixel or 7.5 μm. This movement is quite significant, considering that a spatial resolution at the plane of the DUT of better than 1 μm is expected. On the other hand, no movement of the beam under the objective was observed using the same method. A likely reason is, that the input aperture of the objective is overfilled due to the divergence of the beam from the source to the objective. The movement of the beam did not cause any negative impact on the measurements so far, but this should be reevaluated in due time.

6.2.3. Pulse duration

To investigate the temporal structure of the laser pulses, interferometric autocorrelation measurements (FRAC, fringe resolved autocorrelation) have been carried out. A description of the measurement method can be found in sec. 5.2.5. One measurement is shown in fig. 6.17. The measurement was performed with the sensor 7859-WL-A63-PIN4, biased at 100 V. The sensor was not corrected for tilt after mounting, but since the focal point position of the beam is not changed during a FRAC measurement, this is not expected to have any impact on the result. Data was taken with an NDF angle

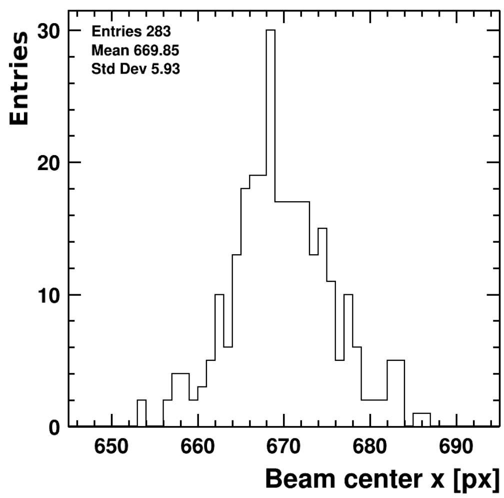

(a) Beam movement in x

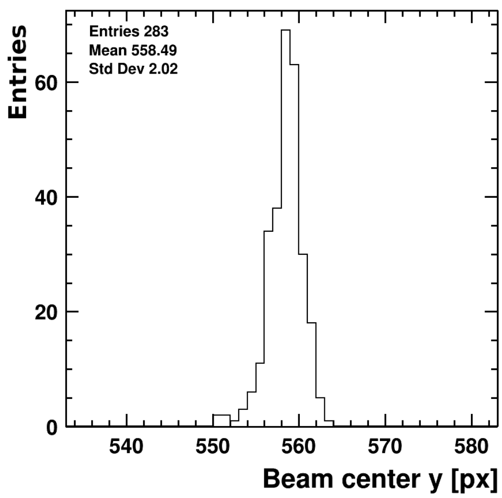

(b) Beam movement in y

Figure 6.16. – Position of the beam center for 283 consecutive images with an IR-camera. Axis units are in number of pixel of the image sensor. The pixel pitch is 3.75 μm.

of 70° and a pulse rate of 200 Hz. The filter angle can not be translated into the pulse energy in nJ, from the calibrations shown before, because a significant amount of energy is lost in the interferometer, due to the metallic mirrors and the cube beamsplitter. The scan was taken with a stepping resolution of the micrometer stage of 100 nm. The micrometer stage movement is converted to the amount of optical delay with the factor $2/c = 6.67128$ fs/μm. c is the speed of light and the factor of 2 accounts for the change in optical path length. The signal, shown here on the y-axis, is the integrated signal (charge) of the respective pulse. The amplitude of the signal can be used as well, which leads to the same result. Also a comparison of the DUT signal and the TPA-reference signal show that both sensors give similar results, as expected, so that in principle no sensor has to be mounted as a DUT for FRAC measurements. The x-axis is set to zero at the center of the interference signal. The signal is normalized to the background signal level at large optical delays. The data and normalization is the same in both figures. The autocorrelation trace is symmetric and shows nearly perfect extinction at zero optical delay. These two points give confidence in the alignment of the interferometer: If there was a significant misalignment, the two pulses could not fully interfere destructively. In fig. 6.17 (a) it is possible to see that the FRAC trace shows some pedestal, which extends up to a delay of about 5 ps. A zoom-in in the signal region beyond 5 ps reveals that, even at the background level, the signal shows some interference. A large pedestal in the laser pulse of larger than 10 ps can also explain, why the expected 8:1 ratio of signal to background can not be achieved. The calculation of the theoretical SNB ratio assumes zero interference at large optical delays. From the measurements it can be concluded that a large picosecond pedestal is present in the pulse temporal structure. The interference at large delays is relatively stable in amplitude. For a chirped pulse, the fringes of the interferometric trace would disappear much earlier because the interfering leading and trailing parts of the pulse have a different instantaneous frequency, which prohibits effective interference. This is an indication that the observed pedestal is not (entirely) due to a chirp in the pulse but due to a narrow bandwidth peak in the pulse spectrum. In sec. 6.3.5 a feature in the measured waveform for irradiated sensors is discussed. This small feature, which precedes the main signal and has a duration of about one nanosecond, could be explained by a large pedestal in the laser pulse, if the duration of the pulse pedestal is in the order of $\approx ns$. It has to be confirmed, if it is the case for this laser. From the measurement the fringe averaged autocorrelation trace is calculated and the full width at half maximum of the main signal peak is extracted as $FWHM_{IA}$ = 616 fs. The measured pulse width is therefore $\tau = FWHM_{IA} \cdot 0.648$ = 399 fs, assuming a sech^2 shaped pulse.

The pulse was also measured with the commercial autocorrelator FR-103TPM. The measurement

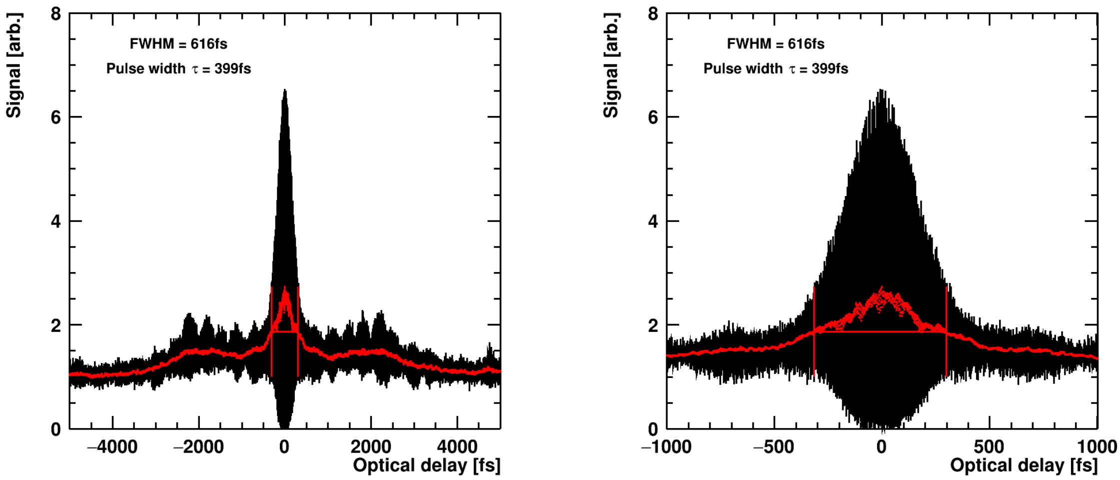

(a) Full scan

(b) Zoom in

Figure 6.17. – Interferometric autocorrelation trace of the laser pulse. The interferometer arm length was changed in steps of 100 nm, corresponding to an optical delay of about 0.67 fs. The left and right figures show the same data with a different axis range. The sensor used for the measurement is 7859-WL-A63-PIN4, biased at 100 V. The laser was pulsed at 200 Hz. The fringe averaged trace is shown in red.

result is shown in fig. 6.18. The laser pulse frequency was at the maximum 8.1 MHz and also the laser pulse energy was maximal. The measurement shows a linear slope, which is visible in the full view of the trace (a). The origin of this could not be found. The broad plateau, from −0.02 s to 0.015 s is believed to result from the rotating mirror assembly. For most positions of the rotation state only the non-delayed half of the beam is entering the sensor. As soon as both parts of the beam are reaching the detector, but still with zero overlap in time, the plateau, which is visible in the measurement, is reached. This corresponds to the usual configuration of two pulses with a large optical delay and therefore has to be understood as the baseline of this trace. The full width at half maximum of the interference signal was measured with respect to this baseline, which results in a value of 410 μs. The time axis of this trace can be converted to the respective amount of optical delay by multiplication with a factor of 1.6 fs/μs. The pulse width is therefore $\tau = 410\ \mu\text{s} \cdot 1.6\ \text{fs}/\mu\text{s} \cdot 0.648 = 425\text{fs}$.

The measurement with the FR-103TPM is very close to the result obtained by Fyla (434 fs, fig. 6.4) with a similar autocorrelator. These two values are about 30 fs larger than the result from the measurement with the custom Michelson interferometer (399 fs). Both setups are very sensitive to the alignment. In addition, the calculation of the pulse duration depends on the definition of the baseline and the assumed pulse shape. A sech^2 pulse was assumed here, following the procedure of the manufacturer. The significance of the numerical value of the pulse duration should not be over stressed, since the measurements clearly show that the actual pulse shape deviates from the theoretical one, which can impact the process of two-photon absorption, especially in irradiated detectors.

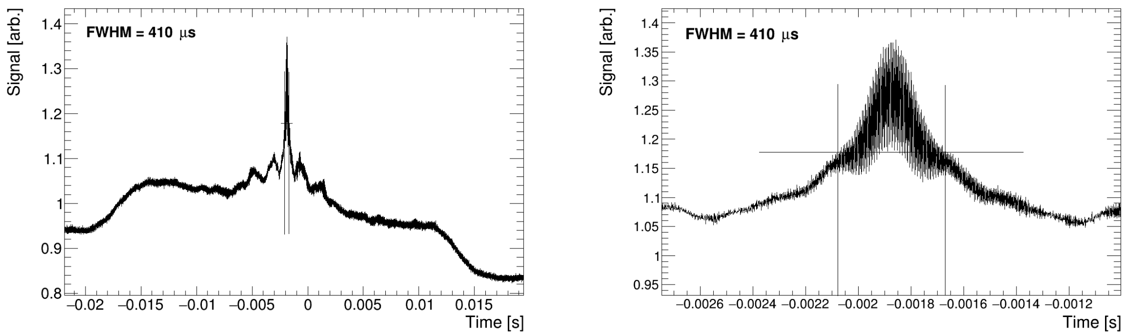

(a) Full scan (b) Zoom in

Figure 6.18. – Autocorrelation trace measured with Femtochrome FR-103TPM.

6.2.4. Temperature dependence of the collected charge

The change of absorption of light in silicon depends on the temperature for mainly two reasons: 1) The silicon bandgap decreases as the temperature increases [128, 10], which is related to the increased inter-atomic spacing. 2) The band-to band absorption in silicon is an indirect process and requires phonons [129]. For these reasons higher light absorption is expected for higher temperature. The collected charge was measured with a charge sensitive amplifier as a function of the sensor temperature, ranging from −20°C to +20°C for multiple laser powers. The DUT is a p-type diode (7859-WL-A63-PIN4), biased at 100V and connected to a charge sensitive amplifier (CxL0058). The sensor is not irradiated. The laser is pulsed at 200 Hz. For each laser power and temperature a full z-scan was performed but only those values of the collected charge are taken into account, for which the focal point of the laser was located in the center of the detector. For each temperature setting the laser power was varied. After changing the temperature the sensor was realigned before starting the measurement, because the alignment was changed due to expansion of the materials. A shift of about 20 μm in x-direction and 200 μm in y-direction was observed between highest and lowest temperature. Fig. 6.19 (a) shows the measured charge values as a function of temperature. Each temperature curve was fitted with a linear function $Q(T) = p_0 + p_1 T$. The charge values are not corrected for fluctuations in the laser power by division by a reference signal because the absolute value of the calibrated output of the amplifier is needed. It was tried to account for fluctuations relative to the mean value at a reference temperature, which did not increase the fit quality. E.g. it can be observed that all charge values at −10°C are systematically too high, which can be attributed to a shift in the laser power. But overall the change of the amount of charge with temperature is higher than the fluctuations, caused by the laser. The slope p_1 of the fitted function, depends on the amount of overall deposited charge. Therefore the value was normalized to the charge value at 0°C (p_1/p_0, normalized temperature coefficient), which is shown in fig. 6.19 (b) as a function of the NDF angle. The weighted average of this coefficient is $< p_1/p_0 >= (0.0059 \pm 0.0004)$ 1/°C. This means e.g. that a change in temperature by 40°C leads to a change in collected charge by about 24%. In literature, an increase of the TPA absorption coefficient by about 10% to 15% between −20°C and +20°C has been measured by recording the transmission through a silicon waveguide at a wavelength of 1.55 μm [130].

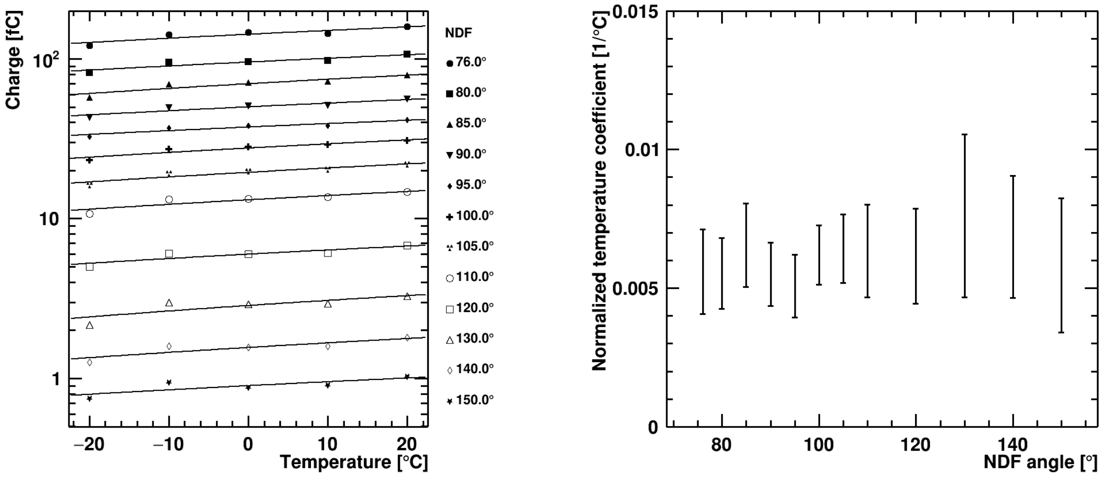

(a) Charge variation with temperature

(b) Normalized temperature coefficient

Figure 6.19. – Variation of collected charge as a function of temperature for different laser powers. Data at a constant laser power was fitted with a linear function (a). The slope, normalized by the value at 0°C, is shown in (b).

6.2.5. Z-scan

The method of TPA-TCT has two identifying features. The quadratic dependence of the signal on the laser power was already demonstrated. The other obvious possibility to test for TPA is to perform a z-scan. Here the DUT is moved along the beam axis at a constant laser power. In an SPA-TCT setup, this would result in a constant signal, since the focusing and defocusing of the beam does not affect the amount of absorbed light, as long as the whole beam cross section enters the sample. In contrast to that, if TPA is the dominant absorption mechanism, the amount of absorbed light depends critically on the position of the focal point. If the focal point is moved outside of the sample and the beam has a short enough Rayleigh length, no signal is expected, even though the full beam is still passing through the detector. This behavior is shown in fig. 6.20. The DUT (FZ200P_05_DiodeL_9) is a 200 μm thick, unirradiated, FZ p-type sensor, which was processed using a deep diffused silicon substrate. The bias voltage of the sensor was varied from 0 to 200 V in steps of 10 V. At each voltage step the DUT was moved across the focal point in the direction of the beam. The light is injected from the top of the device. Fig. 6.20 (a) shows the total collected charge and (b) shows the drift velocity profile. The top side of the detector corresponds to low z-values. The measurement was carried out at a laser pulse frequency of 100 Hz and maximum laser power (0° NDF), but the laser power can not be compared with other measurements, since the alignment was changed at a later point, significantly increasing the power for a given NDF angle. The measurements show that, if the focal point is moved outside of the sensor (above or below), no charge is generated. This is expected, due to the negligible single photon absorption cross section at the used laser wavelength. The charge profile (a) shows how the depletion width increases with bias voltage until the sensor is fully depleted at around 90 V. Note that the horizontal axis (z) indicates the position of the hexapod and was not scaled to correct for the effect of refraction (compare sec. 5.2.4, p. 54). The drift velocity profile indicates the expected behavior of a linearly decreasing electric field inside a homogeneous space charge region. The slope of the rising and falling edges of both graphs, as well as the tails extending beyond the active volume of the sensor, are a result of the finite length of the beam (Rayleigh length). The used objective has a numerical aperture of 0.5. A detailed discussion of the spatial resolution follows in sec. 6.2.7 and sec. 6.3.6. Another point to note is that no reflection of light can be observed at the backside of the device. This is an effect of the deep-diffused support wafer. Different manifestations of reflections are briefly discussed in sec. 6.3.1. From eq. 5.51 the expected charge profile can be calculated under the

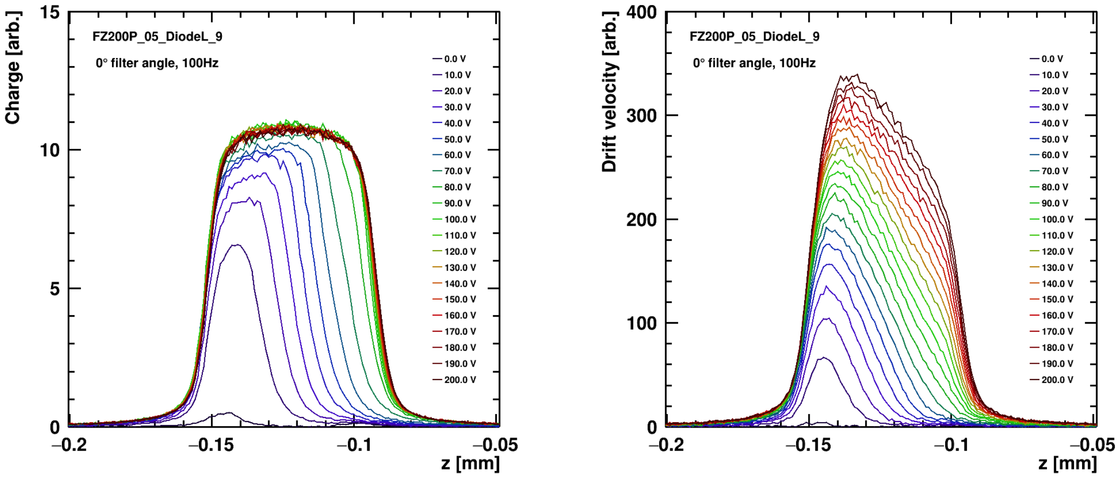

(a) Charge (b) Drift velocity

Figure 6.20. – Charge and drift velocity as a function of the sensor position along the beam axis (z) for different bias voltages. The sensor is a 200 μm thick, unirradiated p-type sensor. Microscope objective: $NA = 0.5$.

assumption of homogeneous charge collection throughout the sensor bulk with

$$N^d_{tpa}(z) = 2\pi \int_{z-d}^{z} \int_0^\infty n_{tpa}(r, z')\, r\, dr\, dz' \tag{6.1}$$

$$= \frac{E_p^2\, n^2\, \beta_2 \sqrt{\ln 4}}{4\, c\, \hbar\, \pi^{\frac{3}{2}}\, \tau} \cdot \left[\tan^{-1}\left(\frac{(d-z)}{z_0}\right) + \tan^{-1}\left(\frac{z}{z_0}\right)\right]. \tag{6.2}$$

The integration is performed over a volume with thickness d, which corresponds to the thickness of the active volume. Correspondingly, the equation for a one sided z-scan is

$$2\pi \int_{-\infty}^{z} \int_0^\infty n_{tpa}(r, z')\, r\, dr\, dz' = \frac{E_p^2\, n^2\, \beta_2 \sqrt{\ln 4}}{8\, c\, \hbar\, \pi^{\frac{3}{2}}\, \tau} \cdot \left[\pi + 2\tan^{-1}\left(\frac{z}{z_0}\right)\right]. \tag{6.3}$$

Fig. 6.21 shows a z-scan, which was fitted with eq. 6.1. An apparent ambiguity exists in terms of the

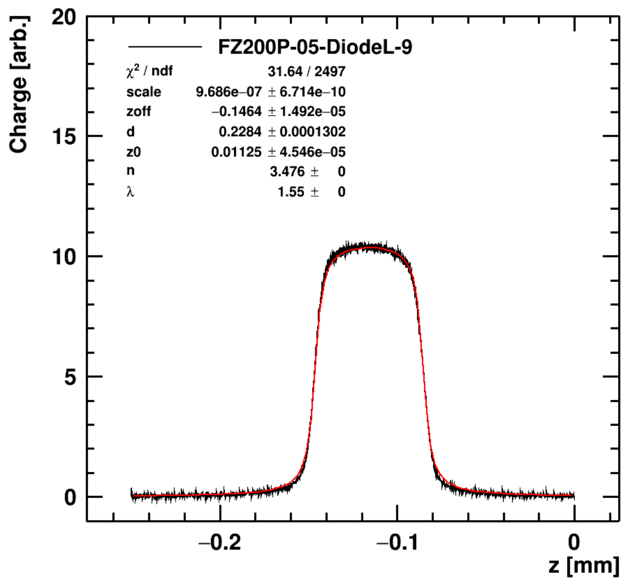

Figure 6.21. – Charge as a function of the hexapod position along the beam axis. The data was fitted with eq. 6.1

scaling of the z-axis to correct for refraction: The slope of the rising and falling edges of the graph is an effect of the extension of the charge generation volume along z and therefore a function of the Rayleigh length z_0 of the beam. But the z-axis itself depends on the beam focusing through the factor $K = z'/z$ from eq. 5.42 (or 5.43) and therefore on z_0. One approach to overcome this, is to measure the Rayleigh length in an independent measurement, scale the z-axis of the z-scan accordingly and fix the fit parameter in eq. 6.1 to the measured value. Another approach is to perform the fit without fixing z_0 and including the scaling factor K into the fit function. The slope of the arctan-function then becomes (K/z_0). The value of this factor is unique for all z_0, which can be seen in fig. 6.22, confirming that this approach is unambiguous. In the shown fit (fig. 6.21) the latter method was used. Some additional uncertainty results from the dependence on the refractive index of silicon. For unirradiated silicon this value is tabulated and can be fixed with good certainty. But for irradiated silicon the refractive index changes, complicating the interpretation of the data.

6.2.6. Sensor positioning and tilt correction

Due to the high spatial resolution of the TPA-TCT, it is necessary to precisely align the DUT with the hexapod axes of movement and with the beam direction. In the following it is described how the different hexapod coordinate systems work together and how they can be used to correct for a tilt of the sensor with respect to the axis of movement.

Hexapod coordinate systems

The hexapod consists of the base plate, six actuator legs and the carriage, on which the sample holder is mounted. To describe the position of the hexapod several distinct coordinate systems, which are

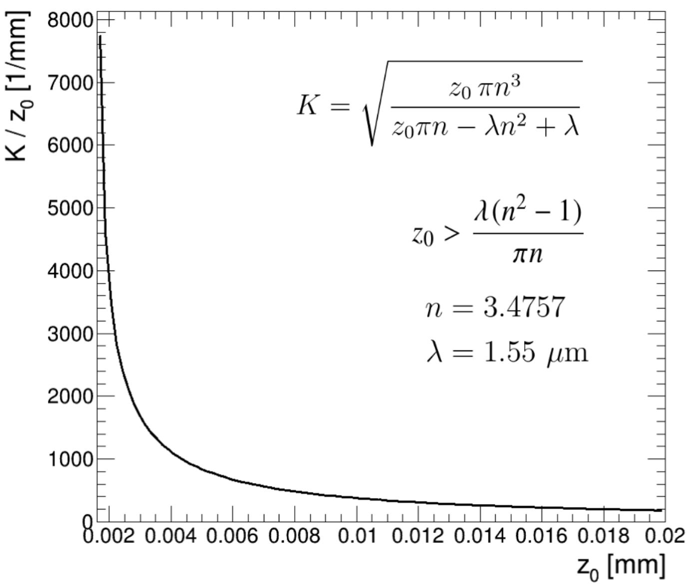

Figure 6.22. – Scaling of the z-axis

shown schematically in fig. 6.23, are used. Of direct relevance to the user is a good understanding of the tool and work coordinate systems. The tool coordinate system is defined with respect to the hexapod's carriage. As the carriage moves, so does the tool coordinate system. The work coordinate system is defined with respect to the world coordinate system and does not move with the hexapod carriage. The coordinates with which the user mostly interacts and which are recorded as the measured position of the hexapod carriage are describing the position of the tool coordinate system with respect to the work coordinate system. The position of the base coordinate system (the position of the hexapod base plate) in the world coordinate system can be redefined. This feature can be used for example if the hexapod is relocated in the experimental setup by using the linear positioning stages, while the work coordinate system maintains its position, e.g. relative to the laser beam. In the default configuration world and base coordinate systems coincide.

The hexapod carriage can be moved in incremental steps along the axes of both the tool and the work coordinate systems. Absolute movements can only be carried out along the axes of the work coordinate system. Spatial scans are only carried out as absolute movements. The position of the tool coordinate system in the work coordinate system is given in the form of six values (x,y,z,u,v,w). x,y and z are the values along the three axes of a right handed Cartesian coordinate system. The orientation of the tool coordinate system (the carriage) is given by angles u,v and w. u,v and w are the angles of rotation around the x,y and z coordinate axes respectively, where a positive angle describes a counter-clockwise rotation, when the respective axis is pointing towards the observer, as is depicted in fig. 6.24. Rotations in $\mathbb{R}^3$ are not commutative. The order, in which the respective rotations are applied, follows the Tait–Bryan convention $z - y' - x''$. The rotations are intrinsic: First the tool system is rotated by angle w around the z-axis, then it is rotated by v around the new y-axis and then it is rotated by u around the new x-axis. Intrinsic rotations are equivalent to extrinsic rotations (rotations around a fixed coordinate system) in reversed order. If used on a column vector, the rotation matrix $R = R_z(w)R_y(v)R_x(u)$ describes an intrinsic rotation in the order $z - y' - x''$ or an extrinsic rotation in the order $x - y - z$.

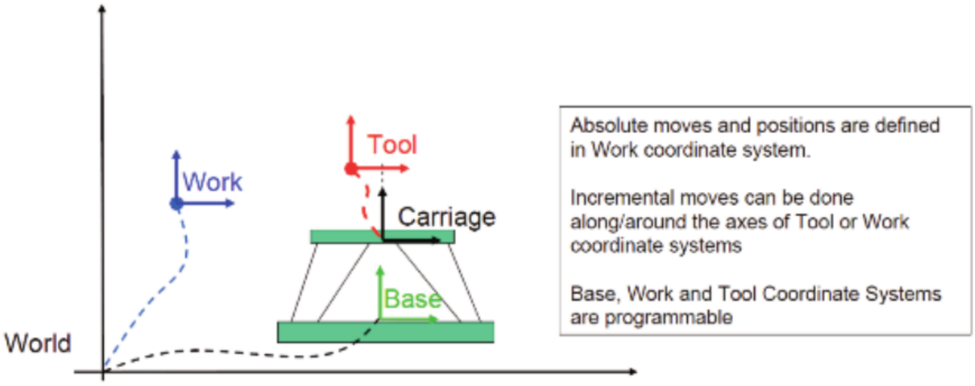

Figure 6.23. – Definition of the hexapod coordinate systems. [131]

$$R_x(u) = \begin{pmatrix} 1 & 0 & 0 \\ 0 & \cos(u) & -\sin(u) \\ 0 & \sin(u) & \cos(u) \end{pmatrix} \tag{6.4}$$

$$R_y(v) = \begin{pmatrix} \cos(v) & 0 & \sin(v) \\ 0 & 1 & 0 \\ -\sin(v) & 0 & \cos(v) \end{pmatrix} \tag{6.5}$$

$$R_z(w) = \begin{pmatrix} \cos(w) & -\sin(w) & 0 \\ \sin(w) & \cos(w) & 0 \\ 0 & 0 & 1 \end{pmatrix} \tag{6.6}$$

Correction of sensor tilt

The orientation of the sensor surface can be obtained from z-scans at different positions on the sensor. A fit to the resulting signal or charge profile can be used to obtain the respective height of the surface for each (x,y) coordinates. The Hesse normal form can be used to perform a fit to the obtained pairs of (x,y,z)-values:

$$\vec{r} \cdot \vec{n}_0 - d = 0 \tag{6.7}$$

The vector $\vec{r}$ denotes any point on the plane, $\vec{n}_0$ is the normal vector to the plane and d is the distance of the plane to the origin. The normal vector $\vec{n}_0 = (n_{0,x}, n_{0,y}, n_{0,z})$ is normalized, $|\vec{n}_0| = 1$. Therefore the only free fit parameters are $n_{0,x}$, $n_{0,y}$ and d. The angles of the x- and y-axes to the sensor-plane measured in the x-z- and y-z-planes respectively are calculated by

$$\alpha = -\arctan(n_{0,x}/n_{0,z})$$
$$\beta = -\arctan(n_{0,y}/n_{0,z}).$$

The angles α and β are defined such that a positive slope of the sensor surface in the x-z- and y-z-planes results in a positive value. It is convenient to use the Hesse normal form if the normal vector and the distance d are used for further calculations. The sensor plane can equally be fitted with

$$z = z_0 + a_x x + a_y y. \tag{6.8}$$

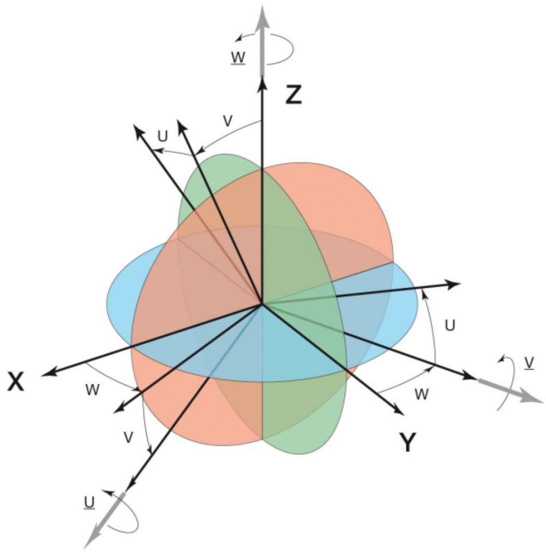

Figure 6.24. – Coordinate axes and angles. [131]

In this case the angles are calculated by $\alpha = \arctan(a_x)$ and $\beta = \arctan(a_y)$. The hexapod carriage is tilted by angles u and v around the axes x and y counter-clockwise when the respective axis is facing towards the observer. Therefore the hexapod carriage has to be moved by angles

$$u = -\beta \tag{6.9}$$
$$v = \alpha \tag{6.10}$$

to position the sensor perpendicular to the z-axis of the hexapod coordinate system.
An example of this is shown in the following. Fig. 6.25 (a) shows the measured drift velocity as a function of the x-y-position. For this measurement the sensor (FZ200P_05_DiodeL_9) was kept at 100 V. The laser was pulsed with 100 Hz. The z-position of the hexapod (here $z = -0.13$ mm) was chosen, such that the focal point of the beam is roughly in the middle of the detector. The drift velocity stated here is simply the value of the transient current signal 500 ps after the start of the signal pulse, corrected for the baseline offset and normalized with a TPA-reference signal. Since the drift velocity depends strongly on the position inside the sensor, in contrast to the collected charge for example, it is used as an indicator of the depth of the focal point inside the sensor. The measurement shows that the drift velocity varies strongly with a change of the sensor position in x and y, which shows that the sensor is tilted with respect to the coordinate axis of the hexapod. One can already see from the drift velocity map, that the tilt is much more pronounced along the y-axis than along the x-axis. To measure the position of the sensor, four scans in z direction at different positions in x and y were performed. In practice, it is useful to perform a larger number of z-scans to detect outliers and eventually systematic shifts due to a non-planar surface. One such scan was shown in fig. 6.21. The equation used for the fit is 6.1. For irradiated detectors this equation does not describe the asymmetric charge collection profile sufficiently. In this case, for alignment, it is only necessary to choose a point along the z-axis by which the position of the sensor can be defined unambigiously, e.g. the maximum or 50% of the rising edge of the charge collection or velocity profile. In this case, the sensor surface, given by the rising edge of the charge profile, is plotted in 6.25 (b) as a function of the x and y values. Note that

the axis of the plot show the position of the hexapod, not the position of the beam on the sensor. The point with the highest value in z is a result of a measurement on the lowest point on the sensor. Nevertheless, since all three axis are inverted, the fitted plane is a good representation of the actual sensor orientation in space. The fit was performed with eq. 6.7 (equivalently eq. 6.8) and the values of the angles u and v, by which the hexapod carriage needs to be tilted, were calculated as outlined above. In this case angles to the x- and y-axis of $\alpha = -0.1754°$ and $\beta = 1.1278°$ were calculated. Therefore the carriage had to be tilted by $u = -1.1278°$ and $v = -0.1745°$. Fig. 6.26 (a) shows the

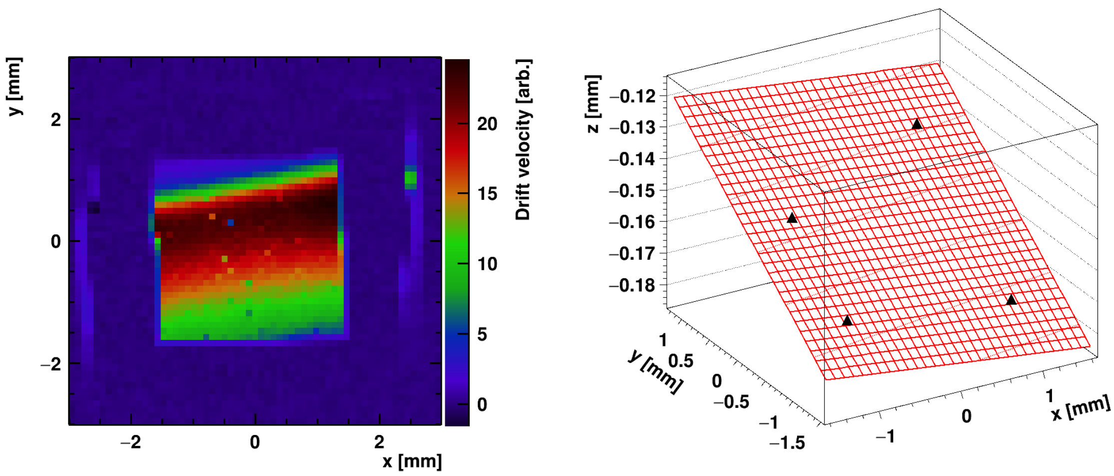

(a) Drift-velocity map

(b) Fitted sensor plane

Figure 6.25. – Sensor before correcting for tilt. (a) Drift velocity at a given position in z as a function of x and y. (b) Black triangles show the z-position of the sensor surfaces as a function of x and y. The plane is a fit with eq. 6.7

same measurement as fig. 6.25 after moving the hexapod carriage by the angles stated above. One can see that the value of the drift velocity is constant, irrespective of the position on the sensor in x and y. This indicates that the sensor surface is now perpendicular to the z-axis of the hexapod. A repetition of the method described above to obtain the orientation of the sensor surface yielded values of $\alpha = -0.0788°$ and $\beta = -0.0321°$. A misalignment of 0.1° results in a height difference of only 5 μm over a distance of 3 mm and is thus acceptable for most cases.
In addition to correcting the sensor orientation with respect to a fixed coordinate system, it is possible to redefine the position and orientation of the hexapod coordinate system. The two most likely use-cases are: (1) It is possible to rotate the coordinate system around the z-axis to change the direction, in which spatial scans are performed. Fig. 6.26 (b) shows the same measurement as (a) but after a rotation of the work coordinate system by −20°. Since the coordinate axes are rotated, the sensor appears to be rotated by +20°. For structured sensors like strip or pixel detectors it is possible to measure along certain axes, if the sensor is not mounted parallel to the default coordinate axes. (2) By default, rotations are performed about the origin of the hexapod coordinate system. An offset between the physical position of the sensor and the coordinate system leads to a high spatial shift, if rotations are performed. E.g. comparing figures 6.25 (a) and 6.26 (a) one observes a large shift in y-coordinates of about 2 mm. This is fixed by redefining the work and tool coordinate systems, such

that their origins coincide with the position at which the DUT is mounted.
It is evident that a tilt correction has to be carried out for spatial scans perpendicular to the beam axis.

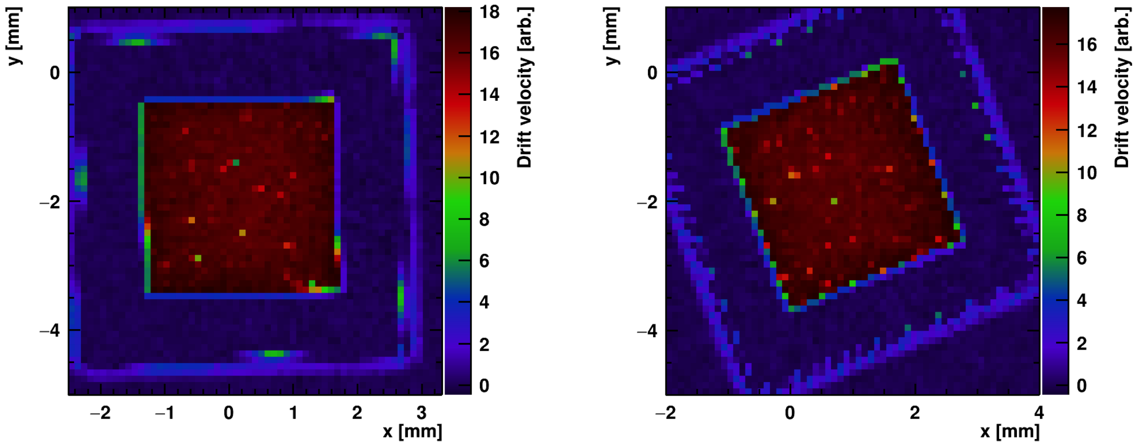

(a) Drift-velocity map after tilt correction (b) Rotation of the coordinate system by −20°

Figure 6.26. – Drift velocity at a given position in z as a function of x and y after tilt correction. The measurement was repeated after rotating the hexapod coordinate system by −20° around the z-axis.

But also for scans along the beam axis features were observed that could not be explained at first, but could be related to a misalignment of the DUT, after some investigation. Therefore, the tilt correction procedure outlined above is now carried out before every measurement after mounting a new device.

6.2.7. Spatial resolution: Knife edge scan

To measure the spatial resolution at the beam focal point a knife edge scan can be carried out. This technique is widely used to measure the intensity profile of laser beams. The intensity of the beam, integrated over the whole transversal profile, is measured while a barrier (knife) is moved across the beam. From this measurement the beam profile can be inferred. Repeating the knife edge scan at different positions along the beam axis leads to a precise measurement of the focal point parameters. In our case the metallization on top of a silicon sensor is used as a knife, as shown in the schematic drawing in 6.27. While this method is convenient, because no manipulation on the setup is necessary, some uncertainty can result from the unknown thickness and edge quality of the metallization. The data presented in the following was taken with the sensor FZ200P_05_DiodeL_9 at a constant bias voltage of 200 V, maximum laser power, a pulse frequency of 100 Hz and 128 averages on the oscilloscope. The signal was read out with a bias-T without the use of an amplifier. The measurement was performed after a 500 mm lens was installed before the objective to investigate if the lens would affect the beam parameters. Fig. 6.27 shows a typical result of a knife edge scan. The charge is shown on a logarithmic scale as a function of the hexapod positions in x and z. The figure is a result of scanning the metal-silicon transition across the focal point of the beam at different positions along the beam axis, as depicted in the schematic drawing. The step size for this measurement was 2 μm in z-direction and 0.5 μm in x-direction. A small step size in x-direction is necessary, to ensure that the

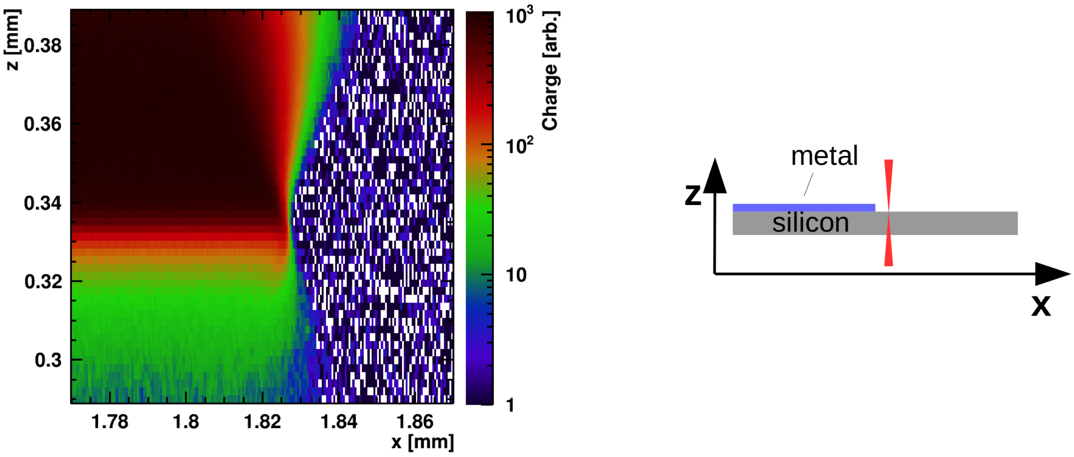

Figure 6.27. – Knife edge scan on the metal-silicon transition on the top side of a pad diode. The metal edge on top of the sensor is moved across the beam in x direction for various heights along the beam axis (z).

beam profile is sampled several times even when the metal edge is in focus. In the right half of the plot in figure 6.27 ($x > 1.83$ mm) the metallization is blocking the light from entering the silicon. In the left top part of the figure ($z > 0.33$ mm) the focal point of the beam is inside the silicon and signal is generated. In the left bottom part of the figure the focal point is above the silicon sensor. It should be noted that some charge is generated as a result of the large Rayleigh length, although at the lowest point of the hexapod, the focal point is about 40 μm above the sensor. The metal-silicon transition in x-direction is best resolved when it is at the height of the focal point. The cone shaped feature in the top half of the figure is a result of the opening angle of the beam and is used to measure the beam width as a function of z. The charge profile in x-direction is fitted with eq. 6.11 for every value of z. The fit parameters are a constant C, an offset in the x-coordinate and the beam radius $w(z)$. The beam irradiance has a Gaussian profile in x-direction, with $w = 2\sigma$. The factor of 2 in the numerator of the error-function is a result of the square dependence of the charge generation on the beam irradiance.

$$f(x) = \frac{C}{w^2(z)} \left[1 + \text{erf} \left(\frac{2(x - x_{off})}{w(z)} \right) \right] \tag{6.11}$$

As an example, two fits are shown in fig. 6.28. The data corresponds to z-positions some distance away from the focal point (left, $z = 0.311$ μm) and directly at the focal point (right, $z = 0.331$ μm). Away from the focal point the maximum charge value is reduced, because part of the beam is outside of the sensor in z-direction, and the slope of the error-function is reduced, due to the out-of-focus beam. The measurement at the focal point shows a higher value of generated charge when the beam is inside the sensor and a steeper onset of the signal when the beam is moved across the metal edge. Noticeable is the narrow peak directly at the transition of zero to maximum charge, which is not described by the fit-function. This feature is only observed when the beam is focused on the metal edge and is therefore believed to be originating from refraction. A refraction pattern in the reflected light can be observed in the infrared camera image and it is possible that the resulting intensity pattern leads to higher charge generation in the sensor as a result of the non-linear absorption process. The obtained values for w are shown as a function of z in fig. 6.29. The horizontal axis (z) shows the coordinate of the hexapod and is not corrected for refraction in silicon to not bias the fit result. The shown error

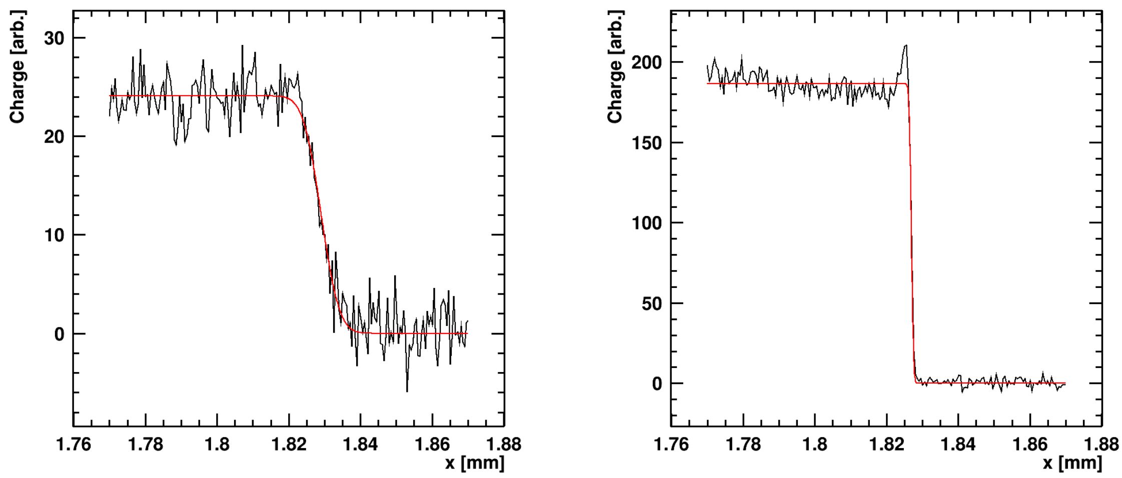

(a) Out-of-focus: $z = 0.311$ mm (b) In-focus: $z = 0.331$ mm

Figure 6.28. – Charge profile for knife edge scans for two different positions along the beam axis. Fit to data with eq. 6.11. Microscope objective NA=0.5

bars are resulting from the uncertainty from the fit to the charge profile in x-direction, without any additional systematic uncertainty. Especially since the higher charge collection due to refraction at the focus is not taken into account in the fit, the stated uncertainties can only be approximate. Larger uncertainties at low values of z are a result of the lower signal to noise ratio, since the beam is mostly outside of the detector. The data is fitted with the function (eq. 5.5, p. 42)

$$w(z') = w_0\sqrt{1 + \left(\frac{z'}{z_0}\right)^2}, \tag{6.12}$$

in which z' is replaced by (eq. 5.42, p. 55)

$$z' = (z - z_{off})\sqrt{\frac{z_0\,\pi n^3}{z_0\pi n - \lambda n^2 + \lambda}}. \tag{6.13}$$

In these equations z is the position of the hexapod carriage, z_{off} is the position of the focal point along the z-axis and n and λ are the refractive index and the vacuum wavelength. In this way unbiased values for the Rayleigh length z_0 and the beam waist radius w_0 in silicon can be obtained, which are independent of any prior assumptions about the beam parameters. These values are also stated in the figure. In this case, values for the Rayleigh length in silicon of $z_0 = 14 \pm 1$ μm and the beam radius at the waist $w_0 = 1.5 \pm 0.1$ μm are obtained. The fit is restricted to a small region around the focal point, where an acceptable fit can be obtained. The values of $w(z)$ further away from the focal point follow the linear equation

$$w(z) = z \cdot \tan\theta = z \cdot \frac{w_0}{z_0} = z \cdot \frac{\lambda}{w_0\pi n} \tag{6.14}$$

with the theoretically optimal values of w_0 and z_0, given by the respective numerical aperture of the microscope objective. Therefore, the fitted value of z_0 can depend also on the chosen fit range. On the other hand, the value for w_0 is given by the minimum of the graph, which results in a more robust measurement. The optimal values are $w_0 = 1$ μm and $z_0 = 6.9$ μm for $NA = 0.5$ in silicon. Some discrepancy between the measured and optimal values is expected.

To overcome the limited accuracy of this method, due to refraction on the metal edge, the DUT could

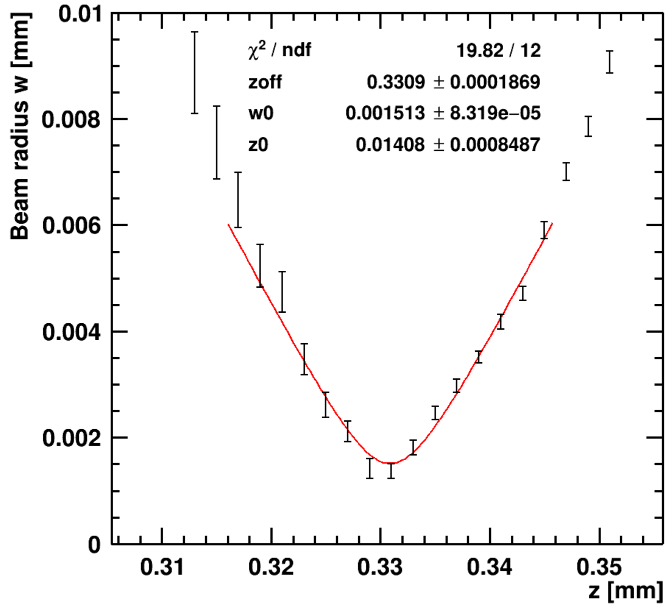

Figure 6.29. – Beam radius w as a function of the hexapod position along the beam-axis. The effect of refraction is included in the fit (eqs. 6.12 and 6.13). Microscope objective NA=0.5.

be replaced by a detector, which is sensitive to 1550 nm light by SPA (e.g. InGaAs). Refraction would still occur, but not lead to any change in the amount of generated charge, due to the linear absorption process.

6.3. Measurements

6.3.1. Reflection of light

Reflections of the laser beam back into the active area can cause a signal, although the focal point would be expected to be outside of the sample. This can complicate the analysis and interpretation of the obtained measurement results. Reflections of light are also present in conventional (SPA) TCT measurements. In fact they are much more likely because reflected light, that can be absorbed via SPA will always contribute to the overall signal, independent of the focal point position. The reflected TPA-beam on the other hand needs to be focused back into the active area. A divergent reflected beam or diffuse scattering will not create additional charge carriers. The difference is that in SPA-TCT it is not attempted to resolve features of the DUT in the direction of the beam axis. For this reason, reflected light, although it contributes to the overall signal, does in most cases not negatively affect the resolution of the measurement. The amount of reflected light and whether or not this needs to be taken into account in the measurement analysis in TPA-TCT depends largely on the respective measurement setup and geometry. In general, three common configurations can be distuinghished:

- **Reflections on metal surfaces** lead to very clear mirror images of the DUT. If the focal point of the beam is located directly at the metal surface, the ellipsoidal part of the beam, where the intensity is high enough to create charge carriers, can be reflected back onto itself. This can lead to a localized volume with very high intensity, such that, due to the square dependence of the generated charge on the light intensity, more charge is created, than if the focal point would be located fully inside the sensor.
- **Reflections on the silicon-air transition**, caused by the abrupt change of the refractive index, lead to a mirror image of the DUT with much decreased signal amplitude.
- **Sensors with a low resistivity support wafer** on the backside, usually do not show a reflection image because the transition of the refractive index is too gradual. On the other hand, deposited charge in this non-active volume can still diffuse into the active region and influence the recorded signal.

Reflections on metal surfaces are briefly discussed in sec. 6.3.3 and 6.3.4. Fig. 6.30 shows the effect of a reflection on the silicon-air transition on the backside of the sensor. The DUT is a 285 μm thick, unirradiated FZ sensor without any support wafer or backside metallization. The DUT was connected to a Cividec current amplifier C2-131 and the measurement was performed at room temperature. The light is injected from the top of the device. Fig. 6.30 (a) shows the collected charge as a function of the z-coordinate for different bias voltages. At low bias voltages (5 to 10 V) two distinct peaks of different amplitude can be observed on opposite ends of the measurement range. At higher bias voltage, the two peaks merge. The feature with the lower amplitude (-5.05 mm $< z < -4.8$ mm) is the mirror image of the actual active volume. The amplitude is about $\approx 10\%$ of the original signal. As a rough estimate, Fresnel equations can be used to calculate the expected amount of reflected light:

$$R_0 = \left| \frac{n_1 - n_2}{n_1 + n_2} \right|^2 . \tag{6.15}$$

This equation yields a value of 30% of reflected light on a Si-air interface. Since the charge depends quadratically on the light intensity, the amplitude of the charge signal would be expected to be around 10%. It can be expected that further effects, like a distortion of the beam on a non-planar surface, would have to be taken into account for a thorough analysis. Fig. 6.30 (b) shows the drift velocity profile (black) and the signal time over threshold at 50% of the pulse amplitude (red). A clear symmetry around the sensor backside ($z = -5.1$ mm) can be observed in the TOT-profile, which is a strong indication, that the signal observed in the region -5.05 mm $< z < -4.8$ mm is caused by reflection.

6.3.2. Interpad region of an HPK2 LGAD

To demonstrate the strength of the TPA-TCT method in resolving structures on silicon detectors the interpad region of an HPK2 LGAD was measured. Extensive studies on similar devices have been carried out, using conventional TCT techniques [132]. The interpad region of LGADs is of special interest because the reduced fill-factor of LGADs is a major limitation for their application in particle tracking. Ways to mitigate these limitations in novel sensor designs are being investigated. These include AC- coupled LGADs (AC-LGADs) [133, 134, 135] or Inverse-LGADs (I-LGADs) [136, 137]. The structures between neighboring LGAD pads usually include the Junction Termination Extension

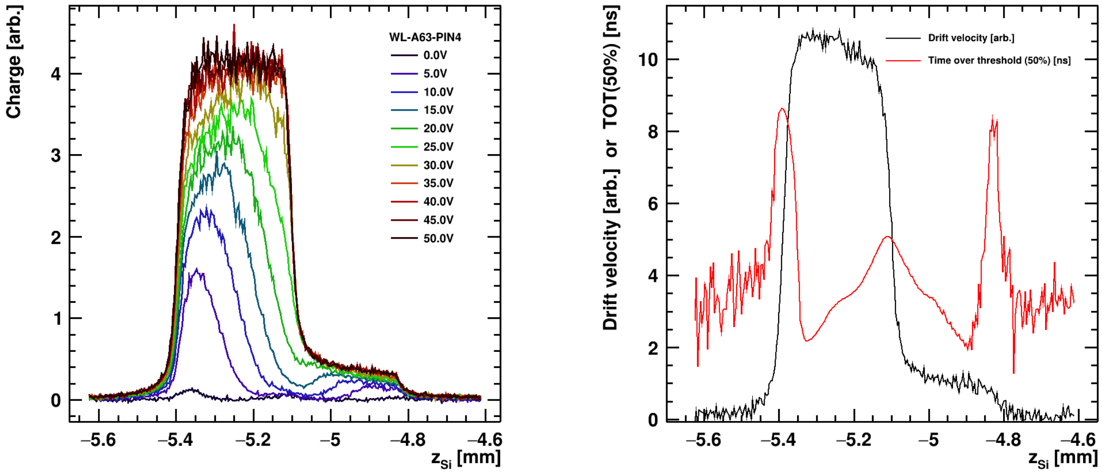

(a) Charge profile (b) Drift velocity and time over threshold

Figure 6.30. – Collected charge, drift velocity and signal time over threshold as a function of the distance along the beam axis. A reflection at the silicon-air interface can be observed.

(JTE) at the boundaries of each pad and a p-stop implant in the middle between pads. A schematic view of the pad and interpad structure of an LGAD is shown in fig. 6.31. The area between active pads forms a no-gain region in which charges are not multiplied, due to the absence of the gain layer. The additional implants (JTE and p-stop) reduce the charge collection efficiency in this region, as part of the generated charge is not amplified. The effect of reduced charge collection in the vicinity

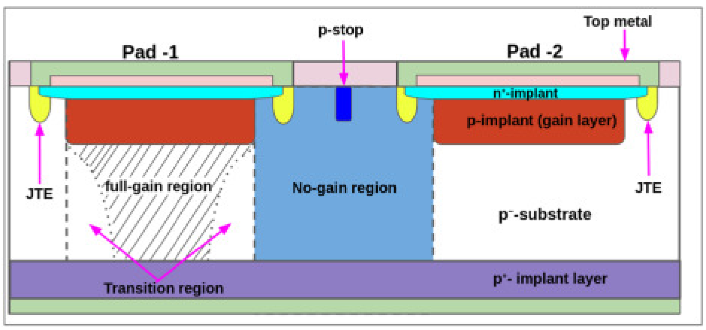

Figure 6.31. – Schematic cross-sectional view of an LGAD, illustrating the gain- and no-gain regions inbetween two neighboring pads. The figure is not to scale. [132]

of the JTE is visible in the simulated distribution of the electric potential and electric field, shown in fig. 6.32 [138]. Both figures show the same geometrical arrangement of the multiplication pad extending to the left and the JTE located at around 60 to 70 μm. Charges drifting to the JTE are contributing to the signal but are not undergoing charge multiplication. Therefore, in the volume from which charges drift to the JTE, indicated by the electric field lines, the measured signal will be significantly reduced, in comparison to the multiplication region. It is evident from the figure that this region extends below the multiplication implant, which significantly reduces the efficiency in the interpad region of the LGAD. This effect is stronger at lower bias voltages and unirradiated sensors. After irradiation the gain is reduced and the effective doping concentration in the bulk is increased, so that the measured width of the region of reduced efficiency is closer to the nominal width of the interpad region [138]. Measurements of the charge collection efficiency in the region between LGAD pads are usually carried out with injecting laser light from the top of the device and scanning across two neighboring pads. Depending on the absorption length of the laser used and the resulting different position of the generated carriers, the obtained width of the interpad region differs. The sensor tested

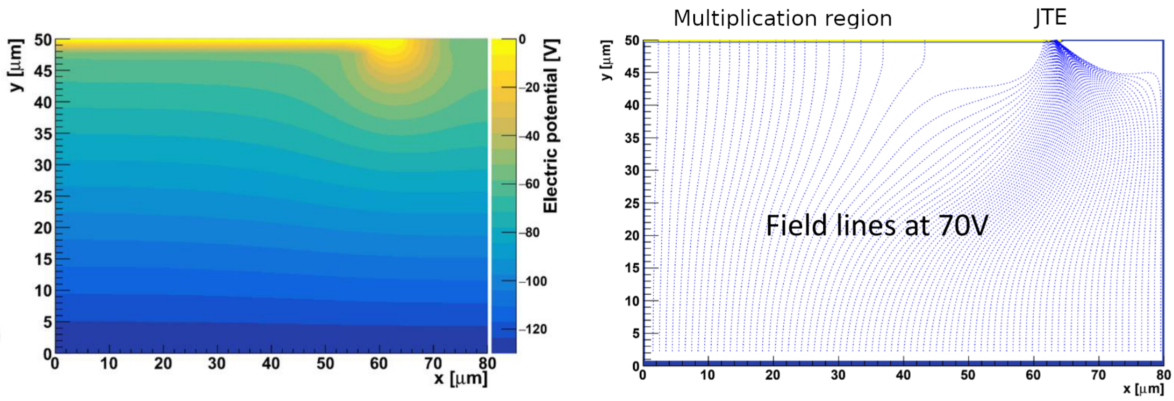

(a) Electric potential at 130 V

(b) Electric field lines at 70 V

Figure 6.32. – Simulation of the electric potential (a) and field (b) in the region between the multiplication region and the JTE. Especially at low bias voltages, the field lines, ending on the JTE, extend below the multiplication region. [138]

here with TPA-TCT is an LGAD with a 5x5 array structure from Hamamatsu production run 2, wafer 28 (HPK2-W28-S1-5x5-LGAD-P14) with the interpad design IP5. The active volume is comprised of 50 μm thick epitaxial p-type silicon. Each pad has an active area of 1.3×1.3 mm and features several openings in the metallization to allow for laser light injection. Microscope images, taken with a Hirox 3D digital microscope[4] can be seen in fig. 6.33 and 6.34. Fig. 6.33 shows a single pad centered in the image, connected with a wire-bond. The boundaries and non-metallized regions in between pads are visible. Each pad features three openings in the metallization. Two are located next to the respective neighboring pads to enable laser measurements across the interpad region and one opening is located near the center of the pad, at the height of the wire-bond. Fig. 6.34 (a) shows a close-up image of the openings across the interpad region. Different implant structures are possible to see as vertical lines in different colors. The distance of the far edge of one opening to the center in between openings is approximately 150 μm. Distance measurements were added to the image manually, using the microscope software. Fig. 6.34 (b) shows a further close-up image with distance measurements indicating the separation between the p-stop implant (purple, centered) and the JTE (green, 23.5 μm to the left and right of the p-stop). IV and CV measurements were taken at the IV/CV probe station before mounting the sensor on a PCB for TCT-measurements. Results of the measurements are shown in fig. A.12 (appendix, p. 125). Both, IV and CV measurements, show a good uniformity in the electrical behavior of the different pads. The gain layer depletion voltage, extracted from the CV measurement, is about 55 V.
For the TPA-TCT measurements, which are shown in the following, only the pad under test is biased

[4]EP-DT Quality Assurance and Reliability Testing Lab, https://qartlab.web.cern.ch/

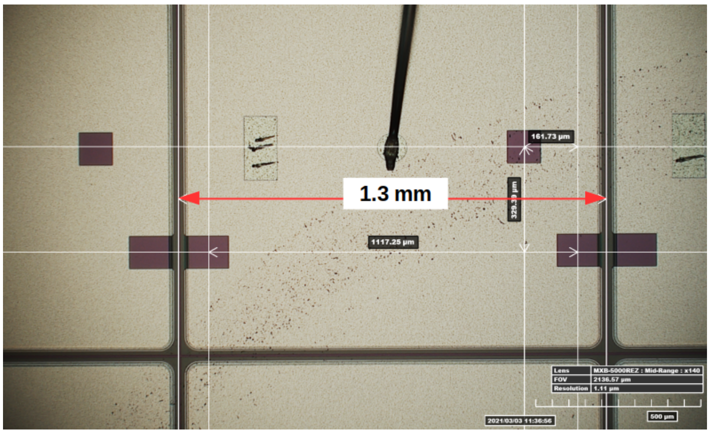

Figure 6.33. – Microscope image of one pad of a HPK2 5x5 LGAD structure. Neighboring pads can be seen in the image. The pad is connected with a single wire bond (center). Each pad has three openings for TCT measurements.

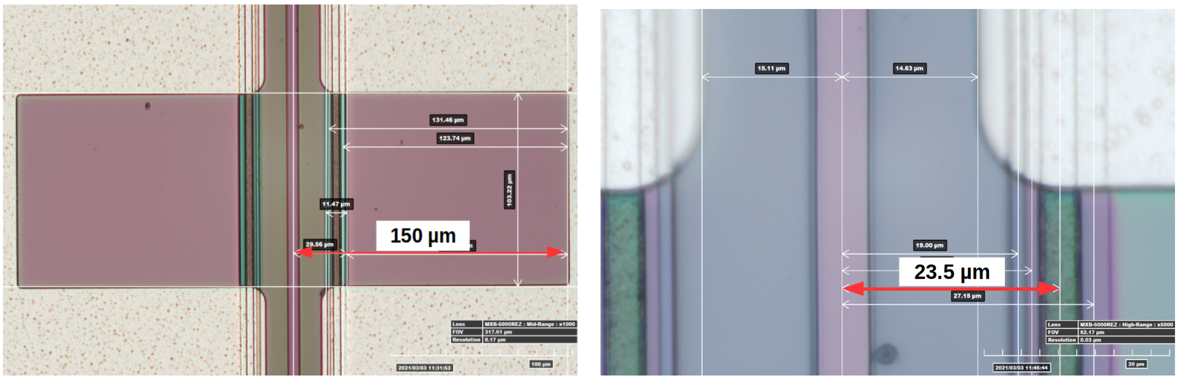

Figure 6.34. – Microscope images with different magnification of the interpad region of an HPK2 5x5 LGAD. JTE and p-stop structures can be identified.

and connected to the read-out. The neighboring pads are left floating. It is therefore possible that charges which are injected in the area of a neighboring pad diffuse into the active volume of the connected pad and are collected there. These contributions can be identified by a very low signal amplitude and large collection times. After mounting the device on the sample holder the initial tilt was measured by performing multiple z-scans in the three openings of the connected pad. As described in sec. 6.2.6, by finding the surface of the sensor at different locations on the device it is possible to calculate the angles to the respective coordinate axes. The plane fit to the obtained points is shown in fig. 6.35 (a). Fig. 6.35 (b) shows the drift velocity in arbitrary units as a function of x and y at the location of one of the openings at the edge of the pad after the tilt of the sensor was corrected. Along z, the focal point was centered in the detector. This measurement was also carried out at the location of the opening on the other side of the pad. The two openings are separated by about 1.1 mm but resulted in the same values for the drift velocity. Therefore, over a scan range of 100 to 200 μm the sensor can be assumed to be flat. The variation of the drift velocity, visible in the figure, can therefore be attributed to a real change in the electric field towards the separation between pads. To correlate the TPA-TCT measurements with the distance measurements in the microscope images, the edge of the opening towards the pad was used. This edge is set to a value of $x = 0$ mm, as can be seen in fig. 6.35 (b). Using this value it is possible to calculate the expected positions of the JTE and p-stop from the microscope distance measurements.

The collected charge as a function of z and x for bias voltages of 40 and 60 V is shown in fig. 6.36.

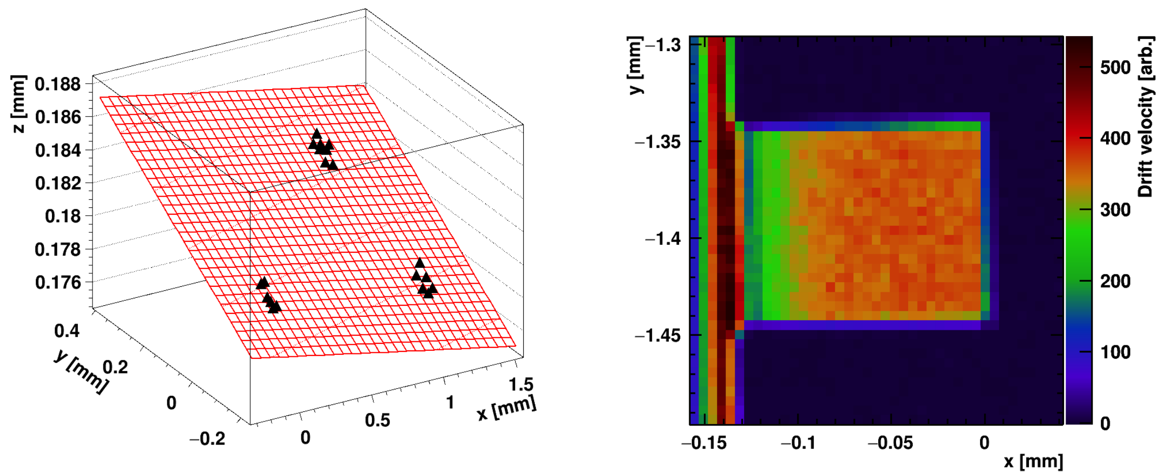

(a) Plane fit to data points at three openings before tilt correction

(b) Single opening after tilt correction

Figure 6.35. – Tilt correction of an HPK2 LGAD. To increase the lever the position of the sensor surface is measured at all three metallization openings. Correct alignment was verified by comparing x-y-scans at all openings (one is shown).

The z-axis is parallel to the beam axis and the light is injected from the top of the device. The z-axis in the figures is multiplied by factor of -3.75 for illustration: The sensor top is now located at the top of the figure to facilitate comparison with fig. 6.31 and the z-scale is corrected for the effect of refraction, to better show the physical dimensions of the sensor. The scan in x-direction was performed from the region in between pads on the left hand side of the figure to the center of the opening on the right hand side. The measurements at the two bias voltages show the situation before and after depletion of the gain layer of the LGAD. The color-scale (charge) is not the same in the two figures. The two maxima on the left in the no-gain region have about the same amplitude, independent of the bias-voltage. The red vertical lines indicate the positions of the p-stop implant (left) and the JTE (right). The positions have been calculated from the microscope images above. Some charge which is injected on the left side of the p-stop is collected by the biased pad on the right. This asymmetry would not be present if the neighboring pad was also biased. The measurements show that before the gain layer is depleted the LGAD pad is mostly inactive but charge is collected in the region around the JTE. At the exact locations of the JTE and p-stop, very little charge is collected. As soon as the gain layer is depleted, the largest signal comes from the pad region because depletion extends into the bulk and charges are being multiplied in the gain layer. Near the JTE and p-stop less charge is collected, because no amplification is happening in these regions. At low voltages a depletion region develops around the JTE and extends beyond the pad and the p-stop respectively, only when the gain layer is depleted, the full pad turns active. The slope of the charge collection profile along z with an apparent peak at the center of the detector is a result of the limited resolution of top-TPA-TCT, due to the elongated focal point along the beam axis. At the top of the sensor (top side of the figure) the volume in which charge is collected extends further to the left than on the bottom. The resulting region of limited amplification below the pad is labelled 'transition region' between the gain and no-gain regions in fig. 6.31. In

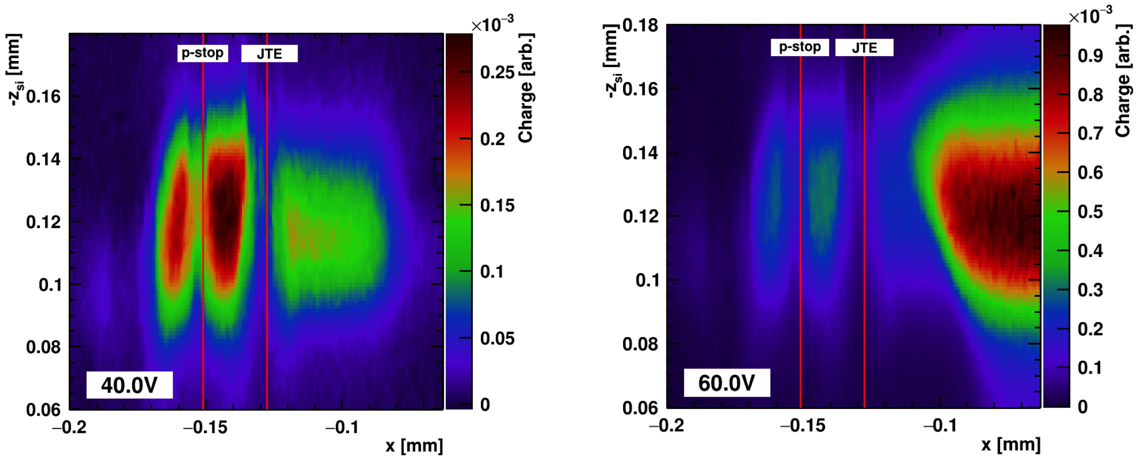

(a) Before gain layer depletion

(b) After gain layer depletion

Figure 6.36. – HPK2 LGAD: Measurement of the collected charge as a function of z and x before (a) and after (b) gain layer depletion. The horizontal axis shows the distance to the silicon-metal edge, located at $x = 0$ mm in fig. 6.35 (b). The red lines are based on the optical distance measurements and indicate the p-stop (left line) and the JTE. The vertical axis is corrected for refraction and inverted, so that the sensor top is located at the top of the figure. Note the different color scales when comparing the two figures.

fig. 6.37 the charge is shown as a function of the x-coordinate for a fixed z-position at different bias voltages. The z-position was chosen, such that the focal point is close to the top surface of the DUT. Again, the positions of the p-stop and JTE, as obtained from the microscope images, are indicated as red lines. The bias voltage was varied from 50 to 60 V. The gain layer depletes at around 55 V. One can see that the amount of collected charge at the position of p-stop and JTE is rather independent of the bias voltage, with the exception of a small increase at the gain layer depletion voltage. The amount of charge under the pad (right hand side of the figure) increases gradually with the bias voltage to the maximum value, such that no sudden increase due to the gain layer depletion is observed. The charge is injected partly in the region of the gain layer and the sensor bulk, but from the usual behavior of LGADs under top injection with red or infrared light, it would be expected that no charge is visible until the gain layer is depleted. This is most likely an effect of charge collection by the JTE, as can be seen in fig. 6.36 (a).

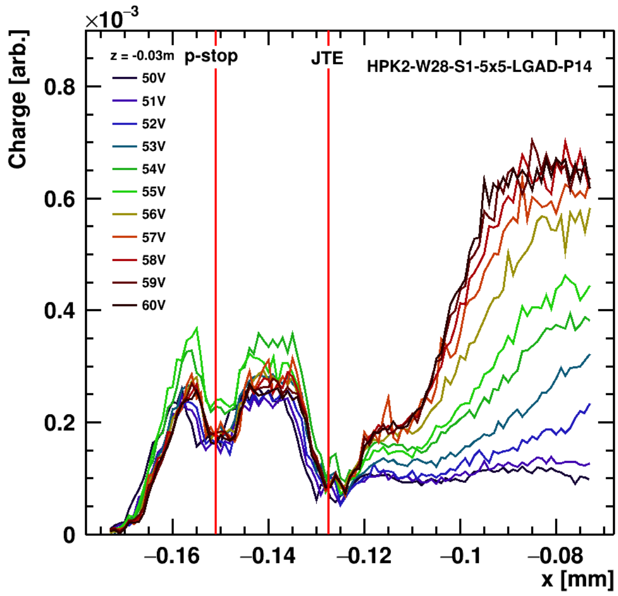

Figure 6.37. – HPK2 LGAD: Charge profile along the x-axis at different bias voltages. The focal point is near the top side of the device. The locations of the p-stop and JTE are indicated by red lines.

6.3.3. Edge-TPA-TCT: HV-CMOS detector

The spatial resolution of TPA-TCT is highest in the direction perpendicular to the beam axis, due to the characteristics of Gaussian beam propagation. Depending on which features in a detector are of interest and what is the aim of the study, it can be beneficial to inject the laser light from the edge of a device and scan perpendicular to the beam axis from top to bottom of the sensor, in analogy to conventional edge-TCT. The main limitation for this method is the large opening angle of the laser beam. For a numerical aperture of $NA = 0.5$ ($NA = 0.14$) the half opening angle is $\theta = 30°$ ($\theta = 8°$). To avoid clipping of the beam on the top or bottom surface of the sensor it is necessary that the scan region is as close as possible to the edge. When the focal point is as far as 50 μm inside the silicon, the beam will start to be clipped when the distance to the top or backside of the sensor is less than about 8 μm.

In a past publication [6], TPA-TCT was tested in an edge-TCT configuration with an HV-CMOS device [139]. Those measurements were carried out at the UPV/EHU laser facility in Bilbao, Spain, and constitute the first tests of edge-TPA-TCT on silicon detectors. The measurements with the CERN setup, presented below, were performed on the same device in a similar configuration and can thus be directly compared. Fig. 6.38 shows a comparison of SPA-TCT with TPA-TCT [6, 140], measured at the UPV/EHU laser facility. The TPA measurement was carried out with a 200 fs-laser at a wavelength of 1300 nm. Shown is the collection time as a function of the spatial coordinates perpendicular to the laser beam. The light was injected from the edge of the device. In both figures, long collection times (red areas) correspond to the undepleted sensor volume, in which charge collection via diffusion into the active region is possible. Located in the figures below the diffusion region is the depleted drift region with short collection times (green area in SPA, blue area in TPA). Only in the TPA measurement (b) the location of the n-implant (light blue) can be identified. The reason for this is the much reduced beam size of the TPA-TCT method compared to SPA-TCT. For the measurements

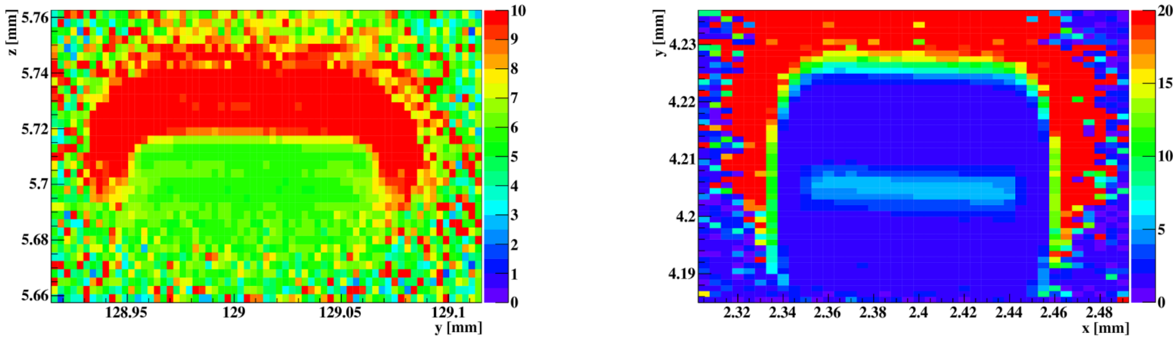

(a) SPA: λ = 1064 nm, σ = 10 μm, 200 ps-pulsed laser (b) TPA: λ = 1300 nm, σ = 1 μm, 200 fs-pulsed laser

Figure 6.38. – HV-CMOS: Comparison of the measured collection time (color scale, time until 98% of charge is collected) as a function of spatial coordinates perpendicular to the beam direction for SPA-TCT (a) and TPA-TCT (b). Long collection times (red) correspond to the undepleted sensor region. The n-implant can only be resolved in the TPA-TCT measurement (light blue). [140]

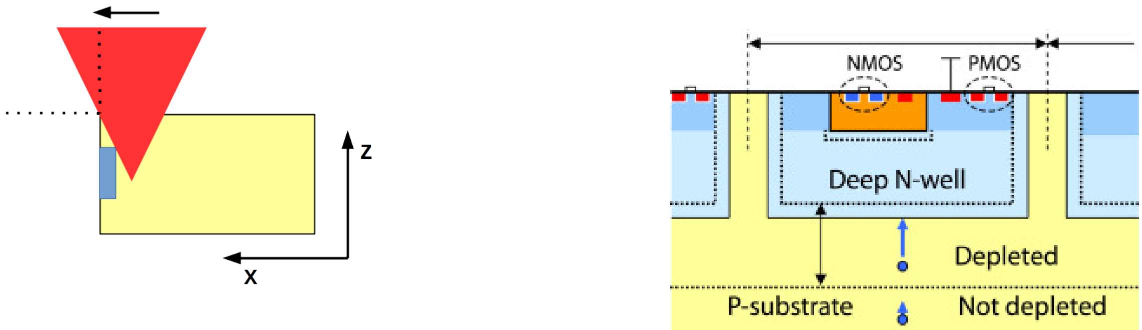

(a) Light injection during e-TPA-TCT measurements (b) Drawing of a CMOS pixel sensor

Figure 6.39. – Drawings of the experimental configuration, indicating the direction of light injection. (a) and a generic CMOS sensor (b). The image is generic. The DUT features a deep n-well test structure for TCT measurements without any MOS implants.

at the CERN TPA-TCT setup the microscope objective with NA = 0.5 was used. An image of the HV-CMOS sensor mounted for edge-TPA-TCT measurements was already shown in fig. 6.7 (b), p. 73. A drawing of the experimental configuration is shown in fig. 6.39 together with a sketch of a standard CMOS device. The active volume has a size of approx. 120×25 μm and is buried 50 μm deep under the surface (in the direction of the beam). This means that, when the focal point is approaching the position of the n-implant, clipping of the beam is expected. Usually, the deep n-well (DNW) acts as collecting electrode and substrate for the MOS transistors. In this case, the DUT features a deep n-well test structure for TCT measurements without any MOS implants. The sensor was biased with 60 V. The spatial scan was performed with a step size of 200 nm in x- and 1 μm in y-direction. Fig. 6.40 shows from left to right: The collection time at 50% of the pulse amplitude (time over threshold), the drift velocity and the charge as a function of x and y. x- and y-axis are identical in all three figures. The x-y-plane is orthogonal to the beam propagation direction. The figure on the left (collection time) can be compared to the measurement at UPV/EHU (fig. 6.38 (b)). Horizontal red lines are drawn across the images to guide the eye. Three signal regions can be identified in the plot of the collection time, which are indicated with a cross respectively: (1) The drift region (red cross) is the fully depleted volume in which the signals are fastest and thus, the collection time is the lowest. The drift region extends from about $x = 0.036$ mm to $x = 0.020$ mm. (2) Slightly slower signals can be identified in a narrow region from $x = 0.036$ mm to $x = 0.041$ mm. This area can be identified with the n-implant (black cross). (3) If charge carriers are deposited beyond the depleted region, they can diffuse into the active volume and be collected. The signal amplitude is much reduced and pulses are very long, due to this process (green cross). The signals corresponding to the positions of light injection in the respective regions are shown in fig. 6.41 (a). Correct interpretation of the drift velocity and charge plots in fig. 6.40 is difficult, because the value of the respective measurement depends on the pulse amplitude. It can be assumed that near the n-implant some fraction of the beam is not entering the sensor, because the opening angle of the beam is too large for the given depth of the scan region. E.g. the gradient in the charge plot that is observed in the drift region is most likely caused by the fact that less light arrives in the sensor instead of a reduced collection efficiency of the DUT. It is likely that the same effect causes the drift velocity to peak apparently on the rear side of the device instead of near the n-implant, where it is expected. On the other hand, the drift velocity shows two sharp transitions from the n-implant to the drift region and from the drift region to the diffusion region. It can be seen that the drift velocity has higher values on the edges of the n-implant, which is a sign that the transition at $x = 0.036$ mm (second red line from top) is physical and not an effect of beam clipping. The integration time for the charge collection plot is 25 ns and therefore a significant amount of charge is seen in the diffusion region, despite the long pulses. The amount that is collected decreases the further away the light is injected from the drift region, which is expected. Fig. 6.41 (b)

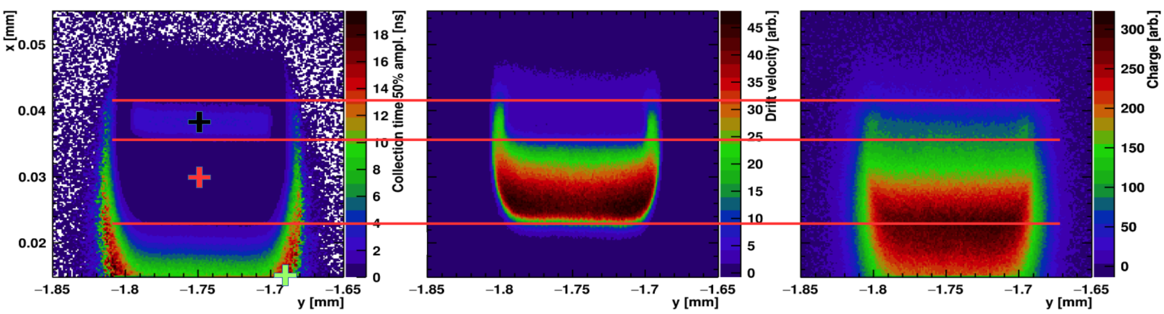

Figure 6.40. – From left to right: Transient pulse width at 50% of the amplitude, drift velocity and collected charge of an HV-CMOS sensor measured with edge-TPA-TCT. x- and y-axis are identical across the three figures. Red lines are drawn to guide the eye. Three signal regions (compare fig. 6.41 (a)) are indicated by three colored crosses in the left figure. Measurements at 60 V bias voltage.

shows a comparison of the charge and collection time profile (here 10% of the pulse amplitude). It is not entirely clear from these measurements where the physical end (top side of the sensor) is located. It can be argued (see also [6]) that light is reflected at the top side silicon/air transition, so that the charge that is observed for $x > 0.038$ mm is a result of this reflection. Supporting arguments are that there is no reason, why the collection times should decrease again, if the beam is further moved outside of the sensor and the fact that the waveforms on the left and right of the n-implant are identical in shape, when normalized to the same amplitude.

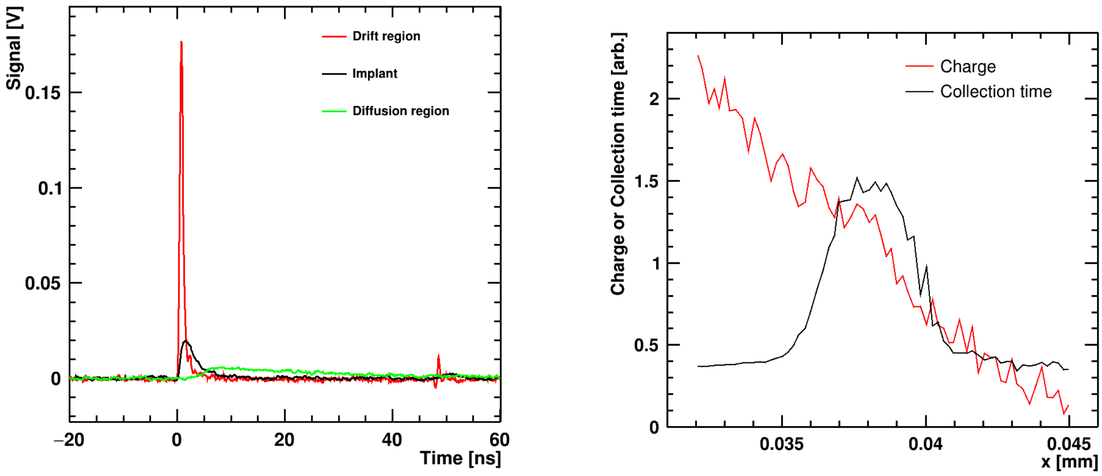

(a) (b)

Figure 6.41. – (a) Transient current signals in three different signal regions. (b) Comparison of the collection time and charge collection profiles at the position of the n-implant.

6.3.4. Backside TPA-TCT: Strip detector

Pad detectors have a constant weighting field but can be difficult to investigate with (SPA) e-TCT measurements because the beam generates charge carriers all along the width of the sensor, so that inhomogeneities at the sensor edges have to be considered. Strip detectors with a single connected read-out strip can be used to overcome this limitation. In this case the light is injected perpendicular to the strip orientation. In this configuration, the weighting field appears similar to that of a pad diode and effects at the edge of the sensor can be avoided. On the other hand, the drift of the charge carriers beneath the neighboring strips influence the measurement and lead to an overestimated charge collection at the sensor backside [141]. It was proposed to investigate the charge collection in strip detectors with injecting the laser light parallel to the strip orientation. This method still has the limit, that the measurement resolution is limited by the beam alignment and divergence of the beam. TPA-TCT provides a way to unambiguously measure the collected charge in a strip detector and investigate charge sharing, as a function of the position of the focal point.
Testing a strip detector with TPA-TCT, the metallization on top of the strip implants prevented the injection of light from the top. Because of the large opening angle of the laser beam, light was almost always lost on the metallization. For this reason the sensor was mounted up-side-down with the backside of the sensor facing the objective, as can be seen in fig. 6.42. Note that the y- and z-axis indicate the movement of the DUT with a fixed location of the focal-point. Therefore, in the following plots, the top side of the sensor is located at high z-values and the backside at low z-values. The sensor under test is a Micron microstrip detector FZP2328-11 with a thickness of 300 μm and a pitch of 80 μm. The strip metallization has a width of 30 μm. The detector is non-irradiated. High voltage is supplied from the backside, while the bias ring was connected to ground. Only a single strip is read out. The AC-pads of two neighboring strips to each side are as well bonded to ground. Fig. 6.43 (a) shows an image of the experimental setup: The whole sensor PCB is mounted up-side-down to allow light injection from the back. Spacers ensure, that neither the sensor nor the wirebonds can

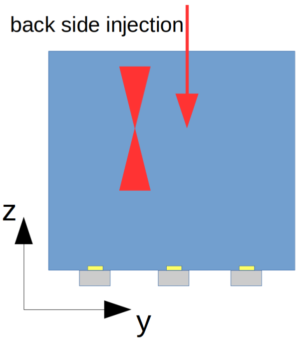

Figure 6.42. – Light injection from the backside of a strip detector.

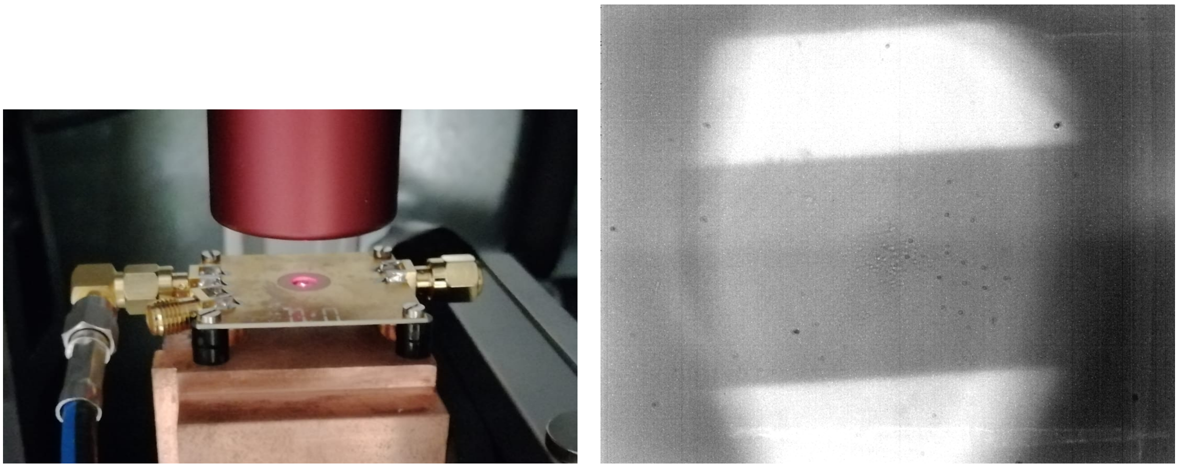

(a) Flipped PCB mounted with spacers

(b) IR image of strip metallization

Figure 6.43. – Photos of the experimental setup for light injection from the backside of a strip detector. The red alignment laser is used to position the sample. In the IR-image the strip metalization can be identified as the bright horizontal bands. The image is obtained through the sensor bulk.

come in contact with the copper cooling block. Effective cooling, in case of an irradiated detector, would not be possible in this configuration. Fig. 6.43 (b) shows an image, taken with the IR-camera with the focus on the top side of the sensor. One can clearly see the strip metallization as bright horizontal bands, which are imaged here through the detector bulk. A measurement was carried out, scanning the DUT in depth (z-direction) and perpendicular to the strip orientation (y-direction), at bias voltages of 25 V and 50 V. The collected charge as a function of position is shown in fig. 6.44 for the two voltages. The backside of the sensor is located approximately at $z = -6.225$ mm. The top side is located at $z = -6.145$ mm. The difference of these values is 80 μm which has to be multiplied by a factor of 3.75 (sec. 5.2.4) to correct for the effect of refraction. Thus a value of 300 μm is obtained for the full sensor thickness. The strip metallization can be clearly identified as the red colored region of highest charge collection. The reason for this high charge collection is the square dependence of the charge on the light intensity: When the light around the focal point is reflected back into the sensor by the metallization, the light intensity increases at this position to a higher value than without reflection. This causes a sharp peak in the charge collection profile. The observed doubling of the collected charge, compared to the situation, when the focal point is fully inside the detector, is

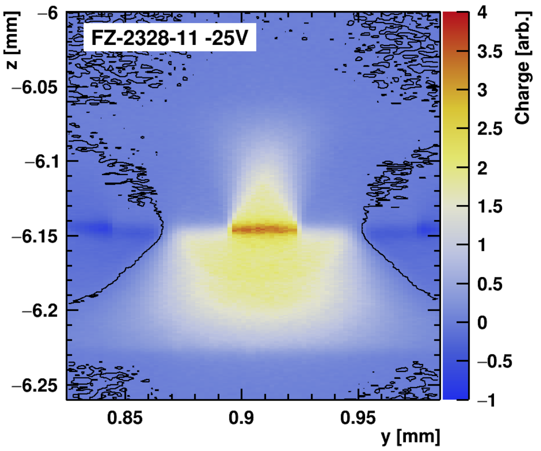

(a) $V_{bias} = -25$ V

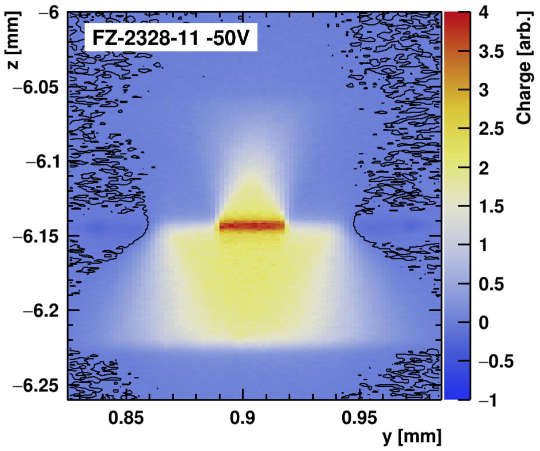

(b) $V_{bias} = -50$ V

Figure 6.44. – Collected charge as a function of position, measured with a strip detector at 25 V (a) and 50 V (b).

expected. When the beam is focused on the metal surface, the irradiance is twice as a high, due to the reflection. But the volume, in which charge is generated is only half as large as the usual charge generation volume, therefore $Q \propto (2I)^2/2 = 2I^2$. A significant amount of light is also apparently collected above the metallization, outside of the detector. These signals originate as well from the reflection on the metallic surface. All strips are equally biased, the charge that is collected in the vicinity of the neighboring strip ($y < 0.86$ mm) is a result of charge sharing by diffusion. Contour lines are drawn for a charge value of 0. Due to the shape of the weighting field, bi-polar signals can occur when the charge is injected near a neighboring strip, but the overall charge should in this case add up to 0. A negative signal, when the charge is injected near a neighboring strip can be caused by capacitive coupling from one strip to the other. In this case also ballistic deficit can have a small contribution. Fig. 6.45 (a) shows the charge profile in z-direction for three different positions in y-direction for a bias voltage of 50 V. The three graphs show again the features explained above: In black, the charge collection with light injection directly beneath the strip implant is shown. The pronounced peak is the result of the increased irradiance due to a reflection of the focal point on the strip metallization. For $z > -6.14$ mm the focal point is in principle already outside of the detector. A back reflection into the active volume causes still some measured charge. The red curve shows the charge profile with light injection between strips. No metallic surface is present in this region, therefore the reflection is less pronounced. Some charge can be observed beyond the boundary of the detector due to the reflection on the silicon-air interface. The decreased collection efficiency towards the rear of the sensor ($z \approx -6.2$ mm) is a consequence of charge sharing with the neighboring pad. If the light is injected under the neighboring strip (green), no charge can be measured. Fig. 6.45 (b) shows the recorded waveforms as a function of z. The signal amplitude is color coded and the time is shown on the horizontal axis. The change of the signal shape can be observed, as the focal point position is changed inside the detector. The symmetry of the figure around a z-value of $z \approx -6.14$ mm is a result of the reflection on the metal surface. The moment of light injection happens at around

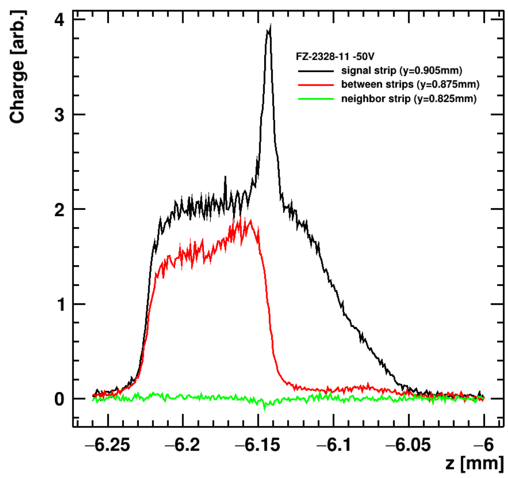

(a) Charge profile

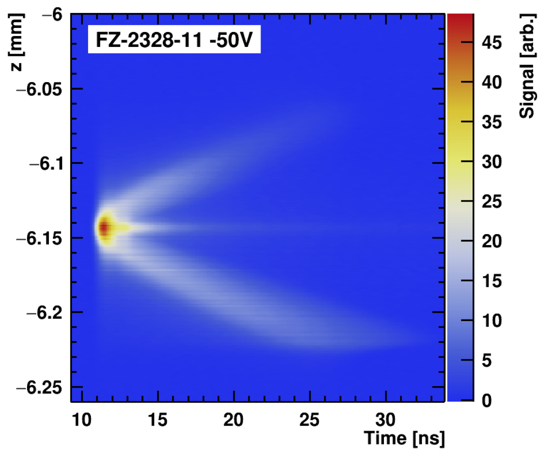

(b) Signal evolution

Figure 6.45. – a) Collected charge as a function of depth inside the sensor (z) for three different y-positions and b) signal evolution in time as a function of z.

$t = 11$ ns. Due to the shape of the weighting field the largest part of the signal is a result of the carrier drift close to the strip implant. For this reason the signal shape is different from the usual superposition of electron and hole drift currents, which is observed in a pad detector. When the focal point is at the backside of the detector (low z-values) the electrons take some time until reaching the front electrode, therefore the the signal peak is delayed, depending on the drift path to the region of high weighting field.

6.3.5. Correction methods for irradiated detectors

Irradiation induced defects in the silicon lattice lead to the possibility of absorption of single photons, even if the photon energy is lower than the band-gap. This leads to a background of single photon absorption (SPA) over the TPA-signal. The SPA-background can be subtracted in two different ways [142].

SPA-subtraction by changing the focal point position

In principle the amount of charge created by SPA does not depend on the position along the beam axis, since it depends linearly on the beam irradiance. But it has to be assumed that the number of absorbed photons for both SPA and TPA is small compared to the overall number of photons available, such that depletion of the beam is negligible. Under this condition the number of created charge carriers from SPA and TPA are independent of each other. Since the recorded signal at a given time after light injection is the sum of the drift currents resulting from the carriers created by SPA and TPA, the TPA-waveform can be obtained if the SPA-waveform is known. For this it is possible to move the focal point of the laser out of the sensor, such that no contribution to the signal by TPA is expected. The signal recorded at this focal point position can be subtracted from all other signals, recorded at

different focal point positions. After subtraction, the signal that is observed when the focal point is inside the active volume of the sensor is assumed to be resulting solely from TPA. It is important to point out that the SPA-background subtraction is done waveform by waveform, such that a full analysis of the pulse shape of the TPA-signal is possible. Important limitations of this method are the assumption of a constant SPA-signal for all focal point positions and the fact that it can be difficult to move the focal point far enough out of the sensor to avoid any contribution from TPA. Depending on the specific device under test, the opening in the top side metallization for laser light injection can be as small as $100 \times 100\ \mu\text{m}^2$. This can make it difficult to move the focal point out of the device, while ensuring that the full beam cross section is still going through the active volume, without clipping the beam on the edges of the metal surface.
At a DUT position z_{spa}, at which the focal point is sufficiently far outside of the active volume, so that the TPA contribution to the signal is negligible, the measured transient current is

$$I(z_{spa}, t) = I_{spa}(t)P(z_{spa}). \tag{6.16}$$

It is assumed now that the signal only varies with z, due to fluctuations of the laser power P from one measurement to the other. $I_{spa}(t)$ is the SPA component of the signal, which is independent of the laser power and the z-position. The laser power is usually recorded as the amplitude of a reference sensor. As such it has the same dimension as the recorded waveform, so that the variable I_{spa}, in principle, is a dimensionless quantity. In addition, in this notation, the SPA signal scales linearly with the recorded laser power P. If instead a non-linear reference sensor (TPA) is used, the square-root of the recorded reference signal has to be used for P. Ideally two reference signals (SPA and TPA) would be recorded at all times to avoid issues from non-optimal correlation, as discussed in sec. 6.2.2.
If the focal point is now moved inside the active volume, TPA contributes to the signal and the recorded waveform is the sum of SPA and TPA contributions

$$I(z, t) = I_{spa}(t)P(z) + I_{tpa}(z, t)P^2(z). \tag{6.17}$$

In contrast to the SPA signal, the TPA contribution I_{tpa} depends on the focal point position. From eqs. 6.16 and 6.17 the TPA contribution can be calculated as

$$I_{tpa}(z, t) = \frac{I(z, t)}{P^2(z)} - \frac{I(z_{spa}, t)}{P(z_{spa})P(z)}. \tag{6.18}$$

Fig. 6.46 shows the SPA and TPA contributions to the charge profile (a) and the signal shape (b). The detector is an irradiated FZ p-type sensor with a thickness of 200 μm, which has been irradiated with neutrons to a fluence of $1.5 \times 10^{15}\ \text{n}_{\text{eq}}/\text{cm}^2$. For the measurements shown the sensor was biased at 600 V. The SPA charge is constant with z by definition, since the same waveform (at the lowest z value for the respective bias voltage) is used for the calculation. When the SPA background is removed the calculated TPA charge reduces to zero when the focal point lies outside the detector, as expected. The SPA subtraction does more than subtracting a constant number from a measurement, as can be seen in the plot of the signal shape (fig. 6.46 (b)). The figure shows the original waveform (SPA+TPA), measured at the backside of the detector ($z = -1.605$ mm). Calculating the SPA and TPA contributions, as outlined above, yields waveforms with different shape. This is expected, since SPA happens everywhere along the beam axis equally. The TPA signal is sensitive to the position of the focal point and therefore the waveforms look differently depending on where the charge is injected. Being able to reconstruct the TPA waveform is important for all quantities that depend on the signal

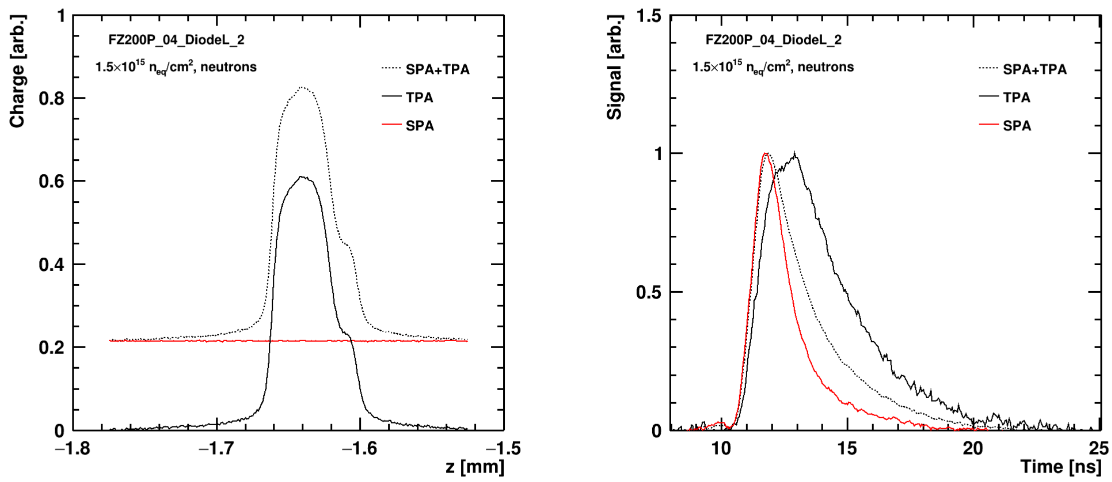

(a) Charge profile (b) Signal

Figure 6.46. – SPA correction by changing the focal point position. (a) Charge profile with SPA and TPA contributions. (b) Signal with SPA and TPA contributions at the sensor backside ($z = -1.605$ mm). All at 600 V.

shape, like the drift velocity, collection time and signal rise time.

SPA-subtraction by changing the laser power

Another method for subtracting the SPA-background from measurements of irradiated devices is to exploit the linear and quadratic dependence of the number of created charge carriers on the laser power for SPA and TPA, respectively. It is assumed that the measured drift current at a given time is the sum of the SPA and TPA-contributions:

$$I(t) = PI_{spa}(t) + P^2 I_{tpa}(t) \tag{6.19}$$

If the signal I is recorded at different laser powers P for otherwise identical experimental conditions (especially the focal point position), eq. 6.19 can be used to obtain the SPA- and TPA waveforms I_{spa} and I_{tpa}. If measurements at two different laser powers (I_1, P_1 and I_2, P_2) are performed, eq. 6.19 forms a system of two equations, which can be solved to obtain

$$I_{spa} = \frac{P_1^2 I_2 - P_2^2 I_1}{P_1 P_2 (P_1 - P_2)} \tag{6.20}$$

$$I_{tpa} = \frac{-P_1 I_2 + P_2 I_1}{P_1 P_2 (P_1 - P_2)}. \tag{6.21}$$

If the measurements are repeated at more than two different laser powers a fit with eq. 6.19 can be used. Again, the above equations assume that P is measured with a linear absorption process (SPA). If the recorded reference signal is obtained by two-photon absorption or second harmonic generation the value for the laser power has to be replaced by $P = \sqrt{P_{tpa}}$.

As shown in sec. 6.2.2 the signals obtained by linear absorption and by a non-linear mechanism (TPA or SHG) are not perfectly correlated. Fluctuations in the pulse temporal shape influence the TPA-signal but not the SPA-signal. For this reason the strict linear and quadratic dependence of SPA and TPA in 6.19 holds only approximately. As discussed above, ideally the power would be measured at the same time independently using single photon absorption for the SPA-contribution, e.g. using the in-built InGaAs-detector of the laser source, and two-photon absorption (or SHG) for the scaling of the TPA-signal. In this case eq. 6.19 is written as

$$I(t) = P_{spa} I_{spa}(t) + P_{tpa} I_{tpa}(t). \tag{6.22}$$

Fig. 6.47 shows a measurement of an irradiated detector at different laser powers. The sensor is

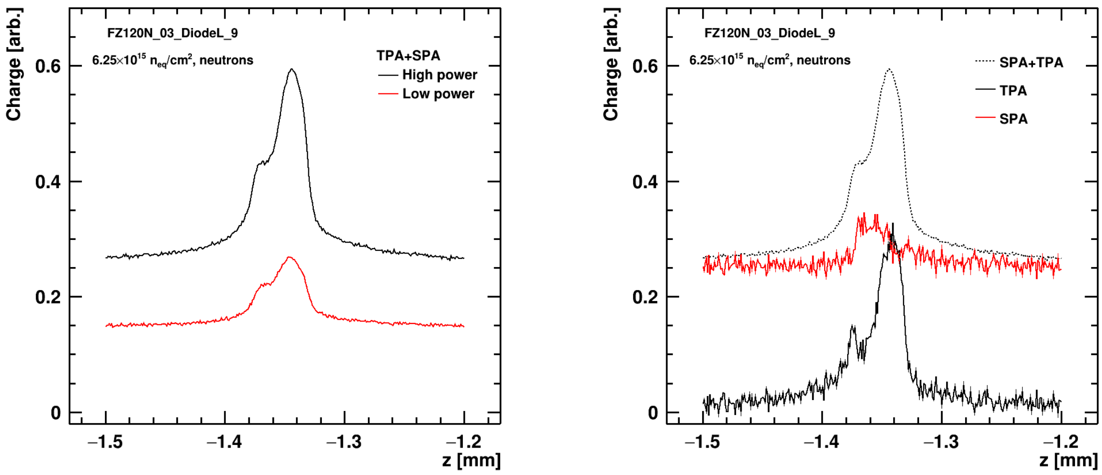

(a) Uncorrected measurements

(b) SPA and TPA contributions

Figure 6.47. – Charge profile of an irradiated detector at two different laser powers. (a) Uncorrected measurements, (b) SPA and TPA contributions to the overall signal.

a Hamamatsu n-type, float-zone sensor with an active thickness of 120 μm. It was irradiated with neutrons to a total fluence of 6.25×10^{15} n_{eq}/cm^2. The sensor was kept at a constant bias voltage of 300 V at a temperature of −20°C. The high and low power measurements correspond to filter angles of 70° and 85°. The sensor was biased with a bias-T and no amplifier was used to avoid saturation at high power. The left figure shows the uncorrected measurements at the two different powers. Both measurements show the signal feature resulting from TPA, when the focal point is inside the detector. When the focal point is outside of the active volume ($z < -1.4$ mm and $z > -1.3$ mm) a constant SPA background is observed. The right figure shows again the uncorrected high power measurement (SPA+TPA), as well as the SPA and TPA contributions, calculated from equations 6.20 and 6.21. As the laser power was recorded using two-photon absorption in a silicon reference diode, the square-root of this value was used for the calculation. As is evident from the figure, the separation of SPA and TPA is not complete, since the location of the sensor can still be identified in what is supposed to be the SPA contribution. In addition the corrected signals show a stronger noise contribution from a limited signal to noise ratio of the reference sensor. It is possible that at the used laser powers an e/h-plasma is created inside the sensor. As discussed in sec. 6.2.1, it was observed that in case of plasma the generated charge does not follow the expected square dependence on the laser power. This is a possible cause of the incomplete SPA correction. The general experience is that the SPA subtraction by changing the focal point position gives more reliable results than the method discussed here. If changing the focal point position is not feasible, e.g. due to the size of the DUT, the method to use different laser powers can be useful.

Pre-pulse feature in irradiated detectors

All measurements with irradiated detectors show a small rise in the signal amplitude before the main signal starts. As an example, fig. 6.48 shows the waveforms of the irradiated samples

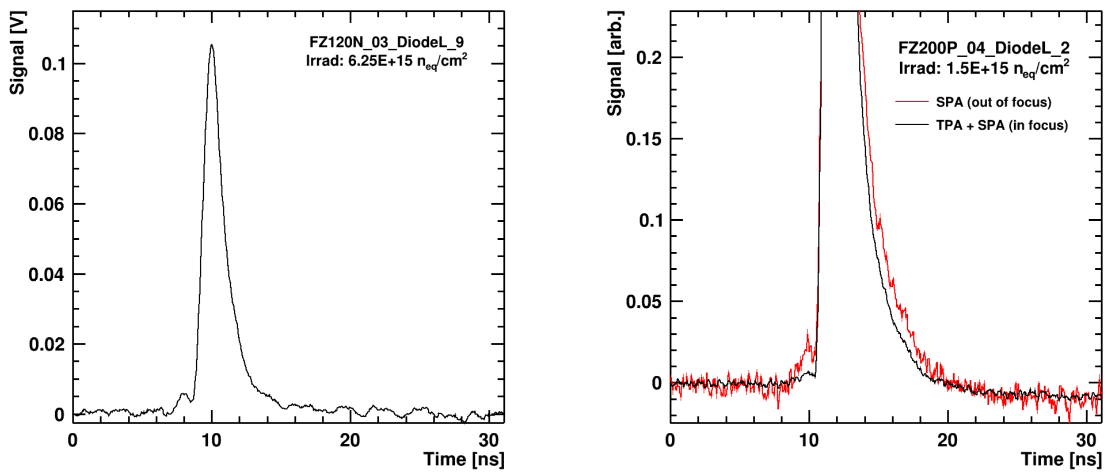

Figure 6.48. – Signal waveforms of irradiated detectors showing a small increase in signal amplitude, before the main pulse arrives.

FZ120N_03_DiodeL_9 and FZ200P_04_DiodeL_2. Before the signal quickly rises to its maximum value, a small increase in the signal, which can be clearly distinguished from the noise, is visible. The signals in fig. 6.48 on the right, measured at different positions of the focal point, are normalized to the same amplitude. The relative increase in magnitude of the feature, when the focal point lies outside the detector, shows that the effect is caused by SPA. The described effect appears in all irradiated detectors and seems to be independent of the used PCBs and amplifiers. The best assumption is that it is caused by the pedestal in the temporal shape of the pulse, described in sec. 6.2.3. The part of the energy, which is stored in the tails of the pulse, would not contribute to the TPA signal but potentially appear in the SPA signal of irradiated detectors. The observed feature in the waveforms has a width of 1 to 2 ns and the pedestal would have to have a comparable width to be the cause of this effect. It could not be confirmed if this is the case at the time of writing.

6.3.6. Microscope objective NA=0.7

For the measurements presented above, an objective with a numerical aperture of $NA = 0.5$ was used. It was found that thin sensors (≈ 50 μm) are only insufficiently resolved along the beam axis, because the volume in which charge is generated is not much smaller than the sensor thickness. For this reason, towards the end of this thesis project, the microscope objective was exchanged against an objective with a higher numerical aperture: M Plan Apo NIR HR 100× with $NA = 0.7$ to achieve a higher resolution [143]. The theoretical beam parameters are $w_0 = 0.705\ \mu$m and $z_0 = 3.501\ \mu$m in silicon (tab. 5.1). A knife-edge scan was performed to measure the beam parameters and compare these against the theoretical values and the ones measured with the $NA = 0.5$ objective. The measurement was carried out with an unirradiated, 50 μm thick diode, Epi50N_07_DiodeL_3, at a bias voltage of −50 V at room temperature. The result of the measurement is shown in fig. 6.49. The beam radius

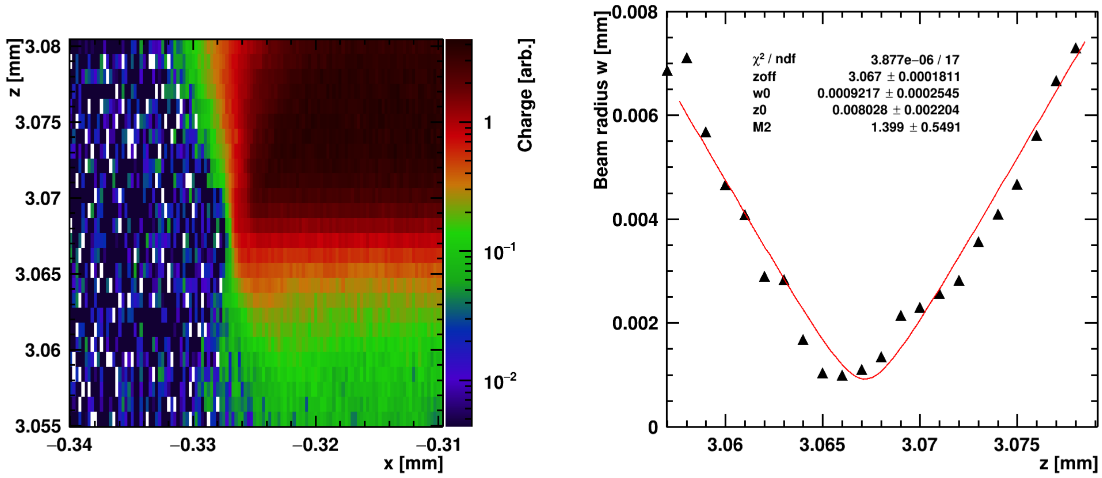

(a) Charge as a function of x and z

(b) Beam radius w as a function of z

Figure 6.49. – Knife edge scan with NA=0.7.

at the waist is $w_0 = 0.9\ \mu$m, which is significantly smaller than the value of 1.5 μm, measured with the different objective with $NA = 0.5$. The Rayleigh length could be reduced from $z_0 = 14\ \mu$m to $z_0 = 8\ \mu$m. The fit quality is not satisfactory, because the measurements show features which are not easy to interpret and are not reflected in the fit-function. The deviation from the model at $z = 3.07$ mm does appear in every knife-edge scan, independent of the DUT or the objective and is most likely related to the effect of refraction on the metal surface, discussed in sec. 6.2.7 (fig. 6.28). Also, the values of the beam radius deviate more and more from the fit-function for z-values farther away from the focal point, therefore the fit results depend on the chosen fit range. The parameter, which is most reliable is the beam waist radius w_0, because it can simply be read from the minimum of the graph. Irrespective of these limitations in the measurement of the spatial resolution, with the new objective the focusing could be very much increased, which will be useful, especially for thin sensors.

For thick devices, with the higher focusing objective ($NA = 0.7$), less charge is measured for a position of the focal point towards the rear side of the sensor, compared with the usual objective ($NA = 0.5$). The effect can clearly be seen in fig. 6.50, which shows a comparison of the collected charge as a function of the position along the beam axis. The DUT is an unirradiated p-type PIN sensor (7859-WL-A63-PIN4) with a thickness of 285 μm. The measurement was carried out at a bias voltage of 200 V at room temperature. Both measurements are normalized to the respective maximum of the collected charge. For a better comparison, the z-axis was multiplied with a factor of 3.75 for

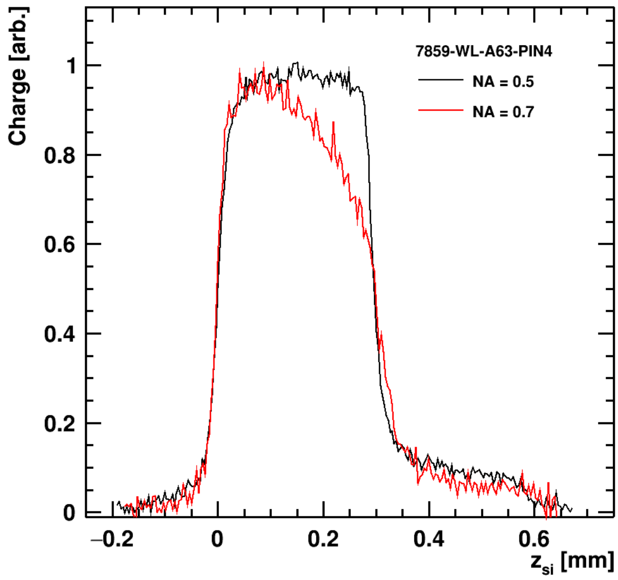

Figure 6.50. – Charge as a function of z, measured with different microscope objectives.

the measurement with $NA = 0.5$ and with 4.12 for the measurement with $NA = 0.7$, to account for the effect of refraction. The effect was reproduced in multiple different measurements. The cause of this is not yet fully understood. The effect is independent of the pulse energy, which makes plasma or non-linear propagation effects unlikely. Also it is not related to a misalignment of the detector. Clipping of the beam can be excluded. By illuminating the device from different directions, it was possible to exclude any effect caused by the DUT. The most plausible explanation is a distortion of the focal point by spherical aberration on the air-si interface. An elongated focal point can be moved partly outside of the DUT when the focal point is moved towards the rear surface. The effect was only observed with the objective with $NA = 0.7$ and is more pronounced at large depths of the focal point inside the DUT. Further investigations are ongoing to find the origin of the reduced charge collection. At the moment, the use of the high focusing objective seems to be limited to sensors with a thickness lower than approximately 100 μm.

7. Summary

Two independent projects were carried out in the course of this thesis work. The highest priority goal was to develop a tabletop TPA-TCT setup, based on the experience made with TPA at UPV/EHU Bilbao. At the start of this thesis project it was clear that TPA could be used to study silicon detectors and that TPA-TCT could complement existing characterization techniques. Easy access to TPA-TCT, on the other hand, would only be possible if a tabletop setup was available. The setup, developed during the course of this thesis, was the first that was developed within the RD50-collaboration and now serves as a prototype for similar projects at other institutes. The full free-space optical setup was planned, purchased and installed in the framework of this thesis. The laser source, which is the heart of the new setup, was custom developed specifically for this application by an external company and was delivered for the first time in July 2019. During the time leading up to the delivery of the laser, the rest of the setup was prepared as best as possible, including optical components, voltage supplies, data acquisition and the motorized positioning stage. In addition, an annealing study of irradiated LGADs was carried out during this time, which is now an additional part of this work. During the first phase of commissioning of the laser, some points for improvement were identified. The laser was eventually send back to the manufacturer to perform an upgrade and received back at CERN in January 2021. The measurements shown in sec. 6 of this work were carried out with the latest version of the laser source. The setup is now in a state, in which measurements can be carried out reliably and studies are ongoing to compare the results obtained to simulated data. Some important lessons were learned during the development of the setup. The importance of being able to correct for fluctuations in the TPA signal by measuring an independent TPA reference signal was not obvious in the beginning. Also, the necessity of using a high resolution multi-axis stage for positioning of the DUT became evident in the first measurements. The analysis of the temporal structure of the pulses proved to be both more important and more difficult than anticipated, especially after the pulse characterization tool initially foreseen was not usable. First results showed that it is possible to perform three dimensional scans of the devices under test and investigate features with unprecedented spatial resolution. Notable examples are the interpad isolation structures of an LGAD, of which SPA-TCT measurements can not match the resolution of TPA. Also, in contrast to SPA-TCT measurements, with TPA-TCT it is possible to resolve the n-implant of an HV-CMOS detector. In some configurations the large opening angle of the beam, necessary to achieve the high spatial resolution, is also a limiting factor, because it is more likely to clip part of the beam and thus reduce the amount of light, which can enter the detector. The effect of beam clipping, the dependence of the measurements on the quality of the focusing and on the temporal structure of the pulses, as well as the fact that artifacts from reflections can be observed, make the analysis of TPA-TCT measurements more challenging. The laser was delivered to several other institutes already and similar setups are being constructed. It is foreseen that TPA-TCT will be established as an additional tool for sensor characterization in the community of radiation detector development.

As mentioned, before the laser for the TPA-TCT setup was delivered, an annealing study to investigate the effects of proton radiation on LGADs was carried out. This study was motivated by previous research, in which seemingly contradicting measurements of the gain layer depletion voltage, for different particle types, energies and fluences, were reported. It was possible to resolve the questions regarding the origin of these discrepancies. An observed increase of the charge collection onset voltage, observed in TCT measurements with red light injection from the front side, could be attributed to a build up of space charge at the rear side of the detector after irradiation. IV and CV measurements, which did not show this increase, indicate that the gain layer depletion voltage is decreased after irradiation by acceptor removal, as expected. The gain, as well as the gain layer depletion voltage, were found to be independent of annealing. Reverse annealing caused the build up of space charge at the sensor backside to vanish, so that the previously increased onset voltage of charge collection with top-TCT was reduced to the same value as observed with IV/CV measurements after sufficient annealing times.

A. Appendix

A.1. Irradiation and Annealing Study of Low Gain Avalanche Detectors

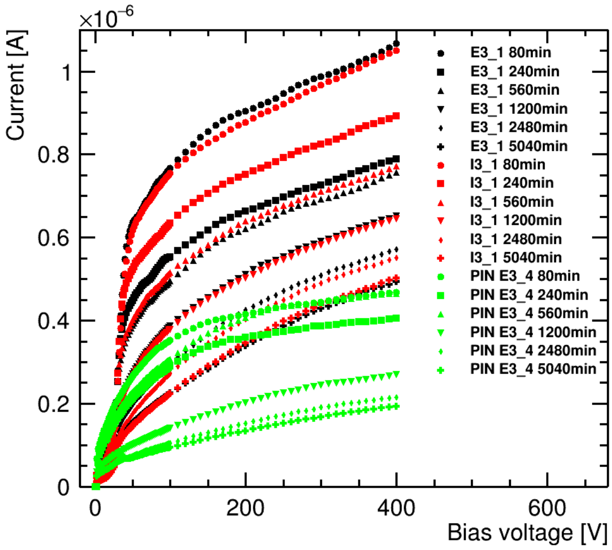

Figure A.1. – Leakage current measurements of the LGAD and PIN samples as a function of bias voltage after irradiation. Accumulated annealing times at 60 °C are indicated in the figure legend. [78]

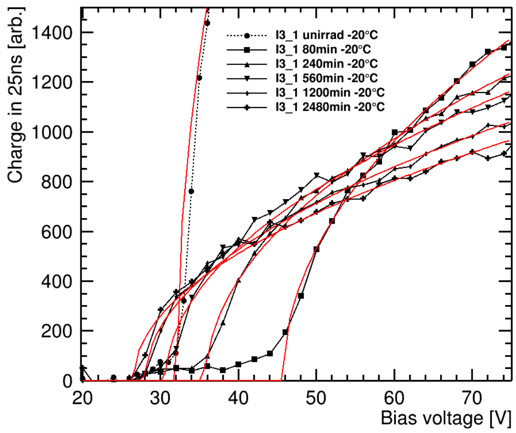

(a) LGAD W5_I3_1

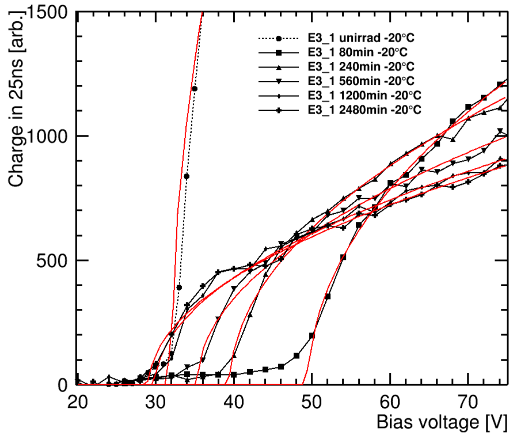

(b) LGAD W5_E3_1

Figure A.2. – Collected charge as a function of bias voltage of LGADs W5_I3_1 and W5_E3_1 after charge injection by a red laser from the front side. The measurement temperature is −20 °C. Accumulated annealing times at 60 °C are indicated in the figure legend. Fits to the data are shown (eq. 4.3), which are used to obtain the value of the onset voltage. [78]

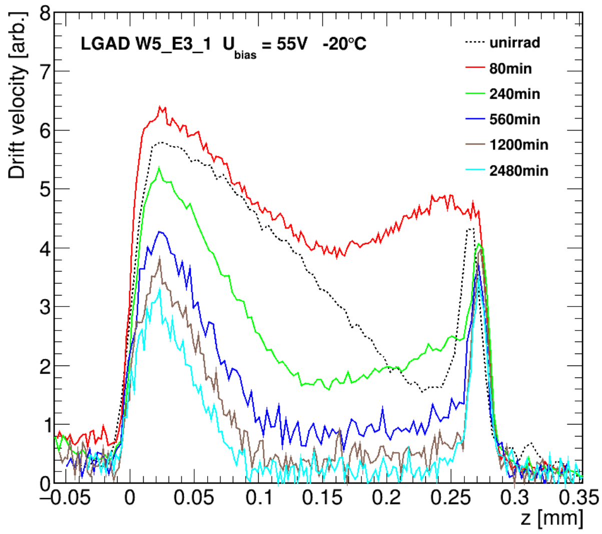

Figure A.3. – Drift velocity as a function of position of the laser beam inside the silicon bulk. Shown is LGAD W5_E3_1 at a bias voltage of 55 V for different annealing times. The left hand side of the figure, at low values of z, correspond to the front side of the detector, where the gain layer is located. [78]

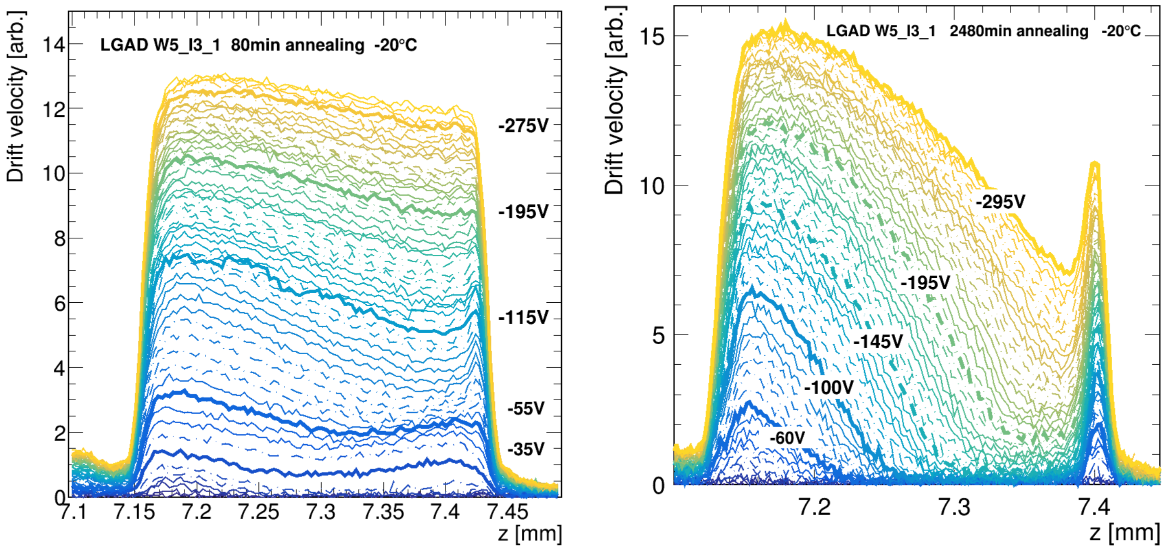

(a) 80min annealing

(b) 2480min annealing

Figure A.4. – Drift velocity as a function of position of the laser beam inside the silicon bulk of sensor W5_I3_1 for different bias voltages and annealing times. [78]

	SET-002840 LGAD_W5_I3_1	filename	tot. annealing min at 60°C
80min @ 60C	done		80
IV -20	18.5.18	MW_LGAD_8622_W5_I3_1_2018-05-18_1.iv	
CV -20	18.5.18	MW_LGAD_8622_W5_I3_1_2018-05-18_1.cv	
RF TCT 20	24.5.18 19:09	2018-05-24_19-09-23_MW_LGAD_8622_W5_I3_1	
RF TCT -20	24.5.18 20:03	2018-05-24_20-03-43_MW_LGAD_8622_W5_I3_1	
eTCT -20	14.6.18 23:22	2018-06-14_23-22-14_MW_LGAD_8622_W5_I3_1	
160min @ 60C	15.6.18		240
IV -20	15.6.18	MW_LGAD_8622_W5_I3_1_2018-06-15_1.iv	
CV -20	15.6.18	MW_LGAD_8622_W5_I3_1_2018-06-15_1.cv	
RF TCT 20	15.6.18 15:49	2018-06-15_15-49-20_MW_LGAD_8622_W5_I3_1	
RF TCT -20	15.6.18 17:03	2018-06-15_17-03-33_MW_LGAD_8622_W5_I3_1	
eTCT -20	9.7.18 15:33	2018-07-09_15-33-19_MW_LGAD_8622_W5_I3_1	
320min @ 60C	10.7.18		560
IV -20	11.7.18	MW_LGAD_8622_W5_I3_1_2018-07-11_1.iv	
CV -20	11.7.18	MW_LGAD_8622_W5_I3_1_2018-07-11_1.cv	
RF TCT 20	16.7.18 8:25	2018-07-16_08-25-14_MW_LGAD_8622_W5_I3_1	
RF TCT -20	16.7.18 11:41	2018-07-16_11-41-41_MW_LGAD_8622_W5_I3_1	
eTCT -20	16.7.18 12:15	2018-07-16_12-15-44_MW_LGAD_8622_W5_I3_1	
640min @ 60C	27.8.18		1200
IV -20	6.9.18	MW_LGAD_8622_W5_I3_1_2018-09-06_1.iv	
CV -20	6.9.18	MW_LGAD_8622_W5_I3_1_2018-09-06_1.cv	
RF TCT 20	30.8.18 9:21	2018-08-30_09-21-31_MW_LGAD_8622_W5_I3_1	
RF TCT -20	30.8.18 10:25	2018-08-30_10-25-00_MW_LGAD_8622_W5_I3_1	
eTCT -20	30.8.18 11:28	2018-08-30_11-28-02_MW_LGAD_8622_W5_I3_1	
1280min @ 60C	6.9.18		2480
IV -20	9.9.18	MW_LGAD_8622_W5_I3_1_2018-09-09_1.iv	
CV -20	9.9.18	MW_LGAD_8622_W5_I3_1_2018-09-09_1.cv	
RF TCT 20	8.9.18 15:21	2018-09-08_15-21-46_MW_LGAD_8622_W5_I3_1	
RF TCT -20	8.9.18 16:55	2018-09-08_16-55-34_MW_LGAD_8622_W5_I3_1	
eTCT -20	9.9.18 13:40	2018-09-09_13-40-53_MW_LGAD_8622_W5_I3_1	
2560min @ 60C	30.10.18		5040
IV -20	16.11.18	MW_LGAD_8622_W5_I3_1_2018-11-16_1.iv	
CV -20			
RF TCT 20	12.11.18 14:14	2018-11-12_14-14-13_MW_LGAD_8622_W5_I3_1	
RF TCT -20	12.11.18 15:50	2018-11-12_15-50-53_MW_LGAD_8622_W5_I3_1	
eTCT -20			

Figure A.5. – Data files of sensor W5_I3_1. Files are available on request.

	SET-002839	filename	tot. annealing
	LGAD_W5_E3_1		min at 60°C
80min @ 60C	done		80
IV -20	18.5.18	MW_LGAD_8622_W5_E3_1_2018-05-18_1.iv	
CV -20	18.5.18	MW_LGAD_8622_W5_E3_1_2018-05-18_1.cv	
RF TCT 20	16.5.18 16:03	2018-05-16_16-03-19_MW_LGAD_8622_W5_E3_1	
RF TCT -20	16.5.18 18:34	2018-05-16_18-34-04_MW_LGAD_8622_W5_E3_1	
eTCT -20	17.5.18 17:22	2018-05-17_17-22-36_MW_LGAD_8622_W5_E3_1	
160min @ 60C	18.5.18		240
IV -20	23.5.18	MW_LGAD_8622_W5_E3_1_2018-05-23_1.iv	
CV -20	23.5.18	MW_LGAD_8622_W5_E3_1_2018-05-23_1.cv	
RF TCT 20	15.6.18 15:12	2018-06-15_15-12-32_MW_LGAD_8622_W5_E3_1	
RF TCT -20	15.6.18 13:26	2018-06-15_13-26-14_MW_LGAD_8622_W5_E3_1	
eTCT -20	4.7.18 10:48	2018-07-04_10-48-59_MW_LGAD_8622_W5_E3_1	
320min @ 60C	10.7.18		560
IV -20	11.7.18	MW_LGAD_8622_W5_E3_1_2018-07-11_1.iv	
CV -20	11.7.18	MW_LGAD_8622_W5_E3_1_2018-07-11_1.cv	
RF TCT 20	13.7.18 10:17	2018-07-13_10-17-06_MW_LGAD_8622_W5_E3_1	
RF TCT -20	6.8.18 10:49	2018-08-06_10-49-11_MW_LGAD_8622_W5_E3_1	
eTCT -20	17.7.18 10:24	2018-07-17_10-24-59_MW_LGAD_8622_W5_E3_1	
640min @ 60C	27.8.18		1200
IV -20	6.9.18	MW_LGAD_8622_W5_E3_1_2018-09-06_1.iv	
CV -20	6.9.18	MW_LGAD_8622_W5_E3_1_2018-09-06_1.cv	
RF TCT 20	30.8.18 18:25	2018-08-30_18-25-13_MW_LGAD_8622_W5_E3_1	
RF TCT -20	30.8.18 19:27	2018-08-30_19-27-57_MW_LGAD_8622_W5_E3_1	
eTCT -20	30.8.18 21:28	2018-08-30_21-28-25_MW_LGAD_8622_W5_E3_1	
1280min @ 60C	6.9.18		2480
IV -20	8.9.18	MW_LGAD_8622_W5_E3_1_2018-09-08_1.iv	
CV -20	8.9.18	MW_LGAD_8622_W5_E3_1_2018-09-08_1.cv	
RF TCT 20	9.9.18 20:46	2018-09-09_20-46-07_MW_LGAD_8622_W5_E3_1	
RF TCT -20	9.9.18 21:29	2018-09-09_21-29-14_MW_LGAD_8622_W5_E3_1	
eTCT -20	9.9.18 21:59	2018-09-09_21-59-25_MW_LGAD_8622_W5_E3_1	
2560min @ 60C	30.10.18		5040
IV -20	2.11.18	MW_LGAD_8622_W5_E3_1_2018-11-02_1.iv	
CV -20			
RF TCT 20	3.11.18 12:27	2018-11-03_12-27-12_MW_LGAD_8622_W5_E3_1	
RF TCT -20	3.11.18 15:40	2018-11-03_15-40-45_MW_LGAD_8622_W5_E3_1	
eTCT -20			

Figure A.6. – Data files of sensor W5_E3_1. Files are available on request.

	SET-002837	filename	tot. annealing
	PIN_W5_E3_4		min at 60°C
80min @ 60C	done		80
IV -20	16.5.18	MW_PIN_8622_W5_E3_4_2018-05-16_1.iv	
CV -20	16.5.18	MW_PIN_8622_W5_E3_4_2018-05-16_1.cv	
RF TCT 20	15.5.18 11:24	2018-05-15_11-24-30_MW_PIN_8622_W5_E3_4	
RF TCT -20	15.5.18 14:07	2018-05-15_14-07-19_MW_PIN_8622_W5_E3_4	
eTCT -20	xxx		
160min @ 60C	16.5.18		240
IV -20	17.5.18	MW_PIN_8622_W5_E3_4_2018-05-17_1.iv	
CV -20	17.5.18	MW_PIN_8622_W5_E3_4_2018-05-17_1.cv	
RF TCT 20	18.5.18 16:11	2018-05-18_16-11-17_MW_PIN_8622_W5_E3_4	
RF TCT -20	18.5.18 17:10	2018-05-18_17-10-01_MW_PIN_8622_W5_E3_4	
eTCT -20	xxx		
320min @ 60C	10.7.18		560
IV -20	10.7.18	MW_PIN_8622_W5_E3_4_2018-07-10_1.iv	
CV -20	10.7.18	MW_PIN_8622_W5_E3_4_2018-07-10_1.cv	
RF TCT 20	17.7.18 18:34	2018-07-17_18-34-25_MW_PIN_8622_W5_E3_4	
RF TCT -20	17.7.18 19:22	2018-07-17_19-22-42_MW_PIN_8622_W5_E3_4	
eTCT -20	xxx		
640min @ 60C	27.8.18		1200
IV -20	5.9.18	MW_PIN_8622_W5_E3_4_2018-09-05_1.iv	
CV -20	5.9.18	MW_PIN_8622_W5_E3_4_2018-09-05_2.cv	
RF TCT 20	31.8.18 9:28	2018-08-31_09-28-16_MW_PIN_8622_W5_E3_4	
RF TCT -20	31.8.18 10:18	2018-08-31_10-18-57_MW_PIN_8622_W5_E3_4	
eTCT -20	xxx		
1280min @ 60C	6.9.18		2480
IV -20	8.9.18	MW_PIN_8622_W5_E3_4_2018-09-08_1.iv	
CV -20	8.9.18	MW_PIN_8622_W5_E3_4_2018-09-08_1.cv	
RF TCT 20	7.9.18 15:42	2018-09-07_15-42-50_MW_PIN_8622_W5_E3_4	
RF TCT -20	7.9.18 17:00	2018-09-07_17-00-10_MW_PIN_8622_W5_E3_4	
eTCT -20	xxx		
2560min @ 60C	30.10.18		5040
IV -20	3.11.18	MW_PIN_8622_W5_E3_4_2018-11-03_1.iv	
CV -20			
RF TCT 20	2.11.18 16:12	2018-11-02_16-12-16_MW_PIN_8622_W5_E3_4	
RF TCT -20	2.11.18 17:37	2018-11-02_17-37-12_MW_PIN_8622_W5_E3_4	
eTCT -20	xxx		

Figure A.7. – Data files of sensor W5_E3_4. Files are available on request.

A.2. Characterization of unirradiated LGADs

An electrical characterization (IV and CV) of unirradiated LGADs from CNM wafer 2 and wafer 5 of run 8622 was carried out. The devices are very similar to the ones presented in the main text sec. 4, p. 29. The sensors from wafer 5 (W5) have a thickness of 277 μm and those from wafer 2 (W2) have a thickness of 278 μm. The active area of the sensors is 3×3 mm^2. All sensors feature a Junction Termination Extension (JTE). The electrical characterization was carried out on the IV/CV probestation (sec. 3.1) at room temperature. The multiplication layer implant dose is 1.8×10^{13} atm/cm2 for W2 and 1.9×10^{13} atm/cm2 for W5.
Fig. A.8 shows measurements of the leakage current at room temperature of PINs (a) and LGADs (b). The LGAD W2_J4_2 showed an exceptionally high leakage current and was excluded from further measurements. The characteristic onset voltage can be seen in the measurements of the LGADs, which is related to the depletion of the gain layer.

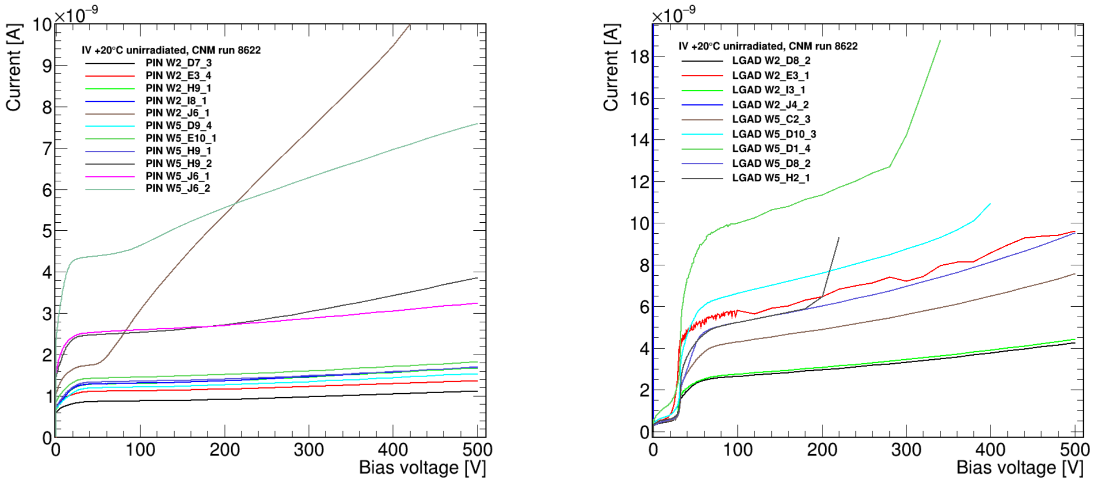

(a) PIN sensors

(b) LGAD sensors

Figure A.8. – Leakage current as a function of bias voltage of PIN (a) and LGAD (b) sensors at +20°C. The devices are from wafer 2 and wafer 5 of CNM run 8622.

Capacitance measurements of the LGADs are shown in fig. A.9. Measurements were carried out at room temperature at an AC frequency of 10 kHz. The figure on the left (a) shows the capacitance in logarithmic scale as a function of bias voltage. The figure on the right (b) shows the value of $1/C^2$ as a function of bias voltage. Both figures show an inset with a zoom to the region around the gain layer depletion voltage. The end capacitance of all LGADs is around 4 pF, as expected from the device geometries. The insets of both figures clearly show the separation of devices from W2 and W5. LGADs from W2 have a lower gain layer doping than those from W5, therefore the gain layer depletes at a lower bias voltage. The gain layer depletion voltage is around 30 V for W2 and 33 V for W5, as can be seen in the inset of fig. A.9 (b). Fig. A.10 shows the effective doping concentration as a function of depth from the sensor top side. A zoom to the region around the gain layer is shown in (b). The value of N_{eff} was calculated from the measurements of the capacitance, using the equations

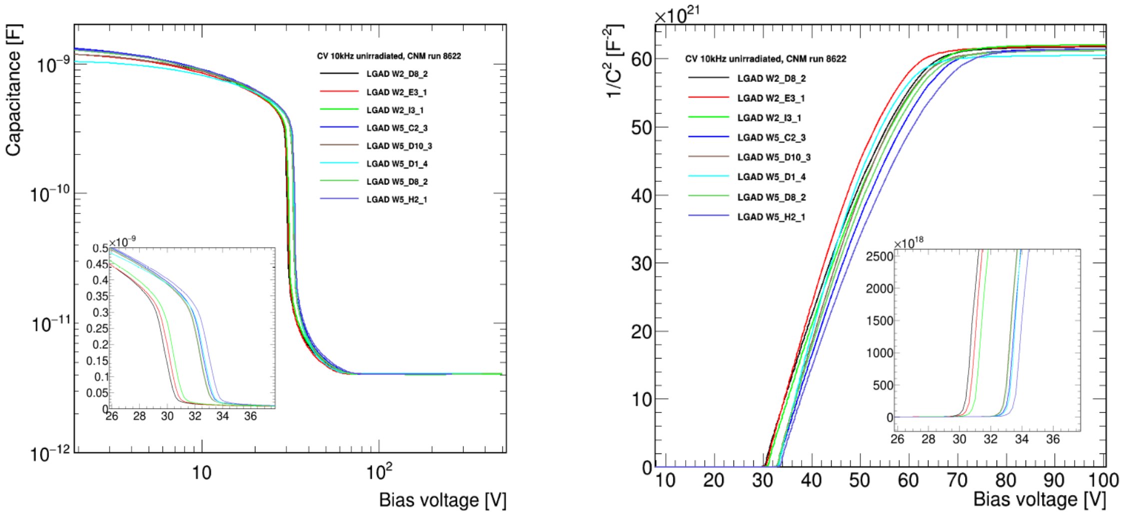

(a) C-V (b) 1/C²-V

Figure A.9. – (a) Capacitance at 10 kHz as a function of bias voltage of the LGAD sensors at +20°C. (b) Value of $1/C^2$ as a function of bias voltage. The figure inset shows a zoom to the bias voltages around the gain layer depletion voltage.

(eqs. 2.8, 2.9, p. 10)

$$N_{eff}(x) = -\frac{C^3}{\epsilon q_e A^2}\left(\frac{dC}{dV}\right)^{-1} \tag{A.1}$$

and

$$x = \frac{\epsilon A}{C}. \tag{A.2}$$

The guard ring was connected, during the measurements, still there is some uncertainty in the lateral extension of the depletion volume. The stated width of 3 mm refers to the gain layer implant. The width of the n$^+$-electrode is 3.2 mm. In the equation above the area A was adjusted, such that the maximum depletion width is in agreement with the nominal thickness of the devices, which resulted in a value of $A = 3.3 \times 3.3$ mm^2. A value of $\epsilon = 11.68 \cdot 8.854187 \cdot 10^{-14}$ F/cm was used. The electron charge is denoted as q_e. In addition to the IV measurements shown above, measurements of the current were repeated for the LGADs with red light injection. For this, a continuous red LED was mounted directly on top of the DUT during IV measurements. The results are shown in fig. A.11. Again, fig. A.11 (b) shows a zoom to the region around the gain layer depletion voltage. The currents are normalized to the respective measurements at low voltages to measure the impact of charge multiplication. The currents without illumination (fig. A.8) are in the order of several nanoampere. With illumination the currents increase to hundreds of microampere and are therefore completely dominated by the continuous charge injection. An increase in current with bias voltage would be primarily attributed to an increase of charge multiplication in the gain layer. In fact, a gain value of $G = 4.75$ was measured with unirradiated sensors from W5 at +20°C, at a bias voltage of 400 V, with TCT (compare fig. 4.8). The normalized current with light illumination, which is reported here is closer to a value of $I_n = 6$ at 400 V for W5. On the other hand, a clear separation of the measured currents, depending on the gain layer doping can be observed. Sensors with a higher gain layer doping (W5) show a stronger

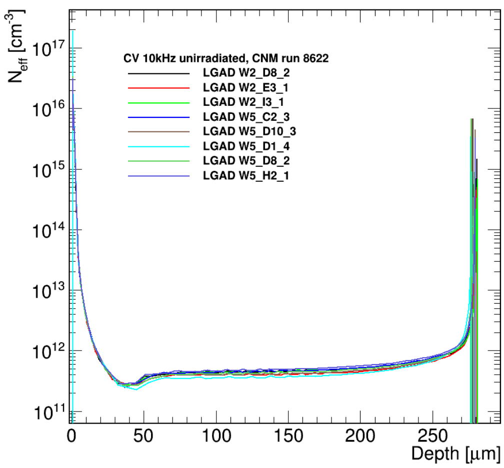

(a) Full plot range

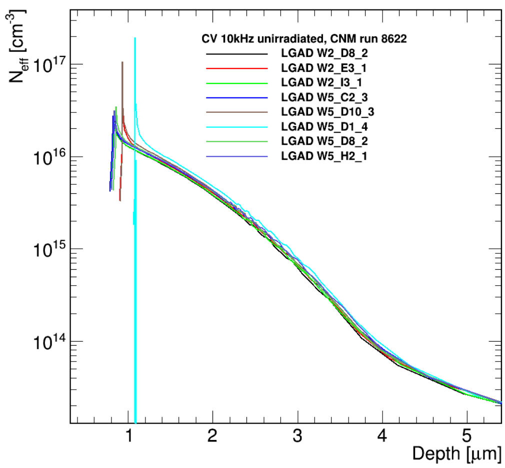

(b) Zoom to the gain layer region

Figure A.10. – (a) Effective doping concentration of the LGAD sensors as a function of depth inside the devices. The values are calculated from CV measurements. (b) Zoom to the region around the gain layer.

multiplication of the current. Most notably, the difference in the amount of current multiplication can be observed already before the gain layer is depleted at around 30 to 33 V (fig. A.11 (b)).

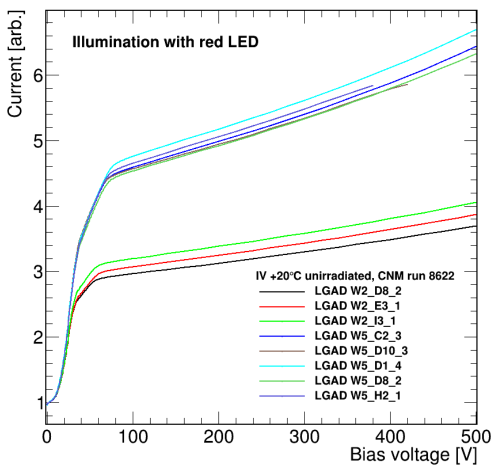

(a) Full plot range

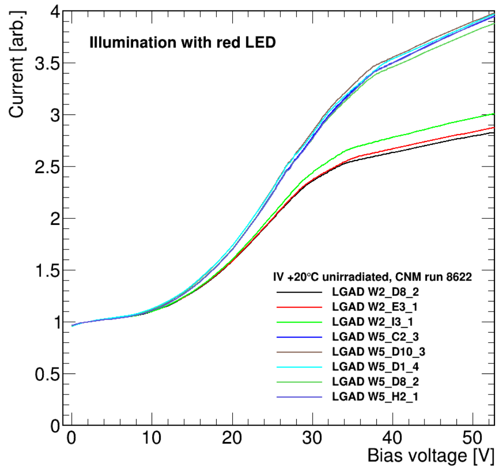

(b) Zoom to low bias voltages

Figure A.11. – (a) Current, measured with continuous injection of red light from the top, as a function of bias voltage for LGADs from wafer 2 and wafer 5 of CNM run 8622. (b) Zoom to low bias voltages. The currents are normalized to the respective value at low bias voltage. The gain layer depletion voltage is 30 V for sensors from wafer 2 and 33 V for sensors from wafer 5.

A.3. IV/CV: HPK2 LGAD

Fig. A.12 shows IV and CV measurements of the LGAD HPK2-W28-S1-5x5-LGAD-P14. The measurements were taken at room temperature (20°C). The CV measurement was performed at an AC-frequency of 10 kHz. The probe needle was connected to each pad individually. The guard ring was connected.

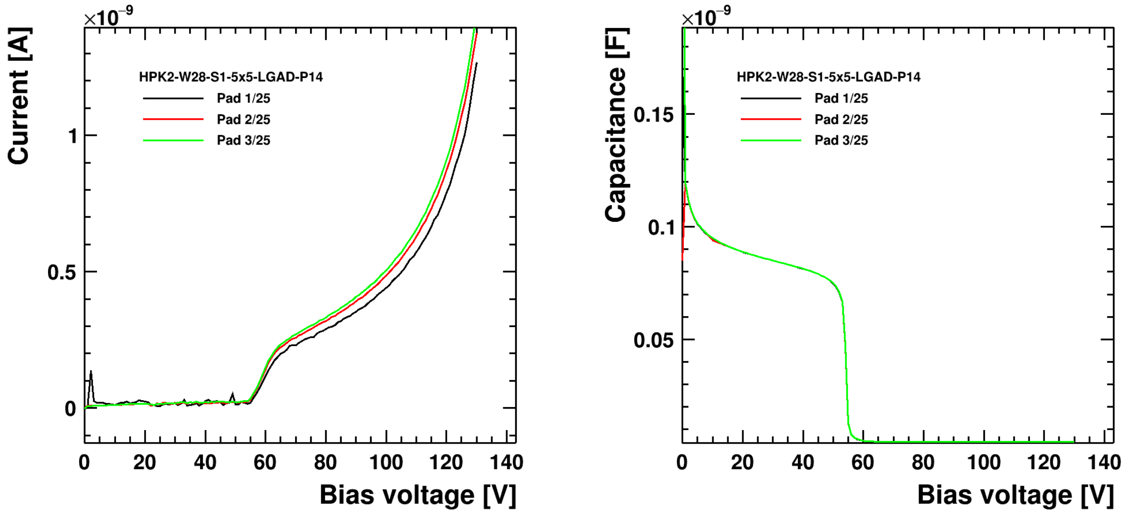

Figure A.12. – Measurements of the leakage current and capacitance for three neighboring pads of an HPK2 5x5 LGAD. The gain layer is depleted at around 55 V. The CV measurements was performed at an AC-frequency of 10 kHz.

Bibliography

[1] ATLAS Collaboration.
"Technical Proposal: A High-Granularity Timing Detector for the ATLAS Phase-II Upgrade".
In: CERN-LHCC-2018-023. LHCC-P-012 (2018).
URL: http://cds.cern.ch/record/2623663.

[2] ATLAS collaboration et al.
"Technical design report for the ATLAS inner tracker pixel detector".
In: *CERN, Geneva, Tech. Rep. CERN-LHCC-2017-021. ATLAS-TDR-030* (2017).

[3] M. Petruzzo.
Fast timing detector developments for a LHCb Upgrade-II.
Tech. rep.
2018.

[4] I Vila et al.
"TPA-TCT: A novel Transient Current Technique based on the Two Photon Absorption (TPA) process".
In: *25th RD50 Workshop, CERN, Geneve*.
2014,
Pp. 17–19.

[5] R Palomo et al.
Two Photon Absorption and carrier generation in semiconductors.
2014.

[6] M. Fernández García et al.
"High-resolution three-dimensional imaging of a depleted CMOS sensor using an edge Transient Current Technique based on the Two Photon Absorption process (TPA-eTCT)".
In: *Nuclear Instruments and Methods in Physics Research Section A: Accelerators, Spectrometers, Detectors and Associated Equipment* 845 (2017), pp. 69–71.

[7] M Fernández García et al.
"On the determination of the substrate effective doping concentration of irradiated HV-CMOS sensors using an edge-TCT technique based on the Two-Photon-Absorption process".
In: *Journal of Instrumentation* 12.01 (2017), p. C01038.

[8] Helmuth Spieler.
Semiconductor detector systems.
Vol. 12.
Oxford university press, 2005.

[9] Leonardo Rossi et al.
Pixel detectors: From fundamentals to applications.
Springer Science & Business Media, 2006.

[10] Simon M Sze and Kwok K Ng.
Physics of semiconductor devices.
John Wiley & Sons, 2007.

[11] Pietro P Altermatt et al.
"Reassessment of the intrinsic carrier density in crystalline silicon in view of band-gap narrowing".
In: *Journal of Applied Physics* 93.3 (2003), pp. 1598–1604.

[12] Hermann Kolanoski and Norbert Wermes.
"Teilchendetektoren".
In: *ISBN 978-3-662-45349-0. Springer-Verlag Berlin Heidelberg* (2016).

[13] "Radiation hard silicon detectors—developments by the RD48 (ROSE) collaboration".
In: *Nuclear Instruments and Methods in Physics Research Section A: Accelerators, Spectrometers, Detectors and Associated Equipment* 466.2 (2001). 4th Int. Symp. on Development and Application of Semiconductor Tracking Detectors, pp. 308 –326.
ISSN: 0168-9002.
DOI: https://doi.org/10.1016/S0168-9002(01)00560-5.
URL: http://www.sciencedirect.com/science/article/pii/S0168900201005605.

[14] Michael Moll.
"Displacement damage in silicon detectors for High Energy Physics".
In: *IEEE Transactions on Nuclear Science* 65.8 (2018), pp. 1561–1582.

[15] D Campbell, A Chilingarov, and T Sloan.
"Frequency and temperature dependence of the depletion voltage from CV measurements for irradiated Si detectors".
In: *Nuclear Instruments and Methods in Physics Research Section A: Accelerators, Spectrometers, Detectors and Associated Equipment* 492.3 (2002), pp. 402 –410.
ISSN: 0168-9002.
DOI: https://doi.org/10.1016/S0168-9002(02)01353-0.
URL: http://www.sciencedirect.com/science/article/pii/S0168900202013530.

[16] P Blood and JW Orton.
"The electrical characterisation of semiconductors".
In: *Reports on Progress in Physics* 41.2 (1978), p. 157.

[17] A. Chilingarov.
"Temperature dependence of the current generated in Si bulk".
In: *Journal of Instrumentation* 8.10 (2013), P10003–P10003.
DOI: 10.1088/1748-0221/8/10/p10003.
URL: https://doi.org/10.1088%2F1748-0221%2F8%2F10%2Fp10003.

[18] William Shockley.
"Currents to conductors induced by a moving point charge".
In: *Journal of applied physics* 9.10 (1938), pp. 635–636.

[19] Simon Ramo.
"Currents induced by electron motion".
In: *Proceedings of the IRE* 27.9 (1939), pp. 584–585.

[20] G. Cavalleri et al.

"Extension of Ramo's theorem as applied to induced charge in semiconductor detectors". In: *Nuclear Instruments and Methods* 92.1 (1971), pp. 137 –140. ISSN: 0029-554X. DOI: https://doi.org/10.1016/0029-554X(71)90235-7. URL: http://www.sciencedirect.com/science/article/pii/0029554X71902357.

[21] G. Cavalleri et al. "On the induced charge in semiconductor detectors". In: *Nuclear Instruments and Methods* 21 (1963), pp. 177 –178. ISSN: 0029-554X. DOI: https://doi.org/10.1016/0029-554X(63)90106-X. URL: http://www.sciencedirect.com/science/article/pii/0029554X6390106X.

[22] Werner Riegler. "An extension of Ramo's theorem for signals in silicon sensors". In: *arXiv preprint:1812.07570* (2018).

[23] M. Albrow et al. "CMS-TOTEM Precision Proton Spectrometer". In: CERN-LHCC-2014-021. TOTEM-TDR-003. CMS-TDR-13 (2014). URL: http://cds.cern.ch/record/1753795.

[24] Gianluigi Casse. "Charge multiplication in highly irradiated planar silicon sensors". In: *PoS VERTEX2010* 20 (2010).

[25] A. G. Chynoweth and K. G. McKay. "Threshold Energy for Electron-Hole Pair-Production by Electrons in Silicon". In: *Phys. Rev.* 108 (1 1957), pp. 29–34. DOI: 10.1103/PhysRev.108.29. URL: https://link.aps.org/doi/10.1103/PhysRev.108.29.

[26] Chynoweth, A. G. "Ionization Rates for Electrons and Holes in Silicon". In: *Phys. Rev.* 109 (5 1958), pp. 1537–1540. DOI: 10.1103/PhysRev.109.1537. URL: https://link.aps.org/doi/10.1103/PhysRev.109.1537.

[27] R. Van Overstraeten and H. De Man. "Measurement of the ionization rates in diffused silicon p-n junctions". In: *Solid-State Electronics* 13.5 (1970), pp. 583 –608. ISSN: 0038-1101. DOI: https://doi.org/10.1016/0038-1101(70)90139-5. URL: http://www.sciencedirect.com/science/article/pii/0038110170901395.

[28] DJ Massey, JPR David, and GJ Rees. "Temperature dependence of impact ionization in submicrometer silicon devices". In: *IEEE Transactions on Electron Devices* 53.9 (2006), pp. 2328–2334.

[29] CR Crowell and SM Sze. "Temperature dependence of avalanche multiplication in semiconductors". In: *Applied Physics Letters* 9.6 (1966), pp. 242–244.

[30] W. Maes, K. De Meyer, and R. Van Overstraeten.
"Impact ionization in silicon: A review and update".
In: *Solid-State Electronics* 33.6 (1990), pp. 705–718.

[31] M. Mandurrino et al.
"Numerical Simulation of Charge Multiplication in Ultra-Fast Silicon Detectors (UFSD) and Comparison with Experimental Data".
In: (2017), pp. 1–4.

[32] Hartmut F-W Sadrozinski, Abraham Seiden, and Nicolò Cartiglia.
"4D tracking with ultra-fast silicon detectors".
In: *Reports on Progress in Physics* 81.2 (2017), p. 026101.
DOI: 10.1088/1361-6633/aa94d3.
URL: https://doi.org/10.1088%2F1361-6633%2Faa94d3.

[33] N. Cartiglia.
"Timing layers, 4- and 5-dimension tracking".
In: *Nuclear Instruments and Methods in Physics Research Section A: Accelerators, Spectrometers, Detectors and Associated Equipment* 924 (2019). 11th International Hiroshima Symposium on Development and Application of Semiconductor Tracking Detectors, pp. 350 –354.
ISSN: 0168-9002.
DOI: https://doi.org/10.1016/j.nima.2018.09.157.
URL: http://www.sciencedirect.com/science/article/pii/S0168900218313147.

[34] H. Spieler.
"Fast Timing Methods for Semiconductor Detectors".
In: *IEEE Transactions on Nuclear Science* 29.3 (1982), pp. 1142–1158.
DOI: 10.1109/TNS.1982.4336333.

[35] I. Tapan et al.
"Avalanche photodiodes as proportional particle detectors".
In: *Nuclear Instruments and Methods in Physics Research Section A: Accelerators, Spectrometers, Detectors and Associated Equipment* 388.1 (1997), pp. 79 –90.
ISSN: 0168-9002.
DOI: https://doi.org/10.1016/S0168-9002(97)00316-1.
URL: http://www.sciencedirect.com/science/article/pii/S0168900297003161.

[36] G. Pellegrini et al.
"Recent technological developments on LGAD and iLGAD detectors for tracking and timing applications".
In: *Nuclear Instruments and Methods in Physics Research Section A: Accelerators, Spectrometers, Detectors and Associated Equipment* 831 (2016). Proceedings of the 10th International "Hiroshima" Symposium on the Development and Application of Semiconductor Tracking Detectors, pp. 24 –28.
ISSN: 0168-9002.
DOI: https://doi.org/10.1016/j.nima.2016.05.066.
URL: http://www.sciencedirect.com/science/article/pii/S0168900216304557.

[37] H. F.-W. Sadrozinski et al.
"Ultra-fast silicon detectors".

In: *Nuclear Instruments and Methods in Physics Research Section A: Accelerators, Spectrometers, Detectors and Associated Equipment* 730 (2013). Proceedings of the 9th International Conference on Radiation Effects on Semiconductor Materials Detectors and Devices, pp. 226 –231.
ISSN: 0168-9002.
DOI: https://doi.org/10.1016/j.nima.2013.06.033.
URL: http://www.sciencedirect.com/science/article/pii/S0168900213008589.

[38] N. Cartiglia.
"Design optimization of ultra-fast silicon detectors".
In: *Nuclear Instruments and Methods in Physics Research Section A: Accelerators, Spectrometers, Detectors and Associated Equipment* 796 (2015). Proceedings of the 10th International Conference on Radiation Effects on Semiconductor Materials Detectors and Devices, pp. 141 –148.
ISSN: 0168-9002.
DOI: https://doi.org/10.1016/j.nima.2015.04.025.
URL: http://www.sciencedirect.com/science/article/pii/S0168900215004982.

[39] M. Centis Vignali et al.
"Deep diffused Avalanche photodiodes for charged particles timing".
In: *Nuclear Instruments and Methods in Physics Research Section A: Accelerators, Spectrometers, Detectors and Associated Equipment* (2019), p. 162405.
ISSN: 0168-9002.
DOI: https://doi.org/10.1016/j.nima.2019.162405.
URL: http://www.sciencedirect.com/science/article/pii/S0168900219309830.

[40] G Pellegrini et al.
"Technology developments and first measurements of Low Gain Avalanche Detectors (LGAD) for high energy physics applications".
In: *Nuclear Instruments and Methods in Physics Research Section A: Accelerators, Spectrometers, Detectors and Associated Equipment* 765 (2014), pp. 12–16.

[41] G Kramberger et al.
"Radiation effects in Low Gain Avalanche Detectors after hadron irradiations".
In: *Journal of Instrumentation* 10.07 (2015), P07006.

[42] Giorgio Apollinari et al.
High-Luminosity Large Hadron Collider (HL-LHC): Technical Design Report V. 01.
CERN, 2017.

[43] FCC collaboration et al.
"FCC-hh: The Hadron Collider: Future Circular Collider Conceptual Design Report Volume 3".
In: *European Physical Journal: Special Topics* 228.4 (2019), pp. 755–1107.

[44] G Lindström, Michael Moll, and E Fretwurst.
"Radiation hardness of silicon detectors–a challenge from high-energy physics".
In: *Nuclear Instruments and Methods in Physics Research Section A: Accelerators, Spectrometers, Detectors and Associated Equipment* 426.1 (1999), pp. 1–15.

[45] Victor AJ Van Lint et al.
"Mechanisms of radiation effects in electronic materials. Volume 1".

In: *NASA STI/Recon Technical Report A* 81 (1980).

[46] M. Huhtinen.
"Simulation of non-ionising energy loss and defect formation in silicon".
In: *Nuclear Instruments and Methods in Physics Research Section A: Accelerators, Spectrometers, Detectors and Associated Equipment* 491.1 (2002), pp. 194 –215.
ISSN: 0168-9002.
DOI: https://doi.org/10.1016/S0168-9002(02)01227-5.
URL: http://www.sciencedirect.com/science/article/pii/S0168900202012275.

[47] Gunnar Lindström.
"Radiation damage in silicon detectors".
In: *Nuclear Instruments and Methods in Physics Research Section A: Accelerators, Spectrometers, Detectors and Associated Equipment* 512.1 (2003), pp. 30–43.

[48] WTRW Shockley and WT Read Jr.
"Statistics of the recombinations of holes and electrons".
In: *Physical review* 87.5 (1952), p. 835.

[49] M. Moll et al.
"Relation between microscopic defects and macroscopic changes in silicon detector properties after hadron irradiation".
In: *Nuclear Instruments and Methods in Physics Research Section B: Beam Interactions with Materials and Atoms* 186.1 (2002), pp. 100 –110.
ISSN: 0168-583X.
DOI: https://doi.org/10.1016/S0168-583X(01)00866-7.
URL: http://www.sciencedirect.com/science/article/pii/S0168583X01008667.

[50] M. Moll, E. Fretwurst, and G. Lindström.
"Leakage current of hadron irradiated silicon detectors – material dependence".
In: *Nuclear Instruments and Methods in Physics Research Section A: Accelerators, Spectrometers, Detectors and Associated Equipment* 426.1 (1999), pp. 87–93.
ISSN: 0168-9002.
DOI: https://doi.org/10.1016/S0168-9002(98)01475-2.
URL: https://www.sciencedirect.com/science/article/pii/S0168900298014752.

[51] Michael Moll.
Radiation damage in silicon particle detectors: Microscopic defects and macroscopic properties.
Tech. rep.
DESY, 1999.

[52] G Kramberger et al.
"Effective trapping time of electrons and holes in different silicon materials irradiated with neutrons, protons and pions".
In: *Nuclear Instruments and Methods in Physics Research Section A: Accelerators, Spectrometers, Detectors and Associated Equipment* 481.1 (2002), pp. 297 –305.
ISSN: 0168-9002.
DOI: https://doi.org/10.1016/S0168-9002(01)01263-3.
URL: http://www.sciencedirect.com/science/article/pii/S0168900201012633.

[53] P. Fernández-Martínez et al.

"Simulation of new p-type strip detectors with trench to enhance the charge multiplication effect in the n-type electrodes".
In: *Nuclear Instruments and Methods in Physics Research Section A: Accelerators, Spectrometers, Detectors and Associated Equipment* 658.1 (2011). RESMDD 2010, pp. 98 –102.
ISSN: 0168-9002.
DOI: https://doi.org/10.1016/j.nima.2011.04.056.
URL: http://www.sciencedirect.com/science/article/pii/S0168900211008400.

[54] G. Casse et al.
"Charge multiplication in irradiated segmented silicon detectors with special strip processing".
In: *Nuclear Instruments and Methods in Physics Research Section A: Accelerators, Spectrometers, Detectors and Associated Equipment* 699 (2013). Proceedings of the 8th International "Hiroshima" Symposium on the Development and Application of Semiconductor Tracking Detectors, pp. 9 –13.
ISSN: 0168-9002.
DOI: https://doi.org/10.1016/j.nima.2012.04.033.
URL: http://www.sciencedirect.com/science/article/pii/S0168900212003889.

[55] G. Casse.
"The RD50 activity in the context of future pixel detector systems".
In: *Journal of Instrumentation* 10.05 (2015), pp. C05020–C05020.
DOI: 10.1088/1748-0221/10/05/c05020.
URL: https://doi.org/10.1088%2F1748-0221%2F10%2F05%2Fc05020.

[56] D. Pitzl et al.
"Type inversion in silicon detectors".
In: *Nuclear Instruments and Methods in Physics Research Section A: Accelerators, Spectrometers, Detectors and Associated Equipment* 311.1 (1992), pp. 98 –104.
ISSN: 0168-9002.
DOI: https://doi.org/10.1016/0168-9002(92)90854-W.
URL: http://www.sciencedirect.com/science/article/pii/016890029290854W.

[57] Renate Wunstorf.
Systematische Untersuchungen zur Strahlenresistenz von Silizium-Detektoren für die Verwendung in Hochenergiephysik-Experimenten.
Tech. rep.
H1 Kollaboration, 1992.

[58] Michael Moll, E Fretwurst, G Lindström, et al.
"Investigation on the improved radiation hardness of silicon detectors with high oxygen concentration".
In: *Nuclear Instruments and Methods in Physics Research Section A: Accelerators, Spectrometers, Detectors and Associated Equipment* 439.2-3 (2000), pp. 282–292.

[59] R. Wunstorf et al.
"Investigations of donor and acceptor removal and long term annealing in silicon with different boron/phosphorus ratios".
In: *Nuclear Instruments and Methods in Physics Research Section A: Accelerators, Spectrometers, Detectors and Associated Equipment* 377.2 (1996). Proceedings of the Seventh European Symposium on Semiconductor, pp. 228 –233.
ISSN: 0168-9002.

DOI: https://doi.org/10.1016/0168-9002(96)00217-3.
URL: http://www.sciencedirect.com/science/article/pii/0168900296002173.

[60] E. M. Donegani, E. Fretwurst, and E. Garutti.
"Defect spectroscopy of proton-irradiated thin p-type silicon sensors".
In: *2016 16th European Conference on Radiation and Its Effects on Components and Systems (RADECS)*.
2016,
Pp. 1–6.
DOI: 10.1109/RADECS.2016.8093113.

[61] M.Moll.
"Acceptor removal - Displacement damage effects involving the shallow acceptor doping of p-type silicon devices".
In: *The 28th International Workshop on Vertex Detectors - Vertex2019, Lopud, Croatia* (2019).

[62] M. Ferrero et al.
"Radiation resistant LGAD design".
In: *Nuclear Instruments and Methods in Physics Research Section A: Accelerators, Spectrometers, Detectors and Associated Equipment* 919 (2019), pp. 16 –26.
ISSN: 0168-9002.
DOI: https://doi.org/10.1016/j.nima.2018.11.121.

[63] SM Mazza et al.
"Properties of FBK UFSDs after neutron and proton irradiation up to 6e15 neq/cm2".
In: *Journal of Instrumentation* 15.04 (2020), T04008.

[64] P.Almeida.
Characterization of acceptor removal in silicon pad diodes irradiated by protons and neutrons.
32nd RD50 Workshop, Hamburg.
2018.

[65] Yana Gurimskaya et al.
"Radiation damage in p-type EPI silicon pad diodes irradiated with protons and neutrons".
In: *Nuclear Instruments and Methods in Physics Research Section A: Accelerators, Spectrometers, Detectors and Associated Equipment* (2019).
ISSN: 0168-9002.
DOI: https://doi.org/10.1016/j.nima.2019.05.062.
URL: http://www.sciencedirect.com/science/article/pii/S0168900219307181.

[66] V Eremin, E Verbitskaya, and Z Li.
"The origin of double peak electric field distribution in heavily irradiated silicon detectors".
In: *Nuclear Instruments and Methods in Physics Research Section A: Accelerators, Spectrometers, Detectors and Associated Equipment* 476.3 (2002). Proc. of the 3rd Int. Conf. on Radiation Effects on Semiconductor Materials, Detectors and Devices, pp. 556 –564.
ISSN: 0168-9002.
DOI: https://doi.org/10.1016/S0168-9002(01)01642-4.
URL: http://www.sciencedirect.com/science/article/pii/S0168900201016424.

[67] G. Kramberger et al.
"Field engineering by continuous hole injection in silicon detectors irradiated with neutrons".

In: *Nuclear Instruments and Methods in Physics Research Section A: Accelerators, Spectrometers, Detectors and Associated Equipment* 497.2 (2003), pp. 440 –449.
ISSN: 0168-9002.
DOI: https://doi.org/10.1016/S0168-9002(02)01927-7.
URL: http://www.sciencedirect.com/science/article/pii/S0168900202019277.

[68] G. Kramberger et al.
"Modeling of electric field in silicon micro-strip detectors irradiated with neutrons and pions".
In: *Journal of Instrumentation* 9.10 (2014), P10016–P10016.
DOI: 10.1088/1748-0221/9/10/p10016.
URL: https://doi.org/10.1088%2F1748-0221%2F9%2F10%2Fp10016.

[69] V. Greco et al.
"Devices optimised for avalanche multiplication".
In: *PoS* (2015), p. 031.

[70] C. Gallrapp et al.
"Study of gain homogeneity and radiation effects of Low Gain Avalanche Pad Detectors".
In: *Nuclear Instruments and Methods in Physics Research Section A: Accelerators, Spectrometers, Detectors and Associated Equipment* 875 (2017), pp. 27 –34.
ISSN: 0168-9002.
DOI: https://doi.org/10.1016/j.nima.2017.07.038.
URL: http://www.sciencedirect.com/science/article/pii/S0168900217307799.

[71] R. Dalal et al.
"TCAD simulation of Low Gain Avalanche Detectors".
In: *Nuclear Instruments and Methods in Physics Research Section A: Accelerators, Spectrometers, Detectors and Associated Equipment* 836 (2016), pp. 113–121.

[72] E. Verbitskaya et al.
"Simulation of Low Gain Avalanche Detector characteristics based on the concept of negative feedback in irradiated silicon detectors with carrier impact ionization".
In: *Journal of Instrumentation* 11.12 (2016), P12012.

[73] Sofia Otero Ugobono.
"Characterisation and Optimisation of Radiation-Tolerant Silicon Sensors with Intrinsic Gain".
PhD. thesis. University of Santiago de Compostela, 2018.

[74] V Eremin et al.
"Development of transient current and charge techniques for the measurement of effective net concentration of ionized charges (Neff) in the space charge region of pn junction detectors".
In: *Nuclear Instruments and Methods in Physics Research Section A: Accelerators, Spectrometers, Detectors and Associated Equipment* 372.3 (1996), pp. 388–398.

[75] G. Kramberger.
"Advanced transient current technique systems".
In: *PoS* (2015), p. 032.

[76] G Kramberger et al.
"Investigation of irradiated silicon detectors by edge-TCT".
In: *IEEE transactions on nuclear science* 57.4 (2010), pp. 2294–2302.

[77] C. Gallrapp et al.

The TCT+ setup - a system for TCT, eTCT and timing measurements.
presented at the 1st TCT Workshop, DESY, Hamburg, Germany, 2015.

[78] Moritz Wiehe et al.
"Study of the radiation-induced damage mechanism in proton irradiated low gain avalanche detectors and its thermal annealing dependence".
In: *Nuclear Instruments and Methods in Physics Research Section A: Accelerators, Spectrometers, Detectors and Associated Equipment* 986 (), p. 164814.

[79] R. Mulargia et al.
"Temperature dependence of the response of ultra fast silicon detectors".
In: *International Workshop on Semiconductor Pixel Detectors for Particles and Imaging (Pixel 2016)* (2016), pp. 1–8.

[80] G. Kramberger et al.
"Radiation hardness of thin low gain avalanche detectors".
In: *Nuclear Instruments and Methods in Physics Research Section A: Accelerators, Spectrometers, Detectors and Associated Equipment* 891 (2018), pp. 68–77.

[81] G. Kramberger.
"Signal development in irradiated silicon detectors".
PhD thesis. Stefan Inst., Ljubljana, 2001.

[82] I. Vila Alvarez, Instituto de Física de Cantabria (CSIC-UC).
Radiation tolerance of thin LGAD detectors and in-depth study of ILGAD timing performance.
14th Trento Workshop on Advanced Silicon Radiation Detectors.
2019.

[83] Raymond N. Williams and Ewan M. Lawson.
"The plasma effect in silicon semiconductor radiation detectors".
In: *Nuclear Instruments and Methods* 120.2 (1974), pp. 261–268.
ISSN: 0029-554X.
DOI: https://doi.org/10.1016/0029-554X(74)90044-5.
URL: https://www.sciencedirect.com/science/article/pii/0029554X74900445.

[84] F.R. Palomo.
Plasma Effects in TCT-TPA.
35th RD50 Workshop, CERN.
2019.

[85] KK Sharma.
Optics: principles and applications.
Academic Press, 2006.

[86] Svelto Orazio.
Principles of lasers.
Springer, New York, 2010.

[87] Robert W Boyd.
Nonlinear optics, 3rd.
Elsevier, 2003.

[88] Claude Rulliere et al.
Femtosecond laser pulses.

Springer, 2005.

[89] Taissija I Trofimowa.
"Wechselwirkung elektromagnetischer Wellen mit Materie".
In: *Physik*.
Springer, 1997,
Pp. 259–264.

[90] Jesse Noffsinger et al.
"Phonon-Assisted Optical Absorption in Silicon from First Principles".
In: *Phys. Rev. Lett.* 108 (16 2012), p. 167402.
DOI: 10.1103/PhysRevLett.108.167402.
URL: https://link.aps.org/doi/10.1103/PhysRevLett.108.167402.

[91] Ricardo R. L. Zucca and Y. R. Shen.
"Wavelength-Modulation Spectra of Some Semiconductors".
In: *Phys. Rev. B* 1 (6 1970), pp. 2668–2676.
DOI: 10.1103/PhysRevB.1.2668.
URL: https://link.aps.org/doi/10.1103/PhysRevB.1.2668.

[92] H. H. Li.
"Refractive index of silicon and germanium and its wavelength and temperature derivatives".
In: *Journal of Physical and Chemical Reference Data* 9.3 (1980), pp. 561–658.
DOI: 10.1063/1.555624.
URL: https://doi.org/10.1063/1.555624.

[93] Malte Ruben Vogt.
"Development of physical models for the simulation of optical properties of solar cell modules".
PhD thesis. Technische Informationsbibliothek (TIB), 2016.

[94] C. Scharf, F. Feindt, and R. Klanner.
"Influence of radiation damage on the absorption of near-infrared light in silicon".
In: *Nuclear Instruments and Methods in Physics Research Section A: Accelerators, Spectrometers, Detectors and Associated Equipment* 968 (2020), p. 163955.
ISSN: 0168-9002.
DOI: https://doi.org/10.1016/j.nima.2020.163955.
URL: http://www.sciencedirect.com/science/article/pii/S0168900220304277.

[95] Raul Del Coso and Javier Solis.
"Relation between nonlinear refractive index and third-order susceptibility in absorbing media".
In: *JOSA B* 21.3 (2004), pp. 640–644.

[96] Maria Göppert-Mayer.
"Über Elementarakte mit zwei Quantensprüngen".
In: *Annalen der Physik* 401.3 (1931), pp. 273–294.

[97] W Kaiser and CGB Garrett.
"Two-photon excitation in CaF2:Eu2+".
In: *Physical review letters* 7.6 (1961), p. 229.

[98] David A Kleinman.

"Laser and two-photon processes".
In: *Physical Review* 125.1 (1962), p. 87.

[99] Stephen Buchner.
Laser Simulation of Single-Event Effects: A state of the art review.
Tech. rep.
Martin Marietta Labs Baltimore MD, 1995.

[100] Dale McMorrow et al.
"Subbandgap laser-induced single event effects: Carrier generation via two-photon absorption".
In: *IEEE Transactions on Nuclear Science* 49.6 (2002), pp. 3002–3008.

[101] R. Paschotta.
'Chromatic Dispersion' in the RP Photonics Encyclopedia.
17.06.2020.
URL: `https://www.rp-photonics.com/`.

[102] Ian Walmsley, Leon Waxer, and Christophe Dorrer.
"The role of dispersion in ultrafast optics".
In: *Review of Scientific Instruments* 72.1 (2001), pp. 1–29.
DOI: `10.1063/1.1330575`.
eprint: `https://doi.org/10.1063/1.1330575`.
URL: `https://doi.org/10.1063/1.1330575`.

[103] Berge Tatian.
"Fitting refractive-index data with the Sellmeier dispersion formula".
In: *Applied optics* 23.24 (1984), pp. 4477–4485.

[104] Moritz Wiehe et al.
"Development of a Tabletop Setup for the Transient Current Technique Using Two Photon Absorption in Silicon Particle Detectors".
In: *IEEE Transactions on Nuclear Science* (2020).

[105] C Hnatovsky et al.
"High-resolution study of photoinduced modification in fused silica produced by a tightly focused femtosecond laser beam in the presence of aberrations".
In: *Journal of applied physics* 98.1 (2005), p. 013517.

[106] Benjamin P Cumming et al.
"Effect of refractive index mismatch aberration in arsenic trisulfide".
In: *Applied Physics B* 109.2 (2012), pp. 227–232.

[107] Jean-Claude M. Diels et al.
"Control and measurement of ultrashort pulse shapes (in amplitude and phase) with femtosecond accuracy".
In: *Appl. Opt.* 24.9 (1985), pp. 1270–1282.
DOI: `10.1364/AO.24.001270`.
URL: `http://ao.osa.org/abstract.cfm?URI=ao-24-9-1270`.

[108] Daniel J Kane and Rick Trebino.
"Characterization of arbitrary femtosecond pulses using frequency-resolved optical gating".
In: *IEEE Journal of Quantum Electronics* 29.2 (1993), pp. 571–579.

[109] C. Iaconis and I. A. Walmsley.
"Spectral phase interferometry for direct electric-field reconstruction of ultrashort optical pulses".
In: *Opt. Lett.* 23.10 (1998), pp. 792–794.
DOI: 10.1364/OL.23.000792.
URL: http://ol.osa.org/abstract.cfm?URI=ol-23-10-792.

[110] Swamp optics.
Optics Tutorial - Interferometric Autocorrelation.
2021.
URL: swampoptics.com.

[111] Jean-Claude Diels and Wolfgang Rudolph.
Ultrashort laser pulse phenomena.
Elsevier, 2006.

[112] Christian Spielmann, Lin Xu, and Ferenc Krausz.
"Measurement of interferometric autocorrelations: comment".
In: *Applied optics* 36.12 (1997), pp. 2523–2525.

[113] Martin A. Green.
"Self-consistent optical parameters of intrinsic silicon at 300K including temperature coefficients".
In: *Solar Energy Materials and Solar Cells* 92.11 (2008), pp. 1305 –1310.
ISSN: 0927-0248.
DOI: https://doi.org/10.1016/j.solmat.2008.06.009.
URL: http://www.sciencedirect.com/science/article/pii/S0927024808002158.

[114] Eric W Van Stryland et al.
"Two photon absorption, nonlinear refraction, and optical limiting in semiconductors".
In: *Optical Engineering* 24.4 (1985), p. 244613.

[115] Nick K Hon, Richard Soref, and Bahram Jalali.
"The third-order nonlinear optical coefficients of Si, Ge, and Si1- x Ge x in the midwave and longwave infrared".
In: *Journal of Applied Physics* 110.1 (2011), p. 9.

[116] Alan D. Bristow, Nir Rotenberg, and Henry M. van Driel.
"Two-photon absorption and Kerr coefficients of silicon for 850–2200nm".
In: *Applied Physics Letters* 90.19 (2007), p. 191104.
DOI: 10.1063/1.2737359.
eprint: https://doi.org/10.1063/1.2737359.
URL: https://doi.org/10.1063/1.2737359.

[117] Mariacristina Rumi and Joseph W Perry.
"Two-photon absorption: an overview of measurements and principles".
In: *Advances in Optics and Photonics* 2.4 (2010), pp. 451–518.

[118] Jet Meitzner et al.
"Time-resolved measurement of free carrier absorption, diffusivity, and internal quantum efficiency in silicon".
In: *Applied Physics Letters* 103.9 (2013), p. 092101.

[119] Rohan D. Kekatpure and Mark L. Brongersma.
"Near-infrared free-carrier absorption in silicon nanocrystals".
In: *Opt. Lett.* 34.21 (2009), pp. 3397–3399.
DOI: 10.1364/OL.34.003397.
URL: http://ol.osa.org/abstract.cfm?URI=ol-34-21-3397.

[120] PE Schmid.
"Optical absorption in heavily doped silicon".
In: *Physical Review B* 23.10 (1981), p. 5531.

[121] IB Bogatyrev et al.
"Non-linear absorption of 1.3-μ m wavelength femtosecond laser pulses focused inside semiconductors: Finite difference time domain-two temperature model combined computational study".
In: *Journal of Applied Physics* 110.10 (2011), p. 103106.

[122] P. P. Pronko et al.
"Avalanche ionization and dielectric breakdown in silicon with ultrafast laser pulses".
In: *Phys. Rev. B* 58 (5 1998), pp. 2387–2390.
DOI: 10.1103/PhysRevB.58.2387.
URL: https://link.aps.org/doi/10.1103/PhysRevB.58.2387.

[123] Hyungson Ki and Jyoti Mazumder.
"Numerical simulation of femtosecond laser interaction with silicon".
In: *Journal of Laser Applications* 17.2 (2005), pp. 110–117.
DOI: 10.2351/1.1848529.
eprint: https://doi.org/10.2351/1.1848529.
URL: https://doi.org/10.2351/1.1848529.

[124] Nadezhda M Bulgakova et al.
"A general continuum approach to describe fast electronic transport in pulsed laser irradiated materials: The problem of Coulomb explosion".
In: *Applied physics A* 81.2 (2005), pp. 345–356.

[125] ZEISS microscopy.
Reflected Light Microscopy.
2021.
URL: http://zeiss-campus.magnet.fsu.edu/articles/basics/reflected.html.

[126] Zafer A Yasa and Nabil M Amer.
"A rapid-scanning autocorrelation scheme for continuous monitoring of picosecond laser pulses".
In: *Optics communications* 36.5 (1981), pp. 406–408.

[127] Thorlabs.
Optical substrates.
2021.
URL: https://www.thorlabs.com/newgrouppage9.cfm?objectgroup_id=6973&tabname=N-BK7.

[128] V Alex, S Finkbeiner, and J Weber.
"Temperature dependence of the indirect energy gap in crystalline silicon".
In: *Journal of Applied Physics* 79.9 (1996), pp. 6943–6946.

[129] James C Sturm and Casper M Reaves.
"Silicon temperature measurement by infrared absorption. Fundamental processes and doping effects".
In: *IEEE Transactions on electron devices* 39.1 (1992), pp. 81–88.

[130] Gary F. Sinclair et al.
"Temperature Dependence of the Kerr Nonlinearity and Two-Photon Absorption in a Silicon Waveguide at 1.55 μm".
In: *Phys. Rev. Applied* 11 (4 2019), p. 044084.
DOI: 10.1103/PhysRevApplied.11.044084.
URL: https://link.aps.org/doi/10.1103/PhysRevApplied.11.044084.

[131] Newport Corporation.
Motion in 3-D: Newport Hexapod Coordinate Systems.
2020.

[132] S. Bharthuar et al.
"Study of interpad-gap of HPK 3.1 production LGADs with Transient Current Technique".
In: *Nuclear Instruments and Methods in Physics Research Section A: Accelerators, Spectrometers, Detectors and Associated Equipment* 979 (2020), p. 164494.
ISSN: 0168-9002.
DOI: https://doi.org/10.1016/j.nima.2020.164494.
URL: https://www.sciencedirect.com/science/article/pii/S0168900220308913.

[133] M. Mandurrino et al.
"Analysis and numerical design of Resistive AC-Coupled Silicon Detectors (RSD) for 4D particle tracking".
In: *Nuclear Instruments and Methods in Physics Research Section A: Accelerators, Spectrometers, Detectors and Associated Equipment* 959 (2020), p. 163479.
ISSN: 0168-9002.
DOI: https://doi.org/10.1016/j.nima.2020.163479.

[134] M. Tornago et al.
"Resistive AC-Coupled Silicon Detectors: Principles of operation and first results from a combined analysis of beam test and laser data".
In: *Nuclear Instruments and Methods in Physics Research Section A: Accelerators, Spectrometers, Detectors and Associated Equipment* 1003 (2021), p. 165319.
ISSN: 0168-9002.
DOI: 10.1016/j.nima.2021.165319.

[135] H. Sadrozinski et al.
Development of AC-LGADs for large-scale high-precision time and position measurements.
TREDI – 16th Workshop on Advanced Silicon Radiation Detectors.
2021.

[136] Esteban Currás et al.
"Inverse Low Gain Avalanche Detectors (iLGADs) for precise tracking and timing applications".
In: *Nuclear Instruments and Methods in Physics Research Section A: Accelerators, Spectrometers, Detectors and Associated Equipment* 958 (2020), p. 162545.

[137] A. Doblas Moreno et al.

Technology Developments on Thin iLGAD Sensors for Pixelated Timing Detectors.
TREDI – 16th Workshop on Advanced Silicon Radiation Detectors.
2021.

[138] Petja Skomina.
Studies of effective inter-pad distance of different HPK and FBK LGADs.
38th RD50 Workshop, CERN.
Jozef Stefan Institute, Ljubljana, 2021.

[139] I Peric.
"Active pixel sensors in high-voltage CMOS technologies for ATLAS".
In: *Journal of Instrumentation* 7.08 (2012), pp. C08002–C08002.
DOI: `10.1088/1748-0221/7/08/c08002`.
URL: `https://doi.org/10.1088/1748-0221/7/08/c08002`.

[140] Marcos Fernández García.
Two Photon Absorption - Transient Current Technique.
2nd TCT Workshop, Ljubljana.
2016.

[141] I. Mandić et al.
"Edge-TCT measurements with the laser beam directed parallel to the strips".
In: *Journal of Instrumentation* 10.08 (2015), P08004–P08004.
DOI: `10.1088/1748-0221/10/08/p08004`.
URL: `https://doi.org/10.1088/1748-0221/10/08/p08004`.

[142] Marcos Fernández García.
Two Photon Absorption-TCT on HV-CMOS, LGADs and diodes.
30th RD50 Workshop, Krakow.
2017.

[143] Sebastian Pape.
A table-top Two Photon Absorption – TCT system: experimental results.
38th RD50 Workshop, CERN.
CERN and Technische Universität Dortmund, 2021.

Acknowledgment

First of all I thank Raúl Montero for his invaluable help with all matters concerning lasers and optics. His advice was crucial for the successful construction of the TPA-setup. Also, I thank Ivan Vila for many interesting discussions about TPA and LGADs and Marcos Fernández García for his continuous mentoring, help and advice. I am happy that Sebastian Pape will take over the TPA-TCT project after my departure and thank him for interesting discussions, excellent questions and support in the laboratory during the last months. Furthermore, my thanks go to all present and former members of the SSD team, especially Laura, Isidre, Sofia, Ana, Esteban, Andrea, Carmel, Anja, Pedro, Matteo, Julian, Vendula, William, Marius, Ruddy and Yana, whose support and team-spirit is second to none. Last but not least I thank my supervisors Michael Moll, Ulrich Parzefall and Christian Weiser for their support and encouragement during my time at CERN and at the University of Freiburg.
This work has been sponsored by the Wolfgang Gentner Programme of the German Federal Ministry of Education and Research.